

Morrell, Rachel Elizabeth (2006) Dosimetry and optimisation in high dose fluoroscopic and fluorographic procedures. PhD thesis, University of Nottingham.

Access from the University of Nottingham repository:

http://eprints.nottingham.ac.uk/10181/1/Rachel%27s_Thesis.pdf

Copyright and reuse:

The Nottingham ePrints service makes this work by researchers of the University of Nottingham available open access under the following conditions.

- Copyright and all moral rights to the version of the paper presented here belong to the individual author(s) and/or other copyright owners.
- To the extent reasonable and practicable the material made available in Nottingham ePrints has been checked for eligibility before being made available.
- Copies of full items can be used for personal research or study, educational, or not-for-profit purposes without prior permission or charge provided that the authors, title and full bibliographic details are credited, a hyperlink and/or URL is given for the original metadata page and the content is not changed in any way.
- Quotations or similar reproductions must be sufficiently acknowledged.

Please see our full end user licence at:

http://eprints.nottingham.ac.uk/end_user_agreement.pdf

A note on versions:

The version presented here may differ from the published version or from the version of record. If you wish to cite this item you are advised to consult the publisher's version. Please see the repository url above for details on accessing the published version and note that access may require a subscription.

For more information, please contact eprints@nottingham.ac.uk

**Dosimetry and Optimisation in High Dose
Fluoroscopic and Fluorographic Procedures**

by

Rachel Elizabeth Morrell, MSc, MIPEM

Thesis submitted to the University of Nottingham
for the degree of Doctor of Philosophy, March 2006

Contents

CHAPTER 1 - INTRODUCTION.....	1
1.1 THESIS OUTLINE	1
1.2 FLUOROSCOPY AND FLUOROGRAPHY	4
1.2.1 <i>Standard Radiography and Fluoroscopy</i>	5
1.2.2 <i>Cardiovascular Imaging and Interventions</i>	6
1.2.3 <i>Mobile Fluoroscopy</i>	8
1.2.4 <i>Imaging Technology</i>	9
1.3 PATIENT RADIATION DOSE	11
1.3.1 <i>Stochastic Effects</i>	11
1.3.2 <i>Deterministic Effects</i>	11
1.3.3 <i>Measures of Radiation Dose</i>	12
1.3.4 <i>Typical doses</i>	13
1.4 OPTIMISATION.....	14
1.5 DOSE REDUCTION MEASURES.....	16
1.5.1 <i>Design Features for Dose Limitation</i>	16
1.5.2 <i>Beam Filtration</i>	18
1.5.3 <i>Operator Practice</i>	21
1.6 SUMMARY	21
CHAPTER 2 - IMAGE QUALITY ASSESSMENT.....	23
2.1 INTRODUCTION.....	23
2.1.1 <i>Image Quality Characteristics</i>	23
2.1.2 <i>Image Quality Assessment</i>	24
2.2 PHYSICAL MEASURES AND MODELLING	25
2.2.1 <i>Signal-to-Noise Ratio</i>	26
2.2.2 <i>Contrast</i>	27
2.2.3 <i>Monte Carlo Modelling</i>	27
2.2.4 <i>Limitations</i>	28
2.3 CONTRAST DETAIL TESTS	28

2.4	FORCED CHOICE EXPERIMENTS	30
2.5	RECEIVER OPERATING CHARACTERISTIC (ROC) STUDIES.....	32
2.5.1	<i>Methodology</i>	32
2.5.2	<i>Practical Considerations</i>	34
2.6	VISUAL GRADING ANALYSIS (VGA)	35
2.7	IMAGE QUALITY CRITERIA.....	37
2.7.1	<i>Cardiac Criteria</i>	37
2.7.2	<i>Image Criteria Score</i>	38
2.7.3	<i>Recommendations Arising from Clinical Experience</i>	39
2.8	OBSERVER VARIATION.....	40
2.9	SUMMARY	41
CHAPTER 3 - SKIN DOSE IN CARDIAC CATHETERIZATION		43
3.1	INTRODUCTION.....	43
3.2	CLINICAL BACKGROUND.....	43
3.2.1	<i>Coronary Angiography</i>	43
3.2.2	<i>Coronary Angioplasty</i>	45
3.3	SKIN DOSE AND DETERMINISTIC INJURIES	47
3.4	LEGISLATION AND GUIDANCE	50
3.5	SKIN DOSIMETRY	51
3.5.1	<i>Dose Area Product</i>	52
3.5.2	<i>Fluoroscopy Time</i>	54
3.5.3	<i>Thermoluminescence Dosimetry</i>	55
3.5.4	<i>Scintillation Detectors and Diodes</i>	56
3.5.5	<i>Film Dosimetry</i>	57
3.5.6	<i>Dose Modelling</i>	59
3.6	DOSE MANAGEMENT	60
3.7	SUMMARY	61
CHAPTER 4 - CALIBRATION OF DOSIMETRY EQUIPMENT		63
4.1	INTRODUCTION.....	63
4.1.1	<i>Objectives</i>	64
4.2	METHOD	65
4.2.1	<i>Film Response Curve</i>	67

4.2.2	<i>Film Consistency</i>	68
4.2.3	<i>Equalisation Filter</i>	69
4.2.4	<i>Backscatter</i>	70
4.2.5	<i>DAP Meter</i>	70
4.3	RESULTS.....	71
4.3.1	<i>Film Response Curve</i>	71
4.3.2	<i>Film Consistency</i>	75
4.3.3	<i>Equalisation Filter</i>	78
4.3.4	<i>Backscatter</i>	79
4.3.5	<i>DAP Meter</i>	80
4.4	DISCUSSION.....	80
4.4.1	<i>Film Response Curve</i>	80
4.4.2	<i>Film Consistency</i>	81
4.4.3	<i>Equalisation Filter</i>	82
4.4.4	<i>Backscatter</i>	84
4.4.5	<i>Definitive Calibration and Overall Uncertainty</i>	85
4.4.6	<i>DAP Meter</i>	87
4.5	SUMMARY.....	88
CHAPTER 5 - SKIN DOSE SURVEY.....		89
5.1	INTRODUCTION.....	89
5.1.1	<i>Objectives</i>	90
5.2	METHOD.....	90
5.2.1	<i>Film Measurements</i>	91
5.2.2	<i>Dose Area Product</i>	92
5.2.3	<i>Complexity Indicators</i>	93
5.3	RESULTS.....	94
5.3.1	<i>Film Measurements</i>	94
5.3.2	<i>Dose Area Product</i>	95
5.3.3	<i>Complexity Indicators</i>	100
5.4	DISCUSSION.....	102
5.4.1	<i>Film Measurements</i>	102
5.4.2	<i>Dose Area Product</i>	103
5.4.3	<i>Complexity Indicators</i>	104

5.4.4	<i>Implications</i>	105
5.5	SUMMARY	106
CHAPTER 6 - SKIN DOSE MODELLING.....		108
6.1	INTRODUCTION.....	108
6.1.1	<i>Objectives</i>	108
6.2	METHOD	109
6.2.1	<i>Data Input</i>	110
6.2.2	<i>Dose Calculation</i>	113
6.2.3	<i>Contribution from Fluoroscopy</i>	118
6.2.4	<i>Comparison of Calculated and Measured Doses</i>	120
6.3	RESULTS	120
6.3.1	<i>Example Dose Map</i>	120
6.3.2	<i>Doses of More than 1 Gy</i>	122
6.3.3	<i>Doses of Less than 1 Gy</i>	123
6.4	DISCUSSION	128
6.4.1	<i>Acquisition Only</i>	128
6.4.2	<i>Estimated Contributions from Fluoroscopy</i>	128
6.4.3	<i>Clinical Usefulness</i>	130
6.4.4	<i>Limitations</i>	130
6.5	SUMMARY	132
CHAPTER 7 - BARIUM ENEMA DOSE REDUCTION.....		133
7.1	INTRODUCTION.....	133
7.1.1	<i>Clinical Background</i>	134
7.1.2	<i>Literature Review</i>	135
7.1.3	<i>Objectives</i>	137
7.2	METHOD	137
7.2.1	<i>Baseline Survey</i>	137
7.2.2	<i>Imaging Protocol</i>	138
7.2.3	<i>Dose Modelling</i>	140
7.2.4	<i>Dose Reduction</i>	143
7.3	RESULTS	145
7.3.1	<i>Baseline Survey</i>	145

7.3.2	<i>Dose Modelling</i>	146
7.3.3	<i>Dose Reduction</i>	150
7.4	DISCUSSION.....	151
7.4.1	<i>Baseline Survey</i>	151
7.4.2	<i>Dose Modelling</i>	152
7.4.3	<i>Dose Reduction</i>	153
7.5	SUMMARY.....	154
CHAPTER 8 - BARIUM ENEMA OPTIMISATION.....		156
8.1	INTRODUCTION.....	156
8.1.1	<i>Literature Review</i>	156
8.1.2	<i>Objectives</i>	158
8.2	METHOD.....	158
8.2.1	<i>Phantom Measurements</i>	158
8.2.2	<i>Tube Loading</i>	160
8.2.3	<i>Clinical Validation</i>	160
8.2.4	<i>Effective Doses</i>	162
8.3	RESULTS.....	162
8.3.1	<i>Phantom Measurements</i>	162
8.3.2	<i>Tube Loading</i>	165
8.3.3	<i>Clinical Validation</i>	166
8.3.4	<i>Effective Doses</i>	169
8.4	DISCUSSION.....	169
8.4.1	<i>Phantom Measurements</i>	169
8.4.2	<i>Tube Loading</i>	171
8.4.3	<i>Clinical Validation</i>	171
8.4.4	<i>Image Quality Considerations</i>	172
8.4.5	<i>Effective Doses</i>	173
8.5	SUMMARY.....	173
CHAPTER 9 - GENERAL DISCUSSION.....		175
9.1	INTRODUCTION.....	175
9.2	CARDIOLOGY: FILM DOSIMETRY.....	176
9.2.1	<i>Research Summary</i>	176

9.2.2	<i>Implications and Limitations</i>	177
9.3	CARDIOLOGY: SKIN DOSE MODELLING	178
9.3.1	<i>Research Summary</i>	178
9.3.2	<i>Implications and Limitations</i>	178
9.4	BARIUM ENEMA OPTIMISATION	179
9.4.1	<i>Research Summary</i>	179
9.4.2	<i>Implications and Limitations</i>	181
9.5	PROPOSALS FOR FURTHER WORK	182
9.5.1	<i>Improvements to Skin Dosimetry Software</i>	182
9.5.2	<i>Patient Counselling and Aftercare</i>	183
9.5.3	<i>Optimisation in the Cardiac Catheterization Laboratory</i>	184
9.5.4	<i>Defining Image Quality Criteria</i>	185
APPENDIX I: MATLAB SCRIPTS		187
	GETRUNDATA.M	187
	RUNMODEL.M.....	189
APPENDIX II: JOURNAL ARTICLES AND CONFERENCE PAPERS		192
	JOURNAL ARTICLES	192
	CONFERENCE PRESENTATIONS	193
REFERENCES		194

Abstract

This thesis describes the search for a practical skin dosimetry method for cardiac catheterization procedures, and the application of an optimisation strategy in barium enema imaging.

Kodak EDR2 film was characterised across the range of exposure conditions used in the cardiac catheterization laboratory. Its dose-response curve was modelled using a novel equation, and overall uncertainty in film response was estimated. The film saturated at 1 Gy, limiting its usefulness for skin dosimetry. Its performance was found to be strongly dependent on beam filtration, an aspect that had not previously been studied.

The film was then used to measure skin doses to patients undergoing coronary angiograms and angioplasties. For angiograms, all skin doses were well below 1 Gy. For angioplasties, 23% of films showed localised saturation, indicating peak skin doses of at least 1 Gy. Dose-area-product was shown to be a poor predictor of high peak skin dose.

A mathematical model was developed and software written, to calculate patient skin dose maps from exposure and projection data stored in the image files. This offered a practical method for assessing the magnitude and approximate location of the peak skin dose. Accuracy was limited by a lack of information regarding fluoroscopic exposures, couch position and beam limitation. After including an estimated contribution from fluoroscopy, the model successfully identified those patients whose skin doses exceeded 1 Gy.

Following a baseline survey of local barium enema practice, several dose reduction methods were considered. It was decided to introduce copper filtration. 0.1 mm copper reduced mean patient DAP by 37%, without any measurable difference in contrast detail detectability. A detailed phantom study determined the optimal copper thickness as 0.3 mm. This reduced mean patient DAP by 55%, relative to the baseline survey. A visual grading analysis study showed no significant difference in clinical image quality.

Acknowledgements

All of the work reported in this thesis was performed at Nottingham City Hospital NHS Trust. I would like to thank the Medical Physics Directorate for funding my study, and allowing me time for research and writing. I am grateful also to the staff in Radiology and Cardiology, who assisted with data collection and image scoring, and without whom the work would not have been possible.

I am grateful to my supervisors Andy Rogers and Prof. Alan Perkins, for all their advice and encouragement throughout the project.

Thanks to Dr. Nick Gibson for his assistance with the stubborn parts of the Matlab code, Dr. Derek Pearson for his advice on statistical techniques, Dr. Ian Goldby for his help with proof-reading, and Dr. James Leggett for his advice on presentation.

Thanks also to the Radiology Physics team for their patience and understanding – Marie, Jenny, Geraldine, Kevin and especially my office mate Jennifer, for patiently enduring all my frenzied reading and writing sessions.

I am grateful to many other friends and family members, who have helped me to stay sane throughout the process. Special thanks are due to Mum, Dad, Rachel, Naomi and Katharine, who have consistently prayed for me and listened patiently to my ranting on numerous occasions.

Chapter 1 - Introduction

1.1 Thesis Outline

X-ray imaging is a vital tool in modern healthcare. It allows the clinician to see inside the patient's body, to diagnose injury and disease, to assess their severity and to measure the effectiveness of treatment given. It also plays a crucial role in positioning medical devices during surgery and minimally invasive interventions. All this is not without a price however, because exposure to ionising radiation carries a risk of detrimental health effects.

Over the years, developments in X-ray imaging technology and in clinical practice have improved safety for both patients and staff. However, the most complex diagnostic and interventional procedures can still involve high radiation doses to the patient. In order to improve the care of patients undergoing these procedures, it is important both to be able to assess doses, and to reduce them as far as clinical image quality requirements allow. The complex nature of these imaging procedures makes dose assessment and optimisation particularly challenging.

The thesis concentrates on two such imaging specialties. The first is cardiac catheterization, which can involve high radiation doses to the patient's skin, and has been associated with skin burns. It is important to be able to identify patients who may be at risk of such adverse effects, in order to offer them appropriate counselling and after-care. Since many different imaging projections are used in a single procedure, it is difficult to determine the exact radiation dose received by each patient. The thesis deals with the development of practical techniques for skin dosimetry.

The second specialty is barium enema imaging. Here, some of the most radiosensitive organs are often in the primary beam, leading to a relatively high risk of induced cancers. The thesis describes the application of an optimisation strategy to reduce doses to barium enema patients, whilst ensuring that image quality remained adequate for diagnosis.

Below is a brief outline of the purpose and content of each chapter. The first three provide a thorough introduction to the field of study. Chapters 4 to 6 describe the work on skin dosimetry in the cardiac catheterization laboratory, whilst 7 and 8 describe the barium enema optimisation study. The final chapter summarises the research undertaken, brings together the individual chapter discussions and proposes relevant further work. The aims and objectives for each stage of the work are stated at the beginning of the experimental chapters.

Chapter 1 – Introduction

This general introduction defines fluoroscopy and fluorography. It describes the technology used in dynamic X-ray imaging, and outlines some common clinical applications. The risks associated with exposure to ionising radiation are outlined, and methods for assessing patient radiation dose are summarised. Typical doses for common fluoroscopic and fluorographic procedures are compared with those from other types of radiological investigation. The need for optimisation of radiation dose and image quality is then introduced, and the legal requirements for optimisation are summarised. The main challenges associated with determining optimised practice are highlighted. The chapter concludes by reviewing equipment design features and operator techniques that reduce patient radiation dose, and considering their effects on image quality.

Chapter 2 – Image Quality Assessment

This chapter addresses the problem of defining and measuring clinical image quality. A review of the literature summarises the various different methods for assessing imaging performance and comparing the efficacy of different imaging techniques. These range from physical measures and observer performance tests on simple phantoms, to large-scale investigations of diagnostic accuracy. The concept of ‘quality criteria’ for clinical images is then discussed.

Chapter 3 – Skin Dose in Cardiac Catheterization

The final introductory chapter explains the clinical background to cardiac catheterization procedures and describes the risk of skin injuries associated with them. A review of the literature identifies and compares the various methods by which skin dose can be measured. An overview of current literature on management of patients thought to have received high skin doses is also given.

Chapter 4 – Calibration of Dosimetry Equipment

This chapter describes the characterisation of Kodak EDR2 film, prior to its use for skin dosimetry in the cardiac catheterization laboratory. The film was characterised in detail across the range of typical exposure conditions, for the processor settings used in the local Radiology department. Its response was found to be strongly dependent on beam filtration, a factor that had not been investigated in previous studies. The relationship between optical density and radiation dose was defined using a novel equation, which gave a better fit to the measured data than any previously reported. The limitations of the film as a dosimeter are described, and the uncertainties in skin dose measurements are estimated. The dose-area-product meter was calibrated in parallel with the film, and its performance is also described.

Chapter 5 – Skin Dose Survey

The film was then used to measure skin dose distributions for patients undergoing coronary angiography and angioplasty procedures. This was its first reported use for patient dosimetry at diagnostic X-ray energies within the UK. Peak skin doses for the coronary angiograms are presented. A significant proportion of angioplasty patients were found to be receiving skin doses in excess of 1 Gy, which is the threshold for dose recording recommended by the International Commission on Radiological Protection and the US Food and Drug Administration. Since the film saturated at 1 Gy, it could not be used to assess these high radiation doses. The need for a more robust and flexible method for routine skin dosimetry is demonstrated.

Chapter 6 – Skin Dose Modelling

A mathematical model was developed, to calculate the skin dose distribution across the patient's back, from the exposure and projection information stored in the image files. This chapter describes the function of the model, and compares calculated peak skin doses with those measured on film. Since projection information was available only for the 'acquisition' parts of the procedure, skin doses could be severely underestimated for procedures involving a large proportion of fluoroscopy. Three methods for estimating the contribution from fluoroscopy were proposed, and their accuracy compared. The model was shown to be a potentially powerful tool for estimation of patient skin doses. Its limitations are discussed.

Chapter 7 – Barium Enema Dose Reduction

The clinical background to barium enema examinations is outlined, and a baseline survey of clinical practice described. Perspex phantoms were used to model a typical examination and determine the relative dose contributions from fluoroscopy, digital spot and screen-film imaging. Several potential dose reduction methods were identified, and each was considered in partnership with clinical staff. Following discussions, it was agreed to introduce copper filtration to the X-ray beams. The effects of 0.1 mm copper on entrance dose and threshold contrast were determined using phantoms. The copper was then introduced in clinical practice, and the survey repeated.

Chapter 8 – Barium Enema Optimisation

This chapter describes the search for the optimal quantity of copper filtration, to achieve the lowest patient radiation doses consistent with obtaining reliable diagnostic images. The effects of varying amounts of copper on patient dose and image quality were simulated using Perspex blocks and a contrast detail phantom. The ‘optimal’ copper thickness was chosen, as that which gave the most appropriate balance between dose and image quality. Following clinical implementation, the adequacy of clinical image quality was verified by means of a visual grading analysis study.

Chapter 9 – General Discussion

This chapter summarises the research described in the thesis, and discusses its main contributions to the field, as well as its strengths and weaknesses. Proposals for further work are then set out. These include establishing protocols for management of patients who may be at risk of skin injuries, developing techniques for the assessment of clinical image quality, and optimisation of catheterization laboratory practice.

Some of the research described in the thesis has also been reported in journal articles and conference papers. These are listed in Appendix II.

1.2 Fluoroscopy and Fluorography

Fluoroscopy and fluorography are forms of dynamic X-ray imaging. Both are very important in modern medicine.

Fluoroscopy is generally performed to aid in the positioning of medical devices within a patient, to localise sites for surgical excision, or to position the patient for static radiographs. It uses relatively low radiation dose rates, typically 10 to 80 $\mu\text{Gy}/\text{min}$ at the detector face. This results in rather noisy images. Fluoroscopic images are not usually recorded.

Fluorography is the acquisition of a series of high definition dynamic images. It is used primarily in angiography, the imaging of contrast-enhanced blood vessels. This is a demanding imaging task, requiring high contrast and sharp edge definition with low noise. Typically, much higher detector doses of around 100 to 300 $\mu\text{Gy}/\text{min}$ are used. Images were traditionally recorded using photographic film, but this has now been largely replaced by digital fluorography. Throughout this thesis, the term ‘fluorography’ refers to digital fluorography.

The basic components of fluoroscopic and fluorographic imaging units are:

- An X-ray tube and generator, which are capable of producing a stable X-ray output over long exposure times;
- A detector, capable of dynamic imaging, which is mounted opposite the X-ray tube;
- Digital image processing and storage facilities;
- A display system, for viewing real-time or recorded image sequences.

The specification of each component of the imaging system depends on the clinical tasks for which it will be used. There are three broad categories of fluoroscopic and fluorographic imaging equipment. These are described in the following subsections, along with some of their clinical applications.

1.2.1 Standard Radiography and Fluoroscopy

Figure 1.1 shows a standard radiography and fluoroscopy unit. These are used mainly for contrast investigations of the gastrointestinal tract and urinary system. In barium meals and enemas, fluoroscopy is primarily used to ensure complete coating of the bowel with barium sulphate, and to position the patient for static radiographs. In

bladder pressure studies and cystourethrography, dynamic images are recorded and used for reporting.



Figure 1.1: Radiography and Fluoroscopy Unit.

The X-ray tube is mounted underneath the couch, and the detector above the patient. They have a limited range of motion, to allow superior-inferior and lateral panning. The couch can be tilted, to image the patient in the erect position. Older units have a carriage for film cassettes mounted below the detector, as shown here. Nowadays, static radiographs are usually captured digitally. Some of the most modern radiography and fluoroscopy units incorporate a digital acquisition facility for recording dynamic image series.

1.2.2 Cardiovascular Imaging and Interventions

Cardiovascular imaging requires the highest specification equipment, capable of extensive fluorographic as well as fluoroscopic imaging. It is used in radiology, cardiology and neurology, to obtain angiograms of the patient's blood vessels, and to perform catheter-based interventions.

In angiography, a catheter is inserted into the origin of the vessel of interest. A radio-opaque dye is then injected, and a sequence of fluorographic images acquired, to demonstrate the vessel lumen. Cardiovascular interventions performed through a catheter include widening of occluded blood vessels and insertion of stents, occlusion of enlarged or bleeding vessels, and insertion of cardiac pacemakers. Some interventional procedures can take up to several hours to complete. The X-ray tube must be built to a high specification, with an advanced cooling mechanism, to enable prolonged usage at high outputs.



Figure 1.2: Cardiovascular Imaging Unit.

Figure 1.2 shows a single plane cardiovascular unit. The tube and detector are mounted on a ‘C-arm’ gantry, anchored to the ceiling of the catheterization laboratory. The gantry can be angled to image the patient from an almost continuous range of projections. Single plane units such as this one are generally used in adult cardiac procedures and interventional radiology, since they provide easy access to the patient for cardiac and haemodynamic monitoring, nursing care and emergency resuscitation.

An alternative configuration is the biplane unit, which has a pair of tube and detector assemblies, mounted in different planes. These have the advantage of being able to obtain images in two different projections for each injection of contrast agent. However, they do not allow such flexibility of access to the patient. They are most often used in neuroradiology, and in paediatric coronary interventions.

1.2.3 Mobile Fluoroscopy

Mobile fluoroscopy units are widely used in arthroscopy, endoscopy and other surgical interventions. Here, the X-ray tube and detector are mounted on a wheeled cart, with the generator and viewing monitors on a second cart, as shown in Figure 1.3. Mobile units cannot withstand such high tube loading, so do not usually offer fluorography. Again, the tube and detector are mounted on a ‘C-arm’ gantry, to allow free rotation about the patient.



Figure 1.3: Mobile Fluoroscopy Unit.

1.2.4 Imaging Technology

Good descriptions of the basic construction and function of X-ray tubes and generators are given in textbooks by Forster (1985), Dowsett *et al* (1998), and Dendy and Heaton (1999). Design features specific to fluoroscopic and fluorographic units include efficient anode heat dissipation and cooling mechanisms, to allow prolonged exposures, facilities for pulsing the X-ray beam, and automatic switching of the focal spot size to provide the best compromise between spatial resolution and tube output, as the patient thickness varies.

Until recently, the image intensifier was the only type of detector available for fluoroscopic and fluorographic imaging. Its basic structure is shown in Figure 1.4. The incoming X-ray photons interact with the input phosphor to produce light. When this is absorbed by the photocathode, electrons are emitted. These are then accelerated, so that they gain energy, and focused down onto the output phosphor. Here they are absorbed, with the emission of many more light photons. The resulting image is captured using a video camera or charge-coupled device (CCD). The imaging units shown in Figure 1.1 and Figure 1.3 have image intensifiers.

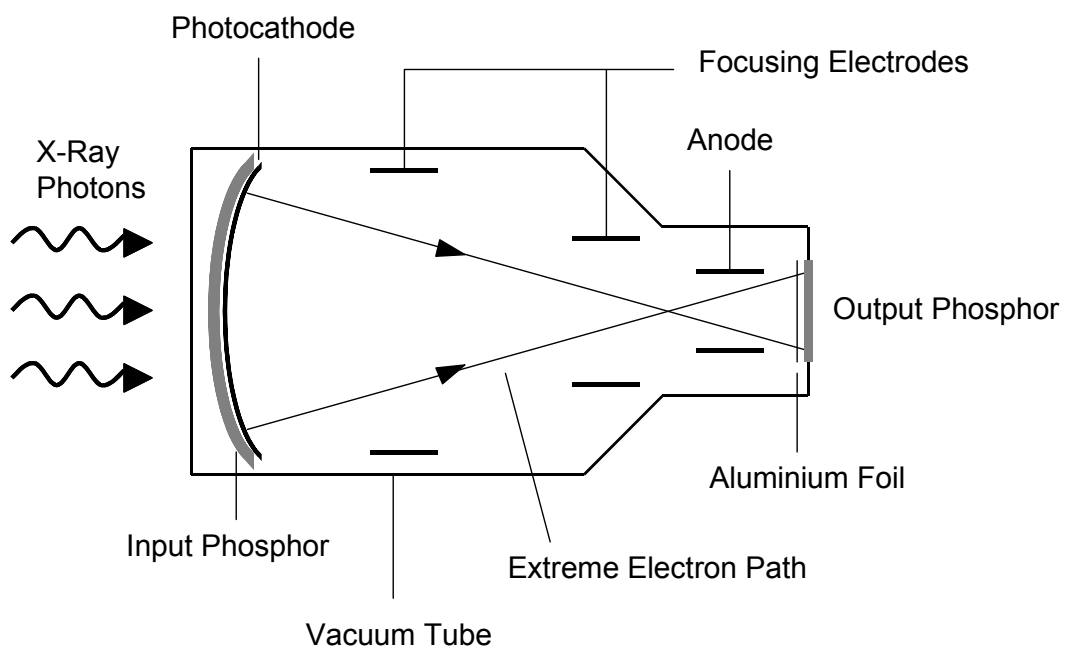


Figure 1.4: Image Intensifier Construction.

In the last few years, direct digital detectors have become available for clinical use, and these have already taken over the market in cardiovascular imaging. Most of these so-called ‘flat panel detectors’ use a layer of scintillating material (caesium iodide), backed by an array of amorphous silicon thin film transistors (TFT), as shown in Figure 1.5. Light produced in the scintillating layer is absorbed in an adjacent TFT element, causing a build-up of charge. The stored charge is then read out electronically. The imaging unit shown in Figure 1.2 has a flat panel detector.

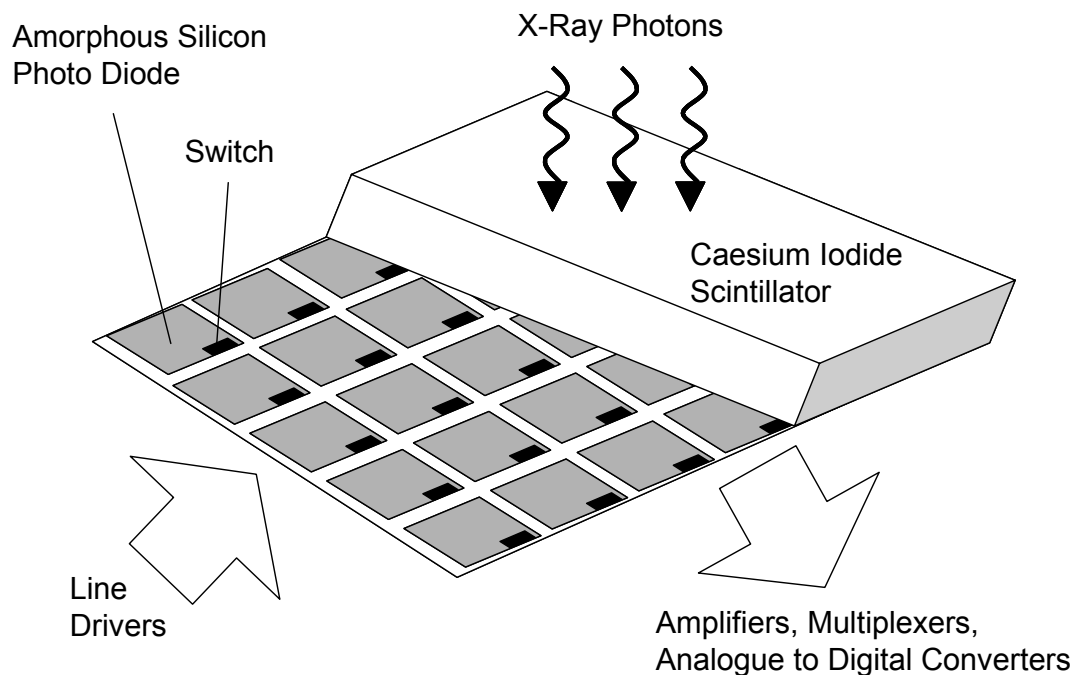


Figure 1.5: Cutaway diagram showing part of a flat panel detector.

The direct digital detector is slightly more efficient than an image intensifier, which allows a corresponding reduction in patient dose. Since the detector array is immediately adjacent to the scintillator, sharper spatial resolution is maintained and the images are not subject to distortion. A more detailed description of the construction and operation of direct digital detectors is given by Moy (2000), Spahn *et al* (2000) and Holmes *et al* (2004).

An anti-scatter grid is usually positioned in front of the detector, to reduce the amount of scattered radiation contributing to the image. On mobile units, the grid is usually fixed. On radiography and fluoroscopy units and on some cardiovascular units, the grid can easily be moved in and out of the beam during clinical procedures.

1.3 Patient Radiation Dose

Fluoroscopic and fluorographic procedures are complex in nature, and can involve relatively high radiation doses to the patient. This is a matter of concern, since exposure to ionising radiation is associated with detrimental health effects.

1.3.1 Stochastic Effects

When ionising radiation interacts with living tissue, some of the electrons are ejected from their orbits, breaking chemical bonds. Individual cells can often repair this damage, but the repair process is occasionally faulty, resulting in mutations. If the chromosomes are damaged, the fault can propagate when the cell divides. In the early stages of pregnancy, this increases the risk of genetic disease in the developing fetus. In all patients, it increases the risk of developing cancers in later life.

These are termed stochastic effects, since there is not thought to be any dose threshold below which they cannot occur. On exposing an organ to ionising radiation, the risk of malignancies developing within that organ is increased by an amount proportional to the dose received.

Symptoms often do not appear until years or even decades after the initial radiation exposure. This makes it impossible to determine which cancers were caused by medical exposures. The National Radiological Protection Board has published estimated risk factors for carcinogenesis, in its document “Estimates of Late Radiation Risks to the UK Population” (National Radiological Protection Board, 1993). These are based largely on studies of atomic bomb survivors and radiation workers.

1.3.2 Deterministic Effects

If a large number of cells in one part of the body are killed or sterilised, deterministic effects such as skin burns and ocular cataracts can occur. Such injuries only develop after a certain dose threshold has been exceeded. Their severity depends on the magnitude of the dose received.

Interventional radiology and cardiology procedures can involve prolonged irradiation of particular areas of the patient's skin, and are known to carry a risk of radiation burns. This was the primary motivation for the skin dosimetry work described in this thesis. The issue is addressed in detail in Chapter 3.

1.3.3 Measures of Radiation Dose

The fundamental dose quantity used in radiology is the absorbed dose to a tissue or organ. This is defined as the energy absorbed per unit mass of tissue, and is given the special unit Gray (Gy), where 1 Gy is equivalent to 1 Joule per kilogram.

Patient radiation dose is commonly measured using a dose-area-product (DAP) meter. This is a transmission ionisation chamber that is fitted at the output window of the X-ray collimator assembly, so as to intercept the whole of the X-ray beam. The charge collected in the chamber is proportional to both radiation dose and beam area. DAP meters are now fitted as standard to new X-ray units, to comply with The Ionising Radiations Regulations 1999. The integral DAP for an examination gives a general indication of the total dose received by the patient, but offers no information about the breakdown of dose to individual organs.

More precise measurements of the doses to particular tissues or organs may be obtained using thermoluminescence dosimeters, scintillation detectors, diodes or radiographic films, all of which are described in more detail in Chapter 3. Direct measurements can be made for organs that are readily accessible. Doses to inaccessible organs can be measured in an anthropomorphic phantom, for typical exposures associated with the procedure of interest.

Alternatively, doses to internal organs may be estimated using Monte-Carlo modelling. This is a computational technique, in which the paths of a large number of photons are tracked in a mathematical model of the human body, and the absorbed dose to each organ is calculated. The National Radiological Protection Board has produced tables of Monte-Carlo data for a series of standard radiographic projections (Hart *et al*, 1994), and these may be interrogated using software such as 'XDOSE' (National Radiation Laboratory, Ministry of Health, Christchurch, New Zealand). There are now also a small number of commercially available software packages for performing Monte-Carlo dose calculations. These are much more flexible, since they

allow the user more control over radiographic parameters such as field size and projection, tube voltage and beam filtration. Examples include ‘PCXMC’ (STUK, Helsinki, Finland) and ODS-60 (Rados Technology, Turku, Finland).

‘Effective’ or ‘whole body’ dose is a measure of the total dose to all the organs of the body, weighted according to their radiation sensitivity (International Commission on Radiological Protection, 1991b). It is an indicator of the risk of inducing stochastic effects, such as cancer (National Radiological Protection Board, 1993). It may be estimated using the Monte-Carlo dosimetry software described above. Effective dose uses a special unit, called the Sievert (Sv).

1.3.4 Typical doses

The National Radiological Protection Board regularly conducts national patient dose surveys, using data from a wide selection of UK hospitals. Table 1.1 shows dose-area-products for a range of fluoroscopic and fluorographic procedures from their most recent survey, published as report NRPB-W14 (Hart *et al*, 2002). Estimated effective doses, from report NRPB-W4, are also shown (Hart & Wall, 2002).

Procedure Type	Mean DAP (Gycm²)	Effective Dose (mSv)
Barium Enema	23.5	7.2
Barium Swallow	8.0	1.5
Urethrogram	4.9	1.1
Coronary Angiogram	30.4	3.1-10.6
Coronary Angioplasty	63.4	5.3-19.5
Nephrostogram	10.4	1.6

Table 1.1: Mean DAP and estimated effective dose for selected fluoroscopic and fluorographic procedures, from NRPB reports W14 (Hart *et al*, 2002) and W4 (Hart & Wall, 2002).

These values may be compared with the other common radiographic procedures listed in Table 1.2. Both DAP and effective dose tend to be much larger for fluoroscopic and fluorographic procedures than for general radiographic examinations. Effective doses are comparable with those obtained in computed tomography (CT).

Procedure Type	Mean DAP (Gycm²)	Effective Dose (mSv)
Abdomen AP	2.5	0.8
Chest PA	0.10	0.02
CT Head	N/A	2
CT Chest	N/A	8
CT Abdomen	N/A	10

Table 1.2: Mean DAP and estimated effective dose for selected general radiography and computed tomography (CT) examinations, from NRPB reports W14 (Hart *et al*, 2002) and W4 (Hart & Wall, 2002). (AP: anteroposterior; PA: posteroanterior; N/A: not applicable.)

Table 1.1 also demonstrates a wide variation in both DAP and effective dose for different types of fluoroscopic and fluorographic procedures. Coronary angioplasties and other vascular interventions are associated with the highest radiation doses, since they can involve prolonged fluoroscopic imaging as well as large numbers of fluorographic image series. Barium enemas carry a relatively high mean DAP and effective dose, since they combine fluoroscopy with multiple radiographs.

1.4 Optimisation

Given the adverse effects associated with exposure to ionising radiation, it is important both to be able to measure patient radiation doses, and to reduce them where possible. Over the years, reductions in patient dose have been achieved through advances in technology and changes in clinical practice. In the UK, repeated national dose surveys by the National Radiological Protection Board have shown a significant lowering of patient dose for individual procedure types (Shrimpton *et al*, 1986; Hart *et al*, 1996; Hart *et al*, 2002). However, whilst some dose reduction measures have a positive effect on image quality, others degrade contrast or increase noise. Thus, it is important not just to reduce doses but to optimise each imaging technique, maximising its efficiency and determining the right balance between dose and image quality.

European Union directive 97/43/Euratom stipulates that: “All doses due to medical exposure for radiological purposes except radiotherapeutic procedures... shall be kept as low as reasonably achievable consistent with obtaining the required diagnostic information...” (The Council of the European Union, 1997). Member states are required to pay special attention to exposures involving high doses to the patient, such as those considered in this study. These requirements have been incorporated into UK legislation in the form of The Ionising Radiation (Medical Exposure) Regulations 2000, which extend the obligations to cover therapeutic as well as diagnostic exposures: “The operator shall select equipment and methods to ensure that for each medical exposure the dose of ionising radiation to the individual undergoing the exposure is as low as reasonably practicable and consistent with the intended diagnostic or therapeutic purpose.”

Thus, radiology providers are under a legal obligation to use the lowest dose that is consistent with obtaining the required clinical information. This raises some important questions, which unfortunately have no straightforward answers.

What image quality is required?

Whilst it is relatively easy to define which structures the clinician needs to be able to see in an image, it is much more difficult to describe how well (s)he needs to be able to see them. There is a conceptual gap between the clinician’s perception of the structures present, and any objective, measurable quantities that the scientist can describe and work with.

The image quality that is required depends strongly on the nature of the imaging task. For example, in interventional cardiology very clear edge definition is needed when imaging the coronary vessels. However, much lower image quality is sufficient for coarse positioning of catheters and guide wires.

How can image adequacy be assessed?

The technical performance of imaging equipment is usually measured using simple test objects, containing regular details of varying size and/or contrast. These tests are both practical and repeatable. However, it is much more difficult to quantify and compare the quality of clinical images, which contain complex structures and varied anatomies and pathologies. Although physical and clinical image quality are clearly

linked, the relationship between them is highly complex and little studied. The issue of image quality assessment is addressed much more fully in Chapter 2.

How can the lowest dose be achieved?

There are a number of different methods for reducing radiation dose, and these affect image quality in different ways. The challenge is to make the most effective use of the imaging equipment, so that the requisite clinical information can be obtained using the lowest practicable dose. Additional factors that may need to be considered when implementing changes in clinical practice are financial cost, impact on clinical workflow, and the maximum load at which the X-ray tube is able to consistently operate.

Some dose reduction methods are well documented and have been adopted as standard practice; others require further exploration. The introduction of new, digital detector technologies presents new opportunities and challenges.

1.5 Dose Reduction Measures

The radiation dose received by the patient depends on both the performance of the imaging equipment, and the technique employed by the operator. This section considers first the design features of modern imaging equipment that limit patient radiation doses, and then the measures that can and should be taken by the operator, to minimise doses wherever possible.

1.5.1 Design Features for Dose Limitation

Modern fluoroscopic and fluorographic imaging systems have a number of design features aimed at minimising patient radiation dose whilst providing good image quality. These include:

Digital image recording. On even the most basic fluoroscopy systems, the final image remains on the screen following termination of the exposure. This allows the operator to spend time studying aspects of the patient's anatomy, without further

adding to their radiation burden. On fluorographic units, digital acquisition provides a permanent record of real-time image series.

Pulsed fluoroscopy. Instead of irradiating the patient and detector continuously, X-rays are emitted in short bursts, which are synchronised with read-out from the detector. More photons are emitted during each pulse than would be emitted in the same time scale during continuous fluoroscopy. This improves the signal to noise ratio, and the spatial resolution of moving objects. The time-averaged dose rate is often lower than for continuous fluoroscopy, resulting in a proportional dose saving.

Spectral filtration. Increasing the amount of X-ray beam ‘filtration’ can substantially reduce the entrance dose to the patient. This method was used in the optimisation study of Chapters 7 and 8, and is described in detail in Section 1.5.2.

Automatic exposure control. The output from the detector is constantly monitored, and kept to a preset value by adjusting the tube voltage (kVp) and current (mA). This automatically compensates for changes in attenuation as different imaging projections are used. The effects on patient dose and image quality depend on the algorithm relating kVp and mA.

Recursive filtering. Image noise can be reduced by means of recursive filtering. Several frames are combined to form each displayed image. This in turn allows a reduction in the dose rate at the detector. However, recursive filtering has a negative impact on both temporal resolution and contrast, for moving objects.

Equalisation filter. If the X-ray beam passes through tissues having very different attenuation properties, or if a portion of the beam misses the patient altogether, glare from the brighter regions of the image can detract from low contrast detail in the darker regions. The purpose of an equalisation filter is to reduce this glare and improve the distribution of displayed pixel values. A metal filter with a wedge-shaped profile is inserted into the X-ray beam, such that the thickest part of the filter covers the low attenuation region. This improves visualisation of low contrast detail. As well as improving diagnostic accuracy, this may allow the observer to reduce the exposure time and hence radiation dose. The filter itself substantially reduces the dose to tissues in its shadow.

Real-time display of radiation dose. All new X-ray units are now fitted with a dose-area-product (DAP) meter. In addition, new cardiovascular units display an indication

of cumulative dose at a fixed point in the X-ray beam, intended to represent the patient skin surface. Such measures are intended to raise operator awareness of patient radiation dose, as this has been shown to encourage more sparing use of radiation (Vehmas, 1997; Yu *et al.*, 2001).

Direct digital detectors. At present, the most common type of detector used in fluoroscopy and fluorography is the image intensifier. Direct digital, or ‘flat panel’ detectors have been introduced in recent years. They have inherently greater detection efficiency than image intensifiers, and this should allow some dose reduction.

1.5.2 Beam Filtration

The beam emitted from an X-ray tube consists of a spectrum of photon energies. The peak energy (kVp) is determined by the potential applied across the tube. A voltage of 80 kV will produce a spectrum something like the blue line in Figure 1.6. It contains a large proportion of low energy photons, including two very large peaks below 10 keV. These photons are readily absorbed in the patient’s body, thus contributing to radiation dose, but not to the formation of the image.

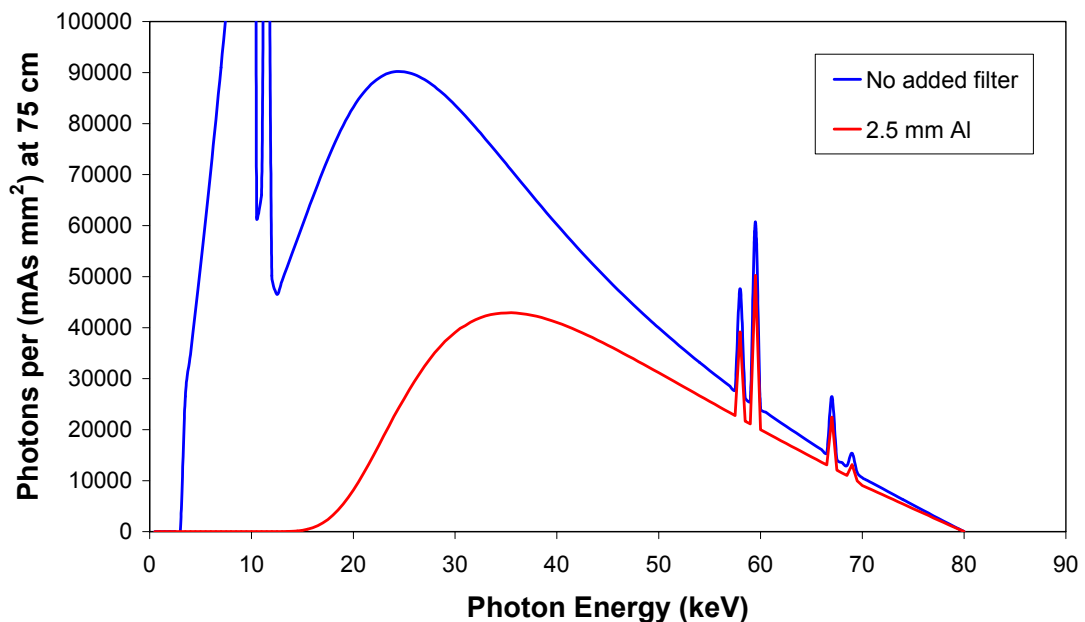


Figure 1.6: Effect of filtration on X-ray spectrum. Data generated using IPEM Report 78 Spectrum Processor (Reilly & Sutton, 1997).

Absorbent material placed between the X-ray source and the patient can be used to 'filter out' the lowest energy photons. The most common filter material is aluminium. According to the UK Medical and Dental Guidance Notes (Institute of Physics and Engineering in Medicine, 2002), filtration equivalent to at least 2.5 mm aluminium must be fitted as standard to medical X-ray tubes. It removes the low energy peaks and raises the mean energy of the X-ray spectrum, as shown by the red line in Figure 1.6. As more filtration is added, the mean spectral energy increases further. Whilst this reduces patient radiation dose, it also degrades image contrast and increases the loading on the X-ray tube, as explained in the following paragraphs.

In X-ray imaging, the most important interaction processes are photoelectric absorption and Compton scatter. Photoelectric absorption occurs more readily in materials with higher atomic numbers, and this is the primary mechanism responsible for imaged contrast between the different structures in the body. It is more likely to take place at low photon energies. As the average spectral energy increases, fewer photons are absorbed and more undergo Compton scattering. Scattered radiation incident on the detector degrades both spatial resolution and contrast. The combined effect of reduced photoelectric absorption and increased Compton scatter can result in loss of visibility of low contrast details. Where additional beam filtration is employed, image contrast may be maintained by reducing the tube voltage.

A further effect of increased filtration is a reduction in photon yield. This may be seen in Figure 1.6, as a reduction in the area under the curve. Since a proportion of the photons are stopped by the filter, the X-ray tube has to work harder to maintain the photon flux at the detector. Thus, tube heat capacity and cooling rate need to be considered, to ensure that the X-ray tube is not overloaded. In order to increase the tube output, many fluoroscopic units automatically raise the tube voltage. Since this degrades image contrast, it may limit the amount of filtration that can be used.

Copper has been recognised as an effective filter material since the nineteen fifties (Trout *et al*, 1952). It has a higher atomic number than aluminium, and 10% greater absorption efficiency (Jennings, 1988). It is physically and chemically stable under normal atmospheric conditions, readily available and inexpensive. Until recently, its application in radiology has been limited, mainly due to the increased tube loading required to maintain image contrast. Although some studies have recommended copper filters of up to 0.3 mm in thickness for chest (Rossi *et al*, 1982; Dobbins *et al*,

2003) and barium enema (Kohn *et al*, 1988; Hansson *et al*, 1997; Geleijns *et al*, 1997; Pärtan *et al*, 2000) examinations, their use has not been widely adopted in clinical practice.

Around the nineteen seventies and eighties, there was considerable interest in filters with higher atomic numbers. Several studies advocated the use of heavy metals such as erbium, gadolinium, holmium and samarium (Atkins *et al*, 1975; Villagran *et al*, 1978; Chakera *et al*, 1982; Fleay *et al*, 1984; Cranage *et al*, 1992). These act as bandpass filters, removing not only the low energy photons from the X-ray spectrum, but also high energy photons above their k-edges, which contribute little to image contrast but add considerable scatter. Reductions in patient entrance dose of up to 50% were reported. However, more detailed studies comparing the performance of a wide range of filter materials have found conventional filters such as copper and iron to be just as effective, whilst placing a smaller load on the X-ray tube (Koedooder & Venema, 1986; Kohn *et al*, 1988; Gagne *et al*, 1994; Sandborg *et al*, 1994a; Hansson *et al*, 1997; Dobbins *et al*, 2003).

In recent years, imaging equipment manufacturers have developed X-ray tubes with advanced cooling mechanisms, which can withstand the increased loads needed to support considerable quantities of beam filtration. This is particularly advantageous in interventional radiology and cardiology, where high quality images are needed to visualise the detailed structure of the small blood vessels, but the patient is at risk of high radiation doses to the skin. A combination of copper filtration with a higher output operating mode has been shown to offer improved iodine contrast for the same patient entrance dose, or reduced dose at the same level of contrast (Hoornaert & Kroon, 1993; den Boer *et al*, 1994a; den Boer *et al*, 1994b). Modern cardiovascular imaging systems are often fitted with optional copper filters up to 0.9 mm in thickness.

A further consequence of this improved X-ray tube technology is that higher atomic number filter materials are receiving renewed attention. The latest cardiovascular imaging systems from Toshiba (Toshiba Medical Systems Corporation, Tochigi, Japan) now employ tantalum k-edge filters.

1.5.3 Operator Practice

The operator has considerable influence over patient radiation dose, and should seek to minimise it by a series of measures such as:

- Minimising the overall exposure time, by working as efficiently as possible and making exposures only when necessary;
- Collimating the beam to the area of interest; as well as reducing the volume of tissue irradiated, this improves low contrast detectability by reducing scatter;
- Minimising the use of high dose rate modes, designed to give enhanced image quality but with an increased dose burden to the patient;
- Minimising the use of magnification modes, which often require a higher dose rate at the detector;
- Using a good spread of X-ray projections, to avoid excessive exposure of any one area of the skin;
- Appropriate use of methods of scatter removal, such as grids. Whilst these remove primarily scattered radiation, they also attenuate the primary beam, so the patient dose must be increased in order to maintain the photon flux at the detector.

1.6 Summary

This chapter introduced fluoroscopy and fluorography, and outlined some of their clinical applications. Basic descriptions of the specialised equipment used in dynamic X-ray imaging were presented.

The risks to the patient from exposure to ionising radiation were described, and the differences between stochastic and deterministic effects explained. The various different methods for assessing patient radiation dose were outlined in brief. Typical doses for fluoroscopic and fluorographic procedures were presented, and compared with typical doses from other radiological investigations. Procedures involving dynamic imaging tend to result in much higher patient doses than are encountered in

general radiography, and to correspond more closely with those found in computed tomography. Cardiac catheterizations and barium enemas were identified as being among the particularly high dose procedures.

The need for optimisation of patient radiation dose and image quality was introduced, and the legal requirements for optimisation were outlined. The law requires that the radiation dose to the patient should be the minimum necessary to give the required clinical information. This implies a need to define image quality requirements for medical exposures. The challenges associated with defining and measuring clinical image quality were highlighted.

The various dose limiting features built into modern fluoroscopic and fluorographic equipment were described, and the effects of each on image quality were considered. The effects of beam filtration were examined in some detail. Dose limitation methods that can and should be employed by the operator were then outlined.

Chapter 2 - Image Quality

Assessment

2.1 Introduction

The goal of radiographic imaging is to demonstrate patient anatomy and pathology well enough to enable reliable, accurate diagnosis or intervention. If the balance between dose and image quality is to be optimised, suitable measures of image quality must first be defined.

This chapter describes several different approaches to image quality assessment. These range from objective, physical measures, and simple estimates of detail visibility, to more sophisticated tests of observer performance, using both phantom and clinical images. Whilst some of these tests are designed to evaluate technical aspects of imaging performance, others are aimed at comparing the information content of clinical images, and assessing observer accuracy in making diagnoses. The various merits and limitations of each method are outlined.

The concept of 'image quality criteria' is then introduced and some examples are given. Finally, some general principles for improving the accuracy and repeatability of observer performance tests are presented.

2.1.1 Image Quality Characteristics

The fundamental characteristics that define image quality are described below.

Contrast. This is essentially the difference in signal intensity on imaging objects that have different attenuation coefficients. The greater the contrast between neighbouring structures, the more readily they can be distinguished. When the primary beam interacts with the patient, some of the X-ray photons are absorbed or scattered, and some pass through the patient to reach the detector. Photoelectric absorption occurs

preferentially in materials with higher atomic numbers, and is the most important interaction process for diagnostic X-ray imaging. The probability of Compton scattering depends on electron density. Hence, it also contributes to image contrast. However, those scattered photons that reach the detector produce a uniform increase in signal intensity across the image, and this has a detrimental effect on contrast.

Noise. This describes the variation in pixel values across an image of a uniform object. The greater the noise, the more difficult it is to distinguish fine detail, and low contrast structures. There are three main sources of noise in a fluoroscopic or fluorographic imaging system. The first is quantum noise, caused by the random nature of the interactions involved in the production and detection of the X-rays. Since X-ray detection follows Poisson statistics, the signal-to-noise ratio can be improved by increasing the X-ray exposure. The second is noise arising from the structure of the detector itself, for example the ‘graininess’ of the phosphor screens in an image intensifier. The third is electronic noise, which affects applied voltages in the detector, as well as the readout circuitry.

Resolution. In a digital imaging system, resolution is limited by the pixel size, by the inherent structure of the detector, and by processes such as scattering of the information carriers within it. Practical image resolution is also limited by geometric unsharpness; the X-ray focal spot has a finite size, and this causes a penumbra at the edges of imaged objects. Another factor affecting the resolution of medical images is motion unsharpness. This can be minimised by asking the patient to keep still and, where relevant, to hold their breath during image acquisition. In coronary imaging, motion unsharpness due to the beating of the heart is minimised by using pulsed imaging, with a rapid frame rate and short pulses.

2.1.2 Image Quality Assessment

In order to optimise imaging techniques, it is essential to be able to define and measure the quality of clinical images, and to assess whether or not they are adequate for their intended purpose. These tasks are particularly challenging, since it is difficult to connect objective measures of technical image quality with clinicians’ reading and perception of the medical image.

Clinical image quality depends on a combination of factors, such as the technical performance of the imaging system, patient cooperation, the skill of the operator and the nature of the imaging task. Image quality requirements can only be understood in relation to a particular medical task, since they depend on the size and contrast of the objects to be imaged, and on the precise clinical question that needs to be answered. What is important is whether the relevant information is contained in the image and can be extracted and interpreted by the viewer. Does the image convey sufficient information for the clinician to make a medical decision with a reasonable degree of accuracy?

The gold standard test of diagnostic accuracy is the clinical outcomes audit. At a defined time interval after exposure, the patient's notes are retrieved and the results of the imaging test are compared with subsequent clinical events or diagnostic investigations. If these studies are to be meaningful, large numbers of patients must be included, and the audit must be performed after an appropriate time interval for the clinical investigation. If the imaging task of interest is early detection of a slowly progressing disease, this may be several months or even years.

For optimisation studies, it is also necessary to have more immediate methods for assessing image adequacy. Before a new technique is trialled on patients, the researchers need to know what its technical effects on image quality will be, in order to predict the likelihood of any changes in the appearance of clinical images. Following implementation, it is important to be able to verify quickly that clinical images continue to fulfil their purpose.

The following sections describe a number of different approaches to image quality assessment. It will be seen that each has both advantages and limitations, and that the fundamental problem of defining what degree of image quality is needed is very difficult in practice.

2.2 Physical Measures and Modelling

The most objective and repeatable way to assess image quality is to measure physical quantities associated with it. This is difficult for clinical images, which are highly complex in nature. Optimisation studies have commonly used simple Perspex

phantoms, with Perspex or iodine-containing details added, to represent clinical imaging tasks such as the detection of low contrast lesions, or visualisation of contrast-filled blood vessels.

2.2.1 Signal-to-Noise Ratio

A systematic approach to optimisation is to compare signal-to-noise ratios for a particular imaging task, using various different imaging conditions. Signal-to-noise ratio (SNR) has been defined by Tapiovaara and Wagner (1985) and later by McParland and Boyd (2000) as

$$SNR = \frac{\overline{S_1 - S_2}}{\sigma(S_1 - S_2)} = \frac{\overline{S_1} - \overline{S_2}}{(\sigma^2(S_1) + \sigma^2(S_2))^{1/2}}$$

Equation 2.1

where $\overline{S_1}$ and $\overline{S_2}$ represent the mean signal intensity in background and signal regions of the image, $\sigma(S_1)$ and $\sigma(S_2)$ the standard deviation in these regions. Other investigators have chosen to consider only the noise in the signal or background regions of the image, not both. Many authors who quote SNR do not state which definition they have used.

Provided that the imaging procedure is quantum noise limited, i.e. the pixel-to-pixel variation in the number of photons detected is greater than the system noise, the SNR varies with the square root of the detector dose. Many researchers have chosen to use the ratio $(SNR)^2/Dose$ as a figure of merit for optimisation, since it is independent of exposure level (Zamenhof, 1982; Boone, 1992; Gagne *et al*, 1994; Tapiovaara & Sandborg, 1995; Dobbins *et al*, 2003; Samei *et al*, 2005; Ullman *et al*, 2005b). For any given procedure type, there will be a series of imaging protocols for which this figure of merit is maximised. An appropriate protocol is then selected from within this set, to give the desired balance between SNR and dose. The dose quantity used in the figure of merit can be tailored to suit the examination type.

2.2.2 Contrast

Contrast is another metric that is commonly used to assess image quality. It is usually defined as the difference between background intensity I_b and signal intensity I_s , divided by background intensity (Kroon, 2003; Samei *et al*, 2005).

$$\text{Contrast} = \frac{I_b - I_s}{I_b}$$

Equation 2.2

An alternative definition adopted by McParland and Boyd (2000) is the ratio of the difference between signal and background intensities, to the sum of the signal and background intensities. Again, many authors who quote contrast values do not specify how they have defined contrast.

2.2.3 Monte Carlo Modelling

Several groups have developed software for mathematical simulation of the imaging process. These generally use Monte Carlo modelling. This powerful computational technique follows the histories of hundreds of thousands of photons as they interact with a virtual phantom and then with a model detector. It enables large-scale studies to be performed quickly and easily, comparing many different combinations of imaging parameters. Whilst many investigators modelled simple Perspex or water phantoms containing contrast details (Zamenhof, 1982; Sandborg & Alm Carlsson, 1992; Tapiovaara & Sandborg, 1995; McParland & Boyd, 2000), others have improved applicability to the clinical situation by using voxel phantoms, developed from computed tomography scans of human subjects (Sandborg *et al*, 2001; Ullman *et al*, 2005a).

The most sophisticated simulations allow the investigator to vary the detector type and efficiency, and the properties of the anti-scatter grid (Sandborg & Alm Carlsson, 1992; Sandborg *et al*, 1993; Sandborg *et al*, 1994b; Kroon, 2003; McVey *et al*, 2003). These can be powerful tools for developing new imaging equipment, tailored to specific clinical applications.

2.2.4 Limitations

Physical measures and modelling of image quality are valuable tools for optimisation. However, each relies on simplifications or assumptions, which limit its accuracy for predicting clinical imaging performance. The outcomes of modelling studies need to be verified empirically, before new techniques are introduced into clinical practice.

Physical measures such as SNR and contrast do not include any consideration of the display and observation stages of the imaging process. They relate to ‘perfect’ observers of the fluoroscopic signal. It is important also to consider the efficiency of (imperfect) human observers, using a real display system. Several different approaches to this are described in the following sections.

2.3 Contrast Detail Tests

Subjective measures of low contrast detectability can be made using standard or custom-built phantoms, and viewing the images by eye. The simplest phantoms contain fixed details of varying size and contrast. Some of the best known are the “Leeds” test objects developed by Hay *et al* (1985) and currently marketed by Leeds Test Objects Limited (Boroughbridge, UK).

Figure 2.1 shows a radiographic image of the Leeds “TO.10” test object. This contains twelve rows of attenuating discs. Each row comprises discs of a different diameter, and the contrast varies from left to right, along each row. The observer views the image under a set of standard conditions, and counts the number of details visible in each row. The results are then compared with tabulated data, relating the number of details seen to threshold contrast, for given X-ray beam quality.

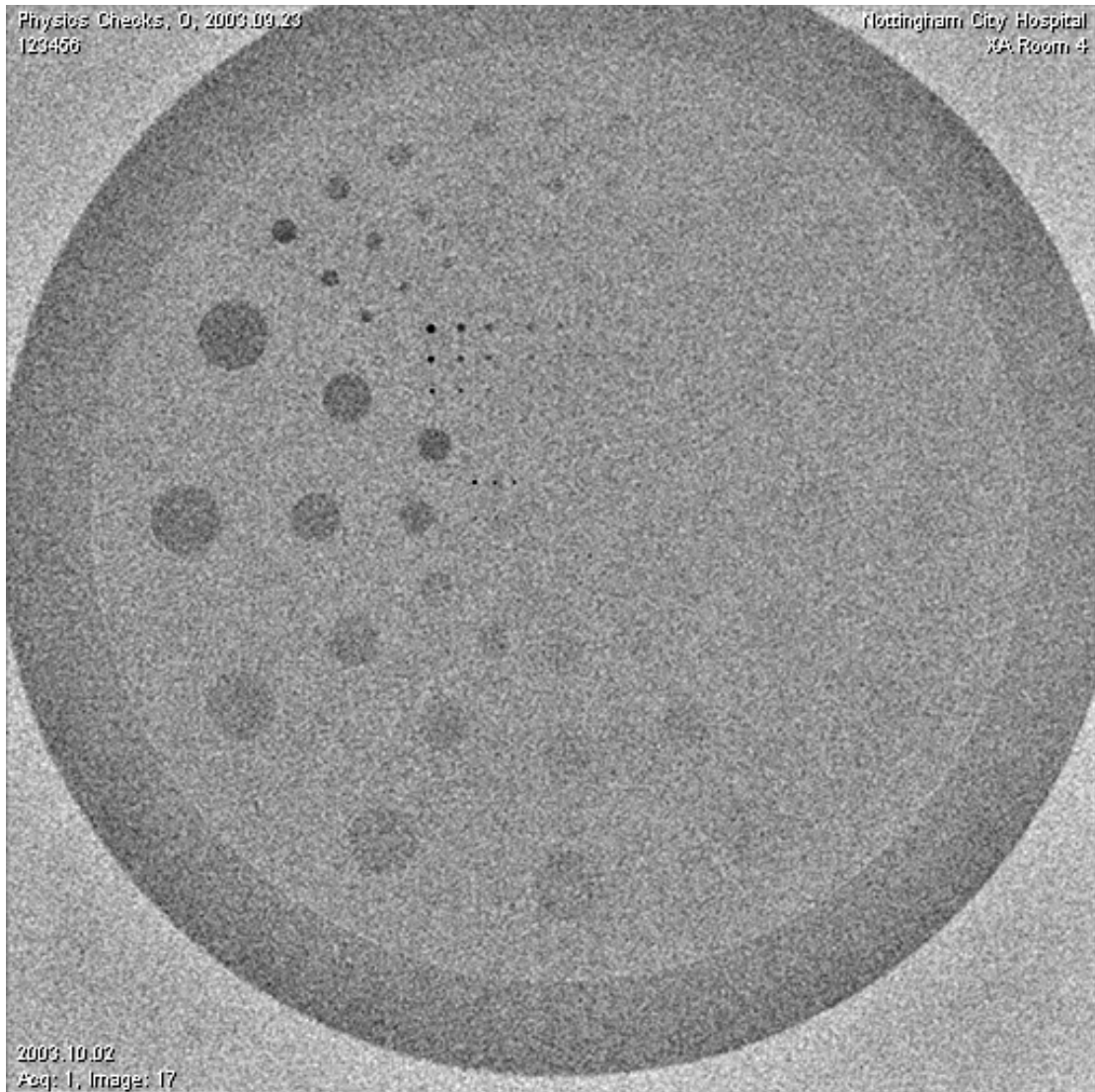


Figure 2.1: Radiographic image of Leeds test object "TO.10".

The tests are quick and easy to perform. They can be reliably used to detect large changes in system performance, and to rank systems according to their contrast and noise characteristics (Cohen *et al*, 1984; Marshall *et al*, 1992; Tapiovaara & Sandborg, 2004). However, they have limited accuracy and reproducibility in identifying absolute threshold contrast, since they depend on the observer's subjective visualisation threshold. This leads to inevitable variation between even the most experienced observers, and between viewing sessions, especially if they are separated by long time intervals.

2.4 Forced Choice Experiments

The forced choice experiment seeks to remove observer bias, by asking the observer to indicate the locations of the details. For each detail size and contrast, an example of the detail's appearance is usually presented to the observer, who is then asked to identify the position of a similar detail, from a fixed number of possible locations.

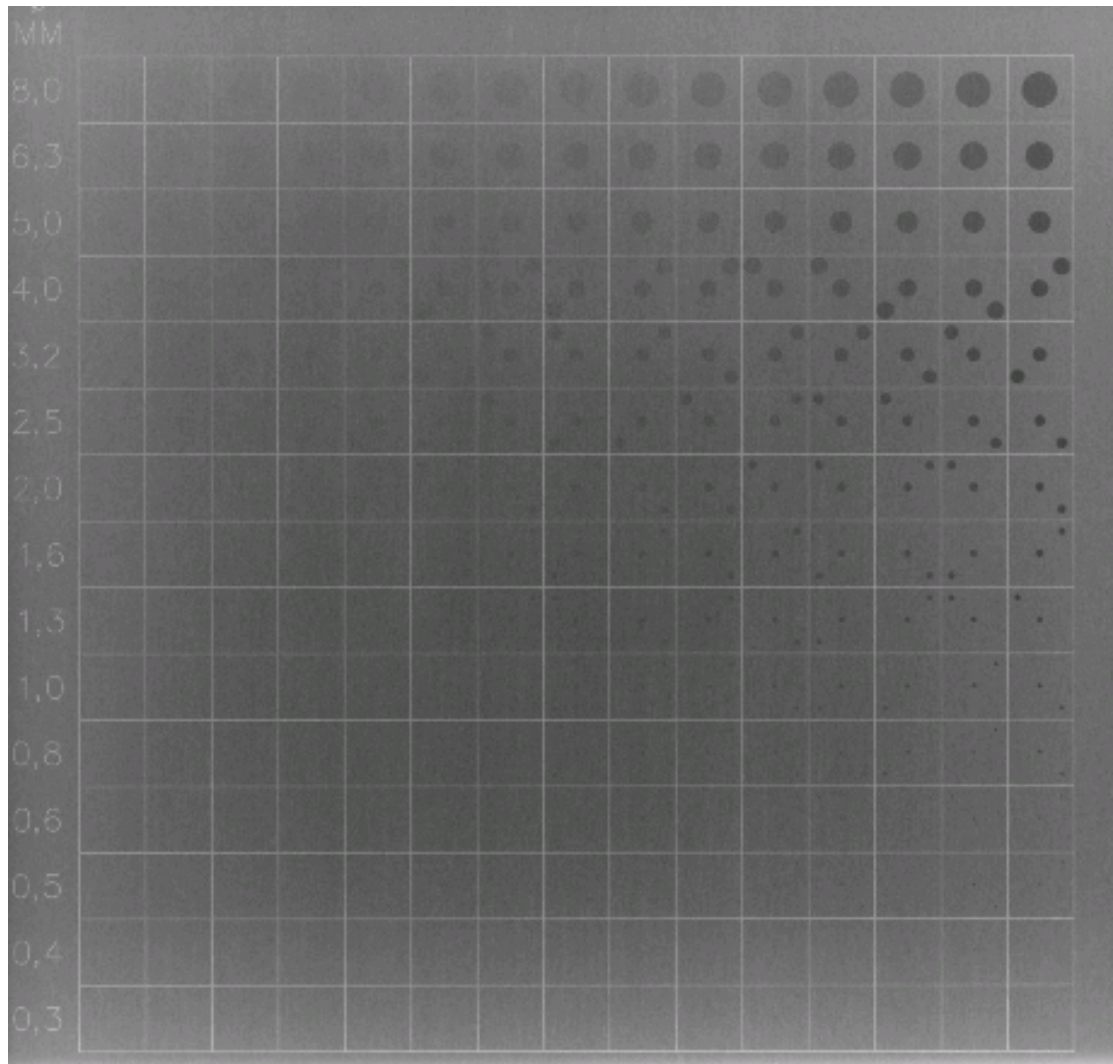


Figure 2.2: Radiographic image of 'CDRAD' phantom, kindly supplied by KCARE (King's College Hospital, London, UK).

A popular phantom for forced choice experiments is CDRAD (Artinis Medical Systems B.V., Andelst, Netherlands). A radiographic image of this test object is shown in Figure 2.2. It consists of a grid of squares. Apart from the top three rows, each square contains two identical details. One is in the centre of the square, and the other is in one of the corners. For each square, the observer must state which corner is

occupied. An ‘image quality factor’ is then calculated, on the basis of the number of correct responses. Whilst the details are again in fixed positions, their layout is irregular compared to the Leeds phantoms, and the observer is unlikely to remember many of the detail positions.

Another approach is to use phantoms with moveable details, such as those manufactured by ALVIM Research & Development Ltd (Jerusalem, Israel). Figure 2.3 shows a photograph of their general radiographic phantom, ‘TRG’. Each column contains 10 discs, five of which have a hole of a particular diameter and depth drilled into them. The positions of the discs can be interchanged, and the observer must decide which discs contain the holes. The numbers of true and false positives are used to calculate detection accuracy for each detail size.

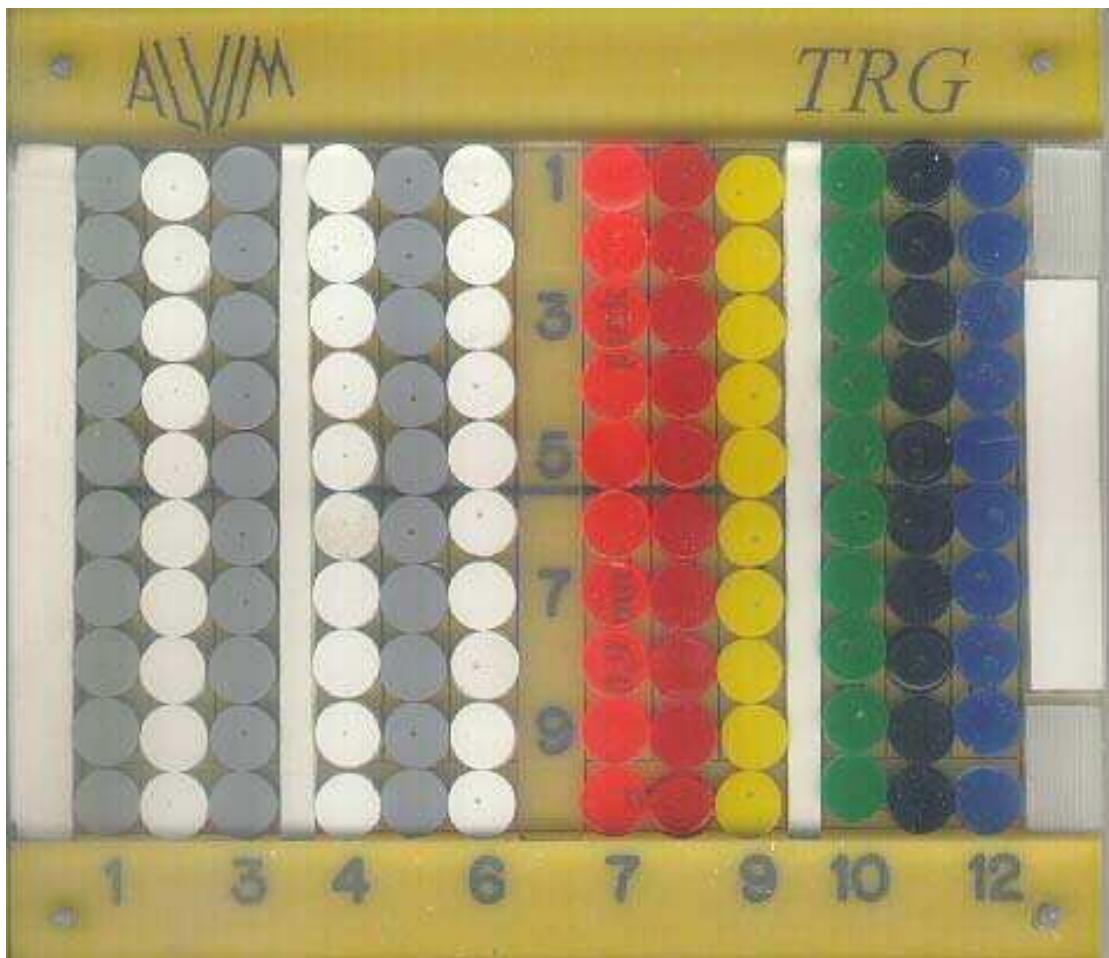


Figure 2.3: TRG phantom (ALVIM R&D, Jerusalem, Israel).

Wilson *et al* (2003) and Jiang and Wilson (2004) used more clinically relevant forced-choice experiments, in which the observers were asked to locate simulated images of vascular stents or guidewires.

The forced choice experiment identifies threshold contrast more reliably than the ‘constant stimulus’ tests of Section 2.3, since it does not depend on a subjective decision threshold. Image scoring is quick, and the results are reproducible. Tapiovaara and Sandborg (2004) found that observers were able to detect objects of much lower contrast in a forced choice experiment than they reported as visible in contrast detail tests.

2.5 Receiver Operating Characteristic (ROC) Studies

Experiments using contrast detail phantoms, although useful for comparing the performance of different imaging systems or techniques, have no direct relation to the effectiveness of a clinical imaging task. Whilst they can indicate which sets of exposure conditions give the most information per unit of dose, they cannot assess which give adequate image quality for diagnosis.

2.5.1 Methodology

Receiver Operating Characteristic (ROC) studies seek to measure observer performance in clinically relevant imaging tasks. In the most basic tests, the observer is presented with a series of images, some of which are normal, and some of which contain real or simulated pathologies. For each one, they are asked to indicate their confidence in the presence or absence of pathology. Scoring is commonly done on a five-point scale, along the lines of the following:

- 0% - definitely negative (normal)
- 25% - probably negative
- 50% - possibly positive

- 75% - probably positive
- 100% - definitely positive (abnormal)

For each level in the scoring system, the true positive rate (sensitivity) is then plotted against the false positive rate (1-specificity), and a curve is fitted to the data. Figure 2.4 shows an example of an ROC plot. The blue line shown is the line of pure chance, representing total inability of the test to distinguish between normal and diseased patients. The red curve is a 'typical' ROC curve for a diagnostic test with 80% accuracy. Each point on the curve corresponds to the sensitivity and false positive rate at a different decision threshold. As the test accuracy improves, the curve moves towards the top left-hand corner of the plot.

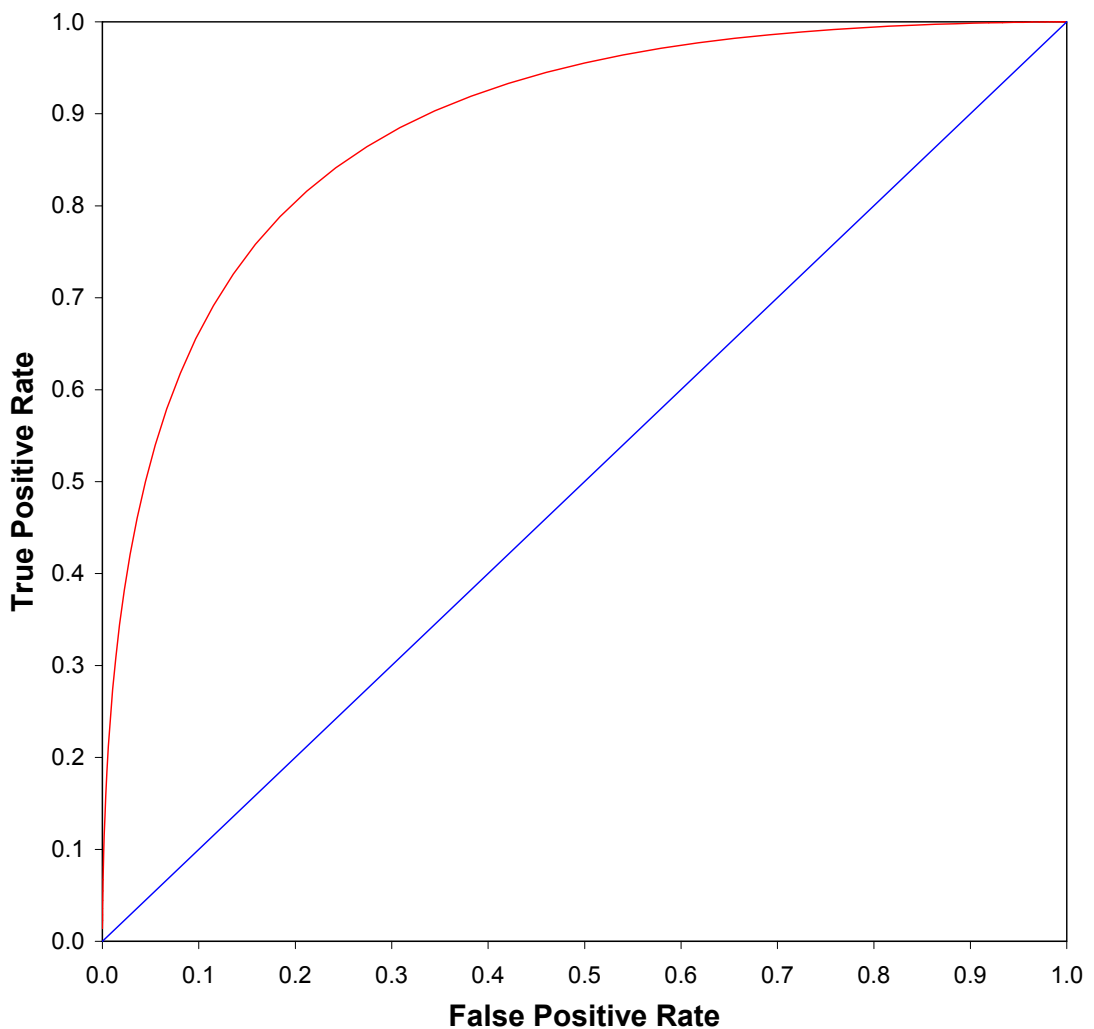


Figure 2.4: Example ROC plot.

The area under the curve indicates the accuracy of the imaging technique. An area of 0.5 would indicate pure guesswork, whereas an area of 1.0 would correspond to a perfect diagnostic test, having 100% sensitivity and specificity.

Basic ROC studies require the observer to make a yes/no decision, which does not reflect the clinical situation. A more realistic approach is Free-response ROC (FROC). Here, there can be an arbitrary number of pathologies in each image. The observer must indicate the positions at which (s)he perceives abnormalities to be present. True positive scores require abnormalities to be identified at the correct locations.

For a more comprehensive explanation of ROC methodology, the reader is referred to Metz (1978) or Obuchowski (2003; 2005). Free-response ROC and associated methods for data analysis are described in detail by Chakraborty and Winter (1990), and Chakraborty and Berbaum (2004).

Two reported studies have performed ROC analysis on images from coronary angiograms (Baker *et al*, 1997; Kerensky *et al*, 2000). Observers were asked to identify features such as filling defects, thrombi, dissections, calcifications and stents. In one study, they were also asked to provide a visual estimate of stenosis severity at a designated location (Kerensky *et al*, 2000).

2.5.2 Practical Considerations

ROC studies are usually performed using selected, randomised clinical images. In order to measure sensitivity and specificity, the investigators need to know the 'correct' diagnosis for each image, and this may not be easy to ascertain. Where possible, the patient's disease status is determined from the outcomes of other clinical tests. Failing this, the diagnosis is agreed for each case by a panel of experts. However an inadequate image could result in an incorrect diagnosis by the expert panel, and this may mask poor diagnostic accuracy.

Some investigators have added simulated pathologies to anatomical phantoms, or real clinical images (Strotzer *et al*, 1998a; Strotzer *et al*, 1998b; Strotzer *et al*, 2000; Tingberg *et al*, 2000; Ludwig *et al*, 2002; Goo *et al*, 2002). This makes it easy to define the 'correct' diagnosis for each case. However, simulated images do not reflect

natural variations in the appearance of normal anatomy and in pathological changes within the patient population.

ROC analysis does not depend on observer decision threshold. In fact, the ROC curve has an infinite number of points, corresponding to every possible decision threshold. It is not affected by disease prevalence, and can be used to compute useful summary measures of test accuracy. However, it does require large-scale studies, involving at least 100 patients. The actual sample size depends upon the disease prevalence in the study population. Observers must be trained in the interpretation of clinical images.

2.6 Visual Grading Analysis (VGA)

Perhaps the simplest method for comparing different imaging techniques is visual grading analysis (VGA). Here, images or features within them are given a relative score, reflecting how well details are visualised. Two different approaches to VGA are described in the literature.

The first approach is to compare each image with a reference image, and score it according to the observer's preference. The most common scoring system is a five-point scale, with gradations essentially as follows (Oda *et al*, 1996; Silber *et al*, 1997; Almen *et al*, 2000; Sund *et al*, 2000; Sandborg *et al*, 2001; Fink *et al*, 2002; Lanhede *et al*, 2002):

- (1) – much poorer than reference image
- (2) – slightly poorer than reference image
- (3) – equivalent to reference image
- (4) – slightly better than reference image
- (5) – much better than reference image.

Such tests are most powerful if paired images are used. This generally involves subjecting patients to an increased radiation burden.

The second approach is to grade individual images according to how well structures can be seen. Scoring is usually done on a four or five point scale, with gradations corresponding to 'excellent', 'good', 'moderate', 'poor' and sometimes 'very poor'

(Cranage *et al*, 1992; Ross *et al*, 1997; Volk *et al*, 2000; Fink *et al*, 2002; Uffmann *et al*, 2005).

Some investigators have graded radiographs according to several aspects of image quality, such as contrast, noise and resolution (Ross *et al*, 1997; Persliden *et al*, 1997; Pärtan *et al*, 2000). The observers are often asked to state whether or not each image is acceptable for diagnosis. Kerensky *et al* (2000) asked observers to rate their confidence in interpreting coronary angiograms, on a scale of 0 to 10.

Visual grading analyses are clearly subjective. Their reliability may be improved by employing multiple observers and averaging their scores. Several studies have calculated normalised visual grading analysis scores (VGAS) (Almen *et al*, 2000; Sund *et al*, 2000; Sandborg *et al*, 2001; Lanhede *et al*, 2002). These may be defined by the equation

$$VGAS = \frac{\sum_{o=1}^{N_o} \sum_{i=1}^{N_i} \sum_{s=1}^{N_s} R_{o,i,s}}{N_o N_i N_s}$$

Equation 2.3

where the relative ratings (R) of the images are summed over the number of observers (o), images (i), and structures (s). N_o is the total number of observers, N_i the total number of images, and N_s the total number of structures compared.

Visual grading analysis is sensitive to small changes in image quality, especially if paired images are used (Tingberg *et al*, 2004). Comparative studies have shown the results to correlate well with ROC analysis (Sund *et al*, 2000; Tingberg *et al*, 2000). It is especially useful for comparing image processing techniques, since paired images can be produced simply by applying different processing algorithms to the same image, without any additional exposure of the patient. Its main disadvantage is that image scoring does not correspond to the clinical imaging task, which is usually lesion detection.

2.7 Image Quality Criteria

In the late eighties, the Radiation Protection Programme of the Commission of the European Communities (CEC) initiated a project to establish radiographic 'quality criteria' for a range of common examination types. These were then subjected to an extensive clinical trial across the European Union, and a set of European Guidelines on quality criteria were published (European Commission, 1996). These set out to define the 'necessary requirements' for an image of 'standard diagnostic quality'. Quality criteria were defined for standard chest, skull, lumbar spine, pelvis, urinary tract and breast images.

2.7.1 Cardiac Criteria

A preliminary set of quality criteria for coronary angiograms has since been proposed by the Italian Society of Invasive Cardiology and the Italian Society of Physics in Medicine, and adopted by the DIMOND group (Bernardi *et al*, 2001b). These are based on the style of the European Guidelines, and use the same terms for degree of visualisation of the relevant structures. The criteria for left coronary angiography are listed below.

1. Performed at full inspiration if necessary to avoid diaphragm superimposition or to change anatomic relationship (in apnoea in any case).
2. Arms should be raised clear of the angiographic field.
3. Visually sharp reproduction of vessel walls.
4. Simultaneous and full opacification of the vessel lumen at least until the first critical lesion ($\geq 70\%$ by visual estimation).
5. Panning should be limited. If necessary, pan in steps rather than continuously, or make subsequent cine runs to record remote structures.
6. Visually sharp reproduction of the origin, proximal, mid and distal portion of the left anterior descending and circumflex arteries, in at least two orthogonal views.

7. Visually sharp reproduction of side branches $\geq 1.5\text{mm}$ of the left anterior descending and circumflex arteries in at least two orthogonal views; the origin should be seen in at least one projection.
8. Visually sharp reproduction of lesions in vessels $\geq 1.5\text{mm}$ in at least two orthogonal views.
9. Visualization of collateral circulation when present.
10. When criteria 6-9 have been fulfilled, avoid extra projections (mainly LAO semi-axial).

The degrees of clarity with which the various features must be visualised are defined as follows.

Visualization – features just visible – characteristic features are detectable, but details are not fully reproduced.

Reproduction – details emerging – details of anatomical structures are visible, but not necessarily clearly defined.

Visually sharp reproduction – details clear – anatomical details are clearly defined.

2.7.2 Image Criteria Score

Bernardi *et al* (2001a) designed a weighted scoring system for evaluating compliance with the DIMOND cardiac criteria. Each arterial branch was scored in turn, with ‘1’ given for each fulfilled criterion and ‘0’ for each unfulfilled criterion. The scores were then summed to give a ‘total quality score’ for the whole examination. This approach of combining scores based on quality criteria into a single index has also been adopted by Almen *et al* (2000), Sund *et al* (2000), Sandborg *et al* (2001) and Lanhede *et al* (2002). ‘Image criteria score’ (*ICS*) is usually defined as an average of the actual scores, over the maximum total score.

$$ICS = \frac{\sum_{o=1}^{N_o} \sum_{i=1}^{N_i} \sum_{c=1}^{N_c} S_{o,i,c}}{N_o N_i N_c}$$

Equation 2.4

where the assigned scores S are summed over number of observers (o), images (i), and criteria (c). N_o is the total number of observers, N_i the total number of images, and N_c the total number of criteria.

Vano *et al* (1995) recommended that ‘the criteria must be sufficiently complete to avoid all films valid for diagnosis meeting all criteria’. This implies a very different understanding of image quality criteria from that originally intended by the CEC Radiation Protection Programme. The criteria were established as requirements that should be met to ensure that a standard image provides adequate diagnostic information. However, these investigators used them as a means of grading diagnostic images according to their relative merit.

The practice of using quality criteria scoring to differentiate degrees of excellence has also been adopted by Almen *et al* (2000) and Lanhede *et al* (2002). Visual grading analysis based on the features defined in the image quality criteria has been found to be an especially sensitive approach to comparing image quality (Almen *et al*, 2000; Tingberg *et al*, 2000; Tingberg *et al*, 2004).

2.7.3 Recommendations Arising from Clinical Experience

A number of general recommendations arising from the initial European trial of the CEC criteria are discussed in detail in European Union report EUR 16635 EN (Maccia *et al*, 1996). The consensus in the literature is that image quality criteria should be as precise and objective as possible, to avoid ambiguity and maximise observer agreement. At the same time, they need to be clinically meaningful, and readily understood and applied in the clinical environment. The wording should be very clear and should relate directly to visualisation or reproduction of specific parts of the anatomy. The criteria should include a range of important feature types, including small structures and low contrast structures, to assess global imaging performance.

Studies using both the CEC chest criteria and the DIMOND cardiac criteria observed that most images failed to satisfy all of the quality criteria, despite being judged adequate for their clinical purpose (Bernardi *et al*, 2001a; Lanhede *et al*, 2002). In some cases, the criteria on which the image fails may not be relevant to that patient’s clinical condition. However, it may also be that some features are still considered

clinically acceptable if the standard is not met. The European Guidelines on Quality Criteria for Diagnostic Radiographic Images (European Commission, 1996) acknowledge that the criteria do not define acceptability for particular clinical indications, since in some cases lower image quality may be sufficient.

Martin *et al* (1999), and Redlich *et al* (2005), point out that it may not be sufficient to use a system of quality criteria based only on the reproduction of normal anatomical structures, since the image quality requirements for viewing pathologies may be more stringent. Bernardi *et al* (2001a) recognized that to fully test the robustness of a scoring system based on image quality criteria, a trial should also include some examinations that are deemed clinically unacceptable.

2.8 Observer Variation

One of the limitations of any observer-based method for evaluating image quality is that the results are subject to both intra- and inter-observer variation. An individual observer's perception of an image is conditioned by their own expectations and preferences. Their decision thresholds will also change as they gain experience in scoring the images, and become more familiar with the questions and issues raised by the trial. Studies in which observers were asked to re-evaluate some of the images after a significant time interval reported that up to 20% of answers changed between the two reading sessions (Almen *et al*, 2000; Lanhede *et al*, 2002).

As has already been described, some image quality tests are more prone to these types of variation than others. Measures that can be taken to reduce the influence of observer error include employing multiple observers, repeating observation sessions and averaging observer scores, allowing a substantial time interval between observation sessions (to reduce memory bias), training the observers in using the scoring system, and familiarising them with the types of images they are likely to see, before commencing the study.

2.9 Summary

The chapter began by defining the fundamental descriptors of image quality: contrast, noise and resolution. A review of the literature then considered various methods for assessing image quality and for determining the adequacy of clinical images.

Objective measurements of physical quantities such as signal-to-noise ratio or contrast give the most reproducible results, but do not include the display and observation steps of the imaging process. Monte-Carlo simulations are a particularly efficient means of seeking an optimized imaging technique. The results should always be verified empirically, before introducing changes to clinical practice.

Contrast detail tests provide a quick and easy check for large changes in system performance, but suffer from considerable intra- and inter-observer variation, since detail visibility depends on the observer's subjective decision threshold. Forced choice experiments remove observer bias, by asking observers to identify the position of a known object, from a number of possible locations. This improves the reliability of the test results.

Receiver operating characteristic (ROC) analysis is a well-established method for determining the diagnostic accuracy of clinical images. However, it requires large-scale clinical studies, and relies on the investigator knowing the 'correct' diagnosis for each case.

In visual grading analysis (VGA), observers are asked either to rate each image against a reference image, or to grade individual images according to their merit. Although subjective, these tests are sensitive to small changes in image quality. Normalised VGA scores provide a direct measure for comparing imaging techniques.

Image quality criteria define the necessary requirements for a standard diagnostic image. They are based on the degree of visualization of important anatomical structures. Some studies have used quality criteria to grade images according to their relative merit, although this seems to deviate considerably from their original purpose.

The chapter concluded with some general principles for improving the accuracy and repeatability of observer performance tests. These included employing multiple

observers, repeating viewing sessions, and providing suitable training and familiarization for observers prior to starting the study.

Chapter 3 - Skin Dose in Cardiac Catheterization

3.1 Introduction

This chapter gives a clinical background to the two most common cardiac catheterization procedures, coronary angiography and coronary angioplasty. It then reports some of the cases of radiation skin injuries cited in the literature, and summarises what is currently known about the relationship between radiation dose and the severity of skin effects. It outlines the various professional guidelines and legislation that have been put in place to tackle the problem of excessive skin doses. A number of different approaches to skin dosimetry have been adopted in the past, and these are described and compared. Finally, the current literature on management of patients thought to be at risk of adverse skin effects is summarised.

3.2 Clinical Background

Coronary heart disease is the most common cause of death in the western world. It is caused by narrowing or occlusion of the coronary arteries, which supply blood to the muscles of the heart. Catheter-based imaging and interventional techniques are now widely used in its diagnosis and treatment.

3.2.1 Coronary Angiography

The coronary angiogram is a diagnostic procedure, performed to image the lumen of one or more of the coronary arteries. It may be used for diagnosis of heart disease, to

assess treatment feasibility, or to evaluate treatment outcomes. It is currently the ‘gold standard’ technique for assessment and classification of coronary plaques.

A catheter with a radio-opaque tip is inserted into the arterial system, usually through the femoral artery. The catheter tip is manipulated into the artery of interest, using fluoroscopic guidance. An iodine-based contrast agent is injected via the catheter, and the artery imaged using fluorography (an ‘acquisition run’). The X-ray tube and detector are then rotated around the patient, and further acquisition runs performed in different projections through the heart, to enable visualisation of all segments of the artery.

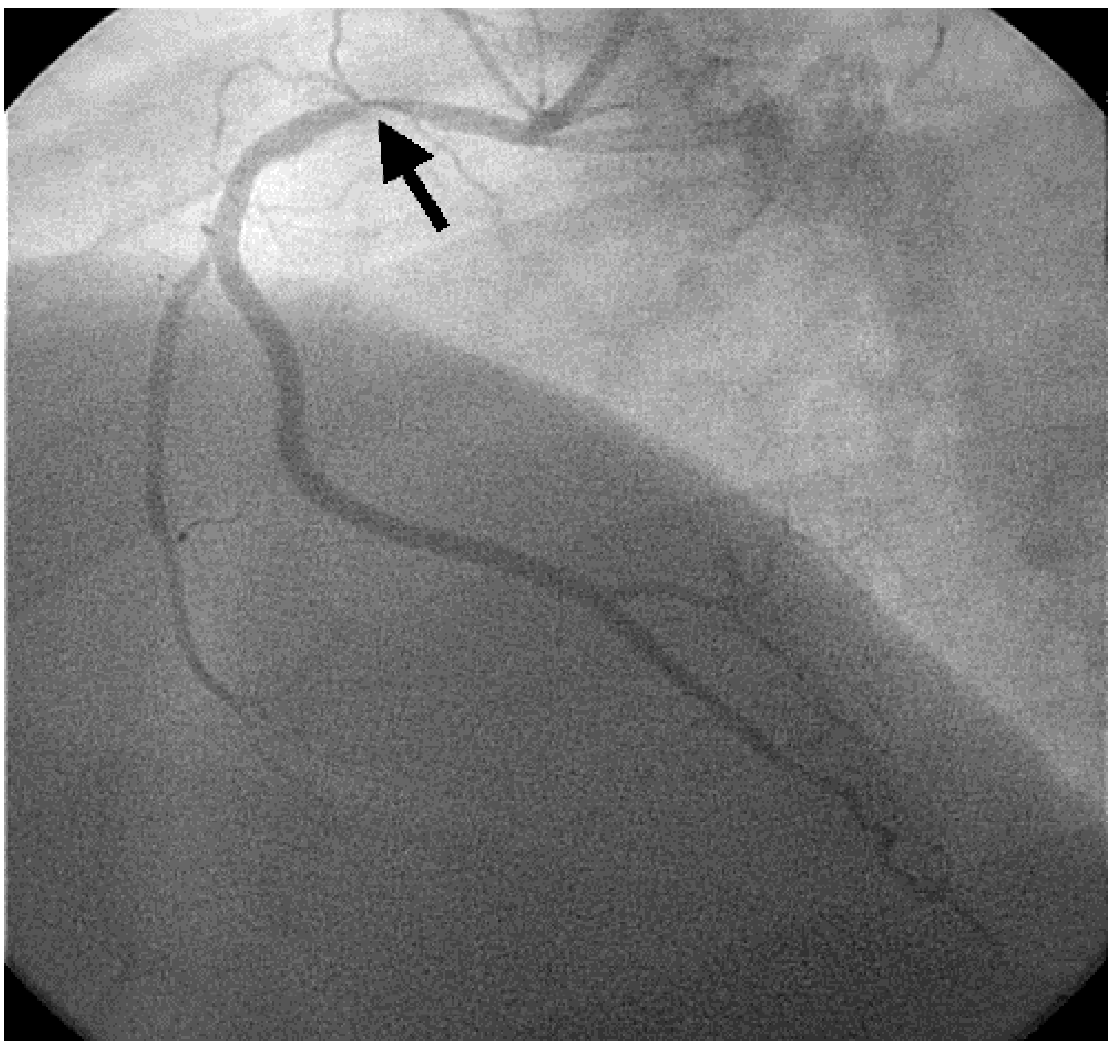


Figure 3.1: Coronary angiographic image, with arrow demonstrating stenosis of the right coronary artery.

Figure 3.1 is an image taken from a coronary angiogram. It is a left anterior oblique view of the right coronary artery. A narrowing (stenosis) is clearly seen at the point indicated by the arrow.

3.2.2 Coronary Angioplasty

Percutaneous transluminal coronary angioplasty (PTCA) is the process of opening up an arterial narrowing, using a specially designed balloon. A catheter is inserted into the affected coronary artery under fluoroscopic guidance, as described above. A contrast agent is injected and the artery imaged using fluorography, to locate the stenosis. An angioplasty balloon is inserted into the stenosis and inflated to increase the vessel lumen. After balloon deflation, the artery is imaged again, to assess the effectiveness of the procedure. Balloon inflation may need to be repeated, if the diameter of the arterial lumen is still insufficient.

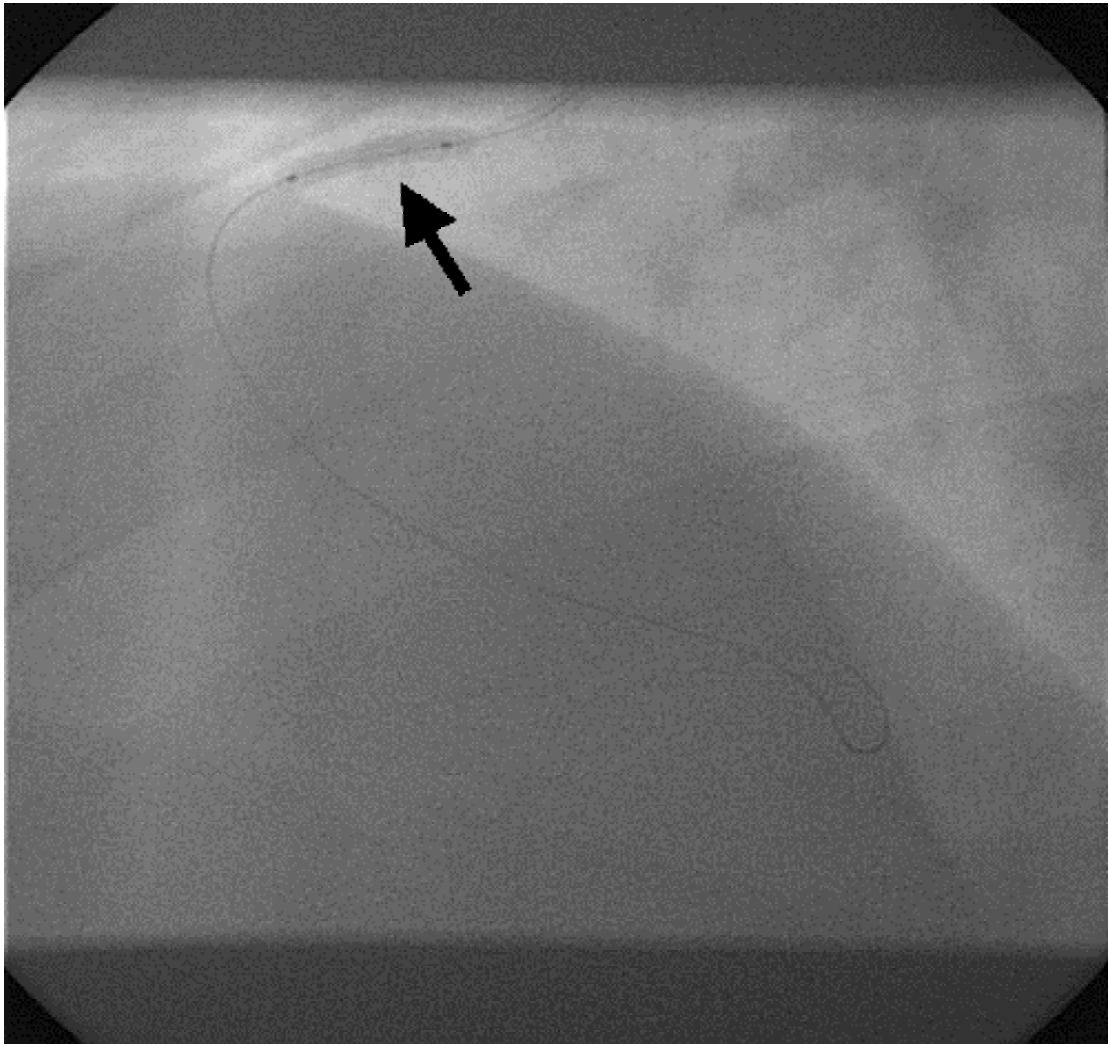


Figure 3.2: Angioplasty balloon, inflated at site of narrowing.

Figure 3.2 shows an inflated angioplasty balloon, at the site of the narrowing shown in Figure 3.1. Figure 3.3 is a post-angioplasty image, demonstrating that the diameter of the vessel has been increased successfully.

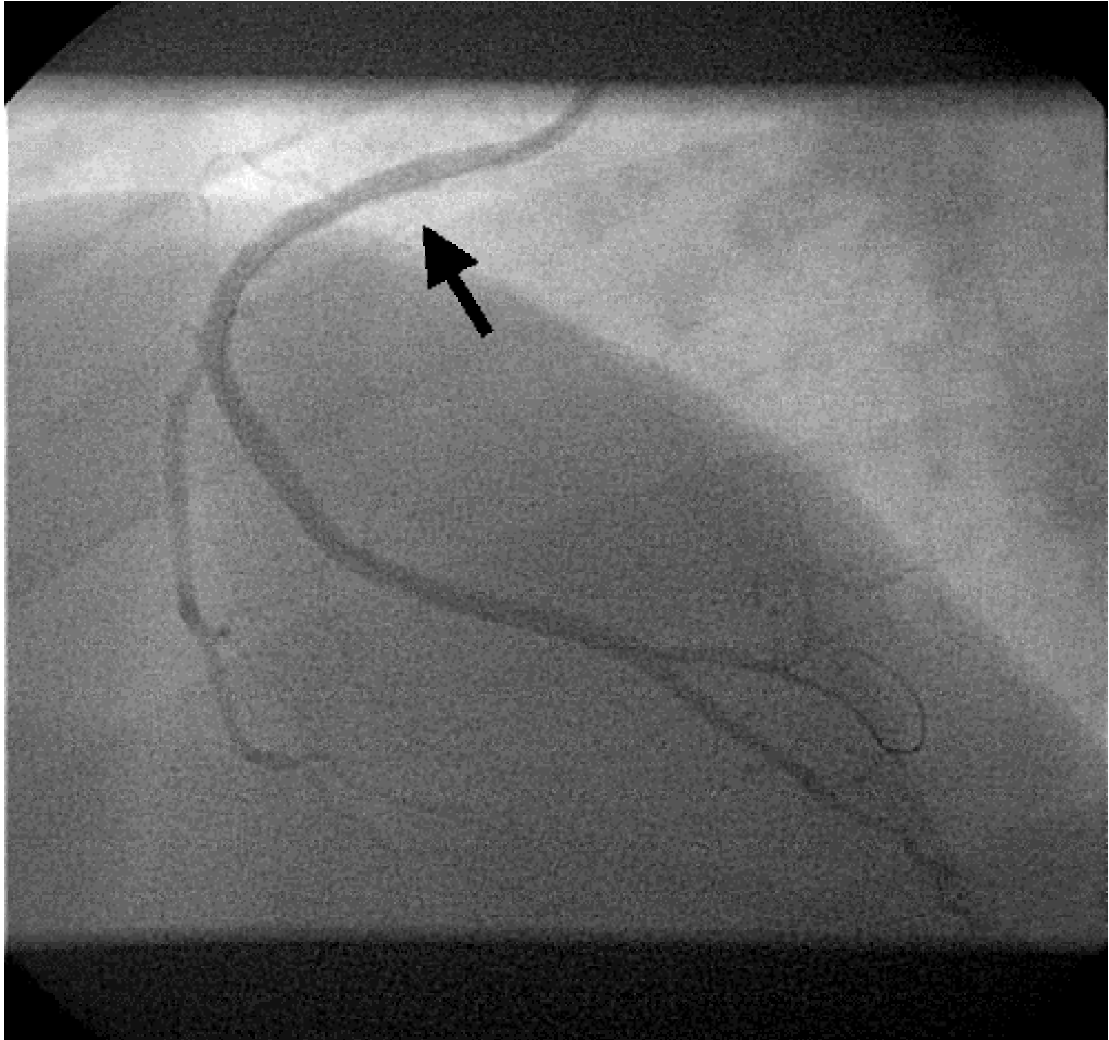


Figure 3.3: Improved blood flow, following coronary angioplasty.

A stent may also be implanted at the angioplasty site, to prevent elastic recoil of the arterial wall. This is a cylindrical scaffold, which is flat-packed and inserted into position via a catheter, and is then expanded using a balloon to match the lumen of the artery.

Each stage of the procedure is documented pictorially, using acquisition runs. Images are taken to demonstrate the anatomy of the coronary arteries before and after the intervention, the positions of balloons and stents, and any complications or transient adverse effects that occur during the procedure.

In 2003, a total of 53,261 percutaneous coronary interventions were performed in the UK (www.heartstats.org), the vast majority of which were coronary angioplasties. This number increases by around 15% each year.

3.3 Skin Dose and Deterministic Injuries

Adverse skin reactions are a familiar side effect in radiotherapy, but are not usually encountered in diagnostic or interventional radiology, where the radiation doses are generally much lower. However, a number of cases of severe skin injuries have been reported following cardiac catheterization procedures. The majority of these were coronary angioplasties (Sovik *et al*, 1996; Shope, 1996; D'Incan *et al*, 1997; Widmark & Hellesnes, 1997; Kawakami *et al*, 1999; Miralbell *et al*, 1999; Dehen *et al*, 1999; Vanō *et al*, 2001a; Koenig *et al*, 2001a) or radiofrequency catheter ablations (Shope, 1996; Rosenthal *et al*, 1997; Vanō *et al*, 1998a; Wong & Rehm, 2004), although a small number of cases have been associated with particularly difficult coronary angiograms (Dehen *et al*, 1999; Koenig *et al*, 2001a). Many of the incidents were caused by out-dated or faulty equipment, or poor radiographic practice, but some were simply due to difficult or repeated procedures resulting in a high cumulative dose.

Deterministic effects such as skin burns only occur above a certain dose threshold, i.e. after a minimum number of cells have been damaged. This threshold depends on a number of factors including patient age, skin site and area of skin affected, and pre-disposing conditions such as diabetes (Food and Drug Administration, 1994; Mayr *et al*, 1997; Wagner *et al*, 1999; World Health Organization., 2000; Vanō *et al*, 2001a; Koenig *et al*, 2001b). If exposures are separated by long time intervals, the severity of skin damage is reduced, since some sub-lethal cell damage can be repaired between fractions.

Effect	Typical Dose	Time to onset	Description
Transient erythema	2 Gy	Hours	Skin reddening, peaking at ~ 24 hours.
Temporary epilation	3 Gy	3 weeks	Temporary hair loss, caused by depletion of germinal layers of the hair follicles.
Main erythema	6 Gy	10 days	Reddening and oedema of the skin. Burning, tenderness and itching.
Permanent epilation	7 Gy	3 weeks	Permanent hair loss.
Dry desquamation	10 Gy	4 weeks	Flaky skin, due to depletion of proliferative cells in basal layer.
Invasive fibrosis	10 Gy	-----	Skin and subcutaneous fat replaced with inflexible, fibrous scar tissue. Skin is tender & movement restricted.
Dermal atrophy	11 Gy	> 14 weeks	Epidermis reduced to a few layers of cells. Hair follicles disappear. Scattered focal discoloration. Irradiated area contracts.
Telangiectasis	12 Gy	> 52 weeks	Atypical dilatation of superficial dermal capillaries.
Moist desquamation	15 Gy	4 weeks	Blistering and sloughing of superficial skin. Continuous weeping from deep cutaneous layers. Pain, and exposure to infection.
Late erythema	15 Gy	6-10 weeks	Dusky or mauve skin discoloration.
Dermal necrosis	18 Gy	> 10 weeks	Microvascular damage leads to progressive vascular insufficiency of the dermis.
Secondary ulceration	20 Gy	> 6 weeks	Delayed healing. Reduction in thickness of the new epidermis.

Table 3.1: Radiation-induced skin injuries, dose thresholds, times to onset and description of symptoms (McLean, 1973; Hopewell, 1990; International Commission on Radiological Protection, 1991a; Wagner *et al*, 1994; Food and Drug Administration, 1994; National Radiological Protection Board, 1996; World Health Organization., 2000; Koenig *et al*, 2001b).

Typical threshold doses are given in Table 3.1, with the time-to-onset and symptoms of associated adverse effects. There can be a considerable time delay between radiation exposure and the onset of symptoms. This means that radiation-induced skin injuries are not always correctly identified, and as a result patients may not receive appropriate treatment and counselling. A number of studies have reported cases of skin injury in which the patients themselves or the dermatologists to whom they were referred were unaware of their exposure to ionising radiation (Lichtenstein *et al*, 1996; D'Incan *et al*, 1997; Vanđ *et al*, 1998a; Koenig *et al*, 2001b). This led to considerable delays in diagnosis and treatment. It is likely that many other such cases have occurred, but have never been identified.

Advances in technology have led to improved dose-efficiency in modern imaging equipment. However, at the same time rapid development of new percutaneous treatment techniques and improved procedural outcomes have led to more and more difficult cases being undertaken. By their nature, these tend to be associated with longer fluoroscopy times and greater numbers of acquisition runs. As the number of interventional devices continues to grow, the trend towards tackling more complex cases is likely to continue.

A growing number of patients now undergo multiple catheterization procedures. A diagnostic angiogram may identify the need for an angioplasty, which will in turn require a follow-up angiogram to check the efficacy of the treatment. In addition, re-stenosis of the artery can occur following angioplasty, and this may necessitate a further intervention. In-stent re-stenosis has been variously estimated to occur in 10 to 50% of cases (Bailey, 2002; Garza *et al*, 2002; Lowe *et al*, 2002; Radke *et al*, 2003). Strategies now being used to combat re-stenosis include long-term drug therapies, intra-vascular brachytherapy, mechanical cutting devices, laser treatments and novel stent designs (Bailey, 2002; Kandzari *et al*, 2002; Garza *et al*, 2002; Gunn *et al*, 2003; Sousa *et al*, 2003a; Sousa *et al*, 2003b). One of the most promising developments is that of drug-eluting stents, which target drug therapy to the vessel wall where they are implanted. However, at present multiple procedures continue to be a reality for many patients.

Those patients who undergo multiple procedures may well receive cumulative doses above the threshold for deterministic effects. Shope (1996) described one particularly extreme case where the patient underwent two coronary angiograms and one

angioplasty on the same day, and developed severe tissue necrosis. There is usually a time interval of at least a few days (if not months or years) between procedures, allowing the skin time for recovery. There is however some evidence that the damage responsible for late radiation effects may be residual, so that the first exposure reduces the skin's tolerance to subsequent radiation (Hansson & Karambatsakidou, 2000; Koenig *et al*, 2001b).

3.4 Legislation and Guidance

In response to the reported incidents, regulatory and advisory agencies have put a range of measures in place to limit patient skin doses from complex catheterization procedures, and to promote good management of patients who may be at risk of radiation induced skin injuries. Of particular relevance to this work are the guidelines published by the US Food and Drug Administration (1994; 1995) and the International Commission on Radiological Protection (2000).

These recommend that:

- Patients undergoing procedures that may cause deterministic effects should be counselled on the risk of skin injuries, and this risk should be addressed on the patient consent form.
- Information should be recorded in the patient's notes, which permits the skin dose from individual procedures to be estimated. This is particularly important for patients who may have received doses sufficient to cause adverse skin reactions. The FDA recommend recording the dose if it exceeds 1 Gy, for all procedures. ICRP Report 85 suggests that recording doses of 3 Gy or more is sufficient, unless the patient is likely to undergo repeat catheterisation, in which case the lower recording threshold of 1 Gy should be used. The physician should record the location and extent of the skin sites irradiated to these levels, and estimate the magnitude of the dose to each one.
- Patients thought to have received a dose that may cause deterministic effects should be counselled after the procedure, on the signs and symptoms they should look out for, and what action to take should any skin changes occur.

Additionally, ICRP Report 85 recommends that patients receiving skin doses of 3 Gy or more should be followed up 10 to 14 days after exposure, to check for any signs of erythema.

The guidelines have several implications for patient dose assessment. Firstly, physicians performing cardiac catheterization procedures need to know the typical skin doses associated with them, so that they can give patients appropriate information on radiation risks, to fulfil the requirements for fully informed consent. Secondly, they must have a means of identifying individual procedures that exceed the dose recording thresholds and put the patient at risk of skin injuries. Thirdly, a method is needed for estimating the magnitude of the skin doses received by these patients, and the location of any high dose regions on the skin. Given the large proportion of patients who now undergo more than one catheterization procedure (around 20% locally), it is advisable to record these details for all procedures resulting in a peak skin dose of more than 1 Gy.

Since cardiac catheterizations are relatively high dose procedures, they must be considered a priority for optimisation under The Ionising Radiation (Medical Exposure) Regulations 2000. The assessment of skin dose is an essential step in this optimisation process, since it informs the development of dose reduction strategies to minimise the potential for skin injuries. Skin dose information for individual patients can also assist the operator in planning subsequent procedures, so as to minimise further irradiation of areas of the skin that have already been subjected to high doses.

3.5 Skin Dosimetry

This section outlines the various methods that have been used for skin dosimetry in the cardiac catheterization laboratory, and considers the merits and limitations of each. The dose indicators most commonly used are dose-area-product and fluoroscopy time, since these are conveniently displayed on the imaging unit. However, these take no account of the wide variation in imaging projections used.

3.5.1 Dose Area Product

Table 3.2 and Table 3.3 summarise mean dose-area-products reported in recent literature, for coronary angiograms and angioplasties. These are arranged in order of increasing DAP.

Reference	Number of Patients	DAP (Gycm ²)
Kuon <i>et al</i> (2003)	140	13
Clark <i>et al</i> (2000)	117	14
Arthur <i>et al</i> (2002)	368	16
Katritsis <i>et al</i> (2000)	16	27
Paisley <i>et al</i> (2004)	3273	27
Efstathopoulos <i>et al</i> (2003)	20	29
Hart <i>et al</i> (2002)	8000	30
Neofotistou <i>et al</i> (2003)	600	39
Tsapaki <i>et al</i> (2003)	195	47
Karambatsakidou <i>et al</i> (2005)	20	49
den Boer <i>et al</i> (2001)	322	52
Lobotessi <i>et al</i> (2001)	18	58
van de Putte <i>et al</i> (2000)	62	61
Fransson and Persliden (2000)	65	63
Hansson and Karambatsakidou (2000)	78	73
Delichas <i>et al</i> (2005)	93	79

Table 3.2: Reported mean DAP values for coronary angiograms.

There are many different factors affecting mean DAP, including the age, construction and performance of the imaging equipment used, patient caseload, local imaging protocols and variations in individual operator technique. Rapid changes in practice and improvements in technology have taken place during the period over which these

data were collected. The more recent studies are likely to have been performed on newer imaging equipment, which tends to have more inbuilt dose reduction features. However, they are also likely to include more complex cases, with more vessels treated and more stents implanted per procedure, which may explain why mean DAP has not necessarily reduced with time.

Reference	Number of Patients	DAP (Gycm ²)
Kuon <i>et al</i> (2002)	46	10
Kuon <i>et al</i> (2003)	116	13
Katritsis <i>et al</i> (2000)	10	36
Karambatsakidou <i>et al</i> (2005)	10	40
Paisley <i>et al</i> (2004)	479	41
Fransson and Persliden (2000)	24	48
Neofotistou <i>et al</i> (2003)	600	55
Hart <i>et al</i> (2002)	334	63
Padovani <i>et al</i> (2001)	232	67 (simple)
	117	96 (medium)
	46	133 (complex)
Tsapaki <i>et al</i> (2003)	97	68
Efstathopoulos <i>et al</i> (2003)	20	75
Delichas <i>et al</i> (2003)	102	86
Widmark <i>et al</i> (2001)	281	89
van de Putte <i>et al</i> (2000)	13	115 (without stent)
	10	166 (with stent)

Table 3.3: Reported mean DAP values for coronary angioplasties. The data from Padovani *et al* (2001) is divided into three groups, according to a complexity index defined in their paper.

The various studies may also have used different systems for classifying examination types. For example, one cardiology department might routinely include left ventriculography as part of the coronary angiogram, where another does not. Some of the angiograms will include both left and right heart catheterisation, whilst in other

cases only one coronary artery was examined. Some of the quoted data for coronary angioplasty includes placement of one or more stents, and this will tend to increase the DAP.

Whilst DAP is a useful indicator of stochastic risk, it is not directly linked to skin dose. During each procedure, the heart is imaged using a number of different projections. The distribution of dose across the patient's skin depends on which projections are used, and for what proportion of the procedure. This can vary greatly from one patient to the next, depending on operator preference, the anatomy of the patient's coronary arteries, and the location and severity of lesions. Thus, there may in fact be a very poor relationship between skin dose and DAP, as reported by van de Putte *et al* (2000), Vanō *et al* (2001b), Waite and Fitzgerald (2001), and Delichas *et al* (2005).

The newest interventional X-ray units also display the cumulative dose at a fixed point in the X-ray beam. This is usually at the 'interventional reference point' defined by the international standard IEC 60601-2-43:2000 (International Electrotechnical Commission, 2000). This point is intended to represent the entrance surface of the patient, and is situated on the central axis of the beam, 15 cm from the centre of rotation of the gantry, in the direction of the focal spot. This quantity only indicates the skin dose that would be received if the whole procedure were performed in a single projection, and gives no information about the actual dose distribution on the skin.

3.5.2 Fluoroscopy Time

Fluoroscopy time has often been used as a patient dose indicator for fluoroscopic and fluorographic procedures. This approach may be reasonable for examination types involving a large quantity of fluoroscopy with a small, set number of radiographs. In cardiac catheterization procedures, a large portion of the dose comes from the acquisition runs, so fluoroscopy time is likely to give a poor indication of patient dose (Hansson & Karambatsakidou, 2000; Lobotessi *et al*, 2001; Neofotistou *et al*, 2003; Efstathopoulos *et al*, 2003). As with DAP, fluoroscopy time takes no account of the different projections used. Fluoroscopy time alone cannot be expected to provide a useful estimate of skin dose.

3.5.3 Thermoluminescence Dosimetry

Thermoluminescence dosimetry (TLD) is a well-established technique in general radiography. Small chips or sachets containing a thermoluminescent material such as lithium fluoride are attached to the patient's skin, and store energy when exposed to X-rays. They are later heated under carefully controlled conditions, and emit light in proportion to the energy stored.

Reference	Number of Patients	Maximum Dose (mGy)
Delichas <i>et al</i> (2005)	39	428
van de Putte <i>et al</i> (2000)	62	412 (without LV)
	15	725 (with LV)
Verdun <i>et al</i> (1998)	≥ 40	847
Waite and Fitzgerald (2001)	9	330

Table 3.4: Maximum skin doses for coronary angiography, measured using TLD. (LV: left ventriculography.)

Reference	Number of Patients	Maximum Dose (mGy)
van de Putte <i>et al</i> (2000)	13	760 (without stent)
	10	1800 (with stent)
Verdun <i>et al</i> (1998)	20	2215
Waite and Fitzgerald (2001)	19	940

Table 3.5: Maximum skin doses for coronary angioplasty, measured using TLD.

A few investigators have reported using TLD to measure skin dose in cardiac catheterization procedures (Verdun *et al*, 1998; van de Putte *et al*, 2000; Waite & Fitzgerald, 2001; Delichas *et al*, 2005). Dosimeters were located at various landmarks on the patient's skin, where the regions of peak dose were expected to occur. Maximum skin doses measured for coronary angiograms and angioplasties are shown in Table 3.4 and Table 3.5. For the angiograms, all measured doses were less than 1 Gy. However, each study found skin doses approaching or exceeding 1 Gy for some angioplasties.

Since each procedure uses a number of different projections, it is impossible to predict the exact location of the peak skin dose in advance. Skin injuries reported in the literature occurred on both sides of the patient's upper back (Sovik *et al*, 1996; Shope, 1996; Widmark & Hellesnes, 1997; Kawakami *et al*, 1999; Miralbell *et al*, 1999; Vanõ *et al*, 2001a; Koenig *et al*, 2001a), on the patient's right side (Koenig *et al*, 2001a) and on the posterior surface of the right arm (Wong & Rehm, 2004). Even if several TLD are used, there is a danger of missing the region of peak skin dose, and thus underestimating the risk of skin injuries. Studies using TLD in conjunction with slow radiographic film have demonstrated that incorrect placement of TLD can lead to large errors in dosimetry (Geise & Ansel, 1990; Vanõ *et al*, 2001b).

In addition, TLD are labour-intensive to use, since each batch requires careful calibration and the chips must be individually prepared and read out each time they are used. Thermoluminescence dosimetry is not a sufficiently practical method for routine dose monitoring in the cardiac catheterization laboratory.

One way to improve coverage of the skin is to use a large array of finely spaced TLD. Geise *et al* (1997) evaluated a 30 cm x 30 cm array of laser heated TLD, and found it to be an accurate tool for skin dosimetry. However, such a system requires specialist equipment, which was not available for the present study.

3.5.4 Scintillation Detectors and Diodes

Hwang *et al* (1998) and Waite and Fitzgerald (2001) evaluated a commercially produced Skin Dose Monitor (McMahon Medical, San Diego, CA). This device contained a small zinc-cadmium scintillator, linked to a light meter. It was attached to the patient's skin using a disposable pad, and could be used to monitor localised skin dose in real-time. Mean doses reported by Hwang *et al* (1998) are shown in Table 3.6. On average, patients received skin doses of more than 1 Gy for angioplasties without stent insertion, and more than 2 Gy for the most complex angioplasties.

Procedure Type	Number of Patients	Mean Skin Dose (mGy)
CA	135	180
PTCA	35	1021
PTCA with single stent	25	1529
PTCA with multiple stents & rotational atherectomy	5	2496

Table 3.6: Mean skin doses measured using a scintillation detector, reported by Hwang *et al* (1998). (CA: coronary angiography; PTCA: percutaneous transluminal coronary angioplasty.)

Karambatsakidou *et al* (2005) reported use of an Unfors Patient Skin Dosimeter (Unfors Instruments, Billdal, Sweden). This had three diodes, which could be placed on the patient's skin prior to exposure.

Since neither of these detectors were transparent to radiation, their use may interfere with clinical imaging. In addition, the detector positions may not correspond to the regions of peak skin dose.

3.5.5 Film Dosimetry

A more robust method of capturing the peak skin dose is to map the dose distribution over a large area, using slow radiographic film. Any regions of high dose can be easily identified and, providing that the film is not saturated, absolute dose measurements can also be made.

Industrial films were used to assess radiation dose from fluoroscopic procedures as early as the nineteen sixties (Blatz & Epp, 1961; Yoshinaga *et al*, 1967). In recent years there has been a growing market for specialist slow films in radiotherapy. Designed for treatment verification imaging and quality control of megavoltage X-ray and electron beams, these films are relatively insensitive to diagnostic X-ray energies. They are supplied paper-wrapped and can be processed in standard radiographic film processors, making them a convenient choice for film dosimetry applications in radiology.

Until recently, the least sensitive of these radiotherapy films was Kodak XV-2, also known as X-OMAT V (Eastman Kodak Company, Rochester, New York). This saturated at around 700 mGy, for exposures in the diagnostic energy range (Fajardo *et al*, 1995; Vanõ *et al*, 2001b). Vanõ *et al* (2001b) used a combination of XV-2 film and TLD to measure skin doses from coronary angiograms and angioplasties. The results are summarised in Table 3.7. Film saturation occurred in two out of the seven angioplasties, indicating that XV-2 film was too sensitive for skin dose measurement in long or complex cardiac catheterization procedures.

Procedure Type	Number of Patients	Dose (mGy)
CA	26	49-711
PTCA	7	169-700+

Table 3.7: Peak skin doses reported by Vanõ *et al* (2001b), measured using a combination of film and TLD. (CA: coronary angiography; PTCA: percutaneous transluminal coronary angioplasty.)

Kodak have now developed an ‘extended dose range’ film, ‘EDR2’ (Eastman Kodak Company, Rochester, New York). This has been used for skin dosimetry in the cardiac catheterization laboratory by Vanõ’s group (Vanõ *et al*, 2003; Guibelalde *et al*, 2003). They reported its saturation point at 1.2 to 1.5 Gy, depending on the processing conditions applied. In a study including complex angioplasties, intravascular brachytherapy and cardiac ablation procedures, film saturation occurred in only about 1% of cases. The film is supplied in 35 x 43 cm sheets, which should be large enough to map the dose distribution across the whole of the patient’s upper back. This type of film appeared to be the most suitable for skin dosimetry in the cardiac catheterization laboratory, and was therefore used in the film dosimetry study of Chapters 4 and 5.

An alternative range of dosimetry films are the ‘Gafchromic’ films from International Specialty Products (Wayne, New Jersey). Specifically designed for patient dosimetry, these are non-light-sensitive, and change colour on exposure to X-rays. At the time of the present study, none were sufficiently sensitive for practical assessment of doses around 1 and 2 Gy. In addition, they were prohibitively expensive at around £30 per sheet.

Studies using film and TLD simultaneously have found the two methods to agree to within about 15 to 20%, for unsaturated areas of the film (Geise & Ansel, 1990; Nicholson *et al*, 2000; Vanõ *et al*, 2001b) This indicates that film dosimetry is a reasonably accurate method for determination of absolute skin doses.

3.5.6 Dose Modelling

Both den Boer *et al* (2001) and Chugh *et al* (2004) have developed real-time dose monitoring systems, to calculate and display cumulative skin dose maps during cardiac catheterization procedures. These alert the operator to any high doses that may be accumulating in particular areas of the skin. This may allow him/her to modify the projections used for the remainder of the procedure, to avoid over-irradiation of those areas, and hence reduce the risk of deterministic effects.

The system developed by den Boer *et al* (2001) was marketed by Siemens Medical Solutions (Munich, Germany) for a while, under the name 'CareGraph'. Miller *et al* (2002) described it as a valuable tool for minimising peak skin dose, and recommended that all manufacturers provide such real-time dose monitoring facilities. However, it has subsequently been withdrawn, due to apparent lack of customer demand. At the time of the present study, there was no commercially available software for mapping skin dose distributions.

Modern cardiovascular imaging units store detailed exposure and projection data in the image files. Vanõ *et al* (2003) extracted this data and used it to calculate skin doses from individual acquisition runs. It should also be possible, using this data, to generate a cumulative dose map for the whole procedure, either retrospectively or in real-time.

Dose modelling is an attractive option, as data could be obtained retrospectively for any patient. The dose maps would provide details of the location and magnitude of the peak skin dose, as recommended by the International Commission on Radiological Protection (2000) and the Food and Drug Administration (1995). If sufficiently well automated, dose modelling could be used as a routine dosimetric tool, with minimal demands on staff time.

Accuracy would be limited by the quantity of information stored by the imaging unit and made available to the user. For example, at present most interventional units store only acquisition runs and not fluoroscopic image sequences. This means that no information is available on the projections used for fluoroscopy. These gaps in the data would require certain assumptions to be made.

3.6 Dose Management

Having implemented a suitable method for patient dosimetry, it is important to establish a protocol for identification and follow-up of patients who may be at risk of deterministic injuries. For convenience, some centres have chosen to use DAP trigger levels for identifying at-risk patients. These are summarised in Table 3.8 and have generally been chosen to correspond to peak skin doses of either 1 or 2 Gy.

Reference	DAP Trigger (Gycm ²)
Cook <i>et al</i> (2004)	100
Hansson and Karambatsakidou (2000)	530 (CA) 250 (PTCA)
Karambatsakidou <i>et al</i> (2005)	470/570 (CA) 210 (PTCA)
McFadden <i>et al</i> (2002)	100
Neofotistou <i>et al</i> (2003)	300
Skinner (2002)	150
Vanõ <i>et al</i> (2003)	180

Table 3.8: Reported DAP trigger levels for identifying patients at risk of skin injuries, following cardiac catheterization procedures. (CA: coronary angiography; PTCA: percutaneous transluminal coronary angioplasty.) The two values given by Karambatsakidou *et al* (2005) for coronary angiography are operator-specific DAP reference values for their two primary operators.

Vanõ *et al* (2003) routinely measure skin dose for intra-coronary brachytherapy, using a combination of film and TLD. Other authors attempt to estimate skin doses for those patients who exceed their DAP trigger levels. Cook *et al* (2004) designed a

spreadsheet to estimate the total dose incident on the patient's skin, from recorded exposure factors. This took no account of the different imaging projections used, but assumed the worst possible case of all exposures using a single projection.

Whilst some hospitals simply advise patients to report any skin effects (Mooney, 2000; Koenig *et al*, 2001b; McFadden *et al*, 2002), others have procedures in place for formally inspecting the patient's skin if a certain dose or DAP threshold is exceeded (Vanō *et al*, 2003; Neofotistou *et al*, 2003; Cook *et al*, 2004). No skin injuries have yet been seen at any of these routine checks. However, in most cases the skin dose was estimated, not measured. Hospitals are likely to over-estimate rather than under-estimate skin doses, since it is better to err on the side of caution when assessing whether there is potential for detrimental health effects. Certainly the software used by Cook *et al* (2004) assumed the worst possible case: that of all radiation exposures coming from the same projection.

The protocol for consenting patients should include information on the risk of deterministic effects associated with the procedure they are about to undergo. In preparing this risk information, consideration should be given to the radiation doses and incidence of skin injuries arising from the procedure at that particular facility. Thus, a thorough local survey of skin dose and deterministic effects is needed, to prepare appropriate risk information that enables fully informed consent.

3.7 Summary

It has been shown that cardiac catheterization procedures can result in high radiation doses to the patient's skin. There are a number of reports of deterministic skin injuries following particularly lengthy or difficult procedures. In order to identify at-risk patients and provide them with appropriate information and clinical follow-up, the US Food and Drug Administration and the International Commission on Radiological Protection have published recommendations that the location and magnitude of high skin doses are recorded in the patient's notes.

The dose quantities most commonly used are dose-area-product and fluoroscopy time. Since many different projections are used in a single procedure, these are unlikely to give an adequate indication of peak skin dose.

Several different dosimeters have been used to obtain direct measurements of skin dose in the cardiac catheterization laboratory. Of these, slow radiographic film seems the most practical, since it captures the dose distribution over a large area, is relatively quick to position and read out, and is invisible on the radiographs. Another dosimetry method offering great potential is skin dose modelling, i.e. calculation of the dose distribution on the patient's skin from the exposure and projection data stored in the image files.

Once a method for assessing skin dose has been adopted, it is important to establish protocols for providing information and follow-up to patients identified as being at risk.

Chapter 4 - Calibration of Dosimetry Equipment

4.1 Introduction

This chapter describes the detailed characterisation of Kodak EDR2 film, in preparation for its use as a skin dosimeter in the cardiac catheterization laboratory. The film was calibrated across the range of typical exposure conditions, and its useful range identified. The relationship between dose and optical density was defined using a novel equation, for a standard set of exposure and processing conditions. The consistency of its response with variations in film batch, time between exposure and processing, and day-to-day variations in processor performance, was investigated. The effects of field size, exposure rate, beam energy and filtration were quantified. The overall uncertainty in dose, for a given optical density, was estimated. The X-ray unit's integral dose-area-product meter was calibrated along with the film, and its performance characteristics are also presented.

In the past, several different models have been used to describe film response. Perhaps the best-known is the 'logit' function, described by Willis and Bencomo (1990). This function may be expressed as

$$L_n = \ln \left(\frac{OD - OD_{\min}}{OD_{\max} - OD} \right)$$

Equation 4.1

where OD is optical density, OD_{\min} is the density of an unexposed part of the film, and OD_{\max} is the density of a saturated part of the film. The logit function has a linear relationship with the natural logarithm of the radiation dose.

$$L_n = b(a + \ln D)$$

Equation 4.2

where D is dose, and a and b are constants. By plotting L_n against $\ln(D)$ and determining the gradient and intercept of the regression line, the relationship between dose and optical density can be defined. Combining Equation 4.1 with Equation 4.2 and rearranging gives optical density in terms of dose.

$$OD = \frac{OD_{\min} + OD_{\max} e^{b(a+\ln D)}}{1 + e^{b(a+\ln D)}}$$

Equation 4.3

Zhu *et al* (2003) proposed the following equation specifically for EDR2 film.

$$OD = OD_{\max} (1 - e^{-\alpha D})$$

Equation 4.4

As before, OD stands for optical density. D is dose in mGy, and α is a constant. The equation may be rearranged to give

$$\alpha = -\frac{1}{D} \ln \left(1 - \frac{OD}{OD_{\max}} \right)$$

Equation 4.5

Thus, the value of α may be determined by plotting the logarithmic term against dose, and finding the gradient. Guibelalde *et al* (2003) took the simpler approach of assuming a linear response for doses of up to 500 mGy. Whilst mathematically convenient, this did not make full use of the film's responsive range. More recently, Karambatsakidou *et al* (2005) approximated dose as a simple exponential function of optical density.

4.1.1 Objectives

The objectives of this investigation were:

- To determine the dose response of Kodak EDR2 film for typical exposure conditions used in the cardiac catheterization laboratory, with the local processing protocol;

- To investigate how the film's response varied with exposure conditions, film batch and processor performance, and hence to estimate the uncertainties in dosimetry measurements;
- To characterise the performance of the X-ray unit's integral dose-area-product meter across the range of typical exposure conditions.

4.2 Method

All exposures were performed using a Philips Integris H5000F cardiac imaging unit (Philips Medical Systems, Best, Netherlands), which was subject to routine quality control checks as recommended by the Institute of Physics and Engineering in Medicine, Report 77 (1997). The X-ray tube potential (kVp) and spectral filter were selected by reprogramming one of the modes on the imaging unit.

Doses were measured using Radcal 9010 series dose meters (Radcal, Monrovia, California), with 6 cc or 60 cc ionisation chambers as appropriate. These were calibrated annually against a secondary standard, and all readings were corrected by the most recent calibration factors. Measurement accuracy quoted by the manufacturer was $\pm 4\%$, with energy and dose rate dependence at $\pm 5\%$ over much wider ranges than were used in this study. For the purpose of error analysis, dose meter performance was considered independent of energy and dose rate.

The experimental set-up used for the majority of exposures is shown in Figure 4.1. The gantry was oriented with the X-ray tube pointing vertically upwards. The couch was positioned at its minimum height, and the detector at its maximum height. The mattress was removed, and two cardboard boxes were stacked on their sides, on the thick part of the couch. The film was positioned inside the lower box, and a flat, 60 cc ionisation chamber inside the upper box. The radiation field was then centred on the ionisation chamber. A two millimetre sheet of lead on top of the boxes drove the X-ray tube current (mA) up to maximum, to keep exposure times down, whilst protecting the image intensifier from over-exposure.

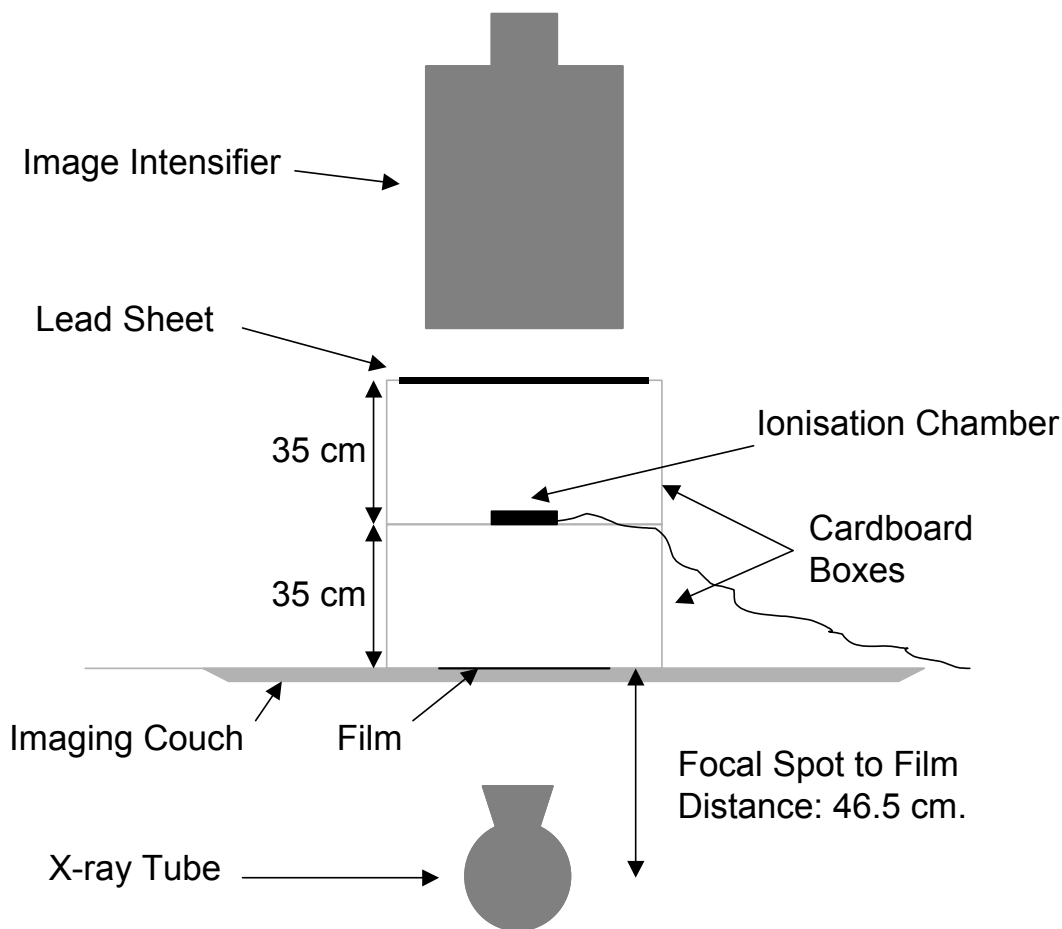


Figure 4.1: Experimental set-up.

The cardboard boxes enabled easily reproducible geometry, whilst maximising the dose rate at the film to minimise exposure times, ensuring that the entire dose meter was irradiated, and avoiding backscatter from the chamber onto the film, or from the lead sheet into the chamber. The dose at the film D_f was calculated from that measured by the ionisation chamber D_c , using an inverse square law correction for distance (Equation 4.6), where x_c was the distance from the focal spot to the chamber, and x_f the distance from the focal spot to the film.

$$D_f = D_c \left(\frac{x_c}{x_f} \right)^2$$

Equation 4.6

In order to provide a means of correcting for variations in processor performance, the leading and trailing edges of each film were exposed twelve times using a Kodak Process Control Sensitometer (Eastman Kodak Company, Rochester, New York).

Unless otherwise stated, they were then stored in a dark room hopper for 24 hours, prior to processing in a Kodak X-OMAT M6B processor (Eastman Kodak Company, Rochester, New York), with Photosol developer and fixer (Photosol Limited, Basildon, UK). The processor was subject to bi-daily quality control checks, in accordance with the Institute of Physics and Engineering in Medicine, Report 77 (1997).

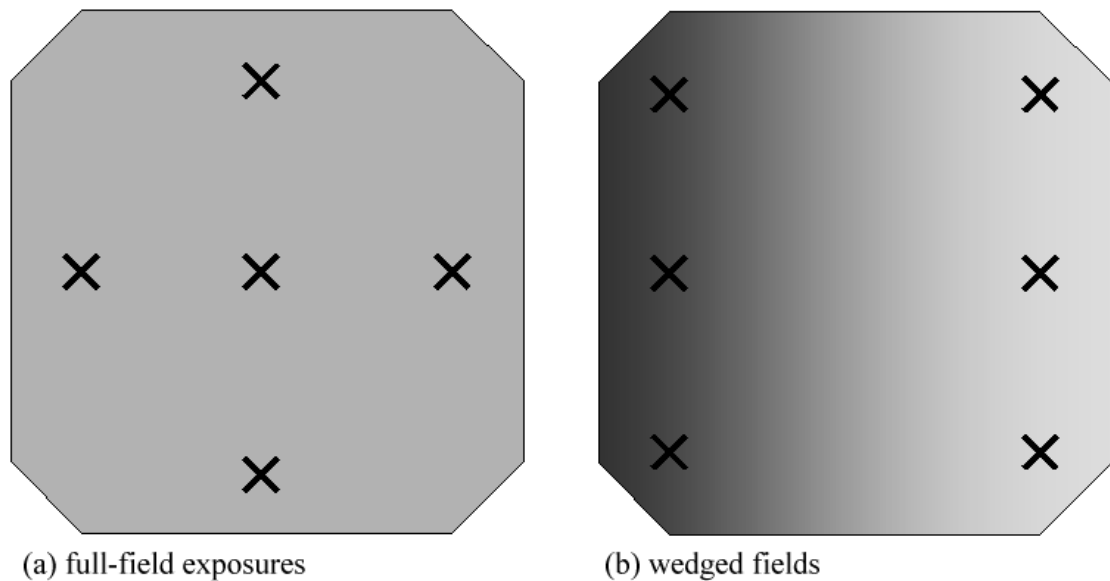


Figure 4.2: Positions of optical density measurements.

Optical densities were measured using a Pehamed “Densoquick 2” densitometer (Pehamed, Sulzbach, Germany). According to the manufacturer’s specification, accuracy was within 1.5%, for densities greater than one. For full-field exposures, the density was measured in the centre of the irradiated area and approximately 1 cm in from each edge, as shown in Figure 4.2(a), and the mean taken. For films with the equalisation filter in place, three measurements were taken for each of the wedged and non-wedged areas, about 1 cm in from the edge, as shown in Figure 4.2(b). To determine base-plus-fog, optical density was measured approximately 2 cm inside each corner of the film, and the four readings were averaged.

4.2.1 Film Response Curve

The film was calibrated at 60, 80 and 110 kVp, at a range of doses from 20 to 1000 mGy. These beam energies were chosen to represent the minimum, typical and

maximum values used in clinical practice. The X-ray tube and its housing, together with the collimator assembly, provided around 2.7 mm aluminium equivalent filtration. The couch provided a further 1.7 mm aluminium equivalent. Measurements were initially made with no additional filtration selected.

In order to define the relationship between dose and optical density, attempts were made to fit first the logit model (Equation 4.1 to Equation 4.3) and then Zhu's model (Equation 4.4 and Equation 4.5) to the data. A new equation was then developed, which was based on Zhu's equation, but normalised so that zero dose corresponded to base-plus-fog, instead of zero density (Equation 4.7).

$$OD = OD_{\max} (1 - e^{-\alpha D}) + OD_{\min} e^{-\alpha D}$$

Equation 4.7

OD was the optical density due to the X-ray exposure, OD_{\max} the saturation density of the film, OD_{\min} base-plus-fog, and D radiation dose. This could be rearranged to give the constant α (Equation 4.8).

$$\alpha = -\frac{1}{D} \ln \left(\frac{OD_{\max} - OD}{OD_{\max} - OD_{\min}} \right)$$

Equation 4.8

For each kVp, α was determined by plotting the logarithmic term against dose, fitting a regression line and determining its gradient.

4.2.2 Film Consistency

A series of exposures were made at 80 kVp, 160 mGy, to investigate the consistency of the film's response and its variation with field size, exposure rate, film batch and day-to-day variations in processor performance.

In order to investigate the stability of the emulsion post-exposure, a number of films were subjected to identical X-ray exposures, and stored in a dark room hopper or in their packets for various time intervals before processing.

The maximum spectral filtration was then selected, and one measurement repeated for each kVp, at 160 mGy. This additional filter consisted of 0.4 mm copper, plus 1.5 mm aluminium.

4.2.3 Equalisation Filter

The X-ray unit's equalisation filter was a semi-circular brass disc, with a tapered straight edge that could be driven into the beam from any direction. Its uniform region had equivalent filtration of 22 mm aluminium, at 80 kVp.

To determine its effect on film response, the filter was positioned with its edge parallel to the anode-cathode axis, and covering approximately half of the image. Two 6 cc ionisation chambers were positioned side-by-side, one in the fully wedged and one in the non-wedged part of the beam (Figure 4.3). At each kVp, two films were exposed, to give doses of 160 mGy first in the wedged, and then in the non-wedged parts of the beam.



Figure 4.3: Dose meter positions for wedge filter measurements.

4.2.4 Backscatter

To quantify the effect of backscatter on film response, the film was placed directly on the couch, with the 60 cc ionisation chamber on top of it. A 20 cm stack of Perspex was positioned above the ionisation chamber, supported by 2 cm blocks at either side (Figure 4.4). Exposures were made at each kVp, first with no additional filtration, and then with the maximum spectral filtration selected. Each film was exposed to around 160 mGy. The Perspex was then removed, and the exposures repeated.

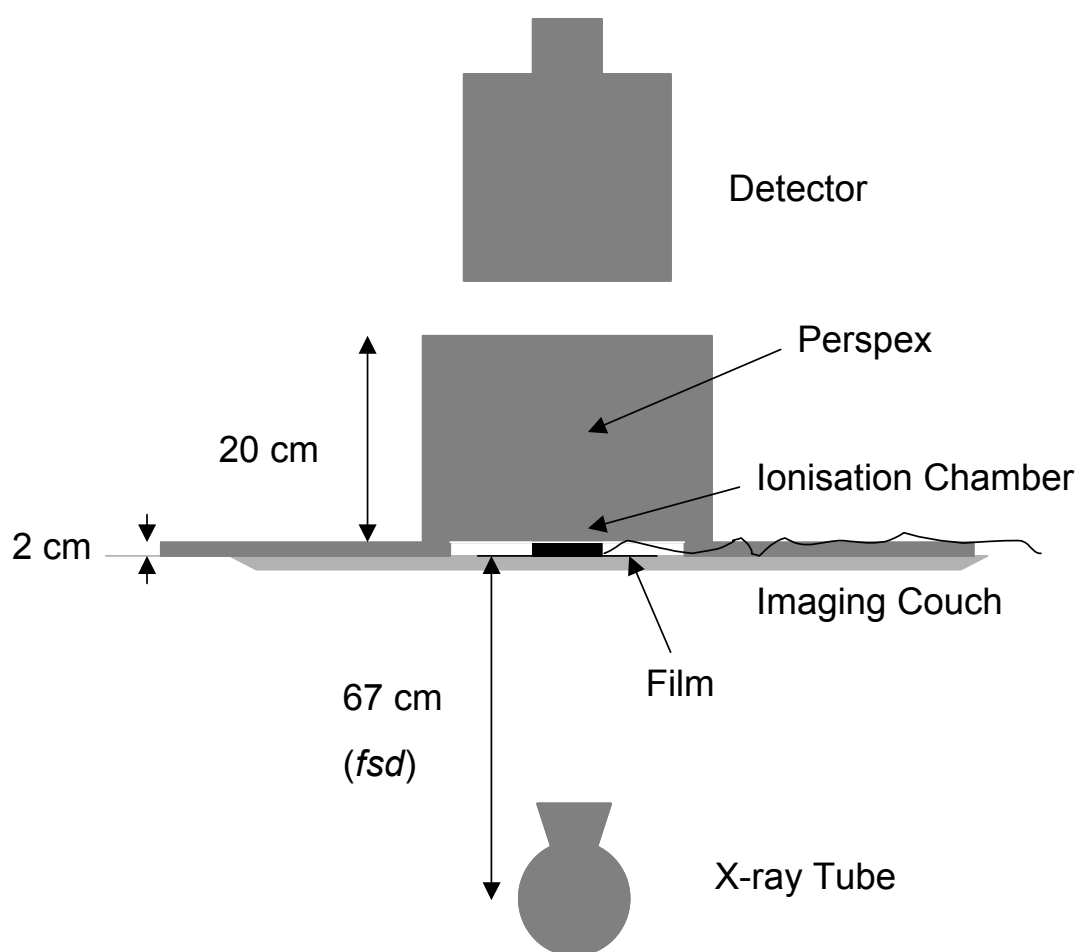


Figure 4.4: Set-up for backscatter investigation.

4.2.5 DAP Meter

The X-ray unit was fitted with an integral 'PTW-Diamentor-M1' DAP meter (PTW-Freiburg, Freiburg, Germany). In order to characterise its performance, displayed DAP was noted before and after each film exposure. The field size was calculated

from the irradiated area on the film, and the ratio of displayed DAP to measured DAP computed for each set of exposure conditions.

4.3 Results

4.3.1 Film Response Curve

Figure 4.5 shows how the optical density varied with dose, at each of 60, 80 and 110 kVp, with no additional filtration. The error bars indicate the accuracy associated with the measuring instruments; $\pm 4\%$ for the dose meters, and $\pm 1.5\%$ for the densitometer.

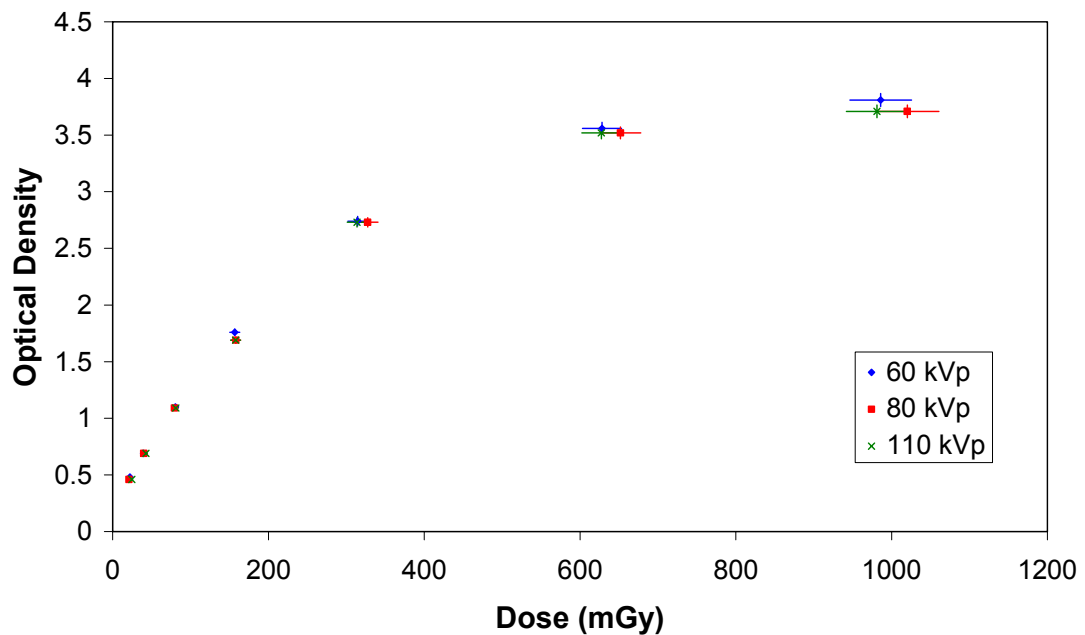
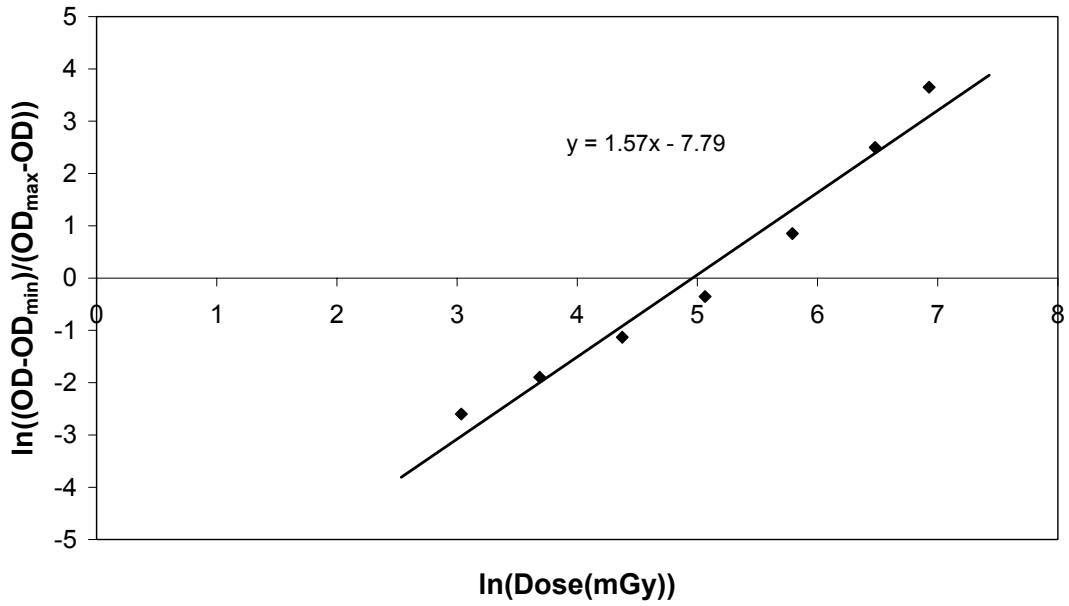
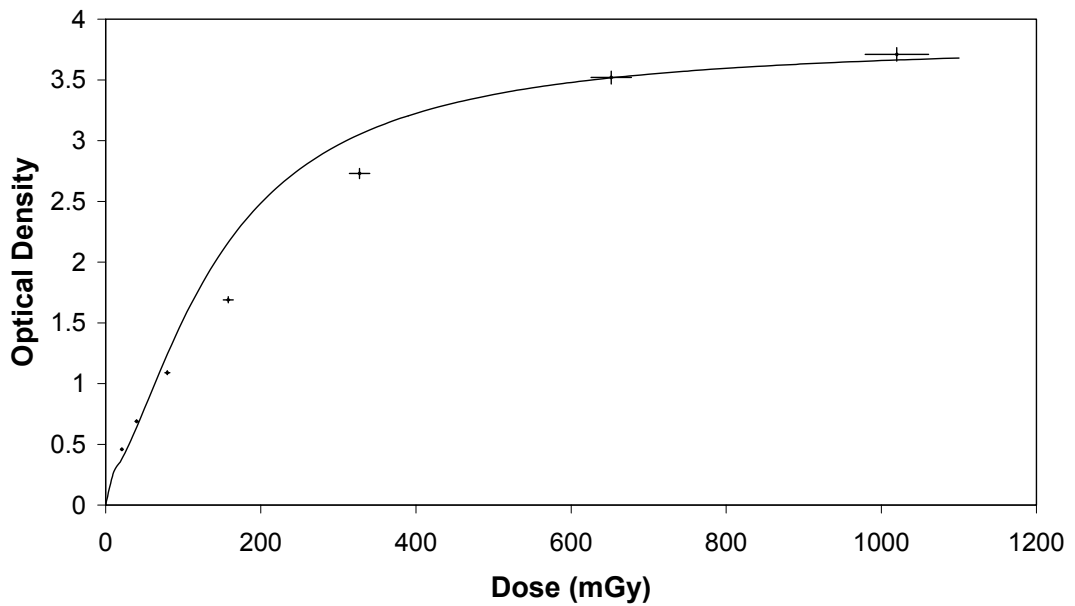


Figure 4.5: Optical density versus dose, for each of 60, 80 and 110 kVp. Error bars indicate accuracy of measuring instruments: $\pm 4\%$ for dose, and $\pm 1.5\%$ for optical density.

Figure 4.6 to Figure 4.8 show the three different models fitted to the data, at 80 kVp. The logit function gave a poor fit to the film response. Zhu's equation represented the data more accurately, but overestimated doses below 100 mGy, since it assumed zero density for zero dose. The new equation offered the best fit to measured data, with improved accuracy at low doses.

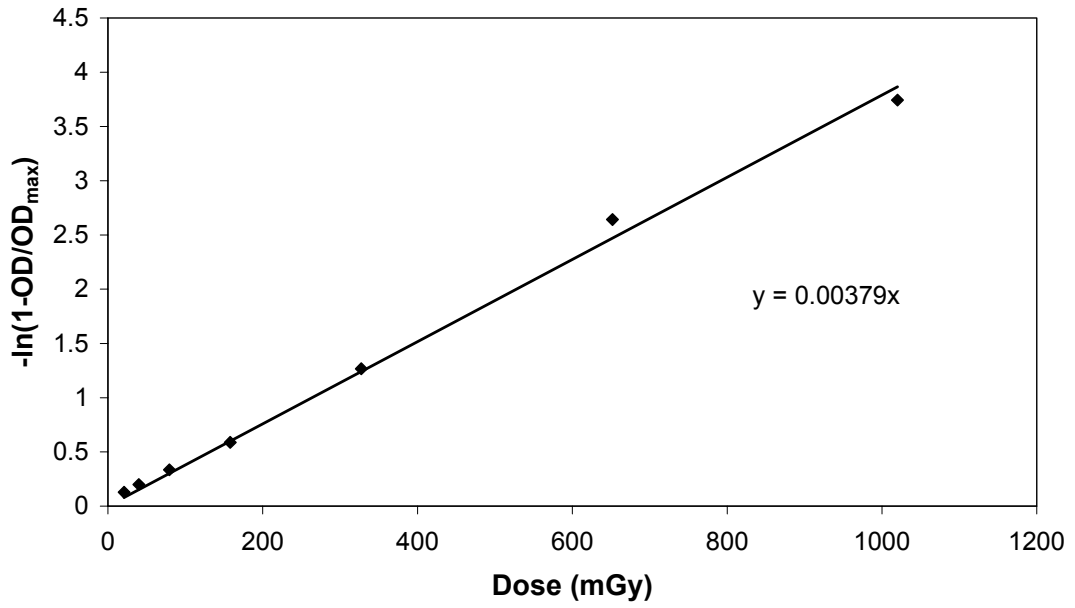


(a)

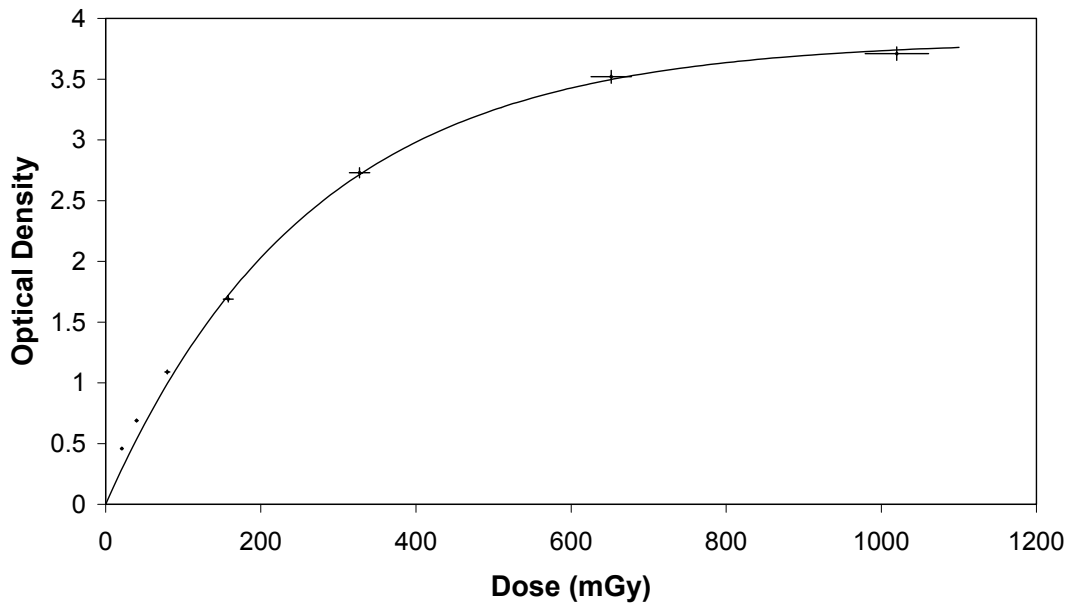


(b)

Figure 4.6: Logit fit to measured data, at 80 kVp. (a) Logit function versus $\ln(\text{Dose})$. (b) Resulting relationship between dose and optical density, shown with empirical data points. Error bars indicate accuracy of measuring instruments: $\pm 4\%$ for dose, and $\pm 1.5\%$ for optical density.

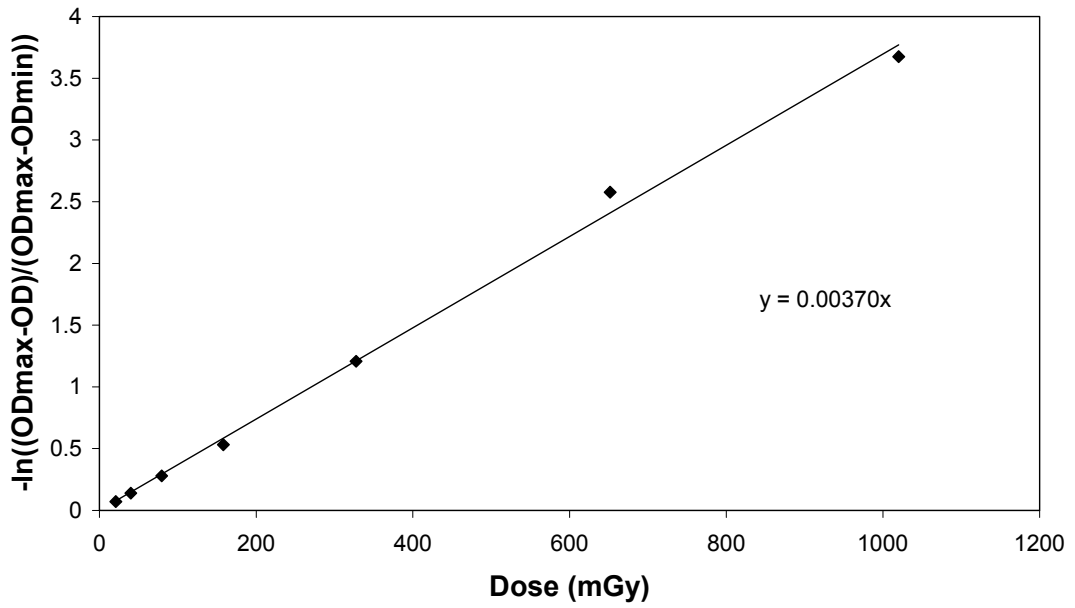


(a)

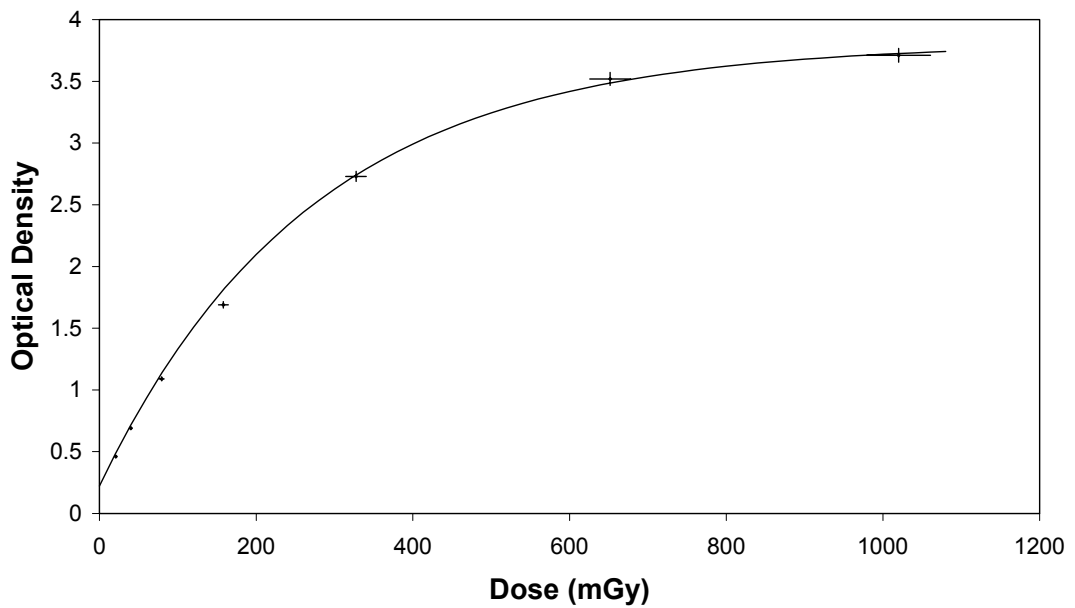


(b)

Figure 4.7: Zhu's model fitted to measured data, at 80 kVp. (a) Logarithmic term plotted against dose, to determine α . (b) Resulting relationship between dose and optical density, shown with empirical data points. Error bars indicate accuracy of measuring instruments: $\pm 4\%$ for dose, and $\pm 1.5\%$ for optical density.



(a)



(b)

Figure 4.8: The new equation fitted to measured data, at 80 kVp. (a) Logarithmic term plotted against dose, to determine α . (b) Resulting relationship between dose and optical density, shown with empirical data points. Error bars indicate accuracy of measuring instruments: $\pm 4\%$ for dose, and $\pm 1.5\%$ for optical density.

The calibration curve defined using the new equation had the same form at each kVp, but slightly different values of α . At each optical density, predicted and measured doses agreed to within $\pm 4\%$ at 60 kVp, $\pm 10\%$ at 80 kVp and $\pm 6\%$ at 110 kVp.

Since an exposure of 160 mGy gave an optical density close to the centre of the film's range, this was chosen as the standard exposure level for all further characterisation measurements.

4.3.2 Film Consistency

Five exposures at 80 kVp, 160 mGy and 23 cm field size, on films from four different batches, processed on different days, showed mean sensitivity of 94.5 mGy per unit of optical density (mGy/OD). The maximum deviation was 4.1 mGy/OD or 4.4%.

Analysis of the sensitometry strips on these films showed considerable variation between the densities of the strips on the leading and trailing edges. In addition, the mean densities of step 17 (the speed step) for individual films varied by up to 0.27 units of optical density, or 26%. Thus, the optical densities due to light exposure appeared far more sensitive to variations in film batch and processor performance than those due to X-ray exposure.

Standard (80 kVp, 160 mGy) exposures made at each of the 17 cm and 23 cm field sizes showed consistency of film response to within 1%. Similar exposures at 5.8, 20 and 190 mA also showed consistency to within 1%.

Table 4.1 shows the film sensitivity measured at 160 mGy, with each kVp and spectral filter combination. The mean sensitivity was 101 mGy/OD. This matched the film's response at 110 kVp, with no additional filtration.

Spectral Filter	mGy/OD		
	60 kVp	80 kVp	110 kVp
Filter 0 (no added filtration)	89	94	101
Filter 1 (0.4 mmCu + 1.5 mmAl)	88	106	130

Table 4.1: Effect of kVp and spectral filter on films exposed to 160 mGy, without backscatter.

For each of the exposures detailed in Table 4.1, the mean spectral energy was estimated using the IPEM Report 78 Spectrum Processor (Reilly & Sutton, 1997). Figure 4.9 demonstrates that the dose required per unit of optical density increased with mean photon energy.

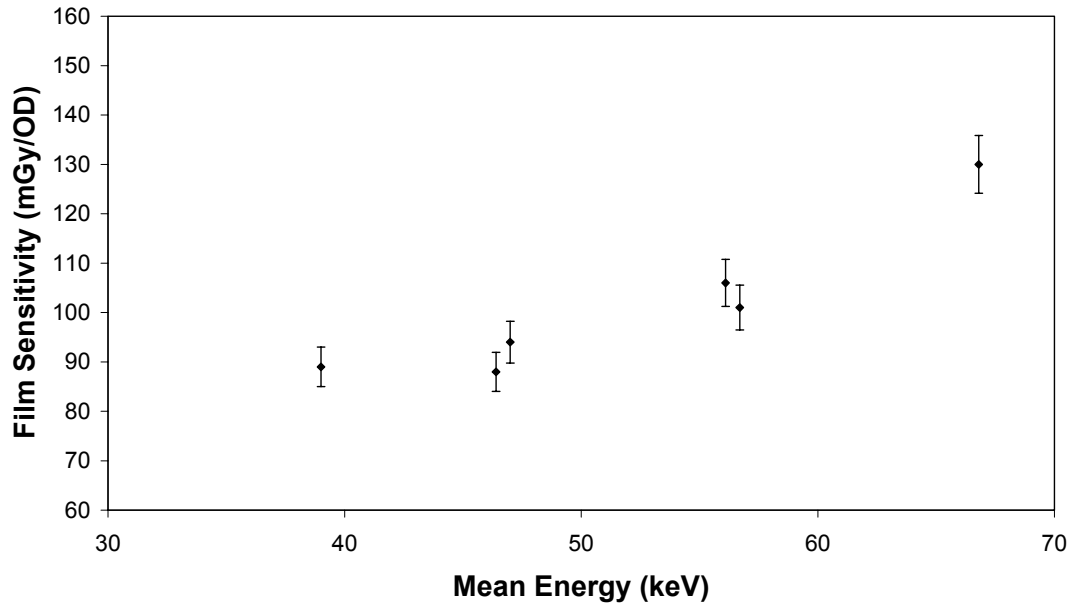


Figure 4.9: Film sensitivity versus mean spectral energy, for the exposures detailed in Table 4.1. The error bars indicate the expected variation of $\pm 4.4\%$ due to film batch and processor performance.

Figure 4.10 shows the variation in film response with time interval between exposure and processing. The horizontal line indicates mean sensitivity, and the error bars show the expected variation of $\pm 4.4\%$ due to film batch and processor performance. It appeared that films processed in the first few minutes following exposure were slightly paler, with an additional 4 mGy required per unit of optical density. Considering only the data for one hour or more, the maximum variation from the mean was 2.6 mGy/OD or 2.7%.

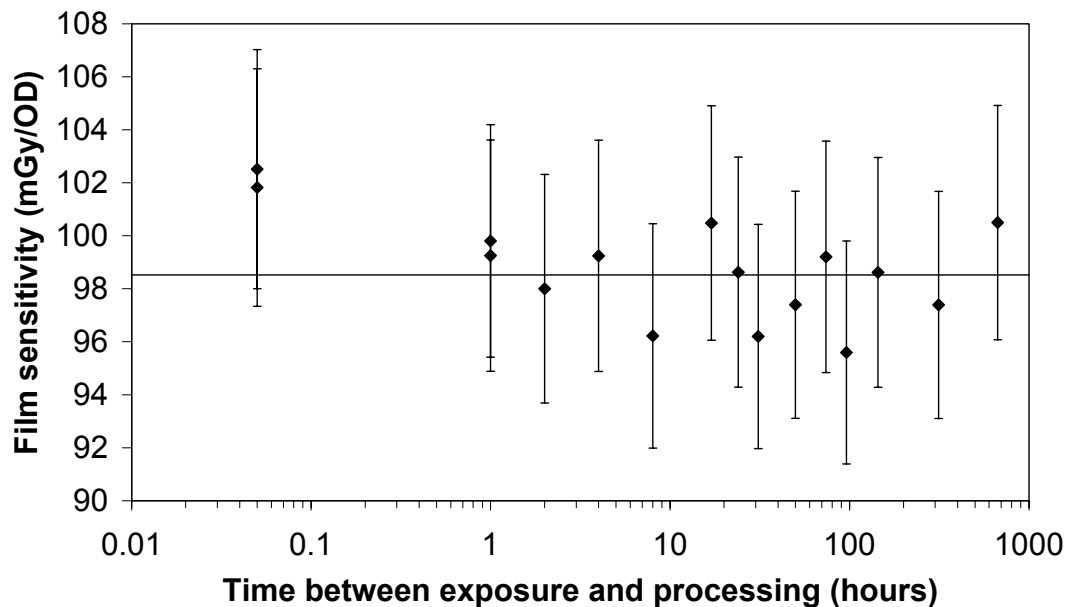


Figure 4.10: Effect of time-to-processing on film sensitivity, at 80 kVp and 160 mGy. The error bars indicate the expected variation of $\pm 4.4\%$ due to film batch and processor performance. The horizontal line shows mean sensitivity.

Several films in one batch showed irregular dark patches, as demonstrated in Figure 4.11(a). Where the artefact extended across the exposed area of the film, this made dose assessment impossible. Three films in another batch demonstrated discrete dark spots, such as that shown in Figure 4.11 (b). These corresponded to localised faults in the light-proofing of the film packets. An image of the printed text from the film packet was visible on several films, but this made negligible difference to measured optical density.

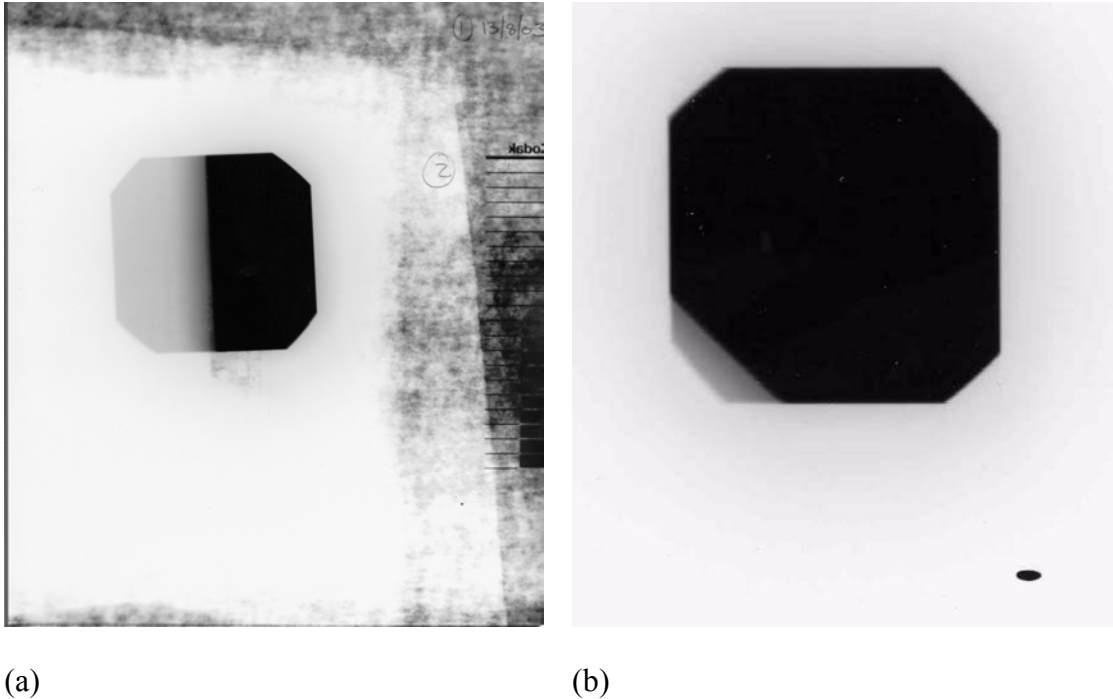


Figure 4.11: Artefacts seen on films. (a) Irregular dark patches around film edges. (b) Discrete dark spot in bottom right-hand corner.

4.3.3 Equalisation Filter

Table 4.2 shows film sensitivity measured in the wedged and non-wedged parts of the beam, with the equalisation filter in place. The sensitivity of 61 mGy/OD measured in the wedged part of the beam at 60 kVp was obtained using a dose of 47 mGy. It may be compared with the sensitivity of 58 mGy/OD, measured at a dose of 40 mGy without the wedge filter in place (Figure 4.5). All other measurements were performed at 160 mGy. The right hand column shows the dose ratio between the fully wedged and non-wedged parts of the beam, for a single exposure. The wedge filter reduced the dose to objects in its shadow by a factor of at least six.

kVp	mGy/OD		$\left[\frac{\text{Dose wedged}}{\text{Dose non-wedged}} \right]$
	wedged	non-wedged	
60	61 (at 47 mGy)	91	1/26
80	113	103	1/12
110	147	104	1/6

Table 4.2: Effects of equalisation filter on film sensitivity and dose. All sensitivity measurements made at 160 mGy, unless otherwise stated.

Comparing Table 4.2 with the top row of Table 4.1, the exposure required to give a particular optical density was increased by up to 47 mGy/OD, or 47%, in the shadow of the wedge filter. The film sensitivity in the non-wedged part of the beam was also reduced slightly (higher dose per OD), compared with that for a beam with no wedge filter in place.

4.3.4 Backscatter

Table 4.3 shows film sensitivity measured with 20 cm Perspex backscattering material, for each kVp and spectral filter. Film sensitivity was reduced (higher dose required to produce a given optical density), compared to Table 4.1. The mean sensitivity was 111 mGy/OD. Again, this matched the film's performance at 110 kVp, with no spectral filtration. Individual measurements varied from the mean by -10% to +24%, across the range of beam qualities investigated.

Spectral Filter	mGy/OD		
	60 kVp	80 kVp	110 kVp
Filter 0 (no added filtration)	110	100	110
Filter 1 (0.4 mmCu + 1.5 mmAl)	103	108	138

Table 4.3: Effect of kVp and spectral filter on films exposed to 160 mGy, with 20cm Perspex backscattering material.

These films showed a backscatter image of the ionisation chamber. As a result, the optical density varied by up to 0.1 between the centre and periphery of the irradiated area. A similar effect was seen in the absence of the Perspex, when the ionisation chamber was positioned directly on top of the film.

4.3.5 DAP Meter

With the ionisation chamber on the couch top, in the absence of backscattering material, the mean ratio of displayed DAP to measured DAP was 1.33. Measurements made at 80 kVp, with no additional filtration, showed reproducibility to within $\pm 3.3\%$. Variations in performance with radiation field size, exposure rate and dose were all within this range. The DAP meter's response varied with kVp and spectral filtration by up to $\pm 10\%$ about the mean.

4.4 Discussion

4.4.1 Film Response Curve

The film saturated at around 1 Gy. This is the threshold recommended by the International Commission on Radiological Protection (2000) and the US Food and Drug Administration (1995), above which the potential for radiation skin injuries should be recorded. The film may be used to identify patients receiving skin doses of 1 Gy or more, but cannot assess peak skin doses for these patients.

The approach taken by Vanõ *et al* (2003) and Guibelalde *et al* (2003) of minimising the developer temperature to increase the film's saturation point was not practical in the present study, since the only available film processor was used primarily for diagnostic films. Besides, their reported saturation point of between 1.2 and 1.5 Gy remained inadequate for assessing doses up to the 2 Gy threshold for deterministic skin effects.

The logit function offered a poor fit to the dose response of EDR2 film. Zhu's model (Equation 4.4) gave a good fit to the data at higher optical densities. However, it associated a dose of zero with an optical density of zero and this caused doses to be overestimated at the bottom end of the range. In reality, the minimum density was given by base-plus-fog, which was about 0.2.

The new model described by Equation 4.7 represented the film's response more accurately, especially at the lower end of the dose range. At 110 kVp, calculated and measured doses agreed to within $\pm 6\%$ at each optical density.

4.4.2 Film Consistency

Variations in film batch and processor performance caused the film's response to vary by up to 4.4%, at 160 mGy. Film sensitivity was consistent to within 1% across the range of field sizes and exposure rates in clinical use. Since this was well within the uncertainty due to film batch and processor performance, film sensitivity may be assumed independent of field size and exposure rate.

The root mean square uncertainty due to the variations in film batch and processing conditions (4.4%), errors in curve fitting (6%), and the accuracy of the measuring instruments (dose meter 4%, densitometer 1.5%), was 8.6%.

The optical densities due to light exposures were far more sensitive to changes in processing conditions than those from X-ray exposures. Given that the film's performance when exposed to X-rays was fairly consistent with day-to-day fluctuations in processing conditions, it seemed unlikely that any correction via light sensitometry would improve accuracy. As a result, it was not pursued further.

With no additional filtration, the film's energy dependence was within the root mean square uncertainty reported above. This is in agreement with the findings of Guibelalde *et al* (2003) and of earlier studies using Kodak XV-2 film (Geise & Ansel, 1990; Vanõ *et al*, 1997; Nicholson *et al*, 2000), which reported energy dependence of 5% or less. However, the present study found the relationship between dose and optical density to be strongly dependent on beam filtration, especially at the high end of the energy range. This effect had not previously been reported. It is an important consideration in the cardiac catheterization laboratory, where heavily filtered beams are often used in some imaging modes.

Throughout the study, the response of the Radcal dose meters was assumed to be independent of filtration. This may not be strictly true. No definitive information was available regarding the dose meters' filtration dependence, although the supplier

advised that it was insignificant. Given their low energy dependence of $\pm 5\%$ over the range 20 keV to 1.33 MeV, this would seem reasonable.

Optical density appeared to increase slightly during the first few minutes following X-ray exposure, and to stabilise within the first hour. After this, the maximum variation from the mean was 2.7%, which was well within the uncertainty attributable to variations in film batch and processor performance. This phenomenon has recently been reported by Childress and Rosen (2004), for EDR2 film exposed to megavoltage photons. In order to allow the emulsion to stabilise, films should be processed at least one hour after exposure.

Three of the films showed discrete dark spots outside the irradiated area, and these were identified with localised faults in the light-proofing of the film packets. It seemed most likely that the irregular dark patches shown in Figure 4.11(a) were also caused by faulty light-proofing. Films showing such artefacts could not be used for dosimetry. Since this investigation, Kodak have changed the design of EDR2 film packets. It may be hoped that this will reduce the incidence of light-leakage artefacts.

4.4.3 Equalisation Filter

At 60 kVp, the film's response was unaffected by the equalisation filter. At higher energies, the dose required to give a particular optical density increased by up to 47% in its shadow.

Although the equalisation filter was often used in clinical procedures, the imaging unit stored no information about when it was used, or about its position in the beam. Whilst in some cases it would be possible to determine its position from the dosimetry film, this would be impossible in regions of the film where several fields overlapped. For the purpose of film dosimetry therefore, it was necessary to assume that the equalisation filter was never used. This would result in skin doses being underestimated. The magnitude of this error was estimated as follows.

The total dose D at any point on the film may come from several fields, some of which are intercepted by the equalisation filter. It may be represented by the sum of the wedged (D_w) and non-wedged (D_n) dose contributions at that point.

$$D = \sum D_w + \sum D_n$$

Equation 4.9

The wedge filter attenuates the beam by a factor of at least 6. Thus, even if it is in place for every field, on average the contribution from the wedged parts will not be more than about 1/6 of the contribution from the non-wedged parts.

$$\sum D_w \approx \frac{1}{6} \sum D_n$$

Equation 4.10

so that

$$D \approx \frac{1}{6} \sum D_n + \sum D_n = \frac{7}{6} \sum D_n$$

Equation 4.11

Assuming a linear response over the dose range of interest, optical density is related to dose by

$$OD \approx c_w \sum D_w + c_n \sum D_n$$

Equation 4.12

where c_w is the calibration factor for the wedged part of the beam, and c_n the calibration factor for the non-wedged part. At 160 mGy, c_w had a minimum value of about $\frac{2}{3}c_n$. Therefore,

$$OD \approx \frac{2}{3}c_n \frac{1}{6} \sum D_n + c_n \sum D_n = \frac{10}{9}c_n \sum D_n$$

Equation 4.13

However, when calculating skin dose from measured optical density, it is necessary to assume that

$$D \approx \frac{OD}{c_n}$$

Equation 4.14

Substituting in the optical density from Equation 4.13 gives

$$D \approx \frac{10}{9} \sum D_n$$

Equation 4.15

The difference between this calculated dose and the actual dose (defined in Equation 4.11) is

$$\left(\frac{10}{9} - \frac{7}{6}\right) \sum D_n = -\frac{1}{18} \sum D_n$$

Equation 4.16

Thus, the dose determined from measured optical density is likely to underestimate the actual dose by up to 1/18, or 6%. The actual dose will be up to 6% higher than that measured using the film.

This error could be larger for regions of the film where the wedged parts of several fields overlap. However, these regions are unlikely to correspond to peak skin dose, since the equalisation filter reduces doses in its shadow by a factor of at least six.

With the equalisation filter in place, the dose per OD in the non-wedged part of the beam was slightly higher than when the filter was not being used. Given the uncertainties due to film batch and processor performance, this result was not significant. However, a possible explanation is the scatter of high energy photons from the filter into the non-wedged part of the field.

4.4.4 Backscatter

The presence of backscattering material reduced film sensitivity, raising the dose required per unit of optical density by up to 24%. This effect was most pronounced for the softest beams.

A backscattered image of the ionisation chamber was visible, even when 20 cm Perspex were positioned close above it. This indicated that the film was not receiving the full amount of backscatter from the Perspex. In order to provide full backscatter conditions, the Perspex would need to be in direct contact with the film. The DAP meter could be used to determine the dose to the film, if it were first calibrated against an ionisation chamber positioned in contact with the Perspex. However, characterising

the film under these conditions would involve considerably more manual handling of the heavy Perspex, which would need to be removed from the couch each time a fresh film was required. For the purpose of the current study, it was assumed that the errors introduced by placing the ionisation chamber between the film and the Perspex would be small compared with the range of film responses due to variations in beam energy and filtration.

4.4.5 Definitive Calibration and Overall Uncertainty

The definitive calibration should reflect the film's performance in the presence of backscatter, since this best represents the clinical situation. On varying the tube potential and spectral filtration, average film performance most closely matched that at 110 kVp, with no additional filtration. This was the case both with and without backscatter. The mean dose required to produce a given optical density increased by 10% in the presence of backscatter. The definitive calibration was therefore modelled on the response curve measured at 110 kVp, with the dose values scaled up by 10%, to simulate the effect of backscatter.

The value of α for the re-scaled data was 2.70×10^{-3} . The mean values of OD_{min} and OD_{max} on the films used to determine α were 0.21 and 3.92 respectively. On rearranging Equation 4.8, this gave a definitive relationship between dose D (in mGy) and optical density OD of

$$D = -\frac{1}{0.0027} \ln\left(\frac{3.92 - OD}{3.71}\right)$$

Equation 4.17

Source(s)	Uncertainty
Film batch, processor performance, curve fitting, instrument calibrations	± 8.6%
Beam energy and spectral filtration	- 10% to + 24%
Equalisation filter	0% to + 6%
Overall	- 19% to + 39%

Table 4.4: Overall uncertainty in film response, at 160 mGy.

Table 4.4 summarises the sources of uncertainty in the film’s response. Linear combination of the expected variations seemed the most realistic approach to estimating overall uncertainty, since the variations in film performance with energy and filtration represented a range of responses rather than statistical uncertainties in the measurements. This gave an overall uncertainty of –19 to +39%, at 160 mGy, which corresponded to a dose range of –30 to +61 mGy.

The uncertainty (in mGy) was assumed to scale linearly with the gradient of the film response curve, described by

$$\frac{dD}{d(OD)} = \frac{e^{\alpha D}}{\alpha(OD_{\max} - OD_{\min})}$$

Equation 4.18

Figure 4.12 shows the definitive calibration curve, with error bars indicating the overall uncertainty at each calibration point. At 1 Gy, the uncertainty was estimated at about –280 to +570 mGy, or –26 to +53%. This was of the same order of magnitude as the uncertainty of ± 30 to 40% reported by Vanđ *et al* (2003) at the high end of the dose range, although these authors had not considered the effects of spectral filtration. The uncertainty interval in the present study was skewed towards higher doses than indicated by the film, due to the enhanced effects of filtration on high energy beams.

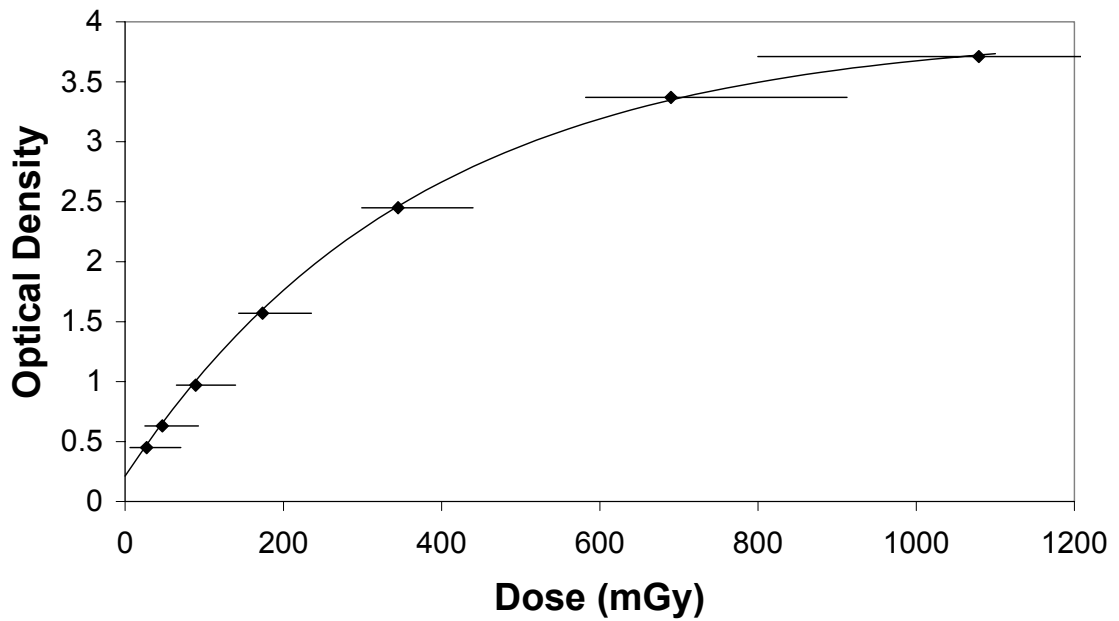


Figure 4.12: Definitive calibration curve, with error bars showing overall uncertainty in dose at each measured optical density.

4.4.6 DAP Meter

The mean ratio of displayed DAP to measured DAP was 1.33. The difference between the two values arose mainly from the service engineers' practice of calibrating the DAP meter without the couch in the beam. Since in clinical practice most of the radiation fields pass through the couch before interacting with the patient, the calibration method used in the present study seemed more appropriate.

With fixed beam quality, the DAP meter's performance was reproducible to within $\pm 3.3\%$. Its response varied with kVp and filtration by $\pm 10\%$ about the mean. A linear combination of this range of responses, with the random variations in performance, gave an overall uncertainty of around $\pm 13\%$. This was greater than the expected variations of up to 10% reported in the literature (Broadhead *et al*, 1997; Vanõ *et al*, 1998b; Hansson & Karambatsakidou, 2000; Kuon *et al*, 2003; Delichas *et al*, 2005). However, previous studies had not considered the effects of beam filtration on DAP meter performance.

4.5 Summary

Kodak EDR2 film was characterised across the range of exposure conditions used in the cardiac catheterization laboratory. Its dose-response curve was successfully modelled, using a novel equation. The film saturated at around 1 Gy, limiting its usefulness as a dosimeter.

Beam filtration was found to be the main factor affecting film sensitivity. Variations in spectral filtration and tube voltage together accounted for a range in dose per optical density of -10% to $+24\%$, at 160 mGy. The effects of beam filtration had not previously been considered by other studies. The equalisation filter altered film sensitivity, but also greatly reduced the dose in its shadow. Its use may cause doses to be underestimated by up to 6%.

Film performance was relatively insensitive to variations in film batch, processor performance, field size and exposure rate. Optical density increased slightly in the first few minutes following exposure, but had stabilised after about an hour. Artefacts were seen on several films, due to faults in the light-proofing of the film packets.

A definitive calibration curve was produced, by re-scaling the response curve measured at 110 kVp to match the film response in the presence of backscatter. Overall uncertainty in the film calibration was estimated at -30 to $+61$ mGy, at 160 mGy. This uncertainty was expected to increase as the film approached its saturation point.

The X-ray unit's integral dose-area-product meter was characterised along with the film. The mean ratio of displayed DAP to measured DAP was 1.33. Again, the DAP meter's performance was most strongly influenced by beam filtration, giving an overall uncertainty in DAP of around $\pm 13\%$.

Chapter 5 - Skin Dose Survey

5.1 Introduction

This chapter presents a survey of skin doses for patients undergoing coronary angiograms and coronary angioplasties. The dose distribution across each patient's back was mapped using Kodak EDR2 film. At the time of the study, no UK researchers had reported using this film for dosimetry at diagnostic energies. The peak skin dose was determined for each patient, and the results are presented by procedure type. There were a number of incidences of film saturation, and the implications of this are discussed.

Dose-area-product (DAP) is the dose quantity most commonly used in the cardiac catheterization laboratory. Its relationship with peak skin dose was examined, to investigate whether it could reliably be used to predict high skin doses. Several authors have reported correlations between DAP and clinical or technical factors related to the complexity of the procedure, such as the number of lesions treated, the condition of the vessel under treatment, the number of stents deployed, and patient weight or body mass index (Bakalyar *et al*, 1997; Bernardi *et al*, 2000; Kuon *et al*, 2003; Larrazet *et al*, 2003). In the present study, potential 'complexity indicators' were identified, and tested to see whether they could improve prediction of peak skin dose from DAP.

The limitations of both the film and dose-area-product measurements are discussed, and the need for a more robust method of assessing skin dose is identified.

5.1.1 Objectives

The objectives of this study were:

- To determine typical peak skin doses for patients undergoing coronary angiograms and coronary angioplasties at Nottingham City Hospital;
- To estimate the percentage of procedures resulting in peak skin doses above the 1 Gy recording level recommended by the International Commission on Radiological Protection and the US Food and Drug Administration;
- To investigate whether peak skin dose could be predicted using DAP, together with some function of procedure complexity.

5.2 Method

Doses were measured for 20 coronary angiograms and 32 coronary angioplasties, performed on the Philips Integris H5000F C-arm imaging unit referred to in Chapter 4. Patients were selected sequentially, and the study included only those procedures performed by in-house consultant cardiologists and the registrars working under their supervision. Fluoroscopy was performed using the “low continuous” factory setting, which had a nominal input dose rate at the detector of 740 nGy/s and employed 0.4 mm copper filtration. All acquisition runs were performed on the “12.5 FPS Coronary” setting, which had a nominal detector input dose rate of 870 nGy/s and used no copper filter.

5.2.1 Film Measurements

Before commencing each procedure, a sheet of 35 x 43 cm EDR2 film was positioned on the imaging table, underneath the mattress. The dotted rectangle in Figure 5.1 illustrates the position and orientation of the film. Its long axis was perpendicular to the long axis of the table, and its top edge was approximately level with the patient's shoulders. Each film packet was labelled to indicate which side was face-up, and which edge closest to the patient's head. Following exposure, a pinhole was made in the corner of the film packet corresponding to the patient's left shoulder, to identify the orientation of the processed film.

The radiographer or nurse controlling the X-ray unit wrote the patient's name, height and weight, and the procedure code on the film packet. The codes were retrospectively checked against the images stored on the server, and altered where necessary. Any procedure involving the use of a balloon and wires was classified as angioplasty. Those where no balloons or wires were seen were designated angiograms.

All films were stored in their packets overnight before processing, to allow the emulsion to stabilise. They were then processed in a Kodak X-OMAT M6B processor (Eastman Kodak Company, Rochester, New York), with Photosol developer and fixer (Photosol Limited, Basildon, UK). The processor was subject to bi-daily quality control checks, in accordance with the Institute of Physics and Engineering in Medicine, Report 77 (1997).

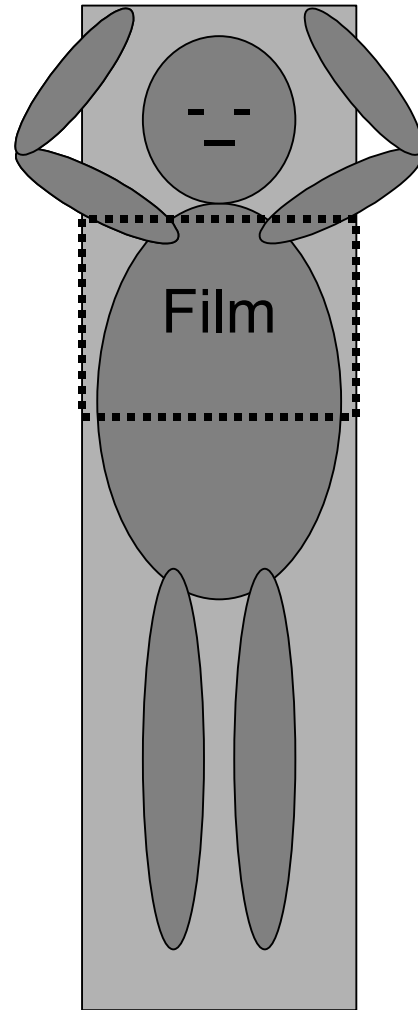


Figure 5.1: Film position and orientation.

The maximum optical density of each film was determined manually, using a Pehamed Densoquick 2 densitometer (Pehamed, Sulzbach, Germany), with readings taken at small increments across the darkest regions. The dose associated with the peak density was then calculated using the film's definitive calibration curve, described in Chapter 4.

5.2.2 Dose Area Product

The DAP for each procedure was measured using the X-ray unit's integral PTW Diamentor M1 dose-area-product meter (PTW-Freiburg, Freiburg, Germany). All readings were divided by the unit's calibration factor of 1.33, determined in Chapter 4. Dose-area-product and fluoroscopy time, together with details of the procedure carried out and equipment used, were stored in a database managed by the Cardiology Department. The number of acquisition runs for each case was obtained retrospectively, from the number of files stored on the image server.

Mean dose-area-products for the two procedure types were compared with values reported in recent literature, as presented in Tables 3.2 and 3.3. For those films that showed no saturation, Pearson correlation coefficients were calculated to determine the degree of association between peak skin dose and each of DAP, fluoroscopy time, number of runs and patient weight, for each procedure type. The significance of the correlations was determined using Student's t-test (Armitage, 1971). In each case the t-statistic (t) was calculated using Equation 5.1, where N was the number of procedures included in the analysis and R was the Pearson correlation coefficient.

$$t = R \sqrt{\frac{N-2}{1-R^2}}$$

Equation 5.1

For each procedure type, the ability of DAP to predict peak skin dose was investigated using a modified version of Bland and Altman's technique for method comparison (Bland & Altman, 1986; Bland & Altman, 1999). Whilst their papers describe how to assess agreement between two methods for measuring the same quantity, the modified technique allows two measurement methods using different units to be compared. It is described in detail on Martin Bland's website (<http://www->

users.york.ac.uk/~mb55/meas/diffunit.htm), and summarised in the following paragraph.

The equation of the regression line linking peak skin dose with DAP was computed, and then used to calculate a ‘predicted peak skin dose’ from each DAP measurement. The standard error SE_i associated with each predicted dose was calculated using

$$SE_i = \sqrt{s^2 \left(1 + \frac{1}{n} + \frac{(x_i - \bar{x})^2}{\sum (x_i - \bar{x})^2} \right)}$$

Equation 5.2

where x_i was the measured DAP, \bar{x} the mean DAP for all data points, n the number of observations, and s^2 the variance of empirical data points about the regression line. Since this standard error varied very little across the measurement range, its mean value was used to calculate the limits of prediction. These were ± 1.96 standard errors above and below the regression line.

5.2.3 Complexity Indicators

For angioplasties only, the database included information on the number of diseased vessels, the number and severity of the lesions treated, and the number of stents deployed. The association between each of these parameters and the ratio of peak skin dose to DAP was determined using the Spearman rank-order correlation coefficient, with a correction for tied rankings. Lesion severity was scored against the classification system published by the American College of Cardiology and the American Heart Association (Ryan *et al*, 1988). For the purpose of statistical analysis, the lesion severity scores of A, B1, B2 and C were transferred onto a numerical scale of 1 to 4. The significance of the correlations was again determined using Student’s t-test.

Only one significant correlate was found. The equation of its regression line was determined, and used to predict the ratio of peak skin dose to DAP for each procedure. This was then multiplied by measured DAP, to generate a predicted skin dose. Predicted and measured doses were compared using a Bland-Altman plot (Bland & Altman, 1986; Bland & Altman, 1999).

5.3 Results

5.3.1 Film Measurements

Figure 5.2 shows a dosimetry film from a coronary angioplasty, viewed as if looking at the patient's back. The patient's left shoulder is indicated by the small black spot in the top left-hand corner of the image. The region of peak skin dose can be readily identified as the darkest patch, in the top right-hand quadrant.



Figure 5.2: A dosimetry film from a coronary angioplasty, viewed as if looking at the patient's back. The black spot in the top left-hand corner indicates the patient's left shoulder.

One film from each procedure type showed abnormally large numbers of radiation fields, with extensive areas of saturation. Since the corresponding dose-area-products were not particularly high, it seemed likely that these films had been left on the imaging table for more than one procedure. Both were excluded from the analysis.

Figure 5.3 shows the distribution of peak skin doses for coronary angiography and angioplasty. Peak skin doses for the angiograms ranged from 70 to 520 mGy, with a mean value of 195 mGy. Seven of the angioplasty films showed localised areas of saturation, implying skin doses of 1 Gy or more.

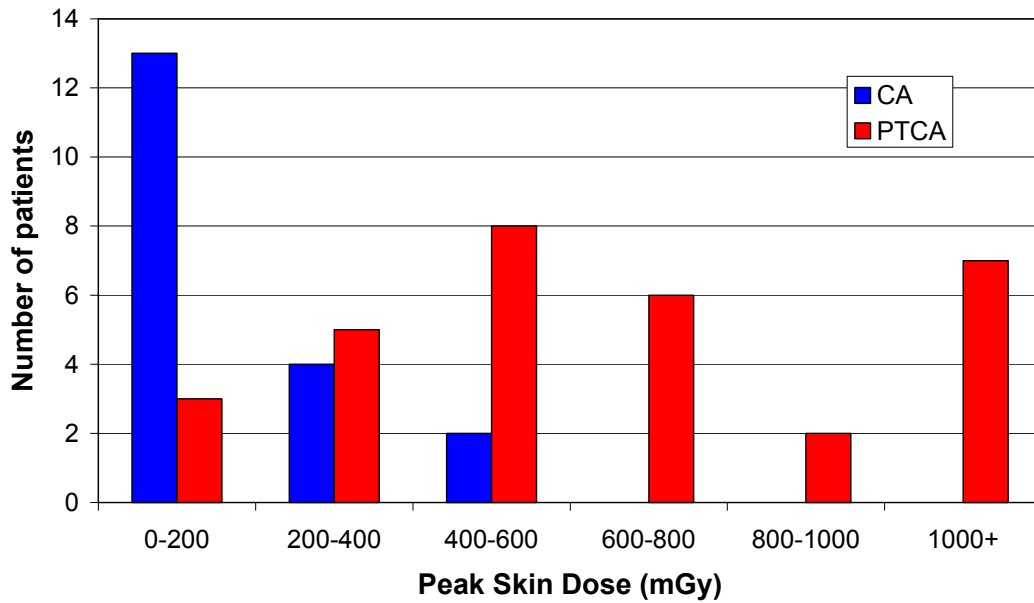


Figure 5.3: Peak skin doses for coronary angiography (CA) and angioplasty (PTCA).

5.3.2 Dose Area Product

One of the angioplasties did not have a DAP value recorded in the database, so was excluded from further data analysis. Table 5.1 shows the mean DAP in Gycm^2 for each procedure type, along with maximum and minimum values.

Procedure Type	Mean	Maximum	Minimum
CA	26	64	12
PTCA	57	215	8

Table 5.1: Mean, maximum and minimum DAP (Gycm^2) for coronary angiography (CA) and angioplasty (PTCA).

Table 5.2 and Table 5.3 summarise the strength of the correlations between peak skin dose and other procedural variables, for the two procedure types. They show the number of procedures included in the analysis, the Pearson correlation coefficient and Student's t-statistic. The final column indicates whether the correlation was significant, at a P-value of 0.05. The critical value of the t-statistic varied between 2.06 and 2.09, for the sample sizes used in the study.

Variable	N	R	t	Significant at P = 0.05?
Dose Area Product	19	0.76	4.83	Yes
Fluoroscopy Time	19	0.22	0.91	No
Number of Runs	19	0.28	1.19	No
Patient Weight	19	0.29	1.24	No

Table 5.2: Procedural variables correlated against peak skin dose, for coronary angiograms. N is the number of procedures included in the analysis, R the Pearson correlation coefficient and t is Student's t-statistic.

For coronary angiography, DAP was the only variable that demonstrated a significant association with peak skin dose. For angioplasty, both DAP and patient weight showed significant association with peak skin dose. These two variables were not independent, since a greater patient entrance dose is needed when the radiation beam has to pass through a greater thickness of tissue.

Variable	N	R	t	Significant at P = 0.05?
Dose Area Product	23	0.61	3.54	Yes
Fluoroscopy Time	23	0.38	1.89	No
Number of Runs	23	0.01	0.05	No
Patient Weight	21	0.44	2.16	Yes

Table 5.3: Procedural variables correlated against peak skin dose, for coronary angioplasties. N is the number of procedures included in the analysis, R the Pearson correlation coefficient and t is Student's t-statistic.

For coronary angiograms, the equation of the regression line linking peak skin dose (*PSD*) in mGy with dose-area-product (*DAP*) in Gy cm^2 was

$$PSD = 7.59 \times DAP - 2.21$$

Equation 5.3

For angioplasties that did not result in film saturation, the corresponding equation was

$$PSD = 6.85 \times DAP + 209$$

Equation 5.4

Figure 5.4 and Figure 5.5 are scatter plots of peak skin dose against DAP, for these procedures. The error bars indicate overall uncertainty in the measurements, as described in Chapter 4. The graphs also show regression lines, and 95% prediction limits calculated by the modified Bland-Altman method. These were 176 mGy above and below the regression line for coronary angiography, and 356 mGy for coronary angioplasty.

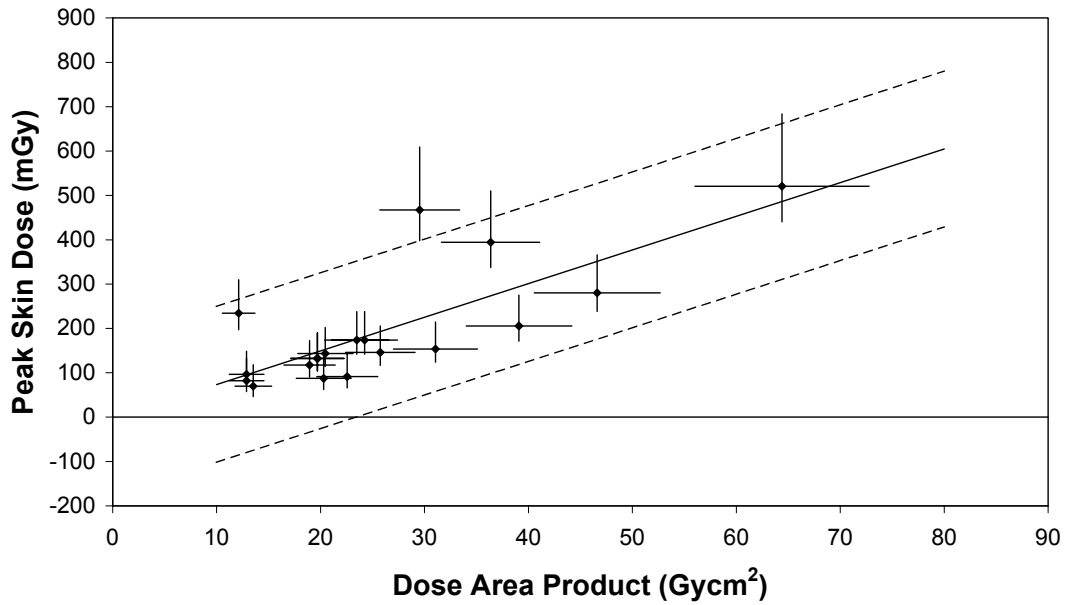


Figure 5.4: Peak skin dose versus dose-area-product, for coronary angiograms. Error bars indicate overall uncertainty in the measurements, as described in Chapter 4. Also shown are linear regression, and 95% prediction limits calculated by the modified Bland-Altman method.

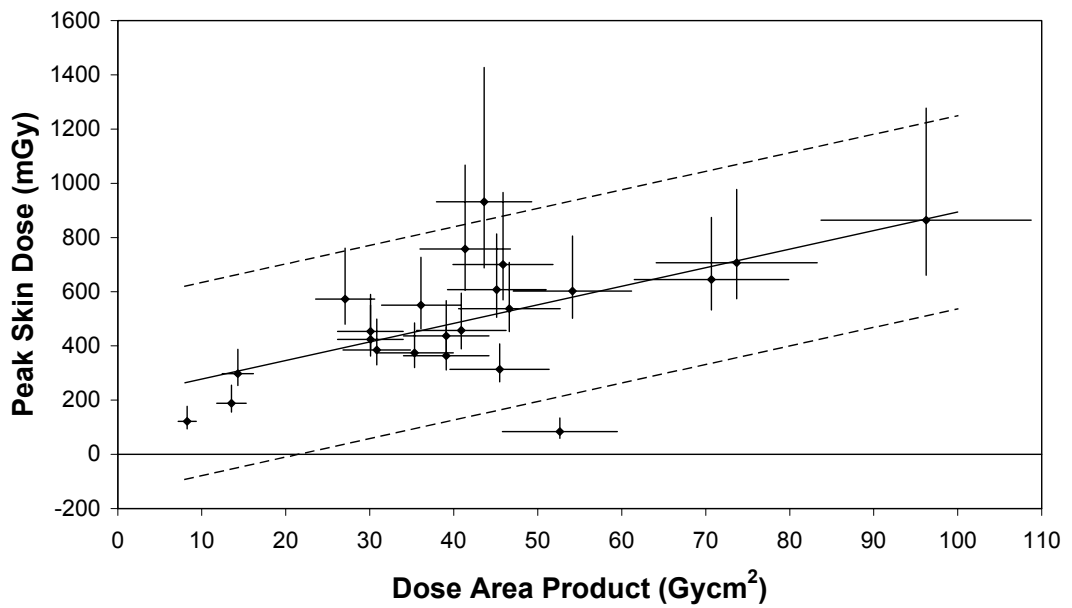


Figure 5.5: Peak skin dose versus dose-area-product, for coronary angioplasties that did not result in film saturation. Error bars indicate overall uncertainty in the measurements, as described in Chapter 4. Also shown are linear regression, and 95% prediction limits calculated by the modified Bland-Altman method.

Peak skin doses predicted from DAP, for all of the coronary angioplasties, are shown in Figure 5.6. For films that showed no saturation, the predicted doses were all less than 1 Gy. Of the seven films having saturated areas, only two had a predicted dose of more than 1 Gy.

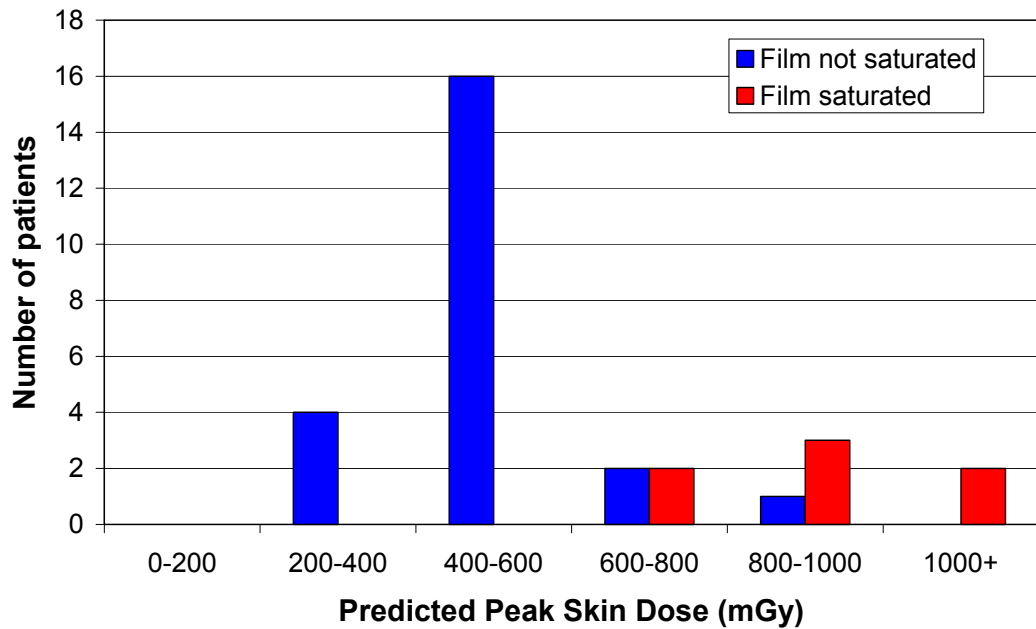


Figure 5.6: Peak skin doses predicted from dose-area-product, for angioplasties with and without film saturation.

5.3.3 Complexity Indicators

Table 5.4 summarises the strength of association between the potential complexity indicators and the ratio of peak skin dose to DAP, for coronary angioplasty. The only indicator that gave a significant correlation was the number of lesions treated. The value of the correlation coefficient was negative, because the ratio of peak skin dose to DAP decreased as the number of lesions increased.

Variable	N	R _s	t	Significant at P = 0.05?
Number of Diseased Vessels	22	0.31	1.47	No
Number of Lesions Treated	22	-0.60	-3.36	Yes
Number of Stents	22	-0.17	-0.77	No
Lesion Severity	20	0.05	0.22	No

Table 5.4: Potential complexity indicators correlated against the ratio of peak skin dose to DAP, for coronary angioplasties. N is the number of procedures included in the analysis, R_s the Spearman rank-order correlation coefficient and t is Student's t-statistic.

The regression line relating PSD/DAP with the number of lesions treated had a gradient of -3.19 and an intercept of 19.3 . The equation used to predict peak skin dose in mGy from a combination of DAP in Gy cm^2 and the number of lesions treated was therefore

$$PSD = DAP \times (19.3 - 3.19 \times \text{lesions})$$

Equation 5.5

Figure 5.7 shows measured versus predicted peak skin doses for those coronary angioplasties that did not result in film saturation. Agreement between measured and predicted values is displayed in Figure 5.8. Predicted peak skin doses were, on average, 15 mGy higher than measured values. The limits of agreement were ± 308 mGy.

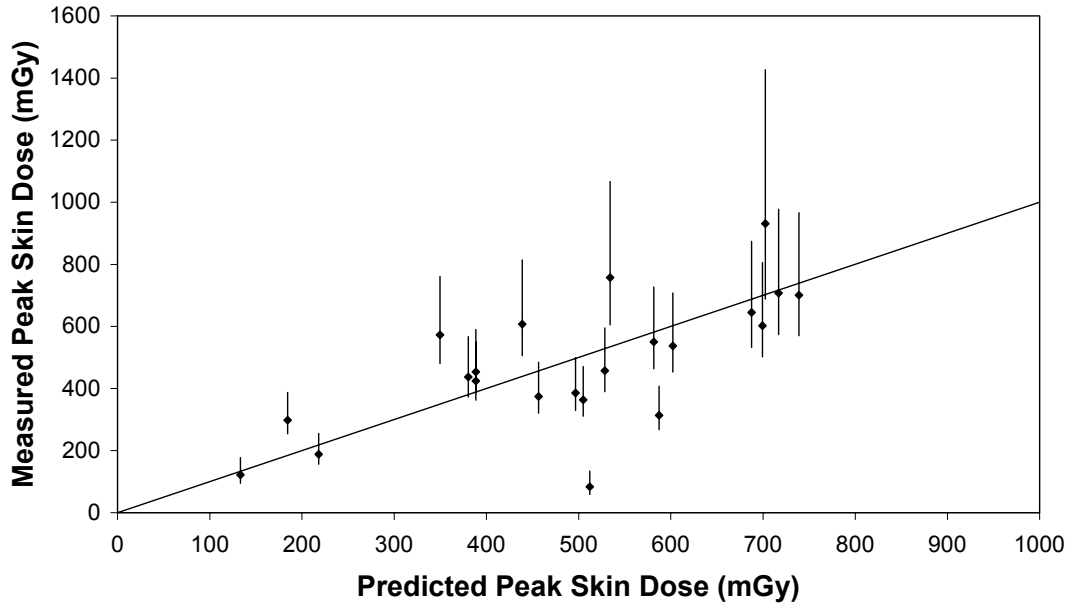


Figure 5.7: Measured versus predicted peak skin dose, calculated using DAP and number of lesions treated, for those coronary angioplasties that did not result in film saturation. The line of equality is shown. Error bars indicate overall uncertainty in the measurements, as described in Chapter 4.

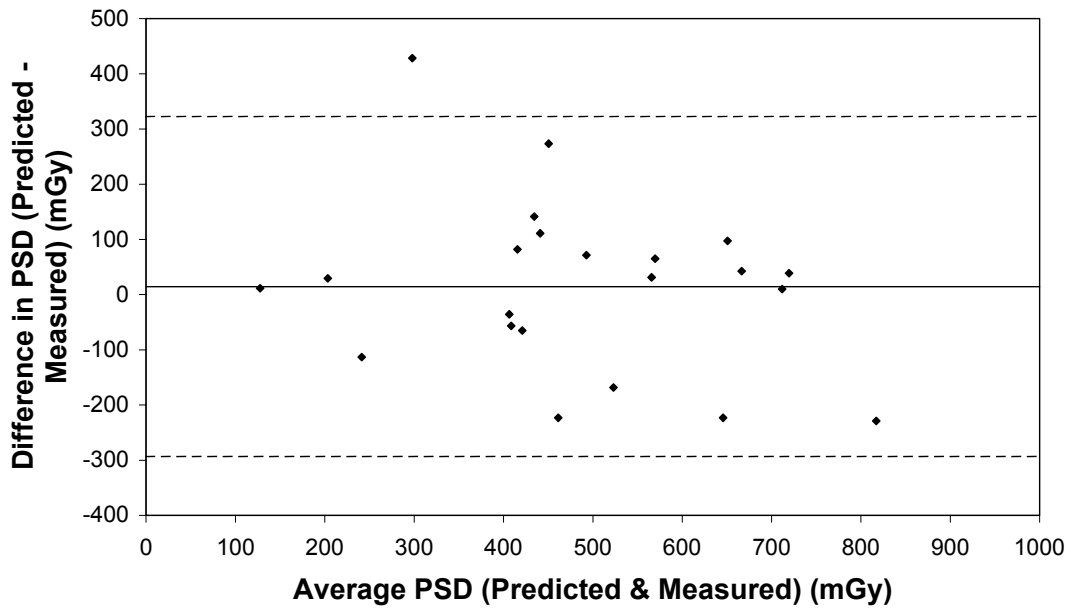


Figure 5.8: Bland-Altman plot comparing predicted and measured peak skin dose (PSD). The solid line indicates the mean difference between the two methods, and the broken lines are the 95% limits of agreement.

Peak skin doses predicted from DAP and number of lesions treated, for all of the coronary angioplasties, are shown in Figure 5.9. Those procedures that did not result in film saturation all had predicted peak doses of less than 1 Gy. Of the seven films having saturated areas, five had predicted doses of more than 1 Gy. The minimum predicted peak skin dose for the saturated films was 777 mGy.

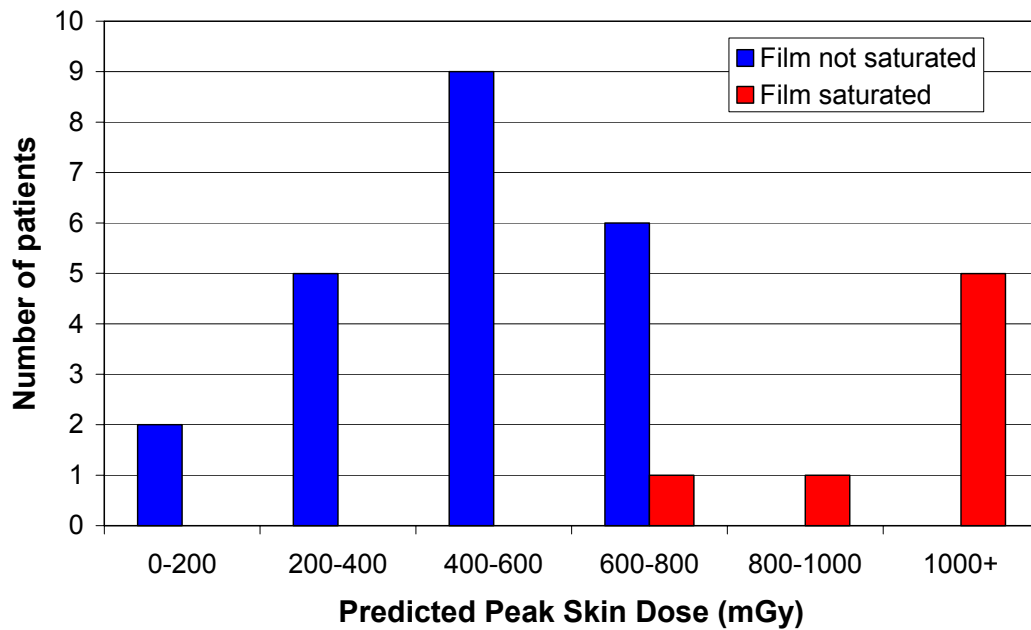


Figure 5.9: Peak skin doses predicted from dose-area-product and number of lesions treated, for angioplasties with and without film saturation.

5.4 Discussion

5.4.1 Film Measurements

For the 19 coronary angiograms for which a valid dosimetry film was obtained, all peak skin doses were well below 1 Gy. This indicated that patients undergoing these diagnostic investigations are unlikely to receive doses sufficient to cause deterministic effects. The maximum observed skin dose was 520 mGy. This was comparable with the results of previous studies using thermoluminescence dosimetry and film, summarised in Tables 3.4 and 3.7.

For the 31 coronary angioplasties, 23% of patients received skin doses of 1 Gy or more, sufficient to saturate the film. It was no surprise to find some incidences of film saturation, given that all three thermoluminescence dosimetry studies listed in Table 3.5 found some skin doses approaching or exceeding 1 Gy. However, it was not expected that such a large proportion of patients would be affected. This was at variance with the findings of Guibelalde *et al* (2003), who reported film saturation in only about 1% of all cardiac catheterization procedures, including complex angioplasties. The difference may be explained at least in part by the higher film saturation point of up to 1.5 Gy obtained with their processing conditions (Vanō *et al*, 2003; Guibelalde *et al*, 2003). The saturation point of 1 Gy found in the present study is likely to be more typical for radiology departments, since few can afford the luxury of running a dedicated film processor set up exclusively to maximise the range of dosimetry film.

For most patients, the radiation fields appeared to be centred reasonably well on the film. This indicated that film positioning was appropriate for the procedure types investigated. The large area of the film should ensure that most of the radiation fields incident on the patient's back are captured. However, when using lateral views and the widest obliques, the radiation beam would not pass through the film. Any high dose regions on the patient's sides would therefore go undetected.

EDR2 film was found to be a relatively convenient medium for measuring skin doses of up to 1 Gy, and for identifying patients who had received doses of 1 Gy or more. It could easily be positioned under the mattress, was invisible on the clinical images, and had no detriment to patient comfort. However, it was not capable of measuring doses of more than 1 Gy when used with a processor set up for diagnostic films. Even if its useful range were extended by adjusting the processing conditions, as described by Guibelalde *et al* (2003), its usefulness would still be limited by its saturation point of at most 1.5 Gy.

5.4.2 Dose Area Product

The mean DAP for coronary angiography was 26 Gy cm^2 . This fell below the centre of the range of mean values published in recent literature (Table 3.2). It compared favourably with typical UK practice, as represented by the most recent national dose

survey from the National Radiological Protection Board, which found a mean DAP of 30 Gy cm^2 (Hart *et al*, 2002).

The angioplasties demonstrated a wider variation in DAP, due to the inherent complexity of positioning the balloons and stents, ascertaining their correct positions, and checking procedural outcomes. This was reflected in the wider range of mean DAPs reported in the literature for these interventional procedures (Table 3.3). Again, the local mean value of 57 Gy cm^2 fell below the centre of the range. It was slightly lower than the mean DAP of 63 Gy cm^2 identified by the National Radiological Protection Board during their national dose survey (Hart *et al*, 2002).

Both procedure types demonstrated a significant correlation between peak skin dose and DAP, for doses of less than 1 Gy. However, for coronary angioplasty in particular, some of the data points deviated considerably from the regression line. The 95% limits of prediction were ± 176 mGy for coronary angiography and ± 360 mGy for coronary angioplasty, indicating that DAP could be used to predict skin doses to within these limits 95% of the time.

On using DAP to predict skin dose, only two of the seven angioplasties resulting in film saturation had predicted doses of more than 1 Gy. Those procedures associated with the highest skin doses often involve a large proportion of imaging in a small number of projections, so that much of the entrance dose is concentrated over a fairly small area of the skin. The equation for predicting peak skin dose from DAP was based on typical practice, and did not take this high field concentration into account. It therefore tended to give poor dose estimates towards the high end of the dose range.

5.4.3 Complexity Indicators

The ratio of peak skin dose to DAP was found to correlate negatively with the number of lesions treated. When a single lesion is treated, the majority of the radiation fields may be concentrated over a fairly small area of the skin, resulting in a high ratio of peak skin dose to DAP. If there are two or more lesions at different locations in the arterial tree, these will need to be imaged from different projections. The skin exposure is therefore likely to be more evenly spread over a larger area, giving a lower PSD/DAP ratio.

On using the number of lesions in combination with DAP to predict peak skin doses for coronary angioplasties, accuracy improved considerably. The 95% prediction limits for unsaturated films were ± 308 mGy. Five of the saturated films were associated with predicted doses of more than 1 Gy, and the other two with predicted doses of at least 777 mGy.

A major limitation of any system based on DAP is that it provides no information about the dose distribution on the patient's skin. Whilst a combination of DAP and number of lesions can give a rough estimate of the magnitude of the peak skin dose, it cannot identify the locations on the skin where injuries may occur.

5.4.4 Implications

About a quarter of the coronary angioplasty patients included in this study received peak skin doses of 1 Gy or more. It was therefore likely that a similar proportion of patients were subjected to doses of at least 1 Gy in routine clinical practice. In order to comply with the recommendations of the US Food and Drug Administration (1995) and the International Commission on Radiological Protection (2000), these patients' peak skin doses should be assessed and recorded.

Given the large proportion of patients receiving skin doses of 1 Gy or more, it seemed likely that some may exceed the 2 Gy threshold for skin erythema. These patients should be monitored for evidence of skin effects, and informed about potential symptoms, and appropriate actions to take should any symptoms occur. At the time of this study however, there was no reliable means of identifying these patients in order to offer them appropriate follow-up.

Thus, the present study clearly identified the need for a more robust dosimetry method that could reliably assess skin doses of more than 1 Gy, and identify the location of such high doses on the patient's skin. The small area dosimeters mentioned in the literature review (thermoluminescence dosimeters, scintillation detectors and diodes) would not meet these requirements, as there is a danger of missing the region of peak skin dose. Other possibilities include Gafchromic films, or the extended dose range computed radiography plates now available for radiotherapy verification imaging. However, both would have considerable cost implications. The option that seemed

most practical was that of dose modelling, since this would have the minimum impact on resources, and on the workload for busy clinical staff.

The high incidence of skin doses of 1 Gy or more also highlighted the need for optimisation of radiological practice in the cardiac catheterization laboratory. Any measures that can reduce the radiation dose to the patient's skin whilst maintaining adequate visualisation of the coronary arteries should be implemented, to minimise the risk of adverse skin reactions.

Mean dose-area-products for both procedure types were below the centre of the ranges reported in recent literature. It seems likely that those facilities operating at higher mean DAPs than those reported here also have a higher incidence of skin doses exceeding 1 Gy. There is a pressing need for improved skin dosimetry methods, and optimisation of radiological practice, across the wider interventional cardiology community.

5.5 Summary

Patient skin doses were measured using Kodak EDR2 film, for 19 coronary angiograms and 31 coronary angioplasties. For coronary angiography, all skin doses were well below 1 Gy, indicating that deterministic skin injuries were unlikely to occur following this type of procedure. For coronary angioplasty, 23% of the films showed some areas of saturation, indicating that these patients had received peak skin doses of at least 1 Gy. It was possible that some of these patients' doses were sufficient to cause deterministic effects. Given that the International Commission on Radiological Protection (ICRP) and the US Food and Drug Administration (FDA) recommend recording doses of more than 1 Gy in the patient's notes, a means for assessing these higher doses is needed.

The results of the study indicated that EDR2 film did not have a sufficient dose range for skin dosimetry in the cardiac catheterization laboratory. This was also likely to be the case at many other facilities, where mean dose-area-products were higher than those reported here. The film may be used to identify patients receiving doses of 1 Gy or more, and who may therefore be at risk of deterministic injuries. However, another method is needed to assess these patients' peak skin doses.

Mean dose-area-products for both procedure types were found to compare favourably with typical UK and European practice. Dose-area-product was shown to be a poor predictor of peak skin dose for coronary angioplasty. Whilst there was a significant correlation between the two quantities, the use of dose-area-product to predict peak skin dose failed to identify most of the patients receiving doses of 1 Gy or more.

The ratio of peak skin dose to DAP correlated negatively with the number of lesions treated. On using a combination of DAP with the number of lesions to predict skin dose for coronary angioplasty, accuracy was improved, with calculated doses for saturated films increasing to at least 777 mGy. However, as with other methods based on DAP, this could not identify the locations of high doses on the patient's skin.

Practical compliance with ICRP and FDA recommendations requires a method for assessment of skin dose that is more accurate than DAP, that provides information about the location of high skin doses, and is applicable over a wider dose range than EDR2 film.

Chapter 6 - Skin Dose Modelling

6.1 Introduction

This chapter describes the development and validation of a mathematical model to calculate the dose distribution in the plane of the couch top, from cardiac catheterization procedures. The mathematical basis for the dose model is presented, and the software used to source, analyse and present the data is described.

Peak skin doses calculated using the model are compared with the film measurements described in Chapter 5. Since fluoroscopic images were not stored, the model needed to estimate and include the dose contribution from fluoroscopy. Three approaches to this problem are described, and the results of each are compared with the film measurements. The clinical usefulness of the software is evaluated, and its limitations are discussed.

Whilst den Boer *et al* (2001) and Chugh *et al* (2004) had previously developed systems for modelling the patient skin dose distribution, none were available commercially at the time of this study. Nor had the mathematical workings of such skin dose models been published in peer-reviewed literature.

6.1.1 Objectives

The aim of this study was to develop software to calculate and display the dose distribution in the plane of the couch top, for individual cardiac catheterization procedures. The specific objectives were:

- To construct a mathematical model to calculate the dose distribution in the plane of the couch top, from exposure and projection data stored in the image files;

- To write software enabling this dose distribution to be calculated and displayed for individual cardiac catheterization procedures;
- To assess the accuracy and reliability of the model, by comparing calculated doses with the film measurements described in Chapter 5;
- To improve the model's accuracy, by including an estimated contribution from fluoroscopy.

6.2 Method

The dose calculation software was developed using Matlab version 7 (The Mathworks, Inc., Natick, Massachusetts). Its function was to extract the relevant data from the image files for a selected cardiac catheterization procedure, calculate the dose distribution in the plane of the couch top, and present this as a graphical display. The computational code used to achieve this is presented in Appendix I. All of the image files were in DICOM standard format (National Electrical Manufacturers Association, 2004), with one file for each acquisition run.

The simplest form of the dose model considered only the acquisition run data, which was stored in the image files. This will be referred to as 'Version 1 (Acquisition Only)', and is described in Section 6.2.2.

Clinical procedures also involve fluoroscopy. However, the fluoroscopic images were not stored, so that no exposure or projection data were available for the fluoroscopic component of the procedure. Where extensive fluoroscopy is performed over a limited range of projections, this could lead to considerable errors in skin dosimetry. Three options for estimating and including the contribution from fluoroscopy were investigated. These are referred to as versions 2 to 4, and described in Section 6.2.3.

6.2.1 Data Input

On starting up the software, the user was prompted to browse the image server, and select the directory containing the desired procedure. Each of the image files in that directory was then interrogated, to obtain the stored exposure and projection data, which was written to a structure array.

Table 6.1 shows this data, for one coronary angiogram. Each row corresponds to one file, i.e. one acquisition run. The columns contain the data fields: acquisition run number (*Run*), number of frames in that run (*Frames*), imaging protocol (*Protocol*), X-ray tube potential (*kVp*), tube current (*mA*), pulse width (*ms*), primary and secondary angles describing the orientation of the imaging unit in degrees (*Ang1* and *Ang2*), source to image distance in millimetres (*SID*) and detector field size in millimetres (*II*).

Run	Frames	Protocol	kVp	mA	ms	Ang1	Ang2	SID	II
1	53	12.5 FPS Coronary	71	613	7	-0	-22	953	170
2	80	12.5 FPS Coronary	84	862	7	42	-32	992	170
3	90	12.5 FPS Coronary	74	713	7	42	16	925	170
4	68	12.5 FPS Coronary	73	703	7	-32	21	945	170
5	75	12.5 FPS Coronary	80	893	7	-32	-18	994	170
6	70	12.5 FPS Coronary	76	778	7	41	-0	985	170
7	71	12.5 FPS Coronary	71	685	7	-35	-0	984	170
8	26	12.5 FPS Coronary	66	475	7	-32	-0	986	230
9	103	12.5 FPS Coronary	70	643	7	-32	-0	986	230

Table 6.1: Example exposure data extracted from image files. kVp, tube potential (kV); mA, tube current (mA); ms, pulse width (ms); Ang1, left-right gantry angulation (degrees); Ang2, cranio-caudal gantry angulation (degrees); SID, focal spot to detector distance (mm); II, field size at detector face (mm).

Ang1 relates to left-right rotation of the gantry, as shown in Figure 6.1(a). It is positive for left anterior oblique and left lateral views, when the detector is towards the patient's left-hand side. *Ang2* describes cranio-caudal rotation, as shown in Figure 6.1(b). It is positive when the detector is closer to the patient's head.

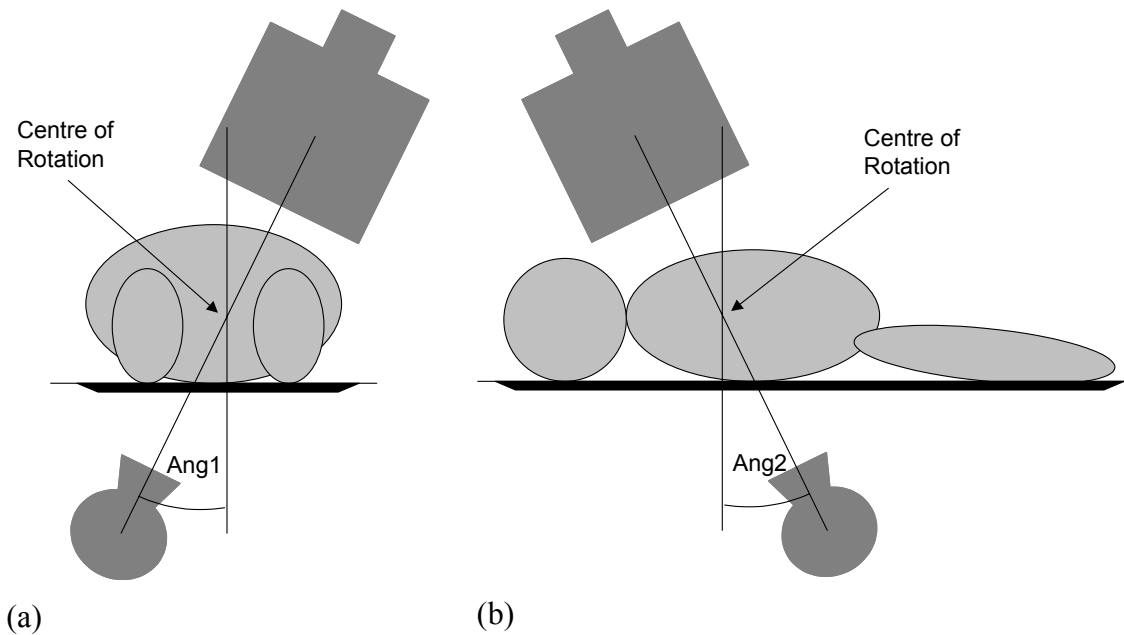


Figure 6.1: Views (a) along the patient couch, and (b) across the patient couch, showing the centre of rotation of the X-ray tube and detector, and angles *Ang1* and *Ang2*.

The model required a number of additional input values, which are described below. These were determined for the Philips Integris H5000F cardiovascular imaging unit referred to in Chapters 4 and 5.

centreheight - The height of the centre of rotation of the gantry, measured from the floor. This was permanently fixed at 107 cm.

radius - The distance from the X-ray focal spot to the centre of rotation. This was fixed at 77.5 cm.

couchheight - The height of the couch above the floor. This could be adjusted during clinical procedures, and was not recorded in the DICOM files. A ‘typical’ value of 87 cm was chosen, based on the recorded SID’s and measured field sizes for a selection of the dosimetry films described in Chapter 5. The model assumed, for simplicity, that no couch panning was used.

ESDR_{phantom} – A standardised measure of dose rate at the X-ray beam entrance site of a Perspex phantom. This quantity was determined as follows.

A calibrated Radcal 9010 series dose meter (Radcal, Monrovia, California) was positioned with its 60 cc ionisation chamber on the imaging couch, centred in the X-ray beam. A 25 cm stack of Perspex was positioned just above it, supported at either

side by a further 2 cm Perspex, as shown in Figure 6.2. The couch height was set to 67 cm above the focal spot, and the SID to 100 cm. The 23 cm field size was selected. An acquisition run was performed using the default clinical acquisition mode ‘12.5 FPS Coronary’, and the entrance dose rate to the Perspex was measured. The displayed exposure factors were 70 kVp, 608 mA and 7 ms.

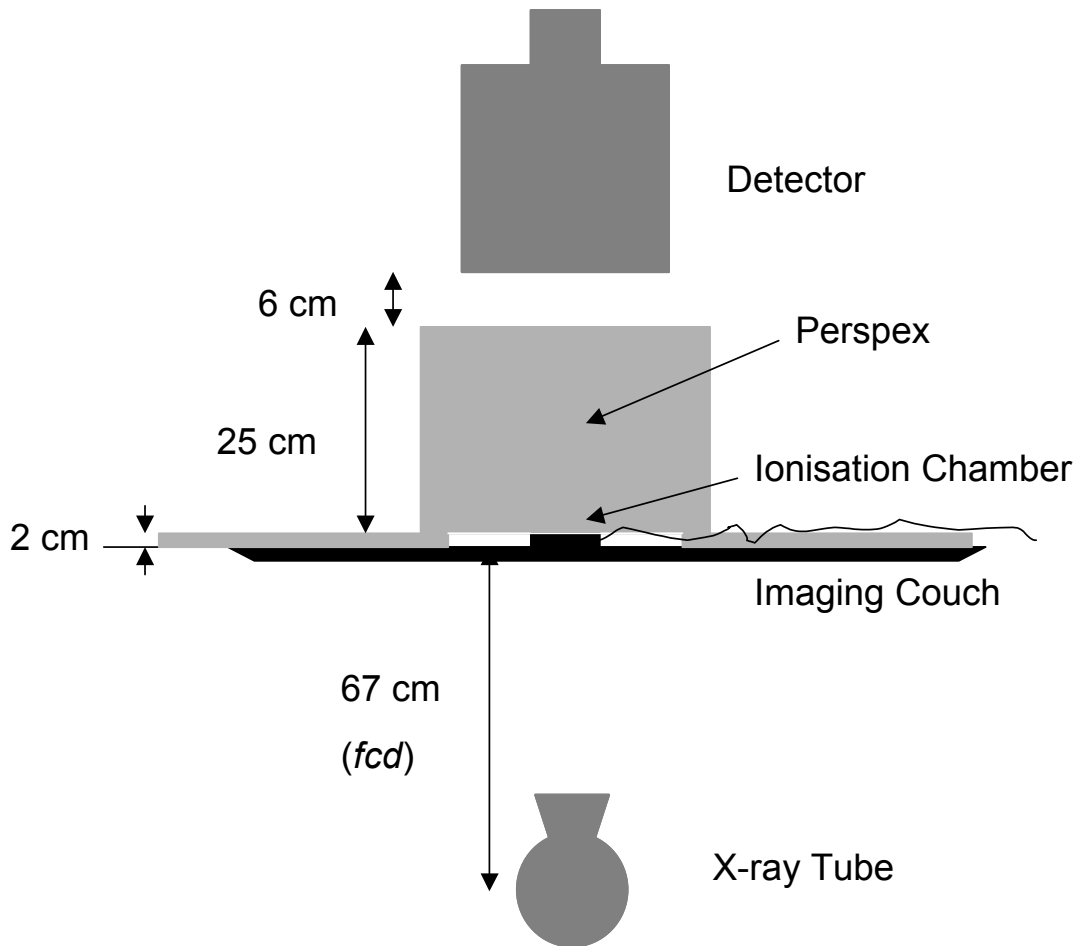


Figure 6.2: Set-up for determination of entrance dose rate to Perspex phantom.

The measured dose rate ($ESDR$) was normalised for tube potential (kV_p), current (mA), pulse time (ms), number of frames per second ($frame\ rate$), and distance in centimetres from the focal spot to the ionisation chamber (fcd), as shown in Equation 6.1.

$$ESDR_{phantom} = \frac{ESDR \times fcd^2}{kV_p^2 \times mA \times ms \times frame\ rate}$$

Equation 6.1

For the imaging unit used in this study, $ESDR_{phantom}$ had a value of 5.97×10^{-5} mGcm²/(kVp²mAs) per frame.

6.2.2 Dose Calculation

This section describes the function of the simplest form of the dose model, ‘Version 1 (Acquisition Only)’. The other versions used the same basic structure, with some modifications as described in Section 6.2.3.

The dose calculation plane was defined by a grid of points at 1 mm intervals in a plane at the height of the couch top, extending from -30 cm to $+30$ cm in the x (cross-couch) direction and -20 cm to $+20$ cm in the y direction (parallel to couch axis). It was described by an array $(x_{film}(i,j), y_{film}(i,j), couchheight)$, where i and j indexed matrix elements in the x and y directions respectively. Figure 6.3 shows the orientation of the calculation plane relative to the patient’s back. Positive x was defined towards the right-hand side of the patient, and positive y towards the patient’s head, so that the dose map appeared as though viewing the patient from behind. It should be noted that the exact position of the patient was not known when performing the dose calculations.

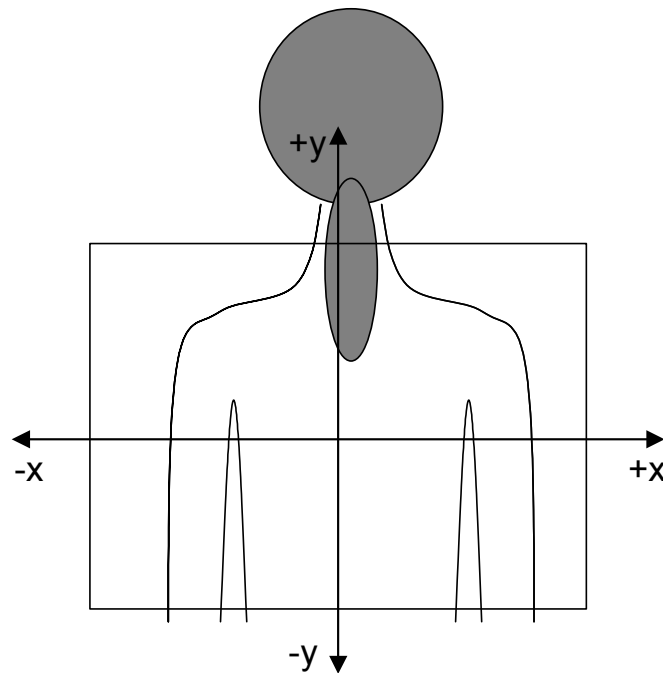


Figure 6.3: Diagram showing orientation of the calculation plane relative to the patient’s back.

For each acquisition run, the position of the focal spot (x_{spot} , y_{spot} , z_{spot}) was calculated using Equation 6.2 to Equation 6.4. The angle conventions used in these equations are illustrated in Figure 6.4.

$$x_{spot} = radius \times \sin(Ang1) \times \cos(Ang2)$$

Equation 6.2

$$y_{spot} = -radius \times \sin(Ang2)$$

Equation 6.3

$$z_{spot} = centreheight - radius \times \cos(Ang1) \times \cos(Ang2)$$

Equation 6.4

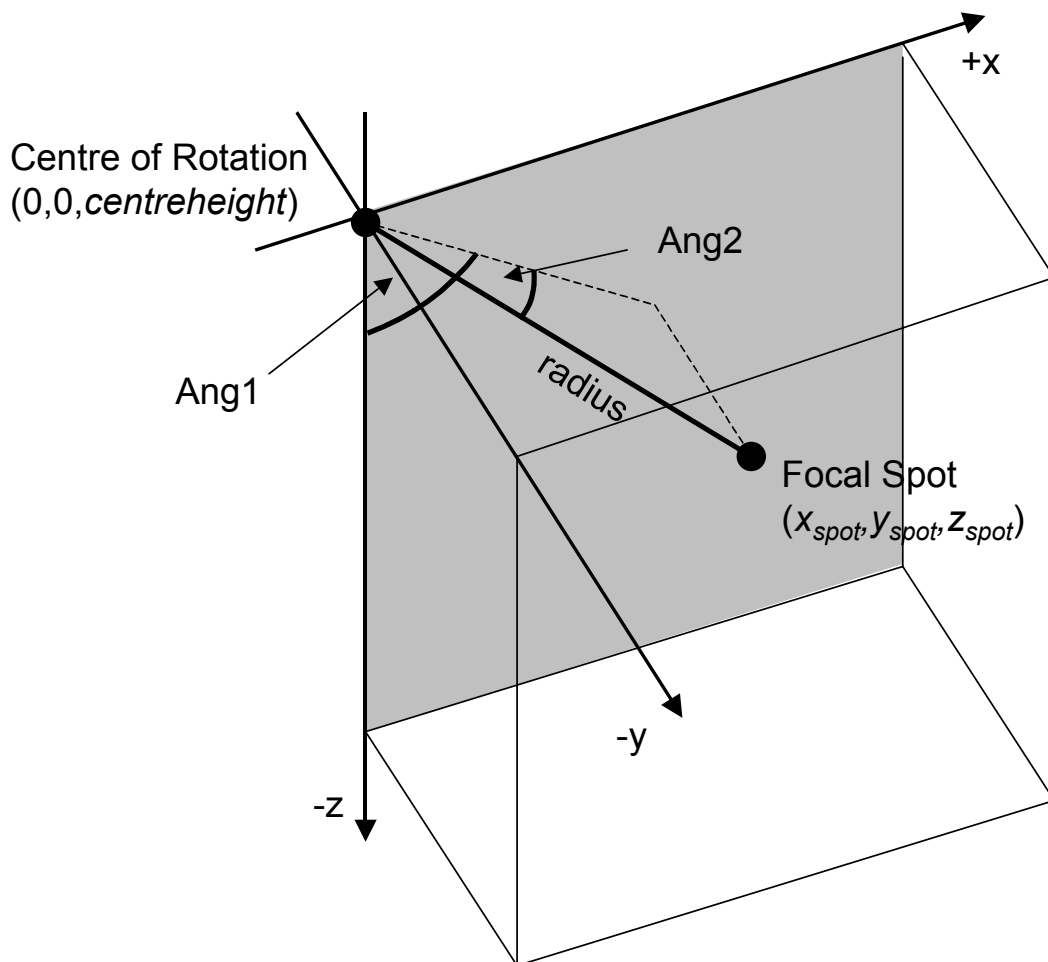


Figure 6.4: Angle conventions used to define focal spot position (Equation 6.2 to Equation 6.4).

The distance $ffd(i,j)$ from the focal spot to each point in the calculation plane was then determined using Pythagoras' law.

$$ffd(i,j) = \left((x_{film}(i,j) - x_{spot})^2 + (y_{film}(i,j) - y_{spot})^2 + (couchheight - z_{spot})^2 \right)^{1/2}$$

Equation 6.5

For a single acquisition run, the dose at each point in the plane, in the absence of beam collimation, would be:

$$dose(i,j) = ESDR_{phantom} \times \frac{kV_p^2 \times mA \times ms \times Frames}{ffd^2(i,j)}$$

Equation 6.6

where kV_p , mA , ms and $Frames$ are the values obtained from the DICOM file for that particular run.

The imaging unit had both circular and square primary collimators, resulting in a radiation field shape that was approximately square, with the corners clipped off. For simplicity, the dose model assumed only square collimation, with a side length defined by the nominal field size. No data were available regarding the use of the secondary collimators or equalisation filter, so these were assumed not to have been used.

The geometry used to calculate beam collimation is shown in Figure 6.5. The angle (θ) between the central axis of the X-ray beam and its collimated outer edge was calculated from the recorded field size (II) and SID, using Equation 6.7.

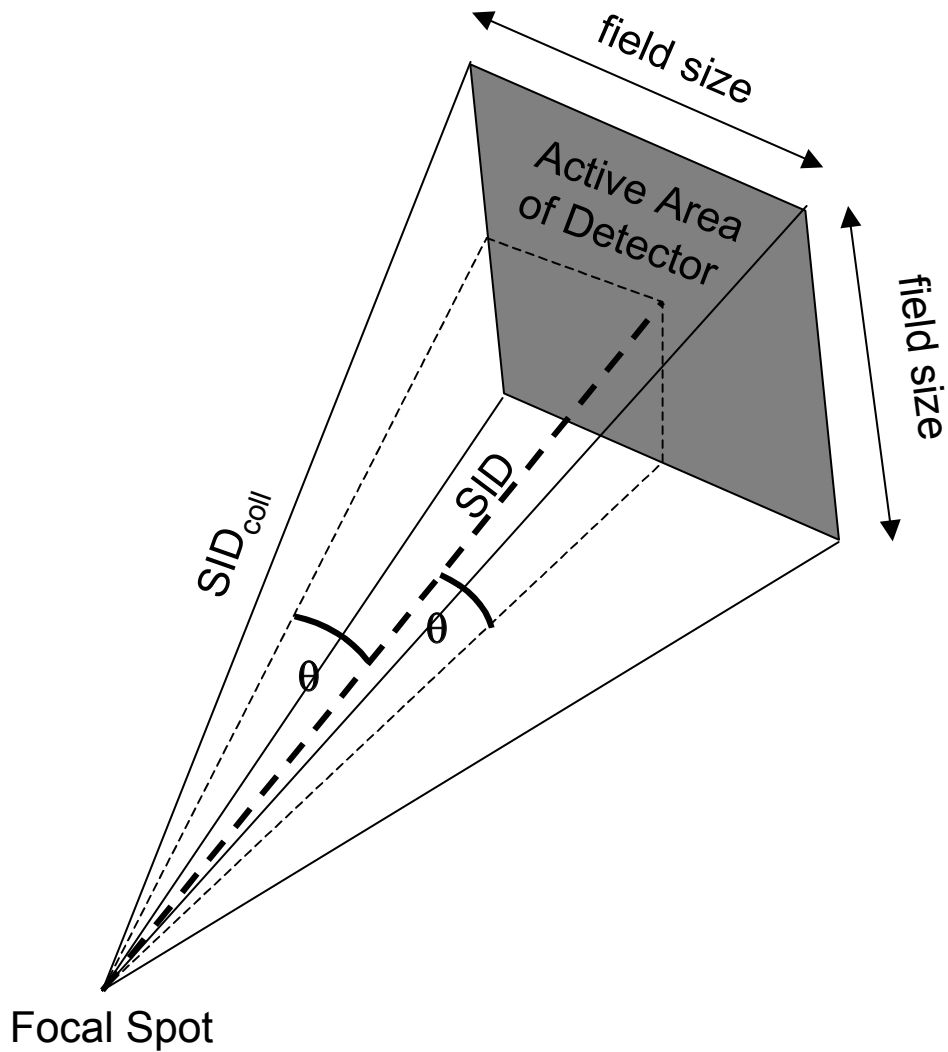


Figure 6.5: Geometry for calculating beam collimation.

$$\theta = \tan^{-1}\left(\frac{II}{2 \times SID}\right)$$

Equation 6.7

' SID_{coll} ' was defined as the distance from the focal spot, to any of the four corners of the collimated field at the detector face. It was calculated from field size (II) and SID (both in centimetres), using Pythagoras' law.

$$SID_{coll} = \left(SID^2 + 2 \times \left(\frac{H}{2} \right)^2 \right)^{1/2}$$

Equation 6.8

The positions of the field corners ($k = 1$ to 4) at the detector face ($x_{coll}(k)$, $y_{coll}(k)$, $z_{coll}(k)$) were calculated using Equation 6.9 to Equation 6.11, with positive and negative values of θ added to angles *Ang1* and *Ang2* in turn.

$$y_{coll}(k) = y_{spot} + SID_{coll} \times \sin(Ang2 \pm \theta)$$

Equation 6.9

$$x_{coll}(k) = x_{spot} - SID_{coll} \times \sin(Ang1 \pm \theta) \times \cos(Ang2 \pm \theta)$$

Equation 6.10

$$z_{coll}(k) = z_{spot} + SID_{coll} \times \cos(Ang1 \pm \theta) \times \cos(Ang2 \pm \theta)$$

Equation 6.11

The four corners of the collimated field were then translated from the detector face onto the plane of the couch top, by means of scaling.

$$x_{couch}(k) = x_{spot} + \frac{(x_{coll}(k) - x_{spot})}{(z_{coll}(k) - z_{spot})} \times (couchheight - z_{spot})$$

Equation 6.12

$$y_{couch}(k) = y_{spot} + \frac{(y_{coll}(k) - y_{spot})}{(z_{coll}(k) - z_{spot})} \times (couchheight - z_{spot})$$

Equation 6.13

To apply the collimation, the values of the dose array defined in Equation 6.6 were set to zero at all locations outside the trapezium formed by these four points.

The total dose array *TotalDose(i,j)* for the procedure was constructed by summing the collimated dose arrays from each acquisition run. It was then displayed as a filled contour map, with annotations indicating the patient's name and procedure date, as well as the maximum dose value. The colour scale of the map was automatically set to match the range of dose values present.

6.2.3 Contribution from Fluoroscopy

The three methods for including an estimated contribution from fluoroscopy are outlined below. Each required a measure of total DAP or fluoroscopy time. These were displayed on the imaging console, and manually logged in a database at the end of each procedure.

Version 2 (Fluoro Correction via DAP)

The total dose array for the acquisition runs $TotalDose(i,j)$ was calculated as described in Section 6.2.2. Dose-area-product in $Gycm^2$ was also calculated for each acquisition run, using Equation 6.14.

$$DAP = \frac{ESDR_{phantom}}{1000 \times 1.3} \times kV_p^2 \times mA \times ms \times Frames \times \left(\frac{II}{SID} \right)^2$$

Equation 6.14

where kV_p , mA , ms , $Frames$, II and SID are the values obtained from the DICOM file for that particular run. The factor of 1000 converted the dose units from mGy to Gy. Since backscatter from the patient is typically around 30%, in the diagnostic X-ray energy range (Jones & Wall, 1985; Dosimetry Working Party of the Institute of Physical Sciences in Medicine, 1992), the factor of 1.3 was included to eliminate the backscatter component of $ESDR_{phantom}$. Measurements made with and without backscattering material as part of the film calibration study of Chapter 4 showed the backscattered fraction to vary between 0.29 and 0.37, across the range of beam conditions investigated.

The DAP from individual acquisition runs was then summed to give acquisition DAP for the whole procedure ($DAP_{Acquisition}$). The total dose array $TotalDose(i,j)$ was multiplied by the ratio of displayed DAP for the whole procedure (DAP_{Total}), to calculated acquisition DAP, to generate the fluoroscopy-corrected dose map.

$$TotalDose(i,j)_{Fluoro\ Corrected} = TotalDose(i,j) \times \left(\frac{DAP_{Total}}{DAP_{Acquisition}} \right)$$

Equation 6.15

Version 3 (Fluoro Correction via Fluoroscopy Time)

The entrance dose rate to the Perspex phantom was re-measured in the default fluoroscopy mode ('Low Fluoro'), as described in Section 6.2.1. It was found to be approximately 40 mGy/min. The displayed exposure factors were 85 kVp and 21.5 mA.

This 'standard' fluoroscopic dose rate was multiplied by the fluoroscopy time (FT) in minutes, to estimate the total dose due to fluoroscopy. This was then divided by the number of acquisition runs ($Runs$), and added to the un-collimated dose array for each run. Thus, Equation 6.6 was modified to

$$dose(i, j) = ESDR_{phantom} \times \frac{kV_p^2 \times mA \times ms \times Frames}{ffd^2(i, j)} + \frac{40 \times FT}{Runs}$$

Equation 6.16

The remainder of the calculation was performed as described in Section 6.2.2.

Version 4 (Fluoro Correction via Concentration Factor)

This version sought to predict peak skin dose from displayed DAP for the whole procedure, coupled with a 'concentration factor' describing how the maximum value of the dose map related to the integral dose over the whole of the map.

The total dose array $TotalDose(i, j)$ for the acquisition runs was calculated as described in Section 6.2.2. Its maximum value ($Dose_{max}$) was determined. The doses at all points in the array were also summed, to give integrated dose over the whole calculation plane. 'Concentration factor' (CF) was defined as the ratio of maximum dose to integrated dose.

$$CF = \frac{Dose_{max}}{\sum_{i, j} Total Dose(i, j)}$$

Equation 6.17

This was then multiplied by displayed DAP (DAP_{total}).

In order to determine the relationship between this new index and peak skin dose, the resulting values were plotted against the measured peak skin doses from Chapter 5,

for those films that showed no saturation. A regression line was fitted to the data, and constrained to pass through the origin. Its gradient λ was 5.53×10^{-6} .

Finally, the peak skin dose (*PSD*) for each procedure was calculated using Equation 6.18.

$$PSD = \frac{CF \times DAP_{Total}}{\lambda}$$

Equation 6.18

6.2.4 Comparison of Calculated and Measured Doses

In order to evaluate the software, dose maps were calculated for each of the procedures that were included in the film dosimetry study of Chapter 5. The dose maps calculated using Version 1 (Acquisition Only) were visually compared with their corresponding films. The area of the dose map covered by the film was roughly identified by the shape and intensity of the radiation fields appearing on each. In ten cases (five coronary angiograms and 5 coronary angioplasties), the peak skin dose identified by the dose map was beyond the edge of the film. These cases were excluded from the analysis. The remaining sample consisted of 14 coronary angiograms and 25 coronary angioplasties.

For each version of the dose model, calculated peak skin doses were compared with those measured on film. For saturated films, calculated peak skin doses were plotted as a histogram. For films that showed no saturation, calculated and measured values were compared using Bland-Altman plots (Bland & Altman, 1986; Bland & Altman, 1999).

6.3 Results

6.3.1 Example Dose Map

Figure 6.6 shows a dose map generated by Version 1 of the software. A visual comparison with the corresponding dosimetry film (Figure 6.7) demonstrated that it

correctly identified the region of maximum dose, in the top right-hand corner. The fields visible on the dose map corresponded reasonably well in shape and intensity with some of those seen on the film. However, fields arising from fluoroscopic exposures were seen only on the film, since the model had no access to projection information for fluoroscopy.

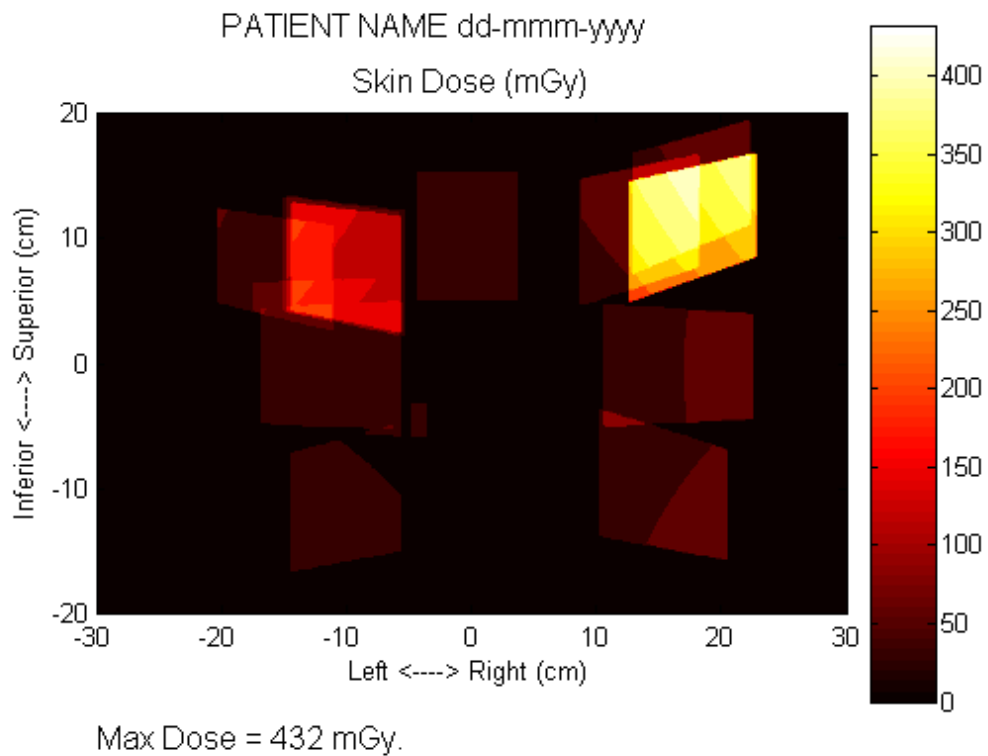


Figure 6.6: Example output from dose model.



Figure 6.7: Dosimetry film for the patient whose calculated skin dose map is shown in Figure 6.6, shown at the same scale.

In this example, the radiation fields on the dose map appeared to cover a larger area than those on the film. Possible reasons for this include difference in couch height between the ‘typical’ value used by the model and the actual value for the procedure, differences between nominal and actual radiation field sizes, and any couch panning that took place during the procedure.

6.3.2 Doses of More than 1 Gy

Six of the angioplasty films showed localised areas of saturation, indicating that these patients had received skin doses of 1 Gy or more. Figure 6.8 shows the calculated doses for these six cases, for each version of the dose model.

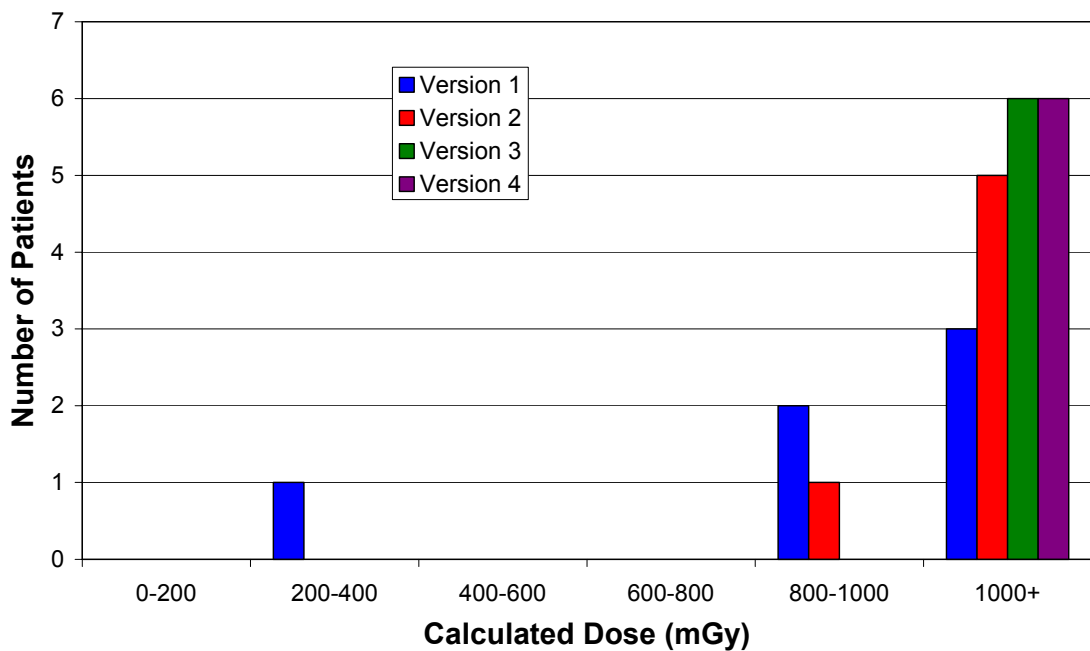


Figure 6.8: Calculated doses for procedures that resulted in film saturation, using each version of the dose model.

Although Version 1 (Acquisition Only) generally calculated doses of at least 800 mGy for these procedures, in one case a dose of only 332 mGy was computed. On applying any of the fluoroscopy correction methods, this patient’s calculated dose increased to more than 1 Gy. When corrected by fluoroscopy time or concentration factor (Versions 3 and 4), the model successfully identified all procedures that resulted in film saturation. Version 2 (Fluoro Correction via DAP) predicted one of

these patients to have a peak skin dose of 928 mGy, and all others to have maximum doses of more than 1Gy.

Versions 2, 3 and 4 all calculated peak skin doses of more than 2 Gy for two of the patients in the study.

6.3.3 Doses of Less than 1 Gy

Figure 6.9 to Figure 6.16 compare calculated and measured doses for all the procedures that did not result in film saturation, i.e. for which measured doses were less than 1 Gy.

For each version of the dose model, calculated peak skin doses were first plotted against measured values. The error bars show the overall uncertainty in the film dosimetry measurements, as described in Chapter 4. Bland-Altman plots were then constructed, to show the differences between calculated and measured values. In each case, the mean difference and 95% limits of agreement are shown.

For Version 1 (Acquisition Only), calculated values were on average 98 mGy lower than measured values. Each of the methods for including fluoroscopy brought the mean difference between calculated and measured peak skin dose closer to zero. Each version of the dose model had limits of agreement between 259 and 273 mGy from the mean.

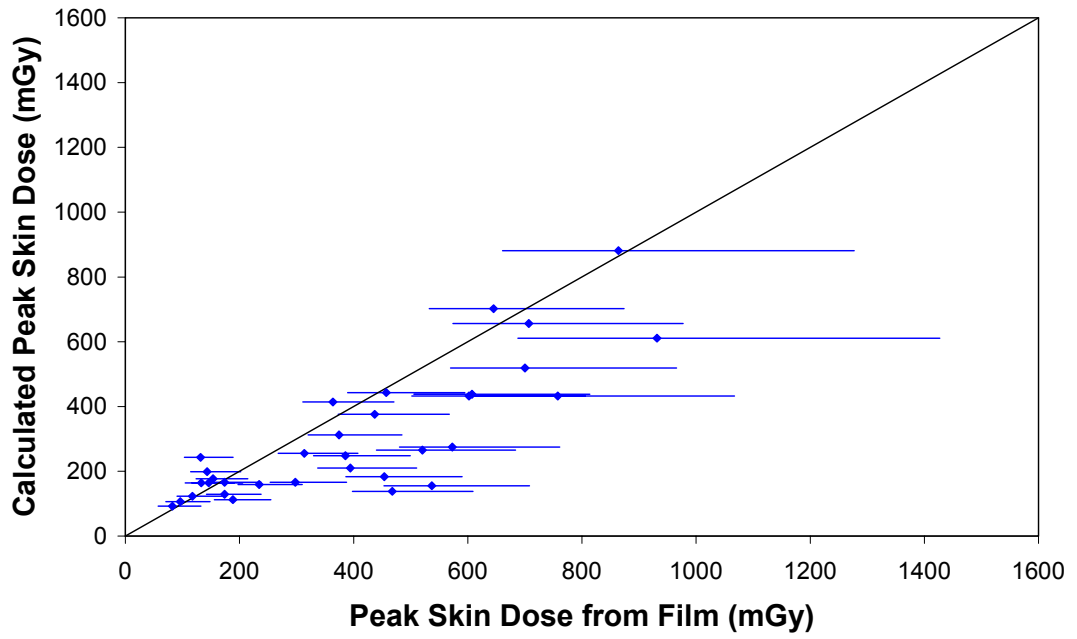


Figure 6.9: Calculated versus measured peak skin doses, for Version 1 (Acquisition Only). The line of equality is shown. Error bars indicate overall uncertainty in the film measurements, as described in Chapter 4.

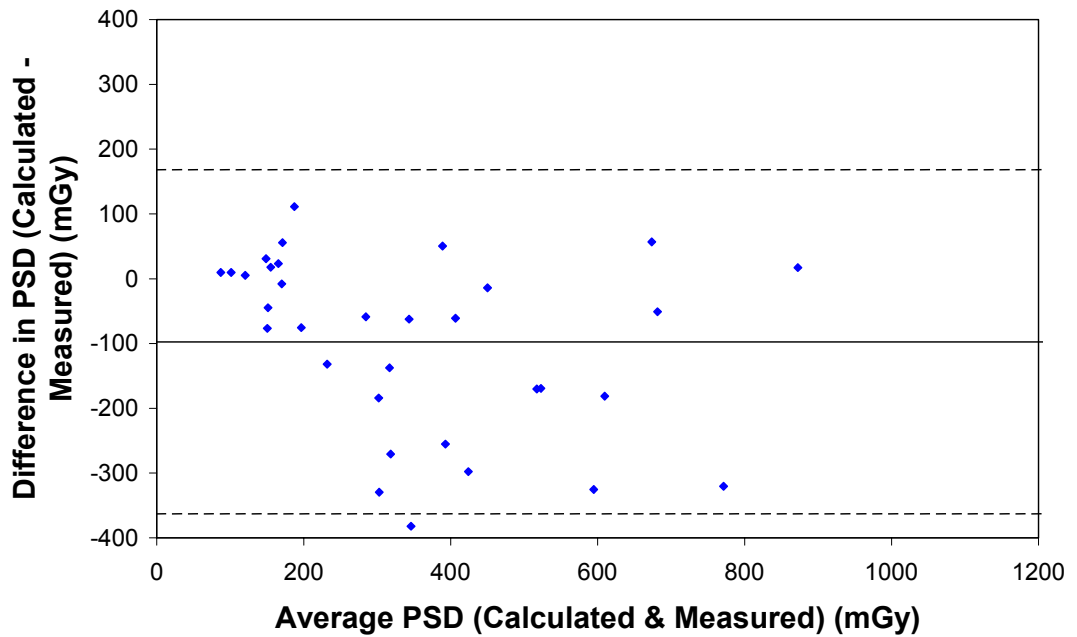


Figure 6.10: Bland-Altman plot comparing calculated and measured peak skin doses, for Version 1 (Acquisition Only). The mean difference and 95% limits of agreement are shown.

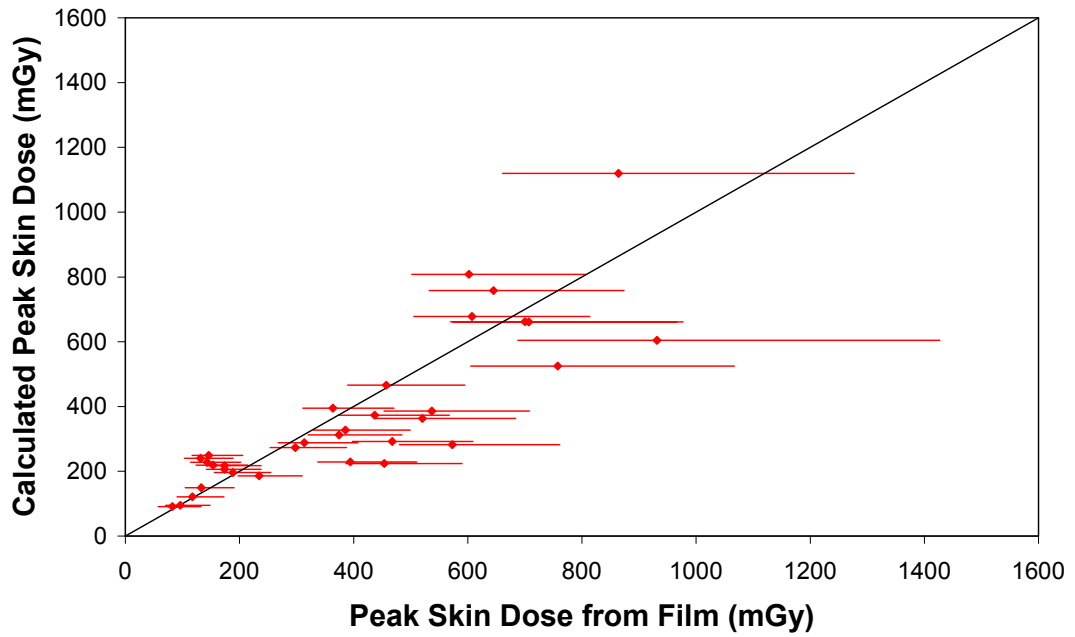


Figure 6.11: Calculated versus measured peak skin doses, for Version 2 (Fluoro Correction via DAP). The line of equality is shown. Error bars indicate overall uncertainty in the film measurements, as described in Chapter 4.

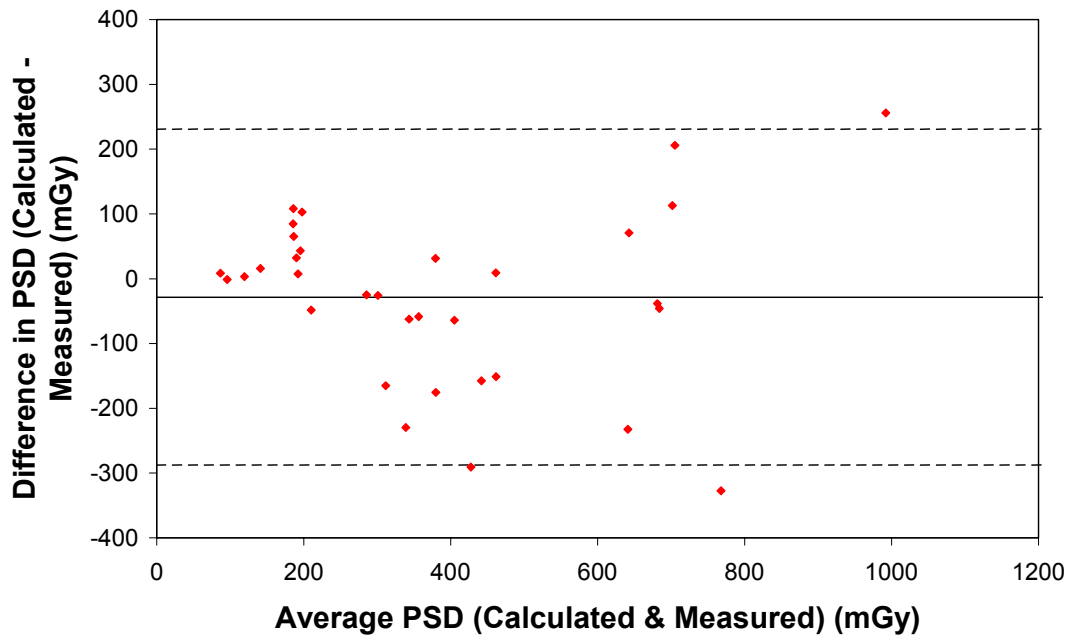


Figure 6.12: Bland-Altman plot comparing calculated and measured peak skin doses, for Version 2 (Fluoro Correction via DAP). The mean difference and 95% limits of agreement are shown.

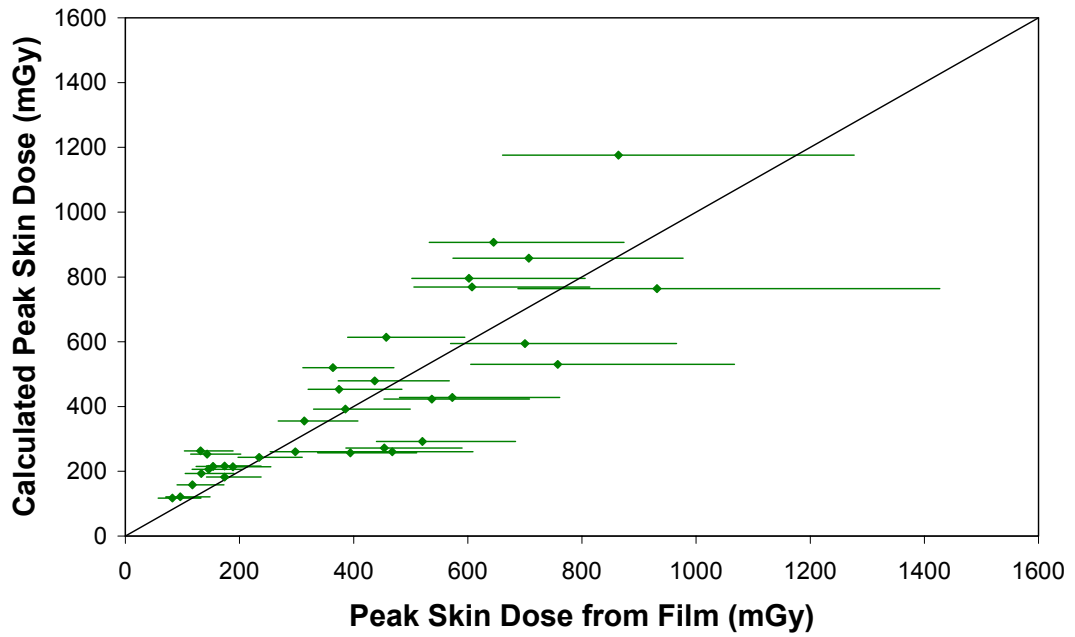


Figure 6.13: Calculated versus measured peak skin doses, for Version 3 (Fluoro Correction via Fluoroscopy Time). The line of equality is shown. Error bars indicate overall uncertainty in the film measurements, as described in Chapter 4.

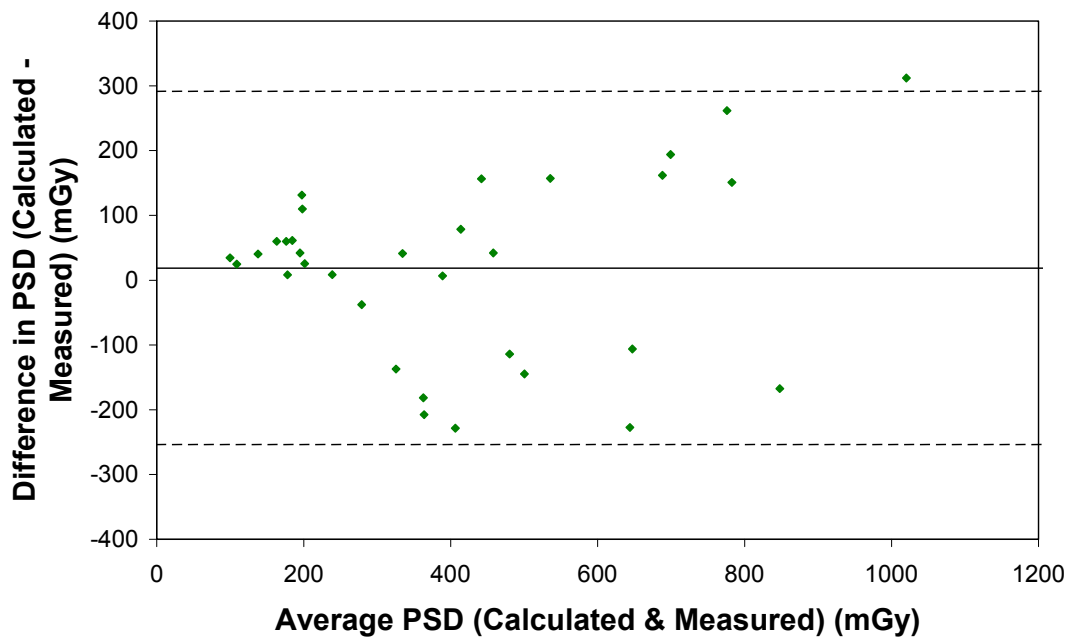


Figure 6.14: Bland-Altman plot comparing calculated and measured peak skin doses, for Version 3 (Fluoro Correction via Fluoroscopy Time). The mean difference and 95% limits of agreement are shown.

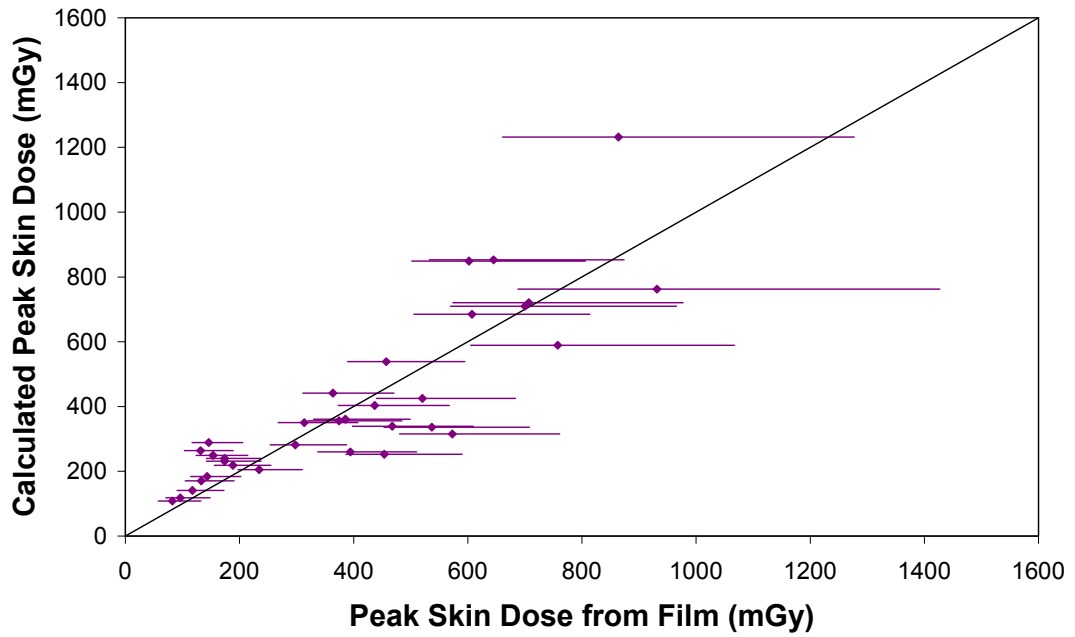


Figure 6.15: Calculated versus measured peak skin doses, for Version 4 (Fluoro Correction via Concentration Factor). The line of equality is shown. Error bars indicate overall uncertainty in the film measurements, as described in Chapter 4.

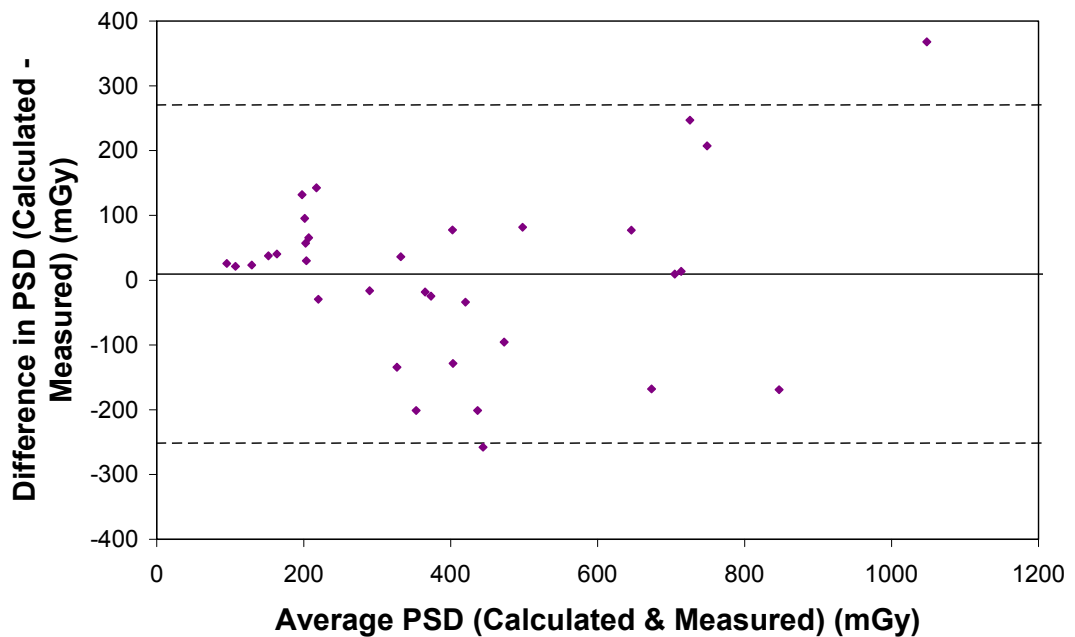


Figure 6.16: Bland-Altman plot comparing calculated and measured peak skin doses, for Version 4 (Fluoro Correction via Concentration Factor). The mean difference and 95% limits of agreement are shown.

6.4 Discussion

6.4.1 Acquisition Only

The simplest version of the dose model, Version 1 (Acquisition Only), used only the acquisition run data stored in the image files, and did not attempt to include fluoroscopy. For films that showed no saturation, calculated peak skin doses were on average 98 mGy lower than measured values, but the two methods agreed to within 270 mGy of the mean, 95% of the time.

For those procedures that had resulted in film saturation, i.e. for which the peak skin dose was 1 Gy or more, calculated doses were generally above 800 mGy. However, the calculated peak skin dose for one of these patients was only 332 mGy. The fluoroscopy time for this procedure had been particularly long, at 25 minutes. On inspecting the film, it was apparent that most of the radiation exposures had been performed in a single projection. In such cases, ignoring the contribution from fluoroscopy causes the peak skin dose to be greatly underestimated. Although this patient had received a skin dose of at least 1 Gy and may be at risk of deterministic effects, the model would not have identified her as being at risk.

6.4.2 Estimated Contributions from Fluoroscopy

Three options for including an estimated contribution from fluoroscopy were explored. Each assumed that fluoroscopic exposures were performed using the same projections in about the same proportions as the acquisition runs. This is not necessarily true, but in the absence of fluoroscopic projection data, it seemed to be the most logical approach.

In Version 2 (Fluoro Correction via DAP), all of the values in the dose map were multiplied by the ratio of displayed DAP for the whole procedure, to calculated DAP for the acquisition runs.

Version 3 (Fluoro Correction via Fluoroscopy Time) used the displayed fluoroscopy time and a standard dose rate to add a fluoroscopic contribution to the dose associated with each acquisition run.

Version 4 (Fluoro Correction via Concentration Factor) calculated a ‘concentration factor’ for the dose map. It then multiplied the concentration factor by displayed DAP and divided by a constant, to estimate the peak skin dose for the whole procedure.

Each of versions 2 to 4 improved the model’s reliability in identifying patients who had received peak skin doses of more than 1 Gy. Versions 3 and 4 estimated peak skin doses of more than 1 Gy for all six of those patients. Version 2 produced peak skin dose estimates of more than 1 Gy for five of them, and 928 mGy for the sixth.

For peak skin doses of less than 1 Gy, all three versions showed mean differences between calculated and measured values of less than 30 mGy. In each case, the 95% limits of agreement were within about 270 mGy from the mean.

Versions 2 and 4 both used displayed DAP to estimate the contribution from fluoroscopy. As described in Chapter 4, the measured DAP at the couch top was around 33% lower than the displayed value. The dose model did not apply this correction factor, because the uncorrected DAP gave better agreement between calculated and measured peak skin doses for Version 2 (Fluoro Correction via DAP). A possible explanation for this is that the actual field sizes were smaller than their nominal specifications, which were used in the dose model. In Version 4 (Fluoro Correction via Concentration Factor), the DAP correction factor would be absorbed into the constant λ .

For Version 4, agreement between predicted and measured peak skin doses was guaranteed by the fact that the same data were used to calculate λ and to predict peak skin doses. Agreement may not be as good for patient procedures not included in this sample.

Perhaps the most reliable way to correct for fluoroscopy would be to multiply the values in the dose map by the ratio of displayed DAP for the whole procedure, to displayed DAP for the acquisition runs. This last quantity was displayed on the imaging unit during procedures, but was not recorded, and could not be accessed retrospectively. It is hoped that in future, summary dose information including total DAP, acquisition DAP and fluoroscopy time will be transferred automatically to the image server, but such functionality was not available at the time of this study.

6.4.3 Clinical Usefulness

For each procedure, the dose modelling software provided an estimate of peak skin dose, and a rough indication of its location on the patient's skin, thereby fulfilling the recommendations for dose recording set out in ICRP Report 85 (International Commission on Radiological Protection, 2000) and the relevant FDA guidelines (Food and Drug Administration, 1995). This dosimetric information could be made available to the cardiologist, to inform patient counselling and follow-up care.

The level of accuracy provided by versions 2, 3 and 4 of the dose model should be sufficient for identifying patients who may be at risk of skin injuries. The FDA point out that highly accurate assessment of skin dose is not necessary. Rather, what is important is being able to recognise when a dose threshold may have been exceeded (Food and Drug Administration, 1995).

The dose modelling approach requires far less involvement from clinical staff than other dosimetric methods, leaving them to concentrate on other aspects of patient care. It does not depend on any advance preparation, such as positioning of dosimeters prior to commencing the procedure. The software used mostly data that was automatically stored by the imaging unit. The only additional data required was displayed DAP or fluoroscopy time. Since these were recorded routinely, peak skin dose could be estimated for any patient. Unlike film dosimetry, there was no upper limit on the doses that could be assessed.

The fact that calculated peak skin doses for two patients exceeded 2 Gy emphasised the need for routine skin dose monitoring in the cardiac catheterization laboratory. Since 8% of the angioplasties in this study were associated with skin doses of at least 2 Gy, it is possible that cumulative doses approaching the 6 Gy threshold for main erythema occasionally occur, particularly among those patients who undergo more than one catheterization procedure in the space of a week or two.

6.4.4 Limitations

The accuracy of the dose model was limited by the quantity of information available. Where essential parameters were not recorded, assumptions had to be made.

The cardiovascular imaging unit used in this study stored only acquisition runs and not fluoroscopic image sequences. This meant that no information was available regarding fluoroscopic projections. Version 1, which ignored the contribution from fluoroscopy, was liable to greatly underestimate peak skin doses for procedures requiring extended fluoroscopy from a limited number of projections. Versions 2, 3 and 4 estimated the contribution from fluoroscopy by assuming that the same projections were used in the same proportions as for acquisition. This may not be a true reflection of clinical practice in all cases. A further weakness of Version 3 (Fluoro Correction via Fluoroscopy Time) was that it assumed the same skin dose rate regardless of the radiographic projection or the size of the patient.

The imaging unit stored no information about the position of the couch. It was therefore necessary to assume a certain couch height, and to ignore any couch movement in the horizontal plane. A variation in true couch height of 5 cm from that used in the model would correspond to an error in calculated dose of about 12%. Since couch position was unknown, it was not possible to identify the exact positions of the radiation fields on the patient's skin.

No data were available regarding the use of the secondary collimators or the equalisation filter. It was therefore assumed that these were never used. This may substantially affect dosimetric accuracy in regions where two or more fields overlap. Radiation field sizes may also have been overestimated by assuming only square primary collimation and nominal instead of actual field sizes. However, it is unlikely that accuracy could be much improved unless the secondary collimators and equalisation filter were taken into account.

The manufacturers of cardiovascular imaging equipment should be encouraged to develop facilities for recording and accessing the above information. This is essential if dosimetric accuracy is to be improved.

As with film dosimetry, the model considered only those radiation beams that passed through the plane of the couch, and ignored any contributions to skin dose from lateral views. It could potentially be improved by using a three-dimensional model of the patient, and estimating skin doses over the whole surface of the thorax. However, this would require couch positioning data, to achieve a worthwhile degree of accuracy.

6.5 Summary

A mathematical model was developed, to calculate the dose distribution in the plane of the couch top from cardiac catheterization procedures, using the exposure and projection data stored in the image files. Software was designed to extract the relevant data, perform the calculations, and display a dose map for each procedure. Peak skin doses were calculated for those procedures that were included in the film dosimetry study of Chapter 5.

The original version of the software used only the information stored in the image files, i.e. only exposure and projection data for the acquisition runs. Peak skin dose was greatly underestimated for one patient, who had received a dose of at least 1 Gy during a procedure that involved extensive fluoroscopy in one projection.

Three methods for including an estimated contribution from fluoroscopy were explored. Each required displayed DAP or fluoroscopy time as an additional input. All three successfully identified those patients who had received skin doses of 1 Gy or more.

For those procedures that did not result in film saturation, calculated and measured peak skin doses were compared using Bland-Altman plots. Each version of the software was found to agree with film measurements to within about 270 mGy.

The software was found to be a potentially useful tool for patient dosimetry in the cardiac catheterization laboratory. Unlike film dosimetry, there was no limit on the magnitude of the doses that could be evaluated. The output dose map gave an indication of the magnitude and position of the peak skin dose on the patient's back, in line with the recommendations for dose recording proposed by the International Commission on Radiological Protection and the US Food and Drug Administration. This should allow the clinician to offer informed counselling and aftercare to patients who may be at risk of deterministic skin injuries.

The main limitations of the dose model arose from the lack of information about couch position and beam limitation. Improvement of dosimetric accuracy is dependent upon manufacturers developing facilities for recording and accessing this data.

Chapter 7 - Barium Enema Dose Reduction

7.1 Introduction

Chapters 7 and 8 together describe an optimisation strategy applied to barium enema imaging. A baseline survey of local imaging practice was first performed, and the results compared with published studies. This identified a number of potential dose reduction techniques, which were considered in consultation with clinical staff. Having decided to introduce copper filtration, the effects of a small amount of copper on dose and image quality were predicted using phantom measurements. The copper was introduced into clinical practice, and the dose survey repeated to determine its effectiveness. Following successful dose reduction, a more detailed study was performed to determine the optimal quantity of copper for barium enema examinations. A copper thickness of 0.3 mm was chosen, following phantom measurements. Its suitability for clinical imaging was verified by means of a visual grading analysis study.

This chapter describes the initial stages of the investigation. It begins by outlining the clinical background to barium enema imaging, and reviewing the literature on patient radiation doses. It then describes the baseline survey, and the local imaging protocol. Several methods for dose reduction are proposed, and the merits of each are considered. The initial series of phantom measurements are described, and the effectiveness of 0.1 mm copper in reducing patient DAP is examined.

Some of the figures quoted in Chapters 7 and 8 differ slightly from those previously presented in a paper by the author (Morrell *et al*, 2004). The reasons for this are as follows. Firstly, the survey data in the paper included some patients who had fewer than six screen-film radiographs. It was subsequently decided that these incomplete

examinations should be excluded from the dose surveys. Secondly, the percentages of patients likely to be affected by saturation of the fluoroscopic exposure factors (Chapter 8) were re-calculated for the thesis, using a simpler method and larger sample sizes.

7.1.1 Clinical Background

The double contrast barium enema examination is performed to identify the cause(s) of pain in, or dysfunction of, the colon. It is effective in the diagnosis of carcinomas and diverticular disease, and in identification of colonic polyps. It involves both fluoroscopic imaging and multiple radiographs of the abdomen. Hence, patients may receive high effective doses of radiation.

The walls of the large bowel are coated with a barium contrast agent, and then imaged from several different projections, in order to visualise the detailed structure of each part of the bowel wall. An example image is shown in Figure 7.1.



Figure 7.1: Example barium enema radiograph.

7.1.2 Literature Review

The National Radiological Protection Board (NRPB) estimate that barium enemas account for 13% of the UK Collective Effective Dose from medical X-rays (Hart & Wall, 2002). Their national dose survey in 1985 (Shrimpton *et al*, 1986) and its subsequent reviews in 1995 (Hart *et al*, 1996) and 2000 (Hart *et al*, 2002) found dose area products for enemas to be substantially greater than those for other barium examinations. The introduction of colon cancer screening in the UK could further increase the number of patients being referred for enema.

Studies of various sizes have sought to assess radiation doses to patients during barium enema examinations. The most practical measure of patient dose and that most commonly used is dose area product (DAP). Table 7.1 shows a selection of data from the literature, including mean DAPs, fluoroscopy times and numbers of radiographs. The data is presented in order of increasing DAP. Where no values for fluoroscopy time or number of radiographs are given, this information was not available from the source material. Some of the studies included more than one X-ray facility, and showed considerable variations in mean DAP between individual X-ray rooms.

The studies associated with the lowest doses were at hospitals where local practice had previously been reviewed, and dose reduction measures applied. Horton *et al* (1992) had minimised the fluoroscopy time by using a standard protocol to coat the patient's bowel with barium as thoroughly as possible before making any exposures. Smiddy *et al* (1996) had reduced the fluoroscopic current to 0.5 mA. Dose reduction techniques reported by other authors include reducing the number of radiographs taken (Booth *et al*, 1998), and removing the anti-scatter grid during the fluoroscopic parts of the examination (Seymour, 1997; Lloyd *et al*, 1998). Each of these methods is associated with a reduction in the number or quality of the images available to the operator and/or reporting clinician.

The use of copper filtration in addition to the existing aluminium has been recommended by Geleijns *et al* (1997), Hansson *et al* (1997), Kohn *et al* (1988), and Pärtan *et al* (2000). A recent survey of hospitals in the West of Scotland found that units employing copper filtration were associated with some of the lowest mean DAPs (Martin, 2004).

Publication	Sample Size	DAP (Gycm²)	Fluoroscopy Time (min)	Number of Radiographs
Horton <i>et al</i> (1992)	50	10.4	0.9	11
Smiddy <i>et al</i> (1996)	< 20	13.7	--	10
Pärtan <i>et al</i> (2000)	36	14.1	2.3	15
Hart & Wall (1994)	19	15.0	--	8.4
Martin (2004)	563	15.2	2.2	12.9
Hetherington <i>et al</i> (1998)	5687	17.2	2.2	11
Broadhead <i>et al</i> (1995)	5150	17.4	2.8	9.5
Hart & Wall (1995)	18	18.3	3.4	10.4
Crawley <i>et al</i> (1998)	1020	18.9	--	--
Geleijns <i>et al</i> (1997)	1733	21.0	--	--
Hart <i>et al</i> (2002)*	49967	23.5	2.2	4 [†]
Hart <i>et al</i> (1996)*	14545	25.8	2.3	10
Lampinen & Rannikko (1999)	89	27.8	3.0	11.2
Warren-Forward <i>et al</i> (1998)	1374	29.2	1.9	7.7
Martin & Hunter (1994)	503	30.8	2.1	10.3
Carroll & Brennan (2003)	151	31.3	--	--
Yakoumakis <i>et al</i> (1999)	22	35.4	6.4	7.3
Calzado <i>et al</i> (1991)	124	48.9	3.9	9.5
Kemerink <i>et al</i> (2001)	150	51	9.7	16
Ruiz-Cruces <i>et al</i> (2000)	42	56.8	3.8	7.7
Delichas <i>et al</i> (2004)	42	60.6	3.4	10

Table 7.1: Mean DAP, fluoroscopy time and number of radiographs from published surveys, presented in order of increasing DAP. The studies marked with a '*' are national dose surveys carried out in the UK by the National Radiological Protection Board (NRPB). The mean number of radiographs quoted for the most recent NRPB survey (†) refers only to screen-film radiographs. The majority of hospitals surveyed obtained at least some of their images using a digital spot device.

7.1.3 Objectives

The objectives of the study were:

- To perform a survey of barium enema practice at Nottingham City Hospital, to establish the local imaging protocol, to obtain baseline patient radiation dose measurements, and to compare local practice with published studies;
- To identify potential opportunities for dose reduction, and to investigate their suitability for, and effectiveness in, the clinical environment.

7.2 Method

7.2.1 Baseline Survey

The survey was carried out in a dedicated examination room, the main components of radiographic equipment being a Philips Super 80 CP generator, with a Philips Scopomatic 66 image intensifier, a Philips SRO 25 50 under-couch X-ray tube and a Philips SRO 33 100 over-couch X-ray tube (Philips Medical Systems, Best, The Netherlands). For the conventional radiographs, Fuji Super HR-L 30 film (Fuji Photo Film Co. Ltd., Tokyo, Japan) was used in conjunction with Kodak Lanex Fast screen cassettes (Eastman Kodak Company, Rochester, New York). The films were processed in a Kodak X-OMAT M6B processor, with Photosol developer and fixer (Photosol Limited, Basildon, UK). All of the imaging equipment was subject to regular quality control checks, as recommended by the Institute of Physics and Engineering in Medicine, Report 77 (1997).

Each X-ray tube was fitted with a VacuDAP 2003 DAP meter (Vacutec, Dresden, Germany). These were networked to a computer, using a custom-built node box and 'DAPNet' software, both supplied by Southern Scientific (Southern Scientific Ltd., Sompting, UK). A barcode reader was used to input the patient's identification number from the request card, and this was then linked to the DAP for each examination. The DAP meters were calibrated to within 5% at 80 kVp, throughout the study.

The total filtration provided by each X-ray tube and its housing was 2.5 mm aluminium equivalent at 80 kVp. The DAP meters provided a further 0.2 mm aluminium equivalent filtration.

Dose area product data from the under-couch and over-couch X-ray tubes were collected for all patients throughout a six-week study period. Additional information was collected by questionnaire, and included patient identification number and examination date, patient height and weight, total fluoroscopy time, number of digital spot and screen-film radiographs. This data was manually transferred into an Excel 2000 spreadsheet (Microsoft Corporation, Redmond, Washington), and matched with the DAP values by means of the patient identification numbers.

Any records that had not been fully completed on the questionnaire were discarded. In a number of cases, the fluoroscopy time recorded by the DAP meter did not match that written on the questionnaire, suggesting that the DAP meter had not always been started and stopped at the beginning and end of each examination. Any examinations showing a discrepancy of more than 20 seconds between the two values were excluded from the analysis. Incomplete examinations having fewer than 6 over-couch radiographs were also excluded.

7.2.2 Imaging Protocol

The examinations were generally performed according to a standard protocol, which is described below. At the time of the study, enemas were performed by any of two gastrointestinal (GI) consultant radiologists, four specially trained radiographers, and several radiology registrars.

The walls of the large bowel were coated with 'Polibar' barium sulphate suspension (E-Z-EM Limited, Bicester, UK). The colon was then inflated with air. During these processes, fluoroscopy was performed at intervals, to track the progress of the barium. The operator asked the patient to turn over, and tilted the couch as necessary, to ensure complete coating of the bowel wall. The exposure factors for fluoroscopy were automatically controlled by the imaging unit.

Radiographs were then taken from several projections, in order to obtain a clear view of each part of the bowel, unobscured by overlying structures. Figure 7.2 is a schematic diagram showing the various regions of the large bowel.

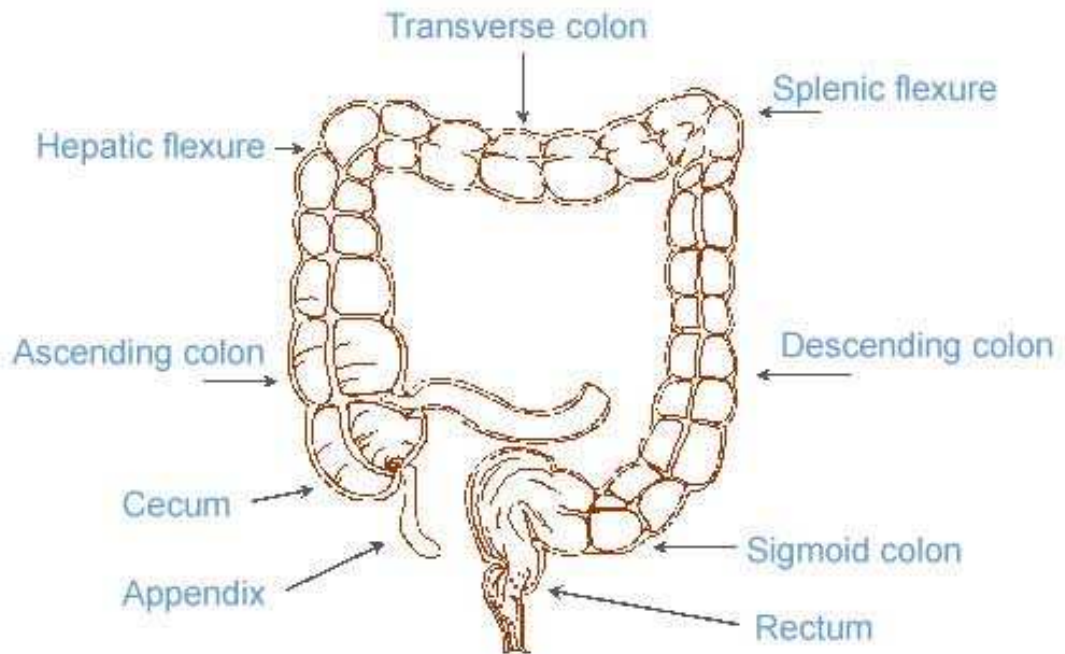


Figure 7.2: Diagram of large bowel. (Reproduced with permission, from <http://www.training.seer.cancer.gov>; funded by the U.S. National Cancer Institute's Surveillance, Epidemiology and End Results (SEER) Program, via contract number N01-CN-67006, with Emory University, Atlanta SEER Cancer Registry, Atlanta, Georgia, U.S.A.)

Digital spot images were taken using the image intensifier, and printed to film. The exposure factors were automatically determined. The following four images were taken as standard:

- Left posterior oblique (LPO) view of sigmoid colon
- Posteroanterior (PA) view of splenic flexure
- Posteroanterior (PA) view of hepatic flexure
- Right lateral (RLAT) view of caecum and rectum

Additional spot images were taken if the operator considered visualisation of any part of the bowel to be inadequate.

Six standard screen-film radiographs of the abdomen were then taken using the over-couch tube. These views were:

- 1 x Prone
- 1 x 30⁰ cranial angled prone
- 2 x 30⁰ anterior oblique, one from each side
- 2 x decubitus films, one with the patient lying on their right side, and one on their left side.

The screen-film radiographs were taken at 96 kVp, unless the patient was particularly large, in which case this was increased to 102 kVp. An automatic exposure control device was used to control the tube current and exposure time for the prone and anterior oblique views. For the decubitus films, the exposure factors were selected manually, using the values from the previous exposures as a guide. A compensation filter was often used for the decubitus films.

7.2.3 Dose Modelling

Patient entrance skin dose is known to vary approximately exponentially with the thickness of the patient. In order to predict the effects of dose reduction techniques, patients were modelled as uniform cylinders of density 1 g/cm³, as described by Chapple *et al* (1995). An “equivalent diameter” d_e in centimetres was calculated for each patient, using Equation 7.1, where *weight* is the patient’s weight in kilograms and *height* is the patient’s height in centimetres.

$$d_e = 2\sqrt{\frac{1000 \times \text{weight}}{\pi \times \text{height}}}$$

Equation 7.1

The validity of this model was checked by plotting the natural logarithm of the dose-area-product against equivalent diameter, for each of the patients in the baseline survey, and calculating the Pearson correlation coefficient between the two quantities.

Entrance surface doses for fluoroscopic, digital spot and screen-film exposures were determined using 34 cm by 34 cm Perspex phantoms, ranging in thickness from 18 cm to 28 cm, to match the spread of patient equivalent diameters. All dose measurements

were performed using a calibrated Radcal 9010 dose meter, with a 60 cc ionisation chamber (Radcal Corporation, Monrovia, California).

For the under-couch exposures (fluoroscopy and digital spot images), the ionisation chamber was placed directly on the couch, with the Perspex supported 2cm above the couch as shown in Figure 7.3. The explorer was positioned at its maximum height. Phantom entrance surface doses for digital spot imaging and dose rates for fluoroscopy were measured for both of the field sizes in clinical use (10 inch and 14 inch diameter).

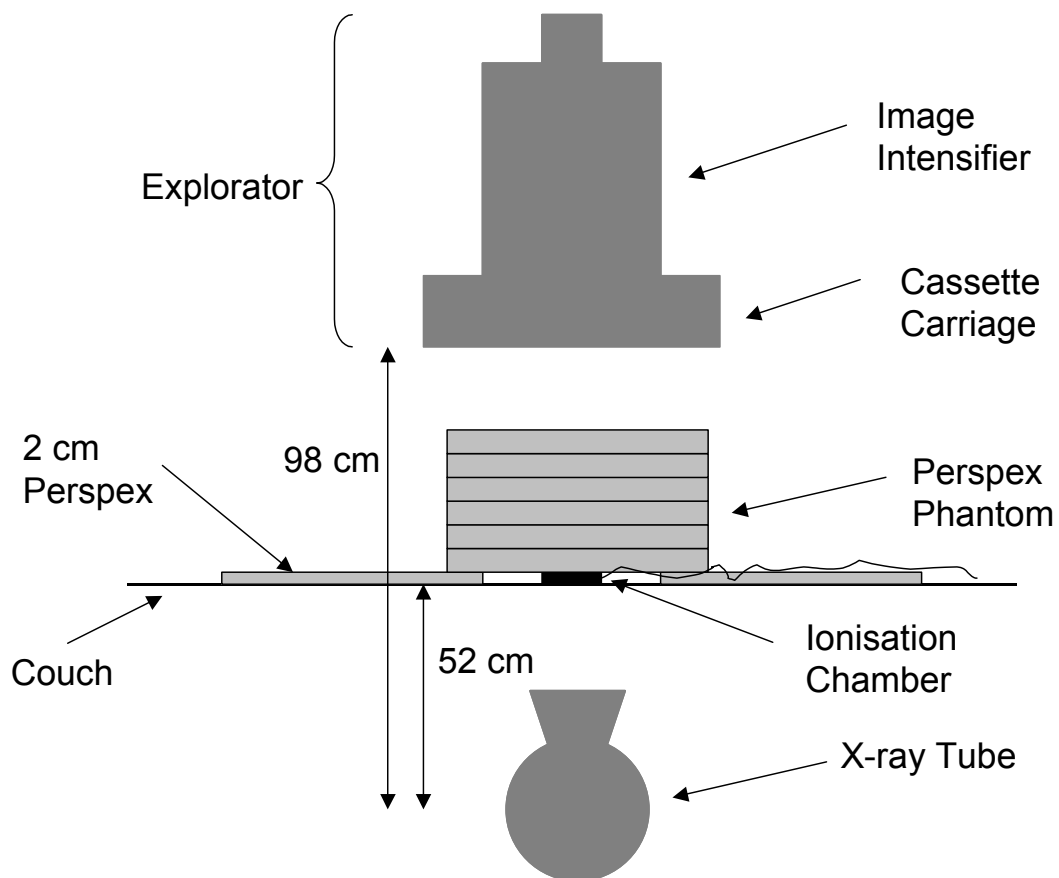


Figure 7.3: Set-up for under-couch phantom exposures.

The DAP (in Gycm^2) associated with each digital spot exposure or each minute of fluoroscopy was then calculated, using Equation 7.2, where $Dose$ was the measured dose in Gray, and $FieldSize$ was the nominal field size at the detector, in square centimetres. The factor of 1.3 was included to remove the contribution from backscatter, and the squared term adjusted the field size to that at the dose measuring point.

$$DAP = \frac{Dose}{1.3} \times FieldSize \times \left(\frac{52}{98}\right)^2$$

Equation 7.2

For the over-couch (screen-film) exposures, the ionisation chamber was positioned on top of the Perspex (Figure 7.4). The distance between the focal spot and the exit surface of the Perspex was 100 cm. The field size was set to 30 cm x 40 cm at one metre, since 35 cm x 45 cm films were generally used for screen-film radiographs.

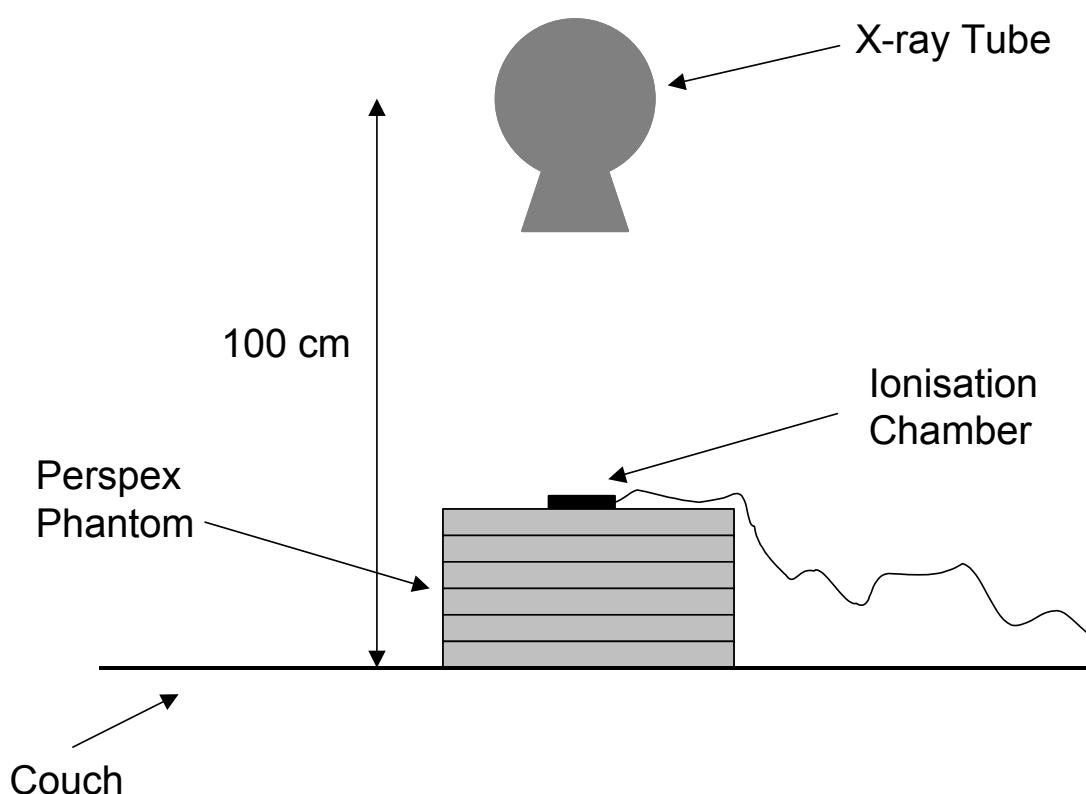


Figure 7.4: Set-up for over-couch phantom exposures.

The DAP for each exposure (in $Gycm^2$) was calculated using Equation 7.3, where *Dose* was the measured dose in Gray, and *P* was the Perspex thickness in centimetres. The factor of 1.3 was included to remove the contribution from backscatter, and the squared term adjusted the field size to that at the dose measuring point.

$$DAP = \frac{Dose}{1.3} \times 30 \times 40 \times \left(\frac{100 - P}{100}\right)^2$$

Equation 7.3

For each imaging mode and field size, the natural logarithm of the DAP or DAP rate was plotted against Perspex thickness. Regression lines were fitted to the data, and the gradient and intercept of each was calculated. These were then combined with each patient's equivalent diameter, fluoroscopy time and number of radiographs of each type, to calculate a "predicted" DAP for each examination, as described in Section 7.3.2. The results of the phantom measurements were also used to estimate the contribution of each part of the examination to the total DAP, for a typical procedure.

7.2.4 Dose Reduction

Several options for dose reduction were considered, in the light of the baseline survey and dose modelling results. These were discussed at a joint meeting with the local Radiation Protection Adviser, one of the gastrointestinal (GI) consultant radiologists, and the superintendent radiographer responsible for barium studies. It was assumed that all operators were already following good practice in terms of radiation protection measures such as collimating the radiation beam to the area of interest, and positioning the image intensifier close to the patient. The options considered were:

Reducing the fluoroscopy time. Horton *et al* (1992) reduced patient doses by minimising the use of fluoroscopy during the barium filling phase. The GI consultant radiologist involved in the present study considered fluoroscopy in this early part of the examination to yield important diagnostic information, and was concerned that any substantial reduction in fluoroscopy time could compromise the diagnostic accuracy of the examination.

Reducing the number of images taken. Again, the GI consultant radiologist was concerned that reducing the number of views would result in loss of diagnostic information. Whilst a smaller image set would be sufficient in some cases, the benefits of procedural standardisation were thought to offset those of this small dose reduction. The use of a standard imaging protocol was thought to encourage consistency of practice among the various staff groups who perform enemas, improve the accuracy and speed of reporting, and facilitate teaching, audit and research.

Exchanging some screen-film radiographs for digital spot images. The dose area product from a typical screen-film radiograph was found to be about 33% greater than that from a typical digital spot image (Table 7.4). It was therefore proposed that more

of the radiographs could be taken using the digital spot device. However, this used a circular field of view, with a maximum diameter of only 14 inches (i.e. 35 cm). Compared to a rectangular 43 cm x 35 cm film cassette, coverage was less well matched to the shape of the colon. Thus, it seemed likely that more digital spot images would be required to cover the same field of view as the screen-film cassette, making this unlikely to be a viable method for dose reduction.

Changing from screen-film to computed radiography (CR). This was unlikely to allow a dose reduction, as the screen-film system in use had a nominal speed of around 600, whereas the local CR system needed to run at an equivalent of 400 speed in order to obtain images with the same noise level. There was also a practical reason against using CR, in that the reader in use at the time took several minutes to process each plate when they were loaded in rapid succession. This would increase the examination time, adding to the patient's discomfort and potentially reducing patient throughput.

Using additional beam filtration. This method was chosen, since it would routinely reduce doses for all patients, without cutting down on the number of views available to the operator or reporting clinician, and whilst maintaining standardisation of the imaging protocol. Increasing the beam filtration can have a detrimental effect on image contrast, so it was necessary to verify that it would not adversely affect the diagnostic quality of the images.

Entrance surface doses and dose rates to Perspex slabs of various thickness were re-measured for fluoroscopic and digital spot exposures, with an additional 0.1 mm copper filtration.

The effect of this additional filtration on fluoroscopic image contrast was determined using a Leeds TO.10 contrast detail test object (Leeds Test Objects Limited, Boroughbridge, UK). The test object was positioned inside the cassette carriage, and the explorer locked at its maximum height. A 1.5 mm copper plate was placed on the couch, such that it completely intercepted the X-ray beam. Fluoroscopic images obtained with and without the additional 0.1 mm copper filtration were scored by two independent observers, and their scores averaged. Threshold contrasts relating to the mean observer scores were determined using the Leeds test object manual (Cowen *et al*, 1992), and a contrast detail diagram was plotted.

The additional filtration was then introduced into clinical practice by selecting the appropriate filter setting on each X-ray tube. This consisted of 0.1 mm copper, along with 1.0 mm aluminium, to absorb the low energy emissions from the copper. The patient dose survey was repeated, as described in Section 7.2.1.

7.3 Results

7.3.1 Baseline Survey

Table 7.2 summarises the results of the baseline survey. Complete data sets were obtained for 59 patients. The mean patient weight was 69 kg.

Measured Parameter	Mean (95% CI)	Median
Fluoroscopy Time (minutes)	1.8 (1.6 – 2.0)	1.6
Number of Digital Spot Images	4.6 (4.4 – 4.9)	4.0
Number of Screen-Film Radiographs	6.0	6.0
Under-Couch DAP (Gycm ²)	12.0 (10.4 – 13.9)	9.5
Over-Couch DAP (Gycm ²)	5.7 (5.0 – 6.6)	5.2
Total DAP (Gycm²)	17.7 (15.6 - 20.3)	15.3

Table 7.2: Summary of baseline survey results. The ranges shown in brackets indicate 95% confidence intervals, calculated using Cox's method.

Exactly six over-couch radiographs were taken for all examinations. Each of fluoroscopy time, number of digital spot images, under-couch, over-couch and total DAP followed log-normal distributions. The 95% confidence intervals were therefore calculated using Cox's method (Zhou & Gao, 1997). The upper and lower confidence limits for parameter x were defined by Equation 7.4, where μ denotes the mean of the bracketed function, σ the standard deviation, and n the sample size.

$$CI_{95\% \pm} = \exp \left\{ \left[\mu(\ln(x)) + \frac{\sigma^2(\ln(x))}{2} \right] \pm 1.96 \left[\frac{\sigma^2(\ln(x))}{n} + \frac{\sigma^4(\ln(x))}{2(n-1)} \right]^{1/2} \right\}$$

Equation 7.4

Figure 7.5 is a frequency histogram of total DAP. Its long right-hand tail is characteristic of a log-normal distribution.

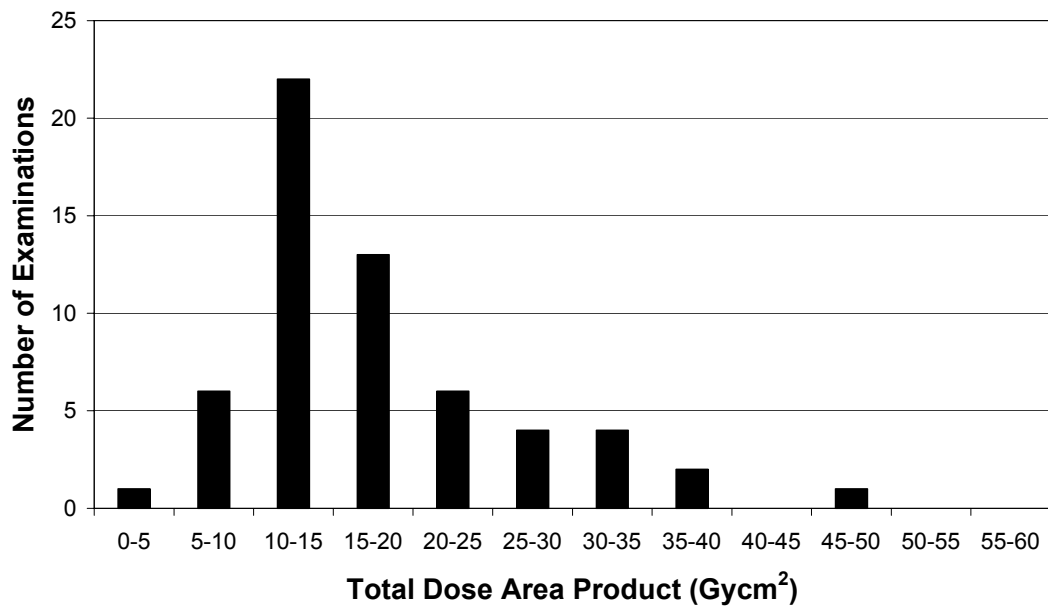


Figure 7.5: Frequency histogram of total DAP.

7.3.2 Dose Modelling

Figure 7.6 is a scatter plot of ln(DAP) against patient equivalent diameter. A regression line has been fitted. The square of the Pearson correlation coefficient (R^2) was 0.43, implying that variations in patient diameter accounted for 43% of the variations in ln(DAP).

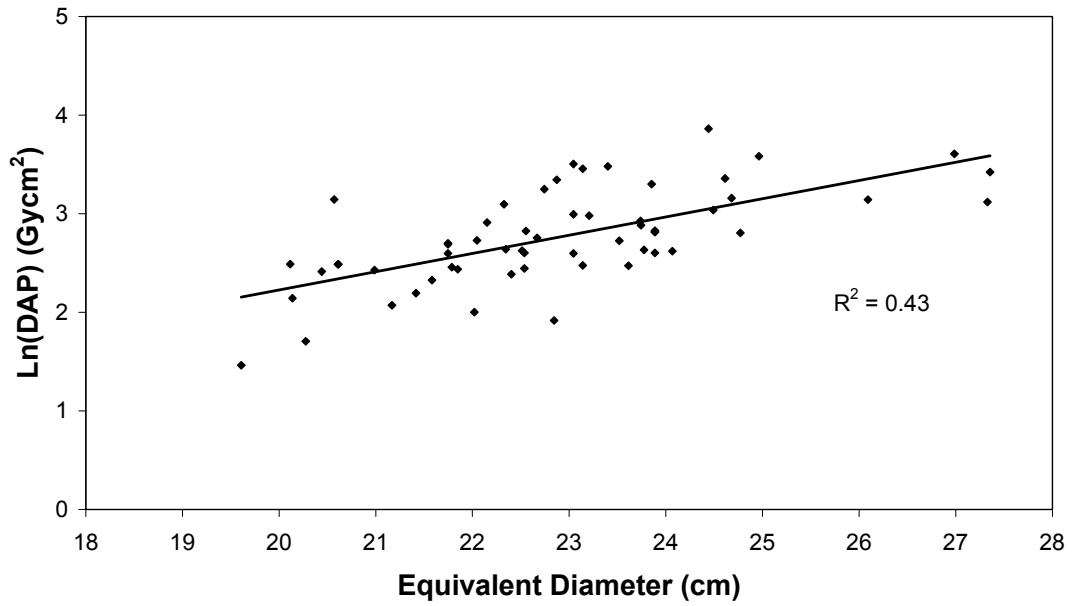


Figure 7.6: Ln(DAP) versus patient equivalent diameter.

Figure 7.7 and Figure 7.8 show the relationship between the natural logarithm of DAP or DAP rate, and Perspex thickness, for each imaging mode and field size investigated. Regression lines were fitted to this data, and their gradients and intercepts are shown in Table 7.3. The final column of the table shows the equations used to calculate predicted DAP contributions for each imaging mode and field size.

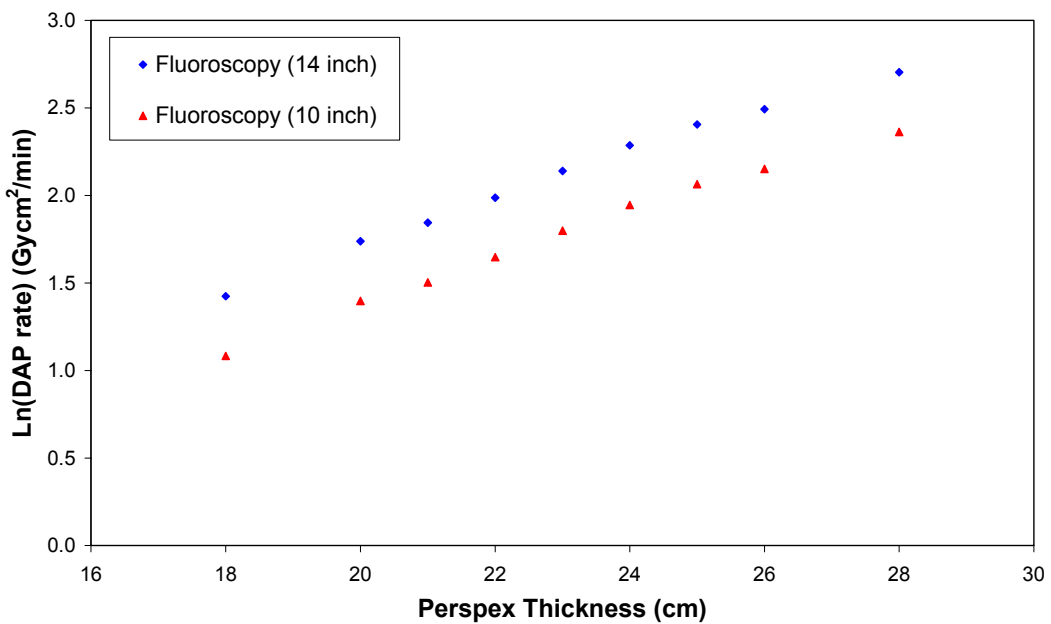


Figure 7.7: Relationship between ln(DAP rate) and Perspex thickness, for fluoroscopy.

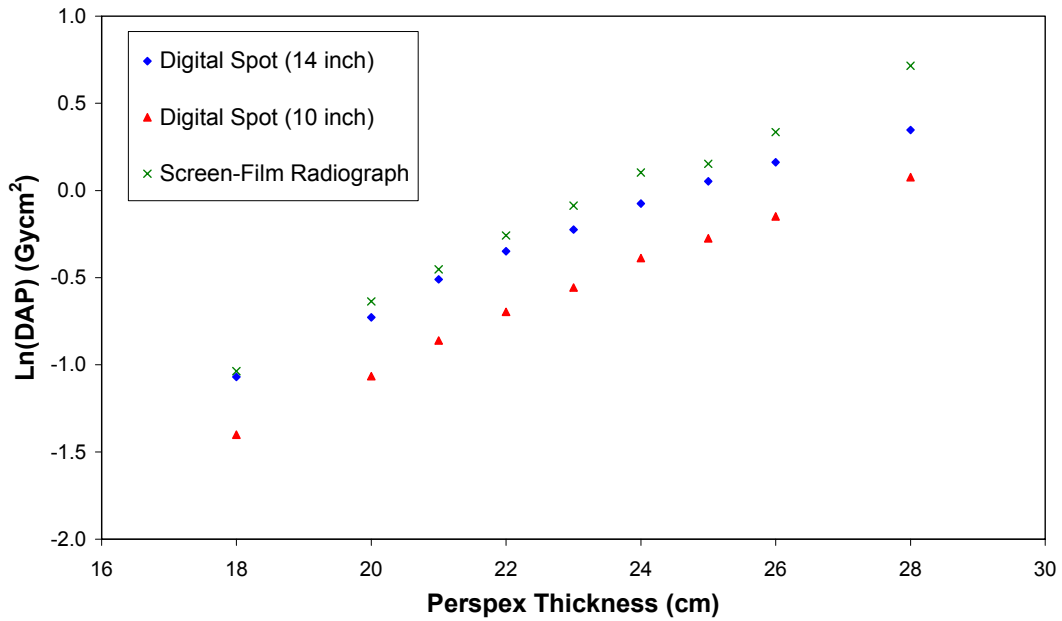


Figure 7.8: Relationship between ln(DAP) and Perspex thickness, for digital spot and screen-film radiographs.

Imaging Mode & Field Size	Gradient (a)	Intercept (b)	Contribution to Total DAP (Gycm ²)
Fluoroscopy (14 inch)	0.129	-0.86	$\frac{1}{2} \times FT \times \exp(a \times d_e + b)$
Fluoroscopy (10 inch)	0.129	-1.20	$\frac{1}{2} \times FT \times \exp(a \times d_e + b)$
Digital Spot (14 inch)	0.143	-3.55	$\frac{1}{2} \times DSI \times \exp(a \times d_e + b)$
Digital Spot (10 inch)	0.149	-4.02	$\frac{1}{2} \times DSI \times \exp(a \times d_e + b)$
Screen-Film Radiograph	0.170	-4.03	$SFR \times \exp(a \times d_e + b)$

Table 7.3: Gradients and intercepts of regression lines relating ln(DAP) or ln(DAP rate) to Perspex thickness, for each imaging mode and field size. The equations in the final column show how the DAP contribution of each field size and mode was calculated, for a patient of equivalent diameter d_e undergoing FT minutes of fluoroscopy, followed by DSI digital spot images and SFR screen-film radiographs. It was assumed that the 10 and 14 inch field sizes were each used for half of the fluoroscopy and half of the digital spot images.

The predicted and measured dose area products for each examination are shown in Figure 7.9. There was a strong correlation between the two, with a squared Pearson correlation coefficient of 0.77. The mean predicted DAP was 21.4 Gy cm^2 .

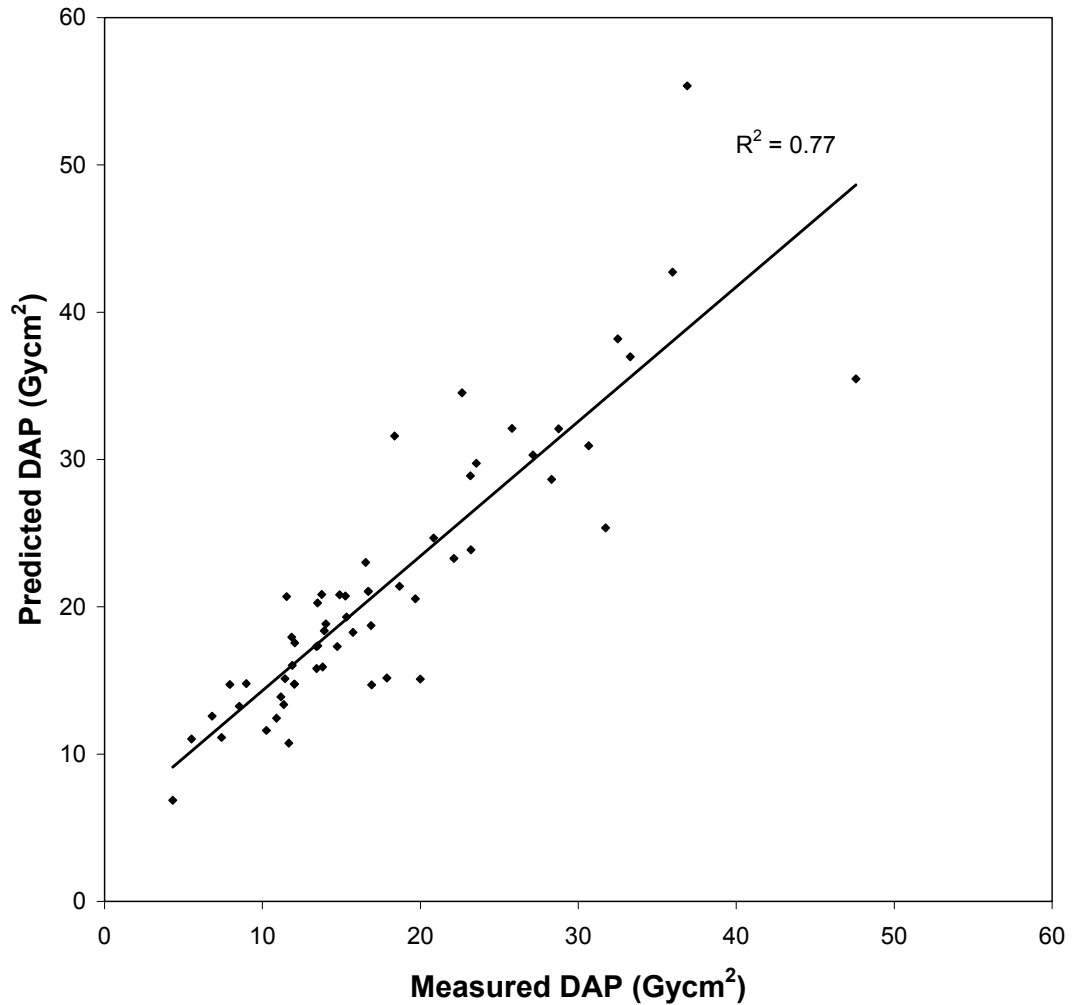


Figure 7.9: Predicted DAP versus measured DAP, for the examinations in the baseline survey.

Table 7.4 shows the measured and predicted contributions of each part of the examination to the total DAP. The measured contributions were based on the mean DAP values listed in Table 7.2. The predicted contributions were calculated using the equations in Table 7.3, with an equivalent diameter of 24 cm, and the median values of fluoroscopy time and numbers of radiographs quoted in Table 7.2.

Component of Examination	Measured DAP Contribution (%)	Predicted DAP Contribution (%)
Fluoroscopy	} 68	58
Digital Spot Images		14
Screen-Film Radiographs	32	28
Total	100	100

Table 7.4: Measured and predicted contributions of each part of the examination to total DAP.

7.3.3 Dose Reduction

On adding 0.1 mm copper filtration, fluoroscopic entrance dose rates and digital spot doses to the 24 cm Perspex phantom were reduced by 34%.

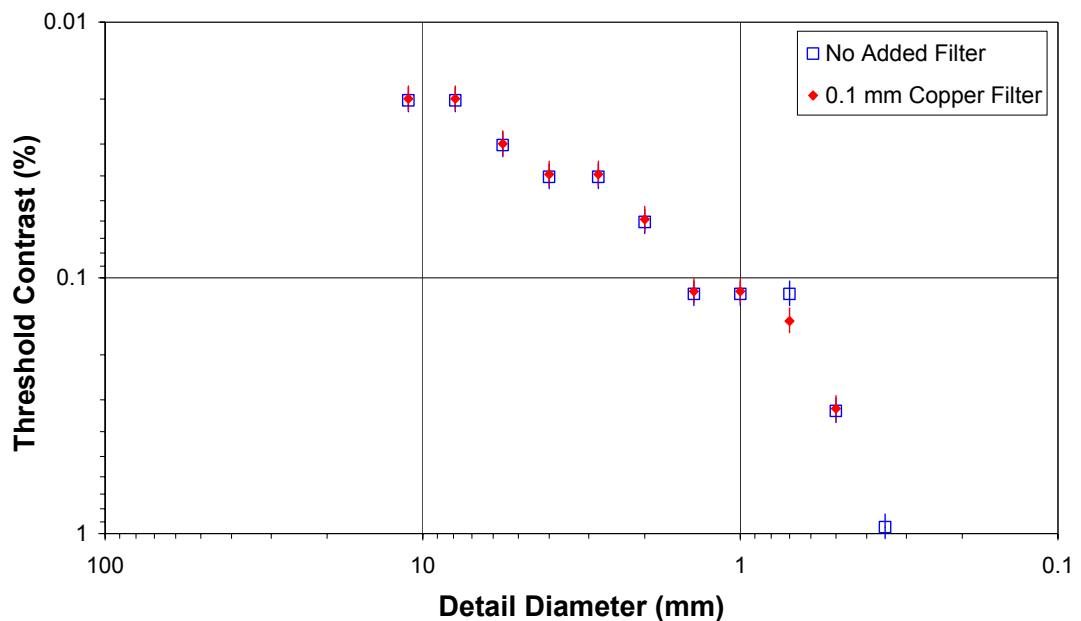


Figure 7.10: Contrast detail diagram for mean TO.10 scores with and without additional 0.1 mm copper filtration. Error bars indicate standard errors of 11% indicated by Marshall *et al* (1992).

Figure 7.10 shows the contrast detail diagram for the TO.10 image scores with and without an additional 0.1 mm copper. The error bars show the standard error of 11% indicated by Marshall *et al* (1992), for one independent viewing by each of two independent observers. At each detail size, individual observer scores varied by up to

1 disc from the mean. On introducing the 0.1 mm copper filter, there was no difference in mean observer scores for the larger discs. At two of the smallest detail sizes, one fewer disc was seen, indicating slightly higher threshold contrast.

The repeat dose survey included 428 examinations. The mean patient weight was 71 kg. A summary of the fluoroscopy times, numbers of images and dose area product data is shown in Table 7.5. The 95% confidence intervals were calculated using Cox's method (Zhou & Gao, 1997). No change in clinical image quality was observed by the operators performing or reporting the examinations.

Measured Parameter	Mean (95% CI)	Median
Fluoroscopy time (minutes)	1.7 (1.6 – 1.8)	1.5
Number of Digital Spot Images	4.9 (4.7 – 5.0)	4.0
Number of Screen-Film Radiographs	6.1	6.0
Under-Couch DAP (Gycm ²)	7.1 (6.7 – 7.4)	6.1
Over-Couch DAP (Gycm ²)	4.1 (3.8-4.4)	3.3
Total DAP (Gycm²)	11.2 (10.6 – 11.7)	9.6

Table 7.5: Summary of the results of the repeat dose survey, using 0.1 mm copper additional filtration. The ranges shown in brackets indicate 95% confidence intervals, calculated using Cox's method.

7.4 Discussion

7.4.1 Baseline Survey

The baseline survey found a mean dose-area-product of 17.7 Gycm², with a 95% confidence interval of 15.6 to 20.3 Gycm². This was considerably lower than many of the published values presented in Table 7.1, and the UK national reference dose of 31 Gycm² (Hart *et al*, 2002).

Only five of the studies in Table 7.1 had demonstrated mean DAPs below the lower 95% confidence limit, and these were generally at centres where radical dose reduction measures had been applied. Horton *et al* (1992) had minimised the use of

fluoroscopy during the barium filling phase, Smiddy *et al* (1996) had adopted a very low fluoroscopic current, and Pärtan *et al* (2000) had introduced 0.3 mm copper filtration. Martin (2004) had included a number of new facilities, which had dose minimisation features such as low dose rate pulsed fluoroscopy and copper filtration. The fact that other investigators had used such techniques to reduce their mean DAPs below that found in the baseline survey suggested that there was also potential for dose reduction at Nottingham City Hospital.

The mean fluoroscopy time of 1.8 minutes was relatively short, compared with most of the studies reported in Table 7.1 This may be one reason for the relatively low mean DAP found in the present study.

The mean number of radiographs was 10.6. This corresponded fairly closely with the national mean of 10 radiographs found in the NRPB dose survey of 1990 to 1995 (Hart *et al*, 1996). The value quoted in the NRPB's 2000 review (Hart *et al*, 2002) included only screen-film radiographs, although most of the hospitals surveyed used digital spot imaging for at least some views. It was therefore not valid to compare total numbers of radiographs with this figure.

The mean patient weight of 69 kg exactly matched that for adult barium enema patients in the 2000 review of the NRPB national dose survey (Hart *et al*, 2002).

7.4.2 Dose Modelling

The strength of the correlation between $\ln(\text{DAP})$ and patient equivalent diameter suggested that the cylinder model should offer a fairly realistic approach to predicting the effectiveness of dose reduction techniques. This was confirmed by the strong correlation between measured and predicted dose area products for the examinations in the baseline survey. The mean predicted DAP was 21.4 Gy cm^2 , which was 21% higher than the measured value of 17.7 Gy cm^2 . The cylinder model tends to overestimate the radiation path length through the patient for anteroposterior (AP) and posteroanterior (PA) views, and underestimate it for lateral and oblique views. The fact that mean predicted DAP was higher than mean measured DAP may be explained by the fact that more AP and PA views than laterals and obliques were used in clinical practice.

According to the dose model, fluoroscopy accounted for 58% of the total DAP for a typical examination. The six screen-film radiographs contributed a further 28%, and the four digital spot images only 14%. Thus, on average, the DAP for each screen-film radiograph was 1.33 times that for a digital spot image. The predicted under-couch and over-couch DAP contributions compared well with the mean values from the baseline survey.

7.4.3 Dose Reduction

The method chosen for dose reduction was the addition of 0.1 mm copper filtration to the under-couch and over-couch X-ray tubes. This allowed the existing imaging protocol to be maintained, without any loss in the number of images available to the operator or to the reporting clinician.

Entrance dose and dose rate measurements to a 24 cm Perspex phantom, representing patients of median size, predicted a 34% reduction in DAP, on adding 0.1 mm copper to the existing filtration of 2.5 mm aluminium. The only observed differences in contrast detail detectability were reductions in visibility of 1 disc for two of the smallest detail sizes. This was no greater than the inter-observer variation in scores. Thus, it seemed reasonable to expect that there would be no perceptible difference in clinical image quality.

After selecting the 0.1 mm copper filters on both X-ray tubes, the mean DAP for patient examinations fell to 11.2 Gy cm^2 . This was a reduction of 37%, in good agreement with the phantom predictions. The reduction in DAP was statistically significant, since the 95% confidence intervals with and without 0.1 mm copper did not overlap. The mean fluoroscopy time and number of radiographs of each type were not significantly different from those measured in the baseline survey, indicating that the reduction in DAP was attributable mainly to the introduction of the copper. The new mean DAP was lower than almost all of the published values listed in Table 7.1.

A formal study of clinical image quality was not carried out at this stage, but the GI consultant radiologist was confident that there was no difference in the appearance of the clinical images, and no changes were reported by any of the other staff who perform or report barium enemas.

The option of changing from screen-film imaging to computed radiography (CR) was rejected, as it would require an increase in patient dose. However, as a result of the national PACS (Picture Archiving and Communications Systems) programme, the Radiology department is likely to go 'filmless' in the near future, making the switch to CR a necessity. In the longer-term future, film, CR and image intensifiers are all likely to be replaced by direct digital detectors. These have been shown to be more efficient than screen-film systems (Strotzer *et al*, 1998a; Strotzer *et al*, 1998b; Aufrichtig, 1999; Strotzer *et al*, 2000; Volk *et al*, 2000; Ludwig *et al*, 2002; Geijer, 2002). Whilst current flat detector technology offers only slightly improved efficiency relative to image intensifiers, future developments are likely to bring further improvements in their performance. The eventual move to direct digital imaging should therefore provide a further opportunity for dose reduction.

Although selective removal of the anti-scatter grid was not considered in this study, it may offer a feasible method for further dose reduction. Its success would depend on individual operators being disciplined about removing and replacing the grid as each examination progressed.

7.5 Summary

The baseline survey found a relatively low mean DAP of 17.7 Gy cm^2 . This was due at least in part to the short mean fluoroscopy time of 1.8 minutes. The literature survey highlighted several dose reduction methods that had been successfully employed at other hospitals. This suggested that there was also potential for local dose reduction.

In order to select Perspex phantoms suitable to the size of the patients in the sample, patients were modelled as uniform cylinders with an equivalent diameter calculated from their height and weight. The dose contributions from the fluoroscopic, digital spot and screen-film exposures were determined using Perspex phantoms of varying thickness. There was a strong correlation between predicted and measured DAP, for the examinations in the baseline survey. The predicted under-couch and over-couch DAP contributions were found to compare well with measured values.

Several dose reduction methods were considered, in consultation with clinical staff. These included reducing the fluoroscopy time or the number of images taken,

exchanging some of the screen-film radiographs for digital spot images, changing from screen-film to computed radiography for the over-couch views, and introducing additional beam filtration. The use of copper filtration was chosen, as allowing routine dose reductions for all patients, without requiring any change to the standardised imaging protocol.

The effects of adding 0.1 mm copper filtration were predicted using entrance dose measurements to Perspex phantoms, and contrast detail tests. The reduction in entrance doses and dose rates to a 24 cm phantom was 34%. There was no measurable change in detectability of the details in the Leeds TO.10 test object.

On introducing the 0.1 mm copper filter in clinical practice, the mean DAP fell by 37% to 11.2 Gy cm^2 . The operators reported no difference in the quality of the clinical images. Thus, copper filtration was shown to be a practical and effective method of dose reduction in barium enema imaging.

Chapter 8 - Barium Enema Optimisation

8.1 Introduction

This chapter describes the second part of the barium enema study. Here, the aim was to determine the optimal quantity of copper for barium enema examinations, i.e. that which would reduce patient doses as far as practicable without compromising diagnostic accuracy.

A brief literature review considers copper thicknesses used by other investigators, and summarises their approaches to image quality assessment.

The effects of various copper filters on dose and image quality were predicted using Perspex phantoms and a contrast detail test object, and the 'optimal' copper thickness chosen. The effects of the additional filtration on X-ray tube loading were considered, and compared with the tube heat capacities and cooling rates, to ensure that neither tube would be in danger of overheating.

The new filter was then introduced in the clinical setting, and the dose survey of Chapter 7 repeated. Clinical images obtained with the old and new filter settings were compared by means of visual grading analysis. The diagnostic adequacy of each examination was assessed by an experienced radiologist. Since the risk of radiation-induced cancer is related more closely to effective dose than to DAP, typical effective doses were estimated for each of the filter settings.

8.1.1 Literature Review

Of those authors who have recommended the use of copper filtration for double contrast barium enemas, Geleijns *et al* (1997) recommended using at least 0.1 mm,

whilst Kohn *et al* (1988) considered 0.2 mm to give acceptable image quality. Hansson *et al* (1997) successfully employed 0.3 mm for paediatric patients, and Pärtan *et al* (2000) reported using 0.3 mm for adults. Despite the considerable promise shown by this technique, at the time of the present study there were no reports of its adoption by UK radiology departments. After completion of this work, Martin (2004) reported the use of 0.2 mm copper in some Scottish hospitals.

When introducing changes in imaging practice that have potential to affect image quality, it is essential to investigate the likely extent of these effects, and to ensure that the resulting images remain adequate for their clinical purpose. Initial estimates can and should be made using contrast detail phantoms. However, a rigorous assessment of changes in clinical image quality should also be made.

Several investigators have compared clinical image quality for barium enemas using visual grading analysis. Hansson *et al* (1997) performed direct comparisons between paired images taken with and without a 0.3 mm copper filter, whilst Smiddy *et al* (1996), Persliden *et al* (1997) and Pärtan *et al* (2000) scored individual images on five-point quality scales. In these last two studies, observers were asked to give scores for noise, sharpness and contrast as well as their overall impression.

The approach taken by Hansson *et al* (1997) had the great advantage that the two filter options could be compared directly for almost identical views of the same patient, eliminating other factors that might affect image quality. However, only one view was considered instead of the examination as a whole, and there was a slightly increased radiation burden to the patients involved in the trial.

Hansson *et al* (1997) studied only paediatric patients, so their results were not necessarily generalizable to adults, where the filter may have a greater effect on contrast and noise, due to the larger average patient size. Pärtan *et al* (2000) studied adult patients, and concluded that 0.3 mm copper filtration was appropriate for the imaging equipment and protocol used at their facility. They did however recommend that each department determine their own optimal filter thickness, since the exact effects of the filtration on image quality depend on the performance of each piece of imaging equipment, and the exposure factors used in the clinical setting.

In order to assess whether the images remained adequate for their clinical purpose, Persliden *et al* (1997) simply asked the observers whether they were confident to give

a diagnosis based upon what they could see. Horton *et al* (1992) backed up observer opinion with an outcomes audit, performed 11 months after the original study.

8.1.2 Objectives

The objectives of this study were:

- To determine the optimal thickness of copper filtration for adult barium enema examinations, with regard to its dose reduction efficiency, its likely effects on image quality, and the increased load on the X-ray tubes;
- To verify the effect of this ‘optimal’ filter on patient DAP and whole body radiation dose;
- To ensure that its use did not compromise the diagnostic quality of the clinical images.

8.2 Method

This study used the same imaging equipment as described in Chapter 7.

8.2.1 Phantom Measurements

The effects of various copper filters on fluoroscopic dose rates and digital spot doses to the entrance surface of a Perspex phantom and to the image intensifier were measured concurrently, using two calibrated Radcal 9010 dose meters with 60 cc ionisation chambers (Radcal Corporation, Monrovia, California), as shown in Figure 8.1. The first ionisation chamber was placed directly on the couch, and the second was taped to the underside of the cassette carriage. The Perspex was supported 2cm above the couch, and the explorer was positioned 5 cm above the Perspex.

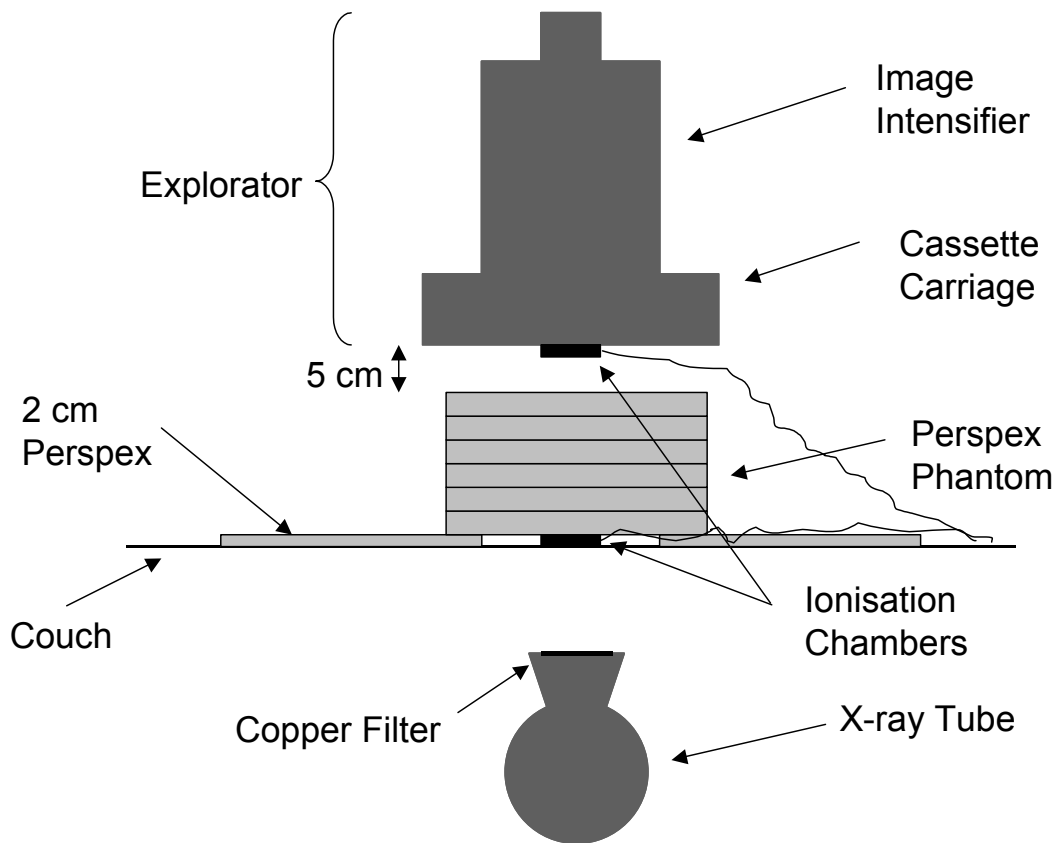


Figure 8.1: Set-up for under-couch phantom exposures.

The effect of each copper filter on entrance dose for over-couch exposures was measured using a single ionisation chamber positioned on top of the Perspex, with the distance from the focal spot to the Perspex exit surface set to 100 cm, as previously described in Chapter 7.

The thickness of the copper filter was varied from 0.0 to 0.7 mm, with a Perspex thickness of 24 cm, chosen to represent patients of median diameter. Copper filters varying from 0.1 to 0.3 mm in thickness were also applied with phantoms ranging from 24 to 30 cm. As well as measuring doses and dose rates to the phantom and detector, tube potential and current or current-time product were noted for each exposure.

Fluoroscopic image contrast was assessed using a Leeds TO.10 contrast detail test object (Leeds Test Objects Limited, Boroughbridge, UK), with a range of copper and Perspex thicknesses. The test object was positioned in the cassette carriage, and the explorator locked at its maximum height. Live fluoroscopic images were scored by two independent observers, who were blinded to the amount of copper and Perspex. In

order to provide a single index of overall image quality, the number of visible details was summed over all the rows in the phantom.

8.2.2 Tube Loading

The heat generated in each of the X-ray tubes was estimated for a typical examination on a median sized patient, with and without the 0.3 mm copper filter in place. The heat (in Joules) generated in a standard medical X-ray tube is given by Equation 8.1, where kVp is the X-ray tube potential, mA is the tube current, and t is the exposure time (Dendy & Heaton, 1999). These exposure factors had previously been noted for fluoroscopic, digital spot and screen-film exposures of a 24 cm Perspex phantom.

$$Heat = 0.95 \times kVp \times mA \times t$$

Equation 8.1

Each examination was assumed to consist of 2 minutes of fluoroscopy, 5 digital spot exposures and six over-couch radiographs. For the under-couch exposures, it was assumed that the 10 inch field size was used throughout, with the image intensifier 5 cm above the patient.

The heating effects of a full day's workload were compared with the heat capacities and cooling rates of each X-ray tube, as taken from the manufacturer's specifications. A full day's examination schedule included 12 patients. Each day was divided into three sessions, starting at 09:00, 11:00 and 14:00. Four patients were booked in each session, at fifteen-minute intervals.

8.2.3 Clinical Validation

Copper filters of 0.3 mm in thickness were then introduced as a clinical service development. The first 0.1 mm copper was selected on the filter wheel inside the housing of each X-ray tube, along with its accompanying 1 mm aluminium. A further 0.2 mm copper were mounted between each X-ray tube and its DAP meter. For the under-couch tube, the copper was taped directly to the underside of the DAP meter. This was not possible for the over-couch tube, since the copper blocked the light beam used for setting X-ray field alignment and collimation. The copper was therefore

taped to a thin sheet of Perspex, so that it could be slid in and out of the beam as required. The patient dose survey described in Chapter 7 was then repeated for a further 24 examinations.

Whilst phantom measurements had shown little degradation in contrast on introducing 0.3 mm copper filtration, the circular contrast details in the TO.10 test object offered a poor approximation to the clinical situation, where the subject of interest was a thin coat of contrast agent lining the intestinal wall. It was therefore important to verify that there was no significant effect on the diagnostic quality of clinical examinations.

A visual grading analysis study was performed on the digital spot and screen-film radiographs for 20 examinations performed with no additional filtration, 21 with 0.1 mm copper, and 21 with the 0.3mm copper filter. Examinations were selected sequentially. Those with fewer than six screen-film radiographs were excluded from the study. The images were retrieved from the film archive and randomised, before being presented to a gastrointestinal (GI) consultant radiologist for blinded scoring.

Images were scored on a scale of 0 to 3 for perceived barium coating, where '0' corresponded to no coating, '1' to poor, '2' to fair and '3' to good. For each examination, the sigmoid colon, splenic flexure and hepatic flexure were each allocated a score based on the digital spot images. The left colon, right colon and transverse colon were each allocated a score based on the screen-film radiographs. The scorer was also asked to suggest reasons for any scores below 3, and to classify each examination as 'diagnostic', 'non-diagnostic' or 'indeterminate'.

The image quality scores for each filter combination were compared for each region of the bowel, using Kruskal-Wallis one-way analysis of variance by ranks (Siegel & Castellan, 1988). This is a powerful non-parametric test for k independent samples of ordinal data. A correction for tied rankings was applied. The null hypothesis was that of no statistically significant difference between the populations from which the three samples were drawn.

In order to confirm the results, Wilcoxon-Mann-Whitney and Kolmogorov-Smirnov tests (Siegel & Castellan, 1988) were also performed for the samples with most and least filtration. These tests were chosen because they are the most powerful for two independent samples of ordinal data.

8.2.4 Effective Doses

Effective doses for each of the three filter settings were estimated using PCXMC version 1.4, a PC-based Monte-Carlo dosimetry package (Finnish Centre for Radiation and Nuclear Safety, Helsinki, Finland). The calculations were based on the standard imaging protocol described in Chapter 7, with the median fluoroscopy time of 1.6 minutes from the baseline survey. The exposure factors and entrance surface doses for each component of the examination were determined from measurements on a 24 cm Perspex phantom, described in section 8.2.1. All entrance surface dose measurements were divided by 1.3, to remove the contribution from backscatter.

The standard adult phantom, with a height of 174 cm and a weight of 71.1 kg, was selected. The under-couch, circular radiation fields were approximated by square fields of equal area. It was assumed that the fluoroscopic projections and field sizes matched those used for digital spot images, and were used in the same proportion. The effect of the compensation filter for decubitus views was not taken into account.

Each exposure was simulated using 15 energy levels, with 20,000 photons in each level. The effective doses from the individual exposures were then summed, to give estimates for the whole examination.

8.3 Results

8.3.1 Phantom Measurements

Figure 8.2 shows the fluoroscopic entrance surface dose rates to a 24 cm Perspex phantom, with varying amounts of copper filtration, at the two field sizes used in clinical practice. The first 0.1 mm copper reduced the entrance dose rate by 34% for both field sizes, and each additional 0.1 mm gave a sequentially smaller dose reduction. Similar dose reductions were also obtained for digital spot, and conventional radiographic exposures.

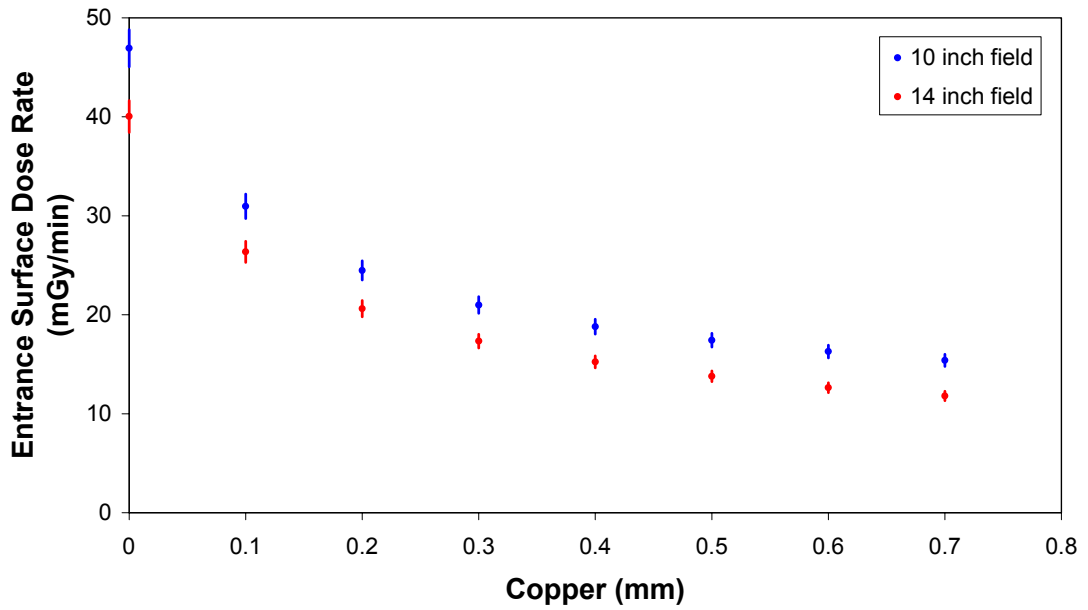


Figure 8.2: Fluoroscopic entrance surface dose rates to a 24 cm Perspex phantom, with various copper filters, at the 14 inch and 10 inch field sizes. (Error bars indicate 4% uncertainty in calibration of dose meter.)

Figure 8.3 shows the corresponding X-ray tube potentials for fluoroscopy. Tube potential increased steadily with increasing filtration, but did not reach its maximum value of 110 kV.

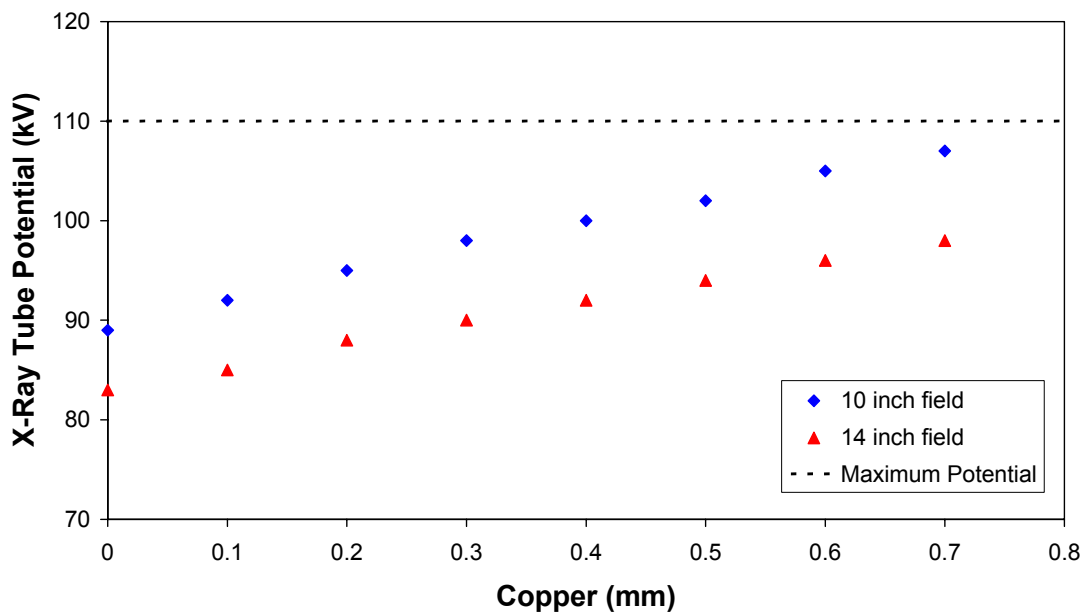


Figure 8.3: X-ray tube potentials for fluoroscopic exposure of a 24 cm Perspex phantom, with various copper filters, at the 14 inch and 10 inch field sizes. The tube potential was automatically controlled, and its maximum permissible value was 110 kV.

When thicker phantoms were imaged, the tube potential and current saturated as copper was added. Once they had reached their maximum values, any increase in beam attenuation led to a reduction in input dose rate to the image intensifier. Table 8.1 shows the thickness of Perspex at which the exposure factors saturated, for each copper filter, at the 10 inch field size. It also shows the percentage of patients in the surveys of Chapter 7 whose equivalent diameters exceeded each thickness, and for whom saturation was therefore likely to occur.

Copper (mm)	Perspex Thickness at which Exposure Factors Saturated (cm)	Patients for whom Saturation Expected to Occur (%)
0	27	5
0.1	26	10
0.2	26	10
0.3	25	19
0.4	24	33

Table 8.1: Perspex thickness at which saturation occurred on 10 inch field, and the percentage of patients whose equivalent diameters exceeded this value, and for whom saturation might therefore be expected to occur.

Table 8.2 shows the image quality scores for the two observers, at the 10 inch field size. On increasing the thickness of the Perspex, fewer details were seen. There was however no consistent trend in image scores with changing copper thickness.

Perspex (cm)	Copper (mm)		
	0.1	0.2	0.3
24	32, 30	33, 28	33, 32
26	29, 29	28, 25	31, 27
28	26, 29	21, 21	25, 20
30	21, 16	19, 12	19, 21

Table 8.2: Observer scores for the Leeds TO.10 test object, with varying amounts of copper and Perspex at the 10 inch field size. (Observer 1, Observer 2.)

On comparing Table 8.1 with Table 8.2, the image quality scores appeared to fall off sharply at about 2 cm Perspex beyond factor saturation. Assuming this to be the case up to 0.4 mm copper, Table 8.3 displays the Perspex thickness at which image contrast was expected to deteriorate, for each copper filter. The percentage of patients in the dose surveys of Chapter 7 whose equivalent diameters exceeded each value, and for whom contrast degradation was therefore likely to occur, is also shown.

Copper (mm)	Perspex Thickness at which Image Contrast Expected to Deteriorate (cm)	Patients for whom Contrast Degradation Likely to Occur (%)
0	29	1
0.1	28	2
0.2	28	2
0.3	27	5
0.4	26	10

Table 8.3: Perspex thickness at which image contrast was expected to deteriorate for various copper filters (10 inch field), and percentage of patients likely to be affected by this.

8.3.2 Tube Loading

For the under-couch tube, the heat generated during fluoroscopy and each of the digital spot radiographs was summed, to give the total heat load for an examination. Without any copper filtration, the exposure factors for a 24 cm Perspex phantom were 89 kVp and 2.9 mA for fluoroscopy, and 88 kVp and 14 mAs for each digital spot image. Thus for two minutes (120 seconds) of fluoroscopy and five digital spot images, the heat generated would be

$$Heat_{U/C,0.0mmCu} = 0.95 \times [89 \times 2.9 \times 120 + 88 \times 14 \times 5] = 35275 \text{ J, or } 35 \text{ kJ.}$$

Equation 8.2

With 0.3 mm copper filtration, the exposure factors were 98 kVp and 2.9 mA for fluoroscopy, and 97 kVp and 14 mAs for each digital spot image. The heat generated during each examination was therefore

$$Heat_{U/C,0.3mmCu} = 0.95 \times [98 \times 2.9 \times 120 + 97 \times 14 \times 5] = 38849 \text{ J, or } 39 \text{ kJ.}$$

Equation 8.3

The heat capacity of the anode was 220 kJ. This was sufficient to absorb all of the heat generated by the four examinations in each session. If the examinations were performed at fifteen-minute intervals, the average rate of heat generation over a session, with the copper filter in place, would be 43 J/s. The maximum anode cooling rate of 450 J/s was more than sufficient to dissipate this heat. The tube heat capacity of 1250 kJ was more than sufficient to absorb all of the heat generated during the full day of twelve examinations, even if there were no significant tube cooling during the day.

The over-couch radiographs were taken at 96 kVp. In the absence of the copper filter, the automatic current-time product for exposure of the 24 cm Perspex phantom was 8 mAs. Thus the heat generated in the tube for the six radiographs in each examination was

$$Heat_{O/C,0.0mmCu} = 0.95 \times 96 \times 8 \times 6 = 4378 \text{ J, or } 4.4 \text{ kJ.}$$

Equation 8.4

With the 0.3 mm copper filter in place, the current-time product increased to 12 mAs. This corresponded to a 50% increase in heat load. The heat generated during all twelve examinations in the daily list would be 79 kJ. This was well below the heat capacity of the anode, which was 230 kJ.

On increasing the Perspex thickness from 24 cm to 30 cm, the tube output increased by up to 80%. As the anode and tube heat capacities were so far in excess of the projected daily heat generation with a 24 cm phantom, neither tube should be at risk of overheating, even if all the patients imaged in a day had equivalent diameters of around 30 cm.

8.3.3 Clinical Validation

Table 8.4 summarises the mean patient equivalent diameter, fluoroscopy time and number of digital spot and screen-film radiographs for the clinical surveys performed at each filter setting. The equivalent diameters were approximately normally

distributed, so 95% confidence intervals were calculated as ± 1.96 standard deviations from the mean. The fluoroscopy times and numbers of digital spot images were log-normally distributed, so 95% confidence intervals were calculated using Cox's method (Zhou & Gao, 1997). For each quantity, the confidence intervals overlapped for all three branches of the study.

Copper	Patient Equivalent Diameter (cm)	Fluoroscopy Time (min)	Number of Digital Spot Images	Number of Screen-Film Radiographs
0.0 mm	22.9 (19.5-26.3)	1.8 (1.6-2.0)	4.6 (4.4-4.9)	6.0
0.1 mm	23.3 (19.0-27.5)	1.7 (1.6-1.8)	4.9 (4.7-5.0)	6.1
0.3 mm	22.4 (18.1-26.7)	1.8 (1.3-2.1)	5.2 (4.5-5.9)	6.0

Table 8.4: Mean patient equivalent diameter, fluoroscopy time, number of digital spot and screen-film radiographs for the clinical studies at each filter setting. The ranges in brackets indicate 95% confidence intervals on the means.

Table 8.5 shows the mean patient DAP for each filter setting, together with the percentage reduction in DAP relative to the baseline survey. The 95% confidence intervals were calculated using Cox's method (Zhou & Gao, 1997).

Copper	Mean Patient DAP (Gycm²)	Reduction in DAP (%)
0.0 mm	17.7 (15.6-20.3)	--
0.1 mm	11.2 (10.6-11.7)	37
0.3 mm	8.0 (6.2-10.1)	55

Table 8.5: Mean patient DAP for each filter, and percentage reduction in DAP. The ranges in brackets indicate 95% confidence intervals, calculated using Cox's method.

In the visual grading analysis study, the majority of examinations in each filtration group were allocated some scores of less than three. Reasons suggested by the radiologist included patient obesity, retained fluid, poor distension of the bowel, overlying structures, and inappropriate printer settings for digital spot views. Since such a high proportion of examinations were affected, it was impractical to eliminate them from the study. Instead, it was assumed that such factors would contribute approximately equally to each arm of the study.

The Kruskal-Wallis statistic for each region of the bowel, and the associated probability of the three samples coming from identical populations, are shown in Table 8.6. Since the probability was in excess of 0.05 for each region, the null hypothesis of no significant difference between the populations could not be rejected.

Image Type	Region	Kruskal-Wallis Statistic	Probability
Digital Spot	Sigmoid colon	3.151	.207
	Splenic flexure	4.548	.103
	Hepatic flexure	0.224	.894
Screen-Film	Left colon	0.440	.803
	Right colon	1.438	.487
	Transverse colon	0.201	.905

Table 8.6: Kruskal-Wallis test statistic and associated probability, for each region of the colon.

Neither the Wilcoxon-Mann-Whitney nor the Kolmogorov-Smirnov tests found any significant difference between the samples obtained with 0.3 mm copper, and without any additional filtration.

All examinations but one were classified as ‘diagnostic’. The remaining one, which was performed using 0.1 mm copper filtration, was classified as ‘indeterminate’ due to poor distension of the colon.

8.3.4 Effective Doses

The estimated effective dose for each filter is shown in Table 8.7, along with the corresponding percentage dose reduction.

Copper	Effective Dose (mSv)	Reduction in Effective Dose (%)
0.0 mm	3.0	--
0.1 mm	2.9	5
0.3 mm	2.7	11

Table 8.7: Effective dose for each filter, and percentage reduction in effective dose.

8.4 Discussion

8.4.1 Phantom Measurements

Entrance doses and dose rates to the Perspex phantoms decreased with increasing copper thickness, across the full range of copper filters investigated. Each additional 0.1 mm reduced the phantom entrance dose by a smaller amount than the last. This was partly due to the beam hardening effect of the copper itself, since an X-ray beam that has already had many of its low energy photons removed is less strongly affected by an additional layer of filter material. It was also partly due to the increase in X-ray tube potential as more filtration was added, since this again results in a more penetrating X-ray beam.

The fluoroscopic tube potential increased steadily with increasing copper thickness. Although it did not reach its maximum value for a 24 cm phantom, saturation of both tube potential and current did occur for thicker phantoms. This resulted in reduced dose rates to the image intensifier, since the X-ray unit could no longer compensate for the increased attenuation. Once saturation had occurred, there was a measurable reduction in low contrast detectability when further attenuation was added. This proved to be the limiting factor in determining how much copper could be used.

The contrast detail tests were performed using Perspex phantoms, in order to determine the effect of the copper filters for a range of patient equivalent diameters. It was not possible to determine absolute contrast values, since the Leeds test object manual (Cowen *et al*, 1992) only gave calibrated contrasts for X-ray beams attenuated with copper. The total number of details visible gave a simple index for comparing detection efficiency under the various exposure conditions, but offered no indication as to the sizes of details that could or could not be seen.

The 0.3 mm copper filter was selected, since it seemed to provide the most appropriate balance between the benefit of dose reduction, and the risk of compromising image quality. The phantom measurements predicted that this would reduce DAP by around 56% relative to the standard filtration of 2.5 mm aluminium. The contrast detail study suggested that there may be an adverse affect on fluoroscopic images of patients with equivalent diameters of 27 cm and above, i.e. around 5% of patients. However, a number of other factors were also taken into account, and these are outlined in the following paragraphs.

Those projections involving a long X-ray path through the patient (lateral and oblique views) would be most readily affected by factor saturation. However, the majority of clinical exposures were anteroposterior (AP) or posteroanterior (PA) projections, for which the ray path was shorter than the patient equivalent diameter. This meant that overall, saturation was likely to occur less frequently than predicted by the phantom measurements.

The phantom study concentrated on the smaller, 10-inch field size, for which the exposure factors saturated more readily. The larger, 14-inch field was used for most of the clinical under-couch views. So again, phantom measurements would tend to overestimate the incidence of saturation.

The clinical diagnoses were based mainly on the radiographs (both screen-film and digital spot). These should not suffer any reduction in detector dose, since the automatic exposure control devices terminated the exposure only after the required number of photons had arrived at the detector. There was however a danger of increased motion unsharpness, due to extended exposure times.

The decision to implement 0.3 mm copper clinically was supported by the fact that both Hansson *et al* (1997) and Pärtan *et al* (2000) had compared barium enema

images taken with and without a 0.3 mm copper filter, and neither had found any visual difference in image quality.

8.4.2 Tube Loading

The introduction of 0.3 mm copper filtration was estimated to increase the under-couch X-ray tube loading by 10%, and the over-couch tube loading by 50%. The anode and tube heat capacities and cooling rates were sufficient to prevent either tube from overheating, when used with the local examination schedule. However, the effect on tube lifetime was unknown.

8.4.3 Clinical Validation

On increasing the thickness of the copper filter to 0.3 mm, the mean patient DAP was reduced to 8.0 Gy cm^2 . This compared favourably with all of the studies listed in Table 7.1. The new mean DAP was 55% lower than that measured in the baseline survey, in close agreement with the predicted DAP reduction of 56% and the figures of 55% at 70 kVp and 59% at 100 kVp quoted by Pärtan *et al* (2000).

The differences in mean patient DAP for the three filter settings were statistically significant, since there was no overlap in the 95% confidence intervals for any two filter combinations. There was no significant difference in fluoroscopy time, number of digital spot images or patient equivalent diameter, so that the reduction in dose may be attributed almost entirely to the increase in filtration.

The Kruskal-Wallis test found no significant difference in image scores, for any of the three filter settings. Since the significance level was set at 5%, there was a 5% probability that the samples were in fact significantly different, and that this was not picked up by the test. However, neither the Wilcoxon-Mann-Whitney nor the Kolmogorov-Smirnov test found any significant difference between the samples with most and least filtration, confirming that there was no measurable difference in the appearance of the images.

All examinations were classified as ‘diagnostic’, except for one in the 0.1 mm copper group. This one was rated ‘indeterminate’, due to poor gaseous distension rather than poor image quality. These results indicated that there was no difference in the

radiologist's confidence to make a diagnosis, on introducing up to 0.3 mm copper filtration.

Again, none of the other operators performing barium enema examinations reported any problems with clinical image quality. Following the satisfactory outcome of the clinical validation, 0.3 mm copper filtration was implemented in routine clinical practice.

8.4.4 Image Quality Considerations

In this study, image scoring was based on perceived barium coating. This index was far from ideal, because it was difficult, if not impossible, to distinguish differences in imaging performance from actual differences in barium coating efficiency. However, it was the only parameter the GI consultant radiologist felt he could score with sufficient confidence. The reliability of the visual grading analysis scores could have been improved by recruiting additional experienced observers. Unfortunately, this was not possible within the time limits of the study, due to the high pressure of clinical workload in the radiology department. However, the use of only a single observer was a major weakness of the study.

A number of the images in each filtration group showed poor perceived coating, which the consultant radiologist attributed to technical factors such as incomplete bowel preparation, inadequate inflation, or poor patient positioning. He also noted that large patients appeared to have poorer coating in the right colon, but that this was probably real, and not an effect of contrast loss. Ideally, technically flawed examinations should be excluded from the study, but this was impractical since so many of the examinations were affected. Instead, it was assumed that these technical factors would contribute approximately equally to each branch of the study.

Most visual grading analysis studies for barium enema examinations have used a five-point scoring scale, which has slightly increased sensitivity compared to the four-point system used in the present study (Smiddy *et al*, 1996; Persliden *et al*, 1997; Hansson *et al*, 1997; Pärtan *et al*, 2000).

The key image quality issue is whether the images enable accurate diagnosis. Whilst visual grading analysis is a sensitive method for identifying changes in image quality,

it gives no indication as to diagnostic adequacy. This study took the same approach as Persliden *et al* (1997), asking the observer whether or not the images were adequate for diagnosis. However, a subjective assessment of diagnostic adequacy is based only on what the observer sees. The image may contain important information that the observer cannot perceive and which, if visible, would alter the diagnosis.

The possibility of performing a clinical outcomes audit was considered. However, it was decided that it would be impractical to perform a study large enough to achieve statistical significance.

8.4.5 Effective Doses

The estimated effective dose for a barium enema examination with no additional filtration was 3.0 mSv. This was comparable with the value of 3.5 mSv estimated by Martin (2004), using the same dosimetry software.

On introducing 0.3 mm copper, the effective dose was reduced by 11%. Although less dramatic than the reduction in DAP, this was still worthwhile in terms of radiation protection, because effective dose is directly related to cancer risk.

8.5 Summary

This chapter addressed the question of how much copper filtration should be used, to optimise the balance between dose and image quality for barium enema examinations.

Measurements using Perspex phantoms predicted a sequentially smaller dose reduction, for each 0.1 mm copper added. On imaging phantoms representing the largest patients, the fluoroscopic exposure factors saturated. This resulted in a reduced dose rate at the detector, and a corresponding reduction in low contrast detectability. Saturation occurred more readily as the quantity of filtration increased.

The copper thickness chosen for clinical implementation was 0.3 mm. Although this had been recommended by two published studies, one on adult and the other on paediatric patients, its use had not been reported within the UK. The mean patient

DAP was reduced to 8.0 Gy cm^2 . This was a reduction of 55%, compared to the baseline survey. The corresponding reduction in effective dose was 11%.

Clinical radiographs obtained using each of the three filter settings (0.0, 0.1 and 0.3 mm copper) were graded according to perceived barium coating, by a GI consultant radiologist. The Kruskal-Wallis test found no significant difference between the image scores for the three groups. In addition, the Wilcoxon-Mann-Whitney and Kolmogorov-Smirnov tests found no significant difference between the two groups using the most and least filtration. The radiologist graded all examinations but one as diagnostic, and this exception he attributed to poor distension of the colon rather than poor image quality.

The introduction of 0.3 mm copper was estimated to increase the X-ray tube loading by 10% for under-couch and 50% for over-couch exposures. This should not put either tube at risk of overheating, with the examination schedule employed locally.

Following the success of the clinical validation, 0.3 mm copper filtration was introduced into routine clinical practice.

Chapter 9 - General Discussion

9.1 Introduction

This chapter summarises the research described in the thesis. The key findings are highlighted, and the main strengths and weaknesses discussed. The findings led to a number of new research questions, and the main avenues of future work are outlined here.

The introductory chapters demonstrated the importance of patient dosimetry and optimisation in high dose fluoroscopic and fluorographic procedures. Both are legal requirements under European Union Directive 97/43/Euratom (The Council of the European Union, 1997), and the two are closely related. Patient dosimetry can help to highlight those procedures that are not optimised, and to identify areas where there is potential for improvement. An important part of the optimisation process is to assess the effects of changes in imaging practice on patient radiation dose, as well as ensuring that image quality remains adequate for its clinical purpose.

In the barium enema study, patient doses were measured using an established technique, and steps were then taken to optimise local imaging practice. In the cardiology study, it was necessary first to develop a suitable technique for patient skin dosimetry, which could then be used to inform the optimisation process. The cardiology part of the thesis concentrates on this topic.

9.2 Cardiology: Film Dosimetry

9.2.1 Research Summary

The most promising skin dosimeter identified by the literature review was Kodak EDR2 film. This was first characterised in detail, across the range of likely exposure and processing conditions. Its calibration curve was described using a novel equation, and variations in film response with changes in exposure and processing conditions were quantified. The film was then used to measure skin dose distributions for a sample of patients undergoing coronary angiography or angioplasty, and the peak skin dose was determined for each patient. The possibility of predicting peak skin dose from a combination of dose-area-product (DAP) and procedural ‘complexity indicators’ was investigated.

The film was found to saturate at around 1 Gy, under local processing conditions. This was somewhat lower than the saturation point of up to 1.5 Gy reported by Guibelalde *et al* (2003) and Vanõ *et al* (2003), who extended the film’s useful range using a dedicated processor with carefully controlled processing conditions.

The new equation used to describe the film response curve gave a better fit to the measured data than any reported in the literature. Film response was fairly consistent with variations in X-ray tube potential, exposure rate, field size, film batch, and day-to-day fluctuations in processor performance. However, it was found to be strongly dependent on the quantity of beam filtration. This aspect of film performance had not previously been studied. It is however an important consideration in the cardiac catheterization laboratory, where heavily filtered beams are often used in some imaging modes.

It took some minutes for the emulsion to stabilise, following exposure. This effect was subsequently reported by Childress & Rosen (2004).

The overall uncertainty in the film’s response was estimated to be -30 to $+61$ mGy, at 160 mGy. This uncertainty increased with dose, and was assumed to vary linearly with the gradient of the calibration curve, making it around -280 to $+570$ mGy at 1 Gy.

For coronary angiography, all measured skin doses were well below 1 Gy. For coronary angioplasty, approximately a quarter of the films showed localised areas of saturation, indicating that those patients had received skin doses of about 1 Gy or more. This was in line with previous studies using thermoluminescence dosimeters or scintillation detectors, which all found some doses approaching or exceeding 1 Gy (Hwang *et al*, 1998; Verdun *et al*, 1998; van de Putte *et al*, 2000; Waite & Fitzgerald, 2001).

Mean dose-area-products were 26 Gy cm^2 for coronary angiography, and 57 Gy cm^2 for coronary angioplasty. Both fell below the centre of the range of published values. It seems likely that those facilities operating at higher mean DAPs than those reported here will also have a higher incidence of skin doses exceeding 1 Gy.

DAP was found to be an unreliable predictor of high skin doses. Prediction accuracy was improved by combining DAP with the number of lesions treated. However, dosimetry methods based on DAP cannot identify the location of the peak dose on the patient's skin.

9.2.2 Implications and Limitations

Since the film saturated at 1 Gy, it was an inadequate dosimeter for coronary angioplasty, where doses of at least 1 Gy occurred frequently. Although Guibelalde *et al* (2003) and Vanđ *et al* (2003) were able to increase the film's saturation point by up to 50% compared to that reported here, it would still be inadequate for assessing doses of 2 Gy or more, i.e. those that may result in deterministic effects.

In order to comply with the recommendations of the Food and Drug Administration (1995) and the International Commission on Radiological Protection (2000), a method for skin dosimetry was required that could assess skin doses above the 1 Gy saturation point of the film, and indicate the locations of any high dose regions on the patient's skin. This was achieved by means of dose modelling software. Alternative approaches include specialist 'Gafchromic' dosimetry films, or the extended dose range computed radiography plates that are now available for radiotherapy verification imaging.

A further limitation of the film dosimetry study was that only those radiation fields passing through the film were captured. If the peak skin dose occurred on the patient's side, it would go undetected.

9.3 Cardiology: Skin Dose Modelling

9.3.1 Research Summary

A mathematical model was then developed, to calculate the dose distribution in the plane of the couch top, from the exposure and projection data stored in the image files. Software was designed to extract the relevant data from the image files, perform the necessary calculations and generate a dose map for each patient. Since no data were available for fluoroscopic exposures, three methods for including an estimated contribution from fluoroscopy were explored. Each required total DAP or fluoroscopy time as an additional input parameter.

Dose maps were generated for all of the procedures included in the film dosimetry study. For those films that showed no saturation, peak skin doses calculated using each version of the software agreed with measured values to within about 270 mGy. The simplest version of the software ignored the contribution from fluoroscopy. As a result, it grossly underestimated the dose to one patient, whose film showed areas of saturation following a procedure that involved a long fluoroscopy time, with few imaging projections. Each of the fluoroscopy correction methods improved the model's reliability in predicting skin doses of 1 Gy or more.

9.3.2 Implications and Limitations

Skin dose modelling proved to be a practical dosimetry method for cardiac catheterization procedures. Since it used the exposure and projection data stored in the image files, a skin dose map could be generated retrospectively for any patient. There was no upper limit on the doses that could be calculated, and no additional workload for clinical staff. The resulting dose map provided a convenient record of both the magnitude and the approximate location of the peak skin dose on the patient's back.

Although two groups had previously developed skin dosimetry software (den Boer *et al*, 2001; Chugh *et al*, 2004), none was available commercially at the time of the study. This thesis presents the mathematical workings of a skin dose model for the first time.

The main limitations of the software arose from the lack of information regarding fluoroscopic exposures, couch position and beam limitation. Whilst it was possible to estimate the fluoroscopic contribution to the dose map, the accuracy of this estimate could vary considerably for individual procedures. It was necessary to assume that the couch position was fixed, and that the secondary collimators and equalisation filter were not used. These assumptions did not reflect clinical practice. Improvement of dosimetric accuracy is dependent upon manufacturers developing facilities for recording and accessing the above information.

As with film dosimetry, the model only considered the dose distribution in a single plane. It could be improved by modelling the patient's thorax in three dimensions. However, this would require couch positioning data, to achieve a worthwhile degree of accuracy.

The most efficient way to make dose calculation software widely available to the cardiology community would be for manufacturers to incorporate it on their imaging units. However, given the apparent commercial failure of Siemens' 'Caregraph' software, manufacturers are unlikely to consider this worth their while unless the standards bodies insist on it.

9.4 Barium Enema Optimisation

9.4.1 Research Summary

A baseline survey of local barium enema practice was carried out, and the results compared with a review of the literature. The mean DAP of 17.7 Gy cm^2 was lower than that found in most published studies. However, some investigators had successfully employed dose reduction techniques, which were then considered for local implementation.

It was decided to introduce copper filtration, since this should allow routine dose reduction for all patients, without any change to the standardised imaging protocol. The effects on DAP and image quality of a small amount of copper (0.1 mm) were first predicted using Perspex phantoms and a contrast detail test object. There was no measurable difference in threshold contrast. The filter was then introduced in the clinical environment, and the dose survey repeated. Mean patient DAP was reduced by 37%. None of the operators performing the examinations reported any difference in the appearance of the clinical images.

An investigation was then conducted to determine the optimal quantity of copper filtration for adult barium enema examinations. A series of phantom measurements demonstrated the effects of increasing copper thickness on both dose and fluoroscopic image quality. For phantoms representing the larger patients, increases in filtration caused the X-ray tube potential and current to saturate, leading to a reduction in contrast detail visibility. A filter thickness of 0.3 mm copper was chosen, as it seemed to give the most appropriate balance between the benefits of dose reduction and the risk of compromising fluoroscopic image quality. Only two published studies had employed such thick copper filters for barium enema examinations; one on adult patients (Pärtan *et al*, 2000), one on paediatrics (Hansson *et al*, 1997), and both outside the United Kingdom.

The filter was then introduced in clinical practice, and the dose survey repeated. Clinical image series performed using each of the three filter settings were allocated scores for perceived barium coating efficiency by a gastrointestinal (GI) consultant radiologist. Scores for each region of the bowel were compared using Kruskal-Wallis analysis of variance by ranks, and no significant differences were found. In order to confirm this result, the scores for images obtained with the most and least filtration were also compared using Wilcoxon-Mann-Whitney and Kolmogorov-Smirnov tests, neither of which found any significant difference. The GI consultant radiologist rated all of the examinations as diagnostic, except for one in the 0.1 mm copper filtration group, which was rated 'indeterminate', due to poor gaseous distension of the colon. These results indicated that there was no perceptible difference in the visual appearance of the images, and that the introduction of the 0.3 mm copper filter did not affect the radiologist's confidence in making diagnoses.

Mean patient DAP was reduced by 55%, relative to the baseline survey. This agreed with the phantom measurements and with the findings of Pärtan *et al* (2000). The corresponding reduction in effective dose was approximately 11%.

The introduction of 0.3 mm copper increased the under-couch tube loading by about 10%, and the over-couch tube loading by about 50%. With the local examination schedule, this did not put either X-ray tube at risk of overheating.

9.4.2 Implications and Limitations

The optimisation strategy employed here has laid a strong foundation for future work. The baseline survey and comparison with published data provided a sound starting point for identifying potential dose reduction techniques. Experiments using Perspex phantoms were shown to give a realistic indication of the effects of changes in imaging technique on patient dose. Measurements of technical image quality enabled informed decisions about changes to clinical practice. These decisions were then backed up by verifying their effects on patient dose and clinical image quality.

Copper filtration of up to 0.3 mm in thickness was shown to be a practical and effective means of dose reduction in barium enema imaging. The present study adds support to the limited existing evidence for this. Copper filters are now built into many new X-ray units, and their availability should be considered when specifying and purchasing new imaging equipment.

The reliability of clinical image scoring was limited by the use of a single observer. Reproducibility can be improved considerably by employing multiple observers, and this should be done for future studies. Perceived barium coating efficiency was by no means an ideal index for assessing clinical image quality, since it was impossible to distinguish genuine poor coating from poor imaging performance. Other investigators have scored images against individual aspects of image quality (noise, contrast and sharpness), as well as the observer's overall impression (Smiddy *et al*, 1996; Persliden *et al*, 1997; Pärtan *et al*, 2000). However, their scores could equally be affected by poor technical performance of the examination.

Although the phantom experiments provided quantitative information about dose and technical aspects of image quality, a subjective judgement still had to be made

regarding the most appropriate quantity of filtration. It could be argued that 0.4 mm copper may actually have been optimal, but the incremental benefits of dose reduction diminish as the filter thickness is increased, and the thicker filter would be more likely to have an adverse effect on clinical image quality.

The study considered a number of dose reduction techniques, but only one was implemented. The intricate relationship between dose and image quality depends on many factors, all of which should be considered if the imaging technique is to be truly optimised. This is a very complex task, and small, individual steps such as those described in this study offer the most practical approach.

9.5 Proposals for Further Work

9.5.1 Improvements to Skin Dosimetry Software

A number of modifications are required, to improve the performance of the skin dosimetry software in preparation for routine clinical use.

At present, it is only capable of calculating dose maps for one particular imaging unit. It is intended that it will be used to calculate doses from at least three catheterization laboratories. To do this, it will need to identify which imaging unit was used, and apply appropriate geometry and standard dose rates for that unit. Since individual imaging units store exposure and projection data in different formats, and sometimes in different fields, customised functions are needed to convert it into a standard format that the dose model can use.

The existing versions of the software assume that X-ray tube output is proportional to the square of the tube potential. Increasingly, a number of imaging modes are available that use different amounts of beam filtration. This strongly affects the relationship between tube potential and output. The software needs to recognise which filter was in place for each acquisition run, and apply an appropriate kV_p /dose relationship.

Subsequent to this study, it was found that 'SID' (focal spot to detector distance) was sometimes stored as '-1'. Discussions with the service engineers indicated that this

was an error code, used when the detector had been moved during the acquisition run. The software needs to substitute these error codes with either a typical, fixed value, or an interpolation of neighbouring SID values.

At the time of writing, the software had to be run manually for each procedure. The corrections for fluoroscopic exposures relied upon manual input of DAP or fluoroscopy time stored in a separate database. This inevitably led to problems with erroneous or missing data. It is hoped that in the near future, summary dose information including DAP and fluoroscopy time will be automatically sent to and stored on the image server. This should allow the dose model to be completely automated – to extract all of the relevant data from the image files as each procedure is completed, to calculate the skin dose distribution, and produce a printed report if the peak skin dose exceeds 1 Gy.

Those investigators who employed real-time dose mapping in the cardiac catheterization laboratory found it to be an effective tool for avoiding high skin doses (den Boer *et al*, 2001; Fletcher *et al*, 2002; Miller *et al*, 2002). Since the operators could see how the cumulative dose was distributed across the patient's skin, they could often modify their projections, to ensure that dose thresholds for deterministic effects were not exceeded. However, such systems require dedicated computing and display facilities in each catheterization laboratory. Unfortunately the necessary resources are not currently available at Nottingham City Hospital, but real-time dose mapping is something that could be considered for the future.

9.5.2 Patient Counselling and Aftercare

Having developed a method for assessing skin dose, the next stage is to consider how that information may be used to provide appropriate counselling and aftercare for any patients who may be at risk of skin injuries. A survey will first be conducted, to determine the incidence of skin injuries following cardiac catheterization procedures. Patients whose peak skin doses exceed 2 Gy will be inspected for evidence of skin erythema before leaving the hospital. Each will be given information about potential skin effects, with instructions to contact the department should any symptoms appear. Patients thought to have received localised doses of more than 3 Gy will be offered a

follow-up inspection after 2 weeks, in accordance with ICRP Report 85 (International Commission on Radiological Protection, 2000).

If no skin injuries are seen over, say, a three month period, then it would seem reasonable to assume that the risks are negligible. If any evidence of skin injuries is seen, then protocols should be developed for providing risk information to patients as part of the consenting procedure, and for identifying and offering appropriate counselling and follow-up to those patients who may be at risk. This will require close collaboration with clinical staff. The project will also require backup from the dermatology department, since any evidence of skin injuries may necessitate referral to a dermatologist.

Another important issue is the monitoring of patients who undergo multiple cardiac catheterization procedures, since it is thought that repeat exposures can result in cumulative effects. Consideration should be given to developing a system for identifying these patients and assessing their cumulative skin doses.

9.5.3 Optimisation in the Cardiac Catheterization Laboratory

The skin dosimetry work reported in this thesis has shown that many patients undergoing cardiac catheterization procedures are subjected to relatively high skin doses of 1 Gy or more. This underlines the need for optimisation programmes in the cardiac catheterization laboratory.

In seeking to optimise radiographic practice, there are many different factors that must be considered. These include X-ray tube potential and current, beam filtration, pulse width, frame rate, detector dose rates and the use of anti-scatter grids. Additional beam filtration will be of particular interest, since this is such an effective method of reducing the dose to the patient's skin. In addition, there is a vast array of parameters in the image processing and display software, which affect the appearance of the images. These govern functions such as noise reduction and edge enhancement, temporal filtering and display lookup tables. It may be that some of these parameters can be adjusted to compensate for changes in imaging conditions. Since these processes are highly complex, it will be necessary to work closely with the equipment manufacturers, to ensure that images are always displayed to their best advantage.

The task of determining a fully optimised imaging protocol is enormous, since there are so many options to be explored, and many are interdependent. The most practical approach is to introduce successive small changes, and to assess the effects of each on dose and image quality. At each stage of the process, the effects of proposed changes will be predicted using Perspex phantoms, and image quality test objects designed to simulate iodine-filled blood vessels. The most promising options will then be trialled in the clinical setting, with close attention being paid to patient doses and clinical image quality.

Another important issue in cardiology is the toxicity of the contrast agents used (McCullough *et al*, 1997; Baker & Baker, 2001; Lindholt, 2003). If imaging performance can be improved, it may be possible to reduce the volume or concentration of the contrast medium, which would in turn reduce the incidence of adverse reactions such as nephropathy.

A recent innovation that is expected to have a considerable impact on catheterization laboratory practice is rotational angiography. Here, the X-ray tube and detector rotate around the patient during digital acquisition, so that many views are obtained for each contrast injection. This has potential to reduce the quantity of contrast media required, and may also have a beneficial effect on skin doses (Raman *et al*, 2004). Again, further study will be required to determine the best way to use this new technology in clinical practice.

9.5.4 Defining Image Quality Criteria

Perhaps the greatest challenge for optimisation is that of determining whether or not image quality is adequate for the clinical task. Outcomes audits are the most reliable method for doing this, but are slow and cumbersome. Visual grading analysis only allows the observer to assess whether the images look acceptable, or to compare them with a set of reference images. It cannot confirm whether all of the clinically important information contained in the image is visible to the observer.

One possible solution would be a scoring system based on image quality criteria. Whilst the quality criteria developed so far have attempted to define the degree of visualisation required for various anatomical structures, the definitions were very much open to observer interpretation. A set of quality criteria that described in an

exact and reproducible manner how well the clinician or radiographer needed to see certain structures, when viewing a certain type of image, for a specified clinical purpose, would be an invaluable optimisation tool. It could be based on verbal description, or on measurable quantities such as contrast and noise in specified regions of the image.

The author is currently developing two pilot scoring systems, which will shortly be trialled for their usability, observer agreement and repeatability. One is a descriptive system based on an expanded version of the standard scoring method for the Leeds TOR(MAM) test object (Leeds Test Objects Limited, Boroughbridge, UK). The second is a system of visual score cards showing simulated vessels at various noise and contrast levels. The observer would select the one that most closely matched particular regions of the clinical image. It is hoped that this may improve reproducibility, by removing the verbal interpretation element from image quality assessment. The response of clinical observers to this system may indicate whether objective measures such as noise and contrast could be used to assess image adequacy for a particular clinical task.

Appendix I: Matlab Scripts

This appendix presents the Matlab scripts used to implement the dose model described in Chapter 6. The first script, ‘GetRunData.m’, extracted the exposure and projection data from the image files. This process was identical, regardless of which version of the dose model was being used.

The second script, ‘RunModel.m’, calculated and displayed the dose map. The non-highlighted text is the computational code for Version 1 (Acquisition Only). The other versions of the software required some additional commands. These are highlighted in yellow for Version 2 (Fluoro Correction via DAP), blue for Version 3 (Fluoro Correction via Fluoroscopy Time) and pink for version 4 (Fluoro Correction via Concentration Factor).

GetRunData.m

```
% Extract procedure identifiers and run data from DICOM headers of all image files,  
% for any single procedure done on Integris H5000F.  
  
% Ask the user to browse for the directory they wish to use, and change to this  
% directory.  
% Pull all the filenames for non-bitmap files out of that directory.  
% Count the files.  
% Clear the structures to which all data will be added.  
  
starting_directory = pwd;  
directory_name = uigetdir('Z:\','Please select the directory for the required...  
examination.');
```

```
cd (directory_name);  
files = dir('*.');  
numberfiles = length(files);  
clear ExamInfo;  
clear RunInfo;  
  
% Add procedure identifiers from first image file to "ExamInfo" structure.  
% Ignore the first two files (“.” and “..”).  
% Patient's and physician's name are stored in structures. Pull out
```

```

% the 'FamilyName' field from the structure.

info = dicominfo(files(3).name, 'dictionary', 'C:\Matlab701 local...
                                patches\toolbox\images\images\dicom-dict.txt');

ExamInfo.Directory = directory_name;
ExamInfo.ExamDate = info.StudyDate;
ExamInfo.PatientName = info.PatientName.FamilyName;
ExamInfo.Procedure = info.PatientID;
ExamInfo.Sex = info.PatientSex;
ExamInfo.BirthDate = info.PatientBirthDate;
ExamInfo.Cardiologist = info.PerformingPhysicianName.FamilyName;

% Trawl through all image files in the directory, extracting selected DICOM
% header info and adding to "RunInfo". Ignore the first two files (".", "..").

j=0;
for i = 3:numberfiles
    info = dicominfo(files(i).name, 'dictionary', 'C:\Matlab701 local...
                                patches\toolbox\images\images\dicom-dict.txt');

    % If info.KVP is a field, add run info to RunInfo structure.
    % Otherwise, go to the next iteration (avoids photo-files, which don't contain this
    % info).

    if isfield(info, 'KVP')
        j=j+1;
        RunInfo(j).KVP = info.KVP;
        RunInfo(j).ExposureTime = info.ExposureTime;
        RunInfo(j).Current = info.XrayTubeCurrent;
        RunInfo(j).PrimaryAngle = info.PositionerPrimaryAngle;
        RunInfo(j).SecondaryAngle = info.PositionerSecondaryAngle;
        RunInfo(j).Frames = info.NumberOfFrames;
        RunInfo(j).Run = info.InstanceNumber;
        RunInfo(j).Protocol = info.ProtocolName;
        RunInfo(j).FieldSize = num2str(info.IntensifierSize);
        RunInfo(j).SID = info.DistanceSourceToDetector;
    end
end

% Return to original directory.

cd(starting_directory);

```

RunModel.m

```
% Calculate a skin dose map looking at the patient's back, using run data
% from RunInfo structure array.

% Create a blank totaldose array.

totaldose = zeros(401,601);
DAPacq = 0;

% Define position of gantry centre, and distance from this to focal spot.
% Define couch height.
% Define normalized entrance dose rate for phantom measurements.

centreheight = 107;
radius = 77.5;
couchheight = 87;
ESDRphantom = 5.97e-5;
displayedDAP = input('Displayed DAP (Gycm^2) = ');
screentime = input('Screening Time (min) = ');
fluororate = 40;

% Define the plane of the couch top.
% Allow 30cm either side of centre in left-right direction.
% Allow 20cm either side of centre in cranio-caudal direction.

for i = 1:401
    for j = 1:601
        xfilm(i,j) = j/10-30.1;
        yfilm(i,j) = 20.1-i/10;
    end
end

% Find out how many elements are in each field of RunInfo structure array.

runs = size(RunInfo,2);

% For each projection, read the angulation information from the RunInfo structure
% array and then calculate doses.

for n = 1:runs

    Ang1 = RunInfo(n).PrimaryAngle*pi/180;
    Ang2 = RunInfo(n).SecondaryAngle*pi/180;

% Calculate focal spot position, in cartesian coordinates.

    xspot = radius * sin(Ang1) * cos(Ang2);
```

```

yspot = -radius * sin(Ang2);
zspot = centreheight - radius * cos(Ang1) * cos(Ang2);

% Calculate distance from focal spot to each point on film, using
% element-by-element multiplication.
% Calculate dose to each point on the film.

ffd = ((xfilm-xspot).^2 + (yfilm-yspot).^2 + (couchheight-zspot)^2).^(.5);
dose = ESDRphantom * ffd.^(-2) * (RunInfo(n).KVP)^2 * RunInfo(n).Current * ...
      RunInfo(n).ExposureTime * RunInfo(n).Frames;
dose = dose + fluororate * screentime / runs;

% Calculate parameters for collimation.
% Start by reading the SID, and calculating theta and SIDcoll appropriate
% to the field size.

SID = RunInfo(n).SID/10;
fieldsize = str2num(RunInfo(n).FieldSize)/10;
theta = atan(fieldsize/(2*SID));
SIDcoll = sqrt(SID^2+2*(fieldsize/2)^2);
DAP = ESDRphantom/1000/1.3 * (RunInfo(n).KVP)^2 * RunInfo(n).Current * ...
      RunInfo(n).ExposureTime * RunInfo(n).Frames * (fieldsize/SID)^2;

% Calculate positions of field corners, on the detector entrance surface.

ycollmax = yspot + SIDcoll * sin(Ang2+theta);
ycollmin = yspot + SIDcoll * sin(Ang2-theta);

xcoll1 = xspot - SIDcoll * sin(Ang1+theta) * cos(Ang2-theta);
xcoll2 = xspot - SIDcoll * sin(Ang1+theta) * cos(Ang2+theta);
xcoll3 = xspot - SIDcoll * sin(Ang1-theta) * cos(Ang2+theta);
xcoll4 = xspot - SIDcoll * sin(Ang1-theta) * cos(Ang2-theta);

zcoll1 = zspot + SIDcoll * cos(Ang1+theta) * cos(Ang2-theta);
zcoll2 = zspot + SIDcoll * cos(Ang1+theta) * cos(Ang2+theta);
zcoll3 = zspot + SIDcoll * cos(Ang1-theta) * cos(Ang2+theta);
zcoll4 = zspot + SIDcoll * cos(Ang1-theta) * cos(Ang2-theta);

% Calculate positions of field corners, on couch.

x1 = (couchheight-zspot) * (xcoll1-xspot) / (zcoll1-zspot) + xspot;
x2 = (couchheight-zspot) * (xcoll2-xspot) / (zcoll2-zspot) + xspot;
x3 = (couchheight-zspot) * (xcoll3-xspot) / (zcoll3-zspot) + xspot;
x4 = (couchheight-zspot) * (xcoll4-xspot) / (zcoll4-zspot) + xspot;

y1 = (couchheight-zspot) * (ycollmin-yspot) / (zcoll1-zspot) + yspot;
y2 = (couchheight-zspot) * (ycollmax-yspot) / (zcoll2-zspot) + yspot;
y3 = (couchheight-zspot) * (ycollmax-yspot) / (zcoll3-zspot) + yspot;
y4 = (couchheight-zspot) * (ycollmin-yspot) / (zcoll4-zspot) + yspot;

```



```
% Zero all dose elements that are outside the collimated area.
```

```
for i = 1:401
    for j = 1:601
        if xfilm(i,j) < x1
            dose(i,j) = 0;
        elseif yfilm(i,j) > (y3-y2)/(x3-x2) * (xfilm(i,j) - x2) + y2
            dose(i,j) = 0;
        elseif xfilm(i,j) > x4
            dose(i,j) = 0;
        elseif yfilm(i,j) < (y4-y1)/(x4-x1) * (xfilm(i,j) - x1) + y1
            dose(i,j) = 0;
        end
    end
end
```

```
% Add to total dose map, and close loop.
```

```
totaldose = totaldose + dose;
DAPacq = DAPacq + DAP;
```

```
end
```

```
totaldose = totaldose * displayedDAP/DAPacq;
CF = max(max(totaldose))/sum(sum(totaldose))
```

```
% Plot this as a filled contour map.
```

```
maxdose = max(max(totaldose));
contours = 0 : maxdose/15 : maxdose;
dosedisplay = int2str(round(maxdose));
```

```
hold off
contourf(xfilm,yfilm,totaldose,contours)
hold on
contour(xfilm,yfilm,totaldose,contours)
```

```
colormap('hot')
colorbar('vert')
axis equal
axis([-30 30 -20 20])
xlabel('Left <----> Right (cm)')
ylabel('Inferior <----> Superior (cm)')
set(gca,'XTick',[-30 -20 -10 0 10 20 30])
set(gca,'YTick',[-20 -10 0 10 20])
title('Skin Dose (mGy)', 'FontSize', 12)
text(-20,27,[ExamInfo.PatientName, ' ', ExamInfo.ExamDate], 'FontSize', 12)
text(-30,-30,['Max Dose = ', dosedisplay, ' mGy.'], 'FontSize', 12)
```

Appendix II: Journal Articles and Conference Papers

This appendix lists journal articles and conference presentations prepared by the author, and relating to the work described in the thesis.

Journal Articles

Morrell R.E., Rogers A.T., Jobling J.C. and Shakespeare K.E. (2004). Barium Enema: Use of Increased Copper Filtration to Optimise Dose and Image Quality. *British Journal of Radiology* **77**:116-122.

Morrell R.E. and Rogers A. (2004). Calibration of Kodak EDR2 Film for Patient Skin Dose Assessment in Cardiac Catheterization Procedures. *Physics in Medicine and Biology* **49**:5559-5570.

Morrell R.E. and Rogers A.T. (2005). Film Dosimetry for Fluoroscopic Procedures: Potential Errors. *Radiation Protection Dosimetry* **114**:147-149.

Morrell R.E. and Rogers A.T. (2006). Kodak EDR2 Film for Patient Skin Dose Assessment in Cardiac Catheterization Procedures. *British Journal of Radiology* (in press).

A further paper titled “A Mathematical Model for Patient Skin Dose Assessment in Cardiac Catheterization Procedures” is also in preparation.

Conference Presentations

Morrell R., Rogers A., Shakespeare K. and Jobling J. (2001). Dose Reduction for Barium Enema Examinations [Poster]. *UK Radiological Congress*; 21-23 May 2001; London, UK.

Rogers A.T., Morrell R., Shakespeare K. and Jobling J.C. (2001). Optimisation in Barium Enemas: How Much Copper? *European Congress of Medical Physics & Clinical Engineering*; 12-14 September 2001; Belfast, UK.

Jobling J.C., Rogers A., Morrell R. and Shakespeare K. (2002). Optimising Dose for Barium Enemas: How Much Copper? *European Society of Gastrointestinal and Abdominal Radiology*; 14-19 April 2002; Orlando, Florida.

Morrell R.E. and Rogers A.T. (2004). Film Dosimetry for Fluoroscopic Procedures: Potential Errors [Poster]. *Second Malmö Conference on Medical X-Ray Imaging: Optimisation Strategies in Medical X-Ray Imaging*; 23-25 April 2004; Malmö, Sweden.

Morrell R.E. and Rogers A.T. (2004). Calibration of EDR2 Film for Skin Dosimetry in Interventional Cardiology [Poster]. *UK Radiological Congress*; 6-8 June 2004; Manchester, UK.

Morrell R.E. and Rogers A.T. (2005). Film Dosimetry in the Cardiac Catheterisation Laboratory. *UK Radiological Congress*; 6-8 June 2005; Birmingham, UK.

Morrell R.E. and Rogers A.T. (2005). Skin Dose Modelling in the Cardiac Catheterisation Laboratory. *UK Radiological Congress*; 6-8 June 2005; Birmingham, UK. [*Winner of IPPEM President's Prize.*]

References

Almen A., Tingberg A., Mattsson S., Besjakov J., Kheddache S., Lanhede B., Mansson L.G. and Zankl M. (2000). The Influence of Different Technique Factors on Image Quality of Lumbar Spine Radiographs As Evaluated by Established CEC Image Quality Criteria. *British Journal of Radiology* **73**:1192-1199.

Armitage P. (1971). Statistical Methods in Medical Research. Oxford, UK: Blackwell Scientific Publications.

Arthur W.R., Dhawan J., Norell M.S., Hunter A.J. and Clark A.L. (2002). Does Cardiologist- or Radiographer-Operated Fluoroscopy and Image Acquisition Influence Optimization of Patient Radiation Exposure During Routine Coronary Angiography? *British Journal of Radiology* **75**:748-753.

Atkins H.L., Fairchild R.G., Robertson J.S. and Greenberg D. (1975). Effect of Absorption Edge Filters on Diagnostic X-Ray Spectra. *Radiology* **115**:431-437.

Aufrichtig R. (1999). Comparison of Low Contrast Detectability Between a Digital Amorphous Silicon and a Screen-Film Based Imaging System for Thoracic Radiography. *Medical Physics* **26**:1349-1358.

Bailey S.R. (2002). Coronary Restenosis: A Review of Current Insights and Therapies. *Catheterization & Cardiovascular Diagnosis* **55**:265-271.

Bakalyar D.M., Castellani M.D. and Safian R.D. (1997). Radiation Exposure to Patients Undergoing Diagnostic and Interventional Cardiac Catheterization Procedures. *Catheterization & Cardiovascular Diagnosis* **42**:121-125.

Baker C.S.R. and Baker L.R.I. (2001). Prevention of Contrast Nephropathy After Cardiac Catheterisation. *Heart* **85**:361-362.

Baker W.A., Hearne S.E., Spero L.A., Morris K.G., Harrington R.A., Sketch M.H., Behar V.S., Kong Y., Peter R.H., Bashore T.M., Harrison J.K. and Cusma J.T. (1997). Lossy (15:1) JPEG Compression of Digital Coronary Angiograms Does Not Limit Detection of Subtle Morphological Features. *Journal of the American College of Cardiology* **96**:1157-1164.

Bernardi G., Padovani R., Morocutti G., Spedicato L., Giannuleas J.D., Neofotistou E., Maginas A., Goicolea J.C., McNeill J. and Vanõ E. (2001a). A Method Based on DIMOND Quality Criteria to Evaluate Imaging in Diagnostic and Interventional Cardiology. *Radiation Protection Dosimetry* **94**:167-172.

Bernardi G., Padovani R., Morocutti G., Spedicato L., Giannuleas J.D., Neofotistou E., Manginas A., Goicolea J.C., McNeill J., Vanõ E., Marzocchi A., Tsapaki V., Fioretti P.M. and Malone J. (2001b). Quality Criteria for Cardiac Images in Diagnostic and Interventional Cardiology. *British Journal of Radiology* **74**:852-855.

Bernardi G., Padovani R., Morocutti G., Vanõ E., Malisan M.R., Rinuncini M., Spedicato L. and Fioretti P.M. (2000). Clinical and Technical Determinants of the Complexity of Percutaneous Transluminal Coronary Angioplasty Procedures: Analysis in Relation to Radiation Exposure Parameters. *Catheterization & Cardiovascular Interventions* **51**:1-9.

Bland J.M. and Altman D.G. (1999). Measuring Agreement in Method Comparison Studies. *Statistical Methods in Medical Research* **8**:135-160.

Bland J.M. and Altman D.G. (1986). Statistical Methods for Assessing Agreement Between Two Methods of Clinical Measurement. *The Lancet* **1**:307-310.

Blatz H. and Epp E.R. (1961). A Photographic Method of Measuring Fluoroscopic Dose to the Patient. *Radiology* **76**:120-121.

Boone J.M. (1992). Parametrized X-Ray Absorption in Diagnostic Radiology From Monte Carlo Calculations: Implications for X-Ray Detector Design. *Medical Physics* **19**:1467-1473.

Booth A., Crawley M.T. and Shine B. (1998). Radiation Dose and Diagnosticity of Barium Enema Examinations by Radiographers and Radiologists: a Comparative Study [Correspondence (2): Author's Reply]. *British Journal of Radiology* **71**:1219.

Broadhead D.A., Chapple C.L. and Faulkner K. (1995). The Impact of Digital Imaging on Patient Doses During Barium Studies. *British Journal of Radiology* **68**:992-996.

- Broadhead D.A., Chapple C.L., Faulkner K., Davies M.L. and McCallum H. (1997).** The Impact of Cardiology on the Collective Effective Dose in the North of England. *British Journal of Radiology* **70**:492-497.
- Calzado A., Vanõ E., Moran P., Castellote C., Ruiz S. and Gonzalez L. (1991).** Estimation of Doses to Patients From "Complex" Conventional X-Ray Examinations. *British Journal of Radiology* **64**:539-546.
- Carroll E.M. and Brennan P.C. (2003).** Radiation Doses for Barium Enema and Barium Meal Examinations in Ireland: Potential Diagnostic Reference Levels. *British Journal of Radiology* **76**:393-397.
- Chakera T.M.H., Fleay R.F., Henson P.W. and Cole S.M. (1982).** Dose Reduction in Radiology Using Heavy Metal Foils. *British Journal of Radiology* **55**:853-858.
- Chakraborty D.P. and Winter L.H.L. (1990).** Free-Response Methodology: Alternative Analysis and a New Observer-Performance Experiment. *Radiology* **174**:873-881.
- Chakraborty D.P. and Berbaum K.S. (2004).** Jackknife Free-Response ROC Methodology. *Proceedings of SPIE* **5372**:144-153.
- Chapple C.-L., Broadhead D.A. and Faulkner K. (1995).** A Phantom Based Method for Deriving Typical Patient Doses From Measurements of Dose-Area Product on Populations of Patients. *British Journal of Radiology* **68**:1083-1086.
- Childress N.L. and Rosen I.I. (2004).** Effect of Processing Time Delay on the Dose Response of Kodak EDR2 Film. *Medical Physics* **31**:2284-2288.
- Chugh K., Dinu P., Bednarek D.R., Wobschall D., Rudin S., Hoffmann K., Peterson R. and Zeng M. (2004).** A Computer-Graphic Display for Real-Time Operator Feedback During Interventional X-Ray Procedures. *Proceedings of SPIE* **5367**:464-473.
- Clark A.L., Brennan A.G., Robertson L.J. and McArthur J.D. (2000).** Factors Affecting Patient Radiation Exposure During Routine Coronary Angiography in a Tertiary Referral Centre. *British Journal of Radiology* **73**:184-189.
- Cohen G., McDaniel D.L. and Wagner L.K. (1984).** Analysis of Variations in Contrast-Detail Experiments. *Medical Physics* **11**:469-473.

Cook A., Walmsley B. and Gallacher D. Management of potential skin burns in cardiac catheter labs. In: IPEM Meetings: Risk Management and Dose Reduction in Diagnostic Radiology; 2004 January 29; Queen Elizabeth Hospital Postgraduate Centre, Birmingham. Institute of Physics and Engineering in Medicine, 2004.

Cowen A.R., Clarke O.F., Coleman N.J., Craven D.M., McArdle S. and Hay G.A. (1992). Leeds X-Ray Test Objects Instruction Manual. Leeds, UK: University of Leeds.

Cranage R.W., Howard C.J. and Welsh A.D. (1992). Dose Reduction by the Use of Erbium Filtration in a General Radiographic Room. *British Journal of Radiology* **65**:232-237.

Crawley M.T., Shine B. and Booth A. (1998). Radiation Dose and Diagnosticity of Barium Enema Examinations by Radiographers and Radiologists: a Comparative Study. *British Journal of Radiology* **71**:399-405.

D'Incan M., Roger H., le Boudec M.C.F. and Souteyrand P. (1997). Radiodermatitis Following Cardiac Catheterization. *Archives of Dermatology* **133**:242-243.

Dehen L., Vilmer C., Humiliere C., Corcos T., Pentousis D., Ollivaud L., Chatelain D. and Dubertret L. (1999). Chronic Radiodermatitis Following Cardiac Catheterisation: a Report of Two Cases and a Brief Review of the Literature. *Heart* **81**:308-312.

Delichas M.G., Hatziioannou K., Papanastassiou E., Albanopoulou P., Chatzi E., Sioundas A. and Psarrakos K. (2004). Radiation Doses to Patients Undergoing Barium Meal and Barium Enema Examinations. *Radiation Protection Dosimetry* **109**:243-247.

Delichas M.G., Psarrakos K., Molyvda-Athanassopoulou E., Giannoglou G., Hatziioannou K. and Papanastassiou E. (2003). Radiation Doses to Patients Undergoing Coronary Angiography and Percutaneous Transluminal Coronary Angioplasty. *Radiation Protection Dosimetry* **103**:149-154.

Delichas M.G., Psarrakos K., Giannoglou G., Molyvda-Athanasopoulou E., Hatziioannou K. and Papanastassiou E. (2005). Skin Doses to Patients Undergoing

Coronary Angiography in a Greek Hospital. *Radiation Protection Dosimetry* **113**:449-452.

den Boer A., de Feijter P.J., Hummel W.A. and Hoornaert B. (1994a). Additional Beam Filtering in Cardiac Fluoroscopy: Clinical Evaluation. Best, Netherlands: Philips Medical Systems.

den Boer A., de Feijter P.J., Serruys P.W. and Roelandt J.R.T.C. (2001). Real-Time Quantification and Display of Skin Radiation During Coronary Angiography and Intervention. *Circulation* **104**:1779-1784.

den Boer A., de Feijter P.J., Hummel W.A., Keane D. and Roelandt J.R. (1994b). Reduction of Radiation Exposure While Maintaining High-Quality Fluoroscopic Images During Interventional Cardiology Using Novel X-Ray Tube Technology With Extra Beam Filtering. *Circulation* **89**:2710-2714.

Dendy P.P. and Heaton B. (1999). Physics for Diagnostic Radiology. Bristol, UK: Institute of Physics Publishing.

Dobbins J.T., Samei E., Chotas H.G., Warp R.J., Baydush A.H., Floyd C.E.J. and Ravin C.E. (2003). Chest Radiography: Optimization of X-Ray Spectrum for Cesium Iodide-Amorphous Silicon Flat-Panel Detector. *Radiology* **226**:221-230.

Dosimetry Working Party of the Institute of Physical Sciences in Medicine (1992). National Protocol for Patient Dose Measurements in Diagnostic Radiology. Chilton, UK: National Radiation Protection Board.

Dowsett D.J., Kenny P.A. and Johnston R.E. (1998). The Physics of Diagnostic Imaging. London, UK: Chapman and Hall Medical.

Efstathopoulos E.P., Makrygiannis S.S., Kottou S., Karvouni E., Giazitzoglou E., Korovesis S., Tzanalaridou E., Raptou P.D. and Katritsis D.G. (2003). Medical Personnel and Patient Dosimetry During Coronary Angiography and Intervention. *Physics in Medicine and Biology* **48**:3059-3068.

European Commission (1996). European Guidelines on Quality Criteria for Diagnostic Radiographic Images. **EUR 16260 EN.** Luxembourg: Office for Official Publication of the European Communities.

Fajardo L.C., Geise R.A. and Ritenoure R.A. (1995). A Survey of Films for Use As Dosimeters in Interventional Radiology. *Health Physics* **68**:595-599.

- Fink C., Hallscheidt P.J., Noeldge G., Kampschulte A., Radeleff B., Hosch W.P., Kauffmann G.W. and Hansmann J. (2002).** Clinical Comparative Study With a Large-Area Amorphous Silicon Flat-Panel Detector: Image Quality and Visibility of Anatomic Structures on Chest Radiography. *American Journal of Roentgenology* **178**:481-486.
- Fleay R.F., Fox R.A., Sprigg A. and Adams J.P. (1984).** Dose Reduction in Paediatric Radiology Using Rare Earth Filtration. *Pediatric Radiology* **14**:332-334.
- Fletcher D.W., Miller D.L., Balter S. and Taylor M.A. (2002).** Comparison of Four Techniques to Estimate Radiation Dose to Skin During Angiographic and Interventional Radiology Procedures. *Journal of Vascular and Interventional Radiology* **13**:391-397.
- Food and Drug Administration (1994).** Avoidance of Serious X-Ray-Induced Injuries to Patients During Fluoroscopically-Guided Procedures. Rockville, Maryland: Center for Devices and Radiological Health.
- Food and Drug Administration (1995).** Recording Information in the Patient's Medical Record That Identifies the Potential for Serious X-Ray Induced Skin Injuries Following Fluoroscopically Guided Procedures. Rockville, Maryland: Center for Devices and Radiological Health.
- Forster E. (1985).** Equipment for Diagnostic Radiography. Lancaster, UK: MTP Press Limited.
- Fransson S.G. and Persliden J. (2000).** Patient Radiation Exposure During Coronary Angiography and Intervention. *Acta Radiologica* **41**:142-144.
- Gagne R.M., Quinn P.W. and Jennings R.J. (1994).** Comparison of Beam-Hardening and K-Edge Filters for Imaging Barium and Iodine During Fluoroscopy. *Medical Physics* **21**:107-121.
- Garza L., Aude Y.W. and Saucedo J.F. (2002).** Can We Prevent in-Stent Restenosis? *Current Opinion in Cardiology* **17**:518-525.
- Geijer H. (2002).** Radiation Dose and Image Quality in Diagnostic Radiology. Optimization of the Dose-Image Quality Relationship With Clinical Experience From Scoliosis Radiography, Coronary Intervention and a Flat-Panel Digital Detector. *Acta Radiologica* **43**:1-43.

Geise R.A. and Ansel H.J. (1990). Radiotherapy Verification Film for Estimating Cumulative Entrance Skin Exposure for Fluoroscopic Examinations. *Health Physics* **59**:295-298.

Geise R.A., Schueler B.A., Lien W. and Jones S.C. (1997). Suitability of Laser Stimulated TLD Arrays As Patient Dose Monitors in High Dose X-Ray Imaging. *Medical Physics* **24**:1643-1646.

Geleijns J., Broerse J.J., Shaw M.P., Schultz F.W., Teeuwisse W., van Unnik J.G. and Zoetelief J. (1997). Patient Dose Due to Colon Examination: Dose Assessment and Results From a Survey in the Netherlands. *Radiology* **204**:553-559.

Goo J.M., Im J.G., Lee H.J., Chung M.J., Seo J.B., Kim H.Y., Lee Y.J., Kang J.W. and Kim J.H. (2002). Detection of Simulated Chest Lesions by Using Soft-Copy Reading: Comparison of an Amorphous Silicon Flat-Panel-Detector System and a Storage-Phosphor System. *Radiology* **224**:242-246.

Guibelalde E., Vanó E., Gonzalez L., Prieto C., Fernandez J.M. and Ten J.I. (2003). Practical Aspects for the Evaluation of Skin Doses in Interventional Cardiology Using a New Slow Film. *British Journal of Radiology* **76**:332-336.

Gunn J., Crossman D., Grech E.D. and Cumberland D. (2003). New Developments in Percutaneous Coronary Intervention. *British Medical Journal* **327**:150-153.

Hansson B., Finnbogason T., Schuwert P. and Persliden J. (1997). Added Copper Filtration in Digital Paediatric Double-Contrast Colon Examinations: Effects on Radiation Dose and Image Quality. *European Radiology* **7**:1117-1122.

Hansson B. and Karambatsakidou A. (2000). Relationships Between Entrance Skin Dose, Effective Dose and Dose Area Product for Patients in Diagnostic and Interventional Cardiac Procedures. *Radiation Protection Dosimetry* **90**:141-144.

Hart D., Hillier M.C. and Wall B.F. (2002). Doses to Patients From Medical X-Ray Examinations in the UK - 2000 Review. **NRPB-W14**. Chilton, UK: National Radiological Protection Board.

Hart D., Hillier M.C., Wall B.F., Shrimpton P.C. and Bungay D. (1996). Doses to Patients From Medical X-Ray Examinations in the UK - 1995 Review. **NRPB-R289**. Chilton, UK: National Radiological Protection Board.

Hart D., Jones D.G. and Wall B.F. (1994). Estimation of Effective Dose in Diagnostic Radiology From Entrance Surface Dose and Dose-Area Product Measurements. **NRPB-R262**. Chilton, UK: National Radiological Protection Board.

Hart D. and Wall B.F. (1994). Estimation of Effective Dose From Dose-Area Product Measurements for Barium Meals and Barium Enemas. *British Journal of Radiology* **67**:485-489.

Hart D. and Wall B.F. (1995). Technical Note: Potentially Higher Patient Radiation Doses Using Digital Equipment for Barium Studies. *British Journal of Radiology* **68**:1112-1115.

Hart D. and Wall B.F. (2002). Radiation Exposure of the UK Population From Medical and Dental X-Ray Examinations. **NRPB-W4**. Chilton, UK: National Radiological Protection Board.

Hay G.A., Clarke O.F., Coleman N.J. and Cowen A.R. (1985). A Set of X-Ray Test Objects for Quality Control in Television Fluoroscopy. *British Journal of Radiology* **58**:335-344.

Hetherington J., Chapple C.L. and Rawlings D.J. (1998). Radiation Dose and Diagnosticity of Barium Enema Examinations by Radiographers and Radiologists: a Comparative Study [Correspondence (3)]. *British Journal of Radiology* **71**:1219-1221.

Holmes D.R., Jr., Laskey W.K., Wondrow M.A. and Cusma J.T. (2004). Flat-Panel Detectors in the Cardiac Catheterization Laboratory: Revolution or Evolution - What Are the Issues? *Catheterization & Cardiovascular Interventions* **63**:324-330.

Hoornaert B. and Kroon J.N. (1993). Additional Beam Filtering in Cardiac Fluoroscopy: Technical Background. Best, Netherlands: Philips Medical Systems.

Hopewell J.W. (1990). The Skin: Its Structure and Response to Ionizing Radiation. *International Journal of Radiation Biology* **57**:751-753.

Horton D., Cook A.M. and Taylor A.D. (1992). Audit in Action: Significant Reduction of Double-Contrast Barium Enema Screening Time With No Loss of Examination Quality. *British Journal of Radiology* **65**:507-509.

Hwang E., Gaxiola E., Vlietstra R.E., Brenner A., Ebersole D. and Browne K. (1998). Real-Time Measurement of Skin Radiation During Cardiac Catheterization. *Catheterization & Cardiovascular Diagnosis* **43**:367-370.

Institute of Physics and Engineering in Medicine (1997). Recommended Standards for Routine Testing of Diagnostic X-Ray Imaging Systems. **Report 77.** York, UK: Institute of Physics and Engineering in Medicine.

Institute of Physics and Engineering in Medicine (2002). Medical and Dental Guidance Notes. York, UK: Institute of Physics and Engineering in Medicine.

International Commission on Radiological Protection (1991a). ICRP Publication 59, The Biological Basis for Dose Limitation in the Skin. *Annals of the ICRP* **22**.

International Commission on Radiological Protection (1991b). ICRP Publication 60: 1990 Recommendations of the International Commission on Radiological Protection. *Annals of the ICRP* **21, No. 1-3.** Oxford, UK: Pergamon Press.

International Commission on Radiological Protection (2000). Report 85: Avoidance of Radiation Injuries From Medical Interventional Procedures. *Annals of the ICRP* **30**:45-47.

International Electrotechnical Commission (2000). Medical Electrical Equipment-Part 2-43: Particular Requirements for the Safety of X-Ray Equipment for Interventional Procedures. **Report 60601-2-43.** Geneva, Switzerland: International Electrotechnical Commission.

Jennings R.J. (1988). A Method for Comparing Beam-Hardening Filter Materials for Diagnostic Radiology. *Medical Physics* **15**:588-599.

Jiang Y. and Wilson D.L. (2004). Optimization of Detector Pixel Size for Stent Visualization in X-Ray Fluoroscopy. *Proceedings of SPIE* **5372**:311-318.

Jones D.G. and Wall B.F. (1985). Organ Doses From Medical X-Ray Examinations Calculated Using Monte Carlo Techniques. **NRPB-R186.** Chilton, UK: National Radiological Protection Board.

Kandzari D.E., Tchong J.E. and Zidar J.P. (2002). Coronary Artery Stents: Evaluating New Designs for Contemporary Percutaneous Intervention. *Catheterization & Cardiovascular Interventions* **56**:562-576.

Karambatsakidou A., Tornvall P., Saleh N., Chouliaras T., Lofberg P.O. and Fransson A. (2005). Skin Dose Alarm Levels in Cardiac Angiography Procedures: Is a Single DAP Value Sufficient? *British Journal of Radiology* **78**:803-809.

Katristsis D., Efstathopoulos E., Betsou S., Korovesis S., Faulkner K., Panayiotakis G. and Webb-Peploe M.M. (2000). Radiation Exposure of Patients and Coronary Arteries in the Stent Era: a Prospective Study. *Catheterization & Cardiovascular Interventions* **51**:259-264.

Kawakami T., Saito R. and Miyazaki S. (1999). Chronic Radiodermatitis Following Repeated Percutaneous Transluminal Coronary Angioplasty. *British Journal of Dermatology* **141**:150-153.

Kemerink G.J., Borstlap A.C.W., Frantzen M.J., Schultz F.W., Zoetelief J. and van Engelshoven J.M.A. (2001). Patient and Occupational Dosimetry in Double Contrast Barium Enema Examinations. *British Journal of Radiology* **74**:420-428.

Kerensky R.A., Cusma J.T., Kubilis P., Simon R., Bashore T.M., Hirshfeld J.W., Jr., Holmes D.R.J., Pepine C.J. and Nissen S.E. (2000). American College of Cardiology/European Society of Cardiology International Study of Angiographic Data Compression Phase I. The Effects of Lossy Data Compression on Recognition of Diagnostic Features in Digital Coronary Angiography. *Journal of the American College of Cardiology* **35**:1370-1379.

Koedooder K. and Venema H.W. (1986). Filter Materials for Dose Reduction in Screen-Film Radiography. *Physics in Medicine and Biology* **31**:585-600.

Koenig T.R., Mettler F.A. and Wagner L.K. (2001a). Skin Injuries From Fluoroscopically Guided Procedures: Part 2, Review of 73 Cases and Recommendations for Minimizing Dose Delivered to the Patient. *American Journal of Roentgenology* **177**:13-20.

Koenig T.R., Wolff D., Mettler F.A. and Wagner L.K. (2001b). Skin Injuries From Fluoroscopically Guided Procedures: Part 1, Characteristics of Radiation Injury. *American Journal of Roentgenology* **177**:3-11.

Kohn M.L., Gooch A.W. and Keller W.S. (1988). Filters for Radiation Reduction: a Comparison. *Radiology* **167**:255-257.

Kroon H. (2003). An Overall X-Ray System Simulation Model Developed for System Design and Image Quality Versus Patient Dose Optimization. *Proceedings of SPIE* **5030**:445-458.

Kuon E., Glaser C. and Dahm J.B. (2003). Effective Techniques for Reduction of Radiation Dosage to Patients Undergoing Invasive Cardiac Procedures. *British Journal of Radiology* **76**:406-413.

Kuon E., Schmitt M. and Dahm J.B. (2002). Significant Reduction of Radiation Exposure to Operator and Staff During Cardiac Interventions by Analysis of Radiation Leakage and Improved Lead Shielding. *American Journal of Cardiology* - 49.

Lampinen J.S. and Rannikko S. (1999). Patient Specific Doses Used to Analyse the Optimum Dose Delivery in Barium Enema Examinations. *British Journal of Radiology* **72**:1185-1195.

Lanhede B., Bath M., Kheddache S., Sund P., Bjorneld L., Widell M., Almen A., Besjakov J., Mattsson S., Tingberg A., Herrmann C., Panzer W., Zankl M. and Mansson L.G. (2002). The Influence of Different Technique Factors on Image Quality of Chest Radiographs As Evaluated by Modified CEC Image Quality Criteria. *British Journal of Radiology* **75**:38-49.

Larrazet F., Dibie A., Philippe F., Palau R., Klausz R. and Laborde F. (2003). Factors Influencing Fluoroscopy Time and Dose-Area Product Values During Ad Hoc One-Vessel Percutaneous Coronary Angioplasty. *British Journal of Radiology* **76**:473-477.

Lichtenstein D.A., Klapholz L., Vardy D.A., Leichter I., Mosseri M., Klaus S. and Gilead L. (1996). Chronic Radiodermatitis Following Cardiac Catheterization. *Archives of Dermatology* **132**:663-667.

Lindholt J.S. (2003). Radiocontrast Induced Nephropathy. *European Journal of Vascular and Endovascular Surgery* **25**:296-304.

Lloyd P., Lowe D., Harty D.S. and Eyes B. (1998). The Secondary Radiation Grid; Its Effect on Fluoroscopic Dose-Area Product During Barium Enema Examinations. *British Journal of Radiology* **71**:303-306.

- Lobotessi H., Karoussou A., Neofotistou V., Louisu A. and Tsapaki V. (2001).** Effective Dose to a Patient Undergoing Coronary Angiography. *Radiation Protection Dosimetry* **94**:173-176.
- Lowe H.C., Oesterle S.N. and Khachigian L.M. (2002).** Coronary in-Stent Restenosis: Current Status and Future Strategies. *Journal of the American College of Cardiology* **39**:183-193.
- Ludwig K., Lenzen H., Kamm K.-H., Link T.M., Diederich S., Wormanns D. and Heindel W. (2002).** Performance of a Flat-Panel Detector in Detecting Artificial Bone Lesions: Comparison With Conventional Screen-Film and Storage-Phosphor Radiography. *Radiology* **222**:453-459.
- Maccia C., Moores B.M. and Wall B.F. (1996).** The 1991 CEC Trial on Quality Criteria for Diagnostic Radiographic Images: Detailed Results and Findings. **EUR 16635 EN.** Luxemburg: Office for Official Publication of the European Communities.
- Marshall N.W., Faulkner K., Kotre C.J. and Robson K. (1992).** Analysis of Variations in Contrast-Detail Measurements Performed on Image Intensifier-Television Systems. *Physics in Medicine and Biology* **37**:2297-2302.
- Martin C.J. (2004).** A Review of Factors Affecting Patient Doses for Barium Enemas and Meals. *British Journal of Radiology* **77**:864-868.
- Martin C.J. and Hunter S. (1994).** Reduction of Patient Doses From Barium Meal and Barium Enema Examinations Through Changes in Equipment Factors. *British Journal of Radiology* **67**:1196-1205.
- Martin C.J., Sharp P.F. and Sutton D.G. (1999).** Measurement of Image Quality in Diagnostic Radiology. *Applied Radiation and Isotopes* **50**:21-38.
- Mayr N.A., Riggs C.E.Jr., Saag K.G., Wen B.C., Pennington E.C. and Hussey D.H. (1997).** Mixed Connective Tissue Disease and Radiation Toxicity: a Case Report. *Cancer* **79**:612-618.
- McCullough P.A., Wolyn R., Rocher L.L., Levin R.N. and O'Neill W.W. (1997).** Acute Renal Failure After Coronary Intervention: Incidence, Risk Factors, and Relationship to Mortality. *American Journal of Medicine* **103**:368-375.

- McFadden S.L., Mooney R.B. and Shepherd P.H. (2002).** X-Ray Dose and Associated Risks From Radiofrequency Catheter Ablation Procedures. *British Journal of Radiology* **75**:253-265.
- McLean A.S. (1973).** Early Adverse Effects of Radiation. *British Medical Bulletin* **29**:69-73.
- McParland B.J. and Boyd M.M. (2000).** X-Ray Image Intensifier Performance and Patient Doses for Combinations of Supplemental Beam Filters and Vascular Contrast Agents. *Physics in Medicine and Biology* **46**:227-244.
- McVey G., Sandborg M., Dance D.R. and Alm Carlsson G. (2003).** A Study and Optimization of Lumbar Spine X-Ray Imaging System. *British Journal of Radiology* **76**:177-188.
- Metz C.E. (1978).** Basic Principles of ROC Analysis. *Seminars in Nuclear Medicine* **8**:283-298.
- Miller D.L., Balter S., Noonan P.T. and Georgia J.D. (2002).** Minimizing Radiation-Induced Skin Injury in Interventional Radiology Procedures. *Radiology* **225**:329-336.
- Miralbell R., Maillet P., Crompton N.E., Doriot P.A., Nouet P., Verin V., Harms and Rouzaud M. (1999).** Skin Radionecrosis After Percutaneous Transluminal Coronary Angioplasty: Dosimetric and Biological Assessment. *Journal of Vascular and Interventional Radiology* **10**:1190-1194.
- Mooney R.B. (2000).** Skin Dose to Patients From Interventional Radiology and Cardiology Procedures With Potentially Long Fluoroscopy Times. *Radiation Protection Dosimetry* **90**:123-126.
- Morrell R.E., Rogers A.T., Jobling J.C. and Shakespeare K.E. (2004).** Barium Enema: Use of Increased Copper Filtration to Optimize Dose and Image Quality. *British Journal of Radiology* **77**:116-122.
- Moy J.-P. (2000).** Recent Developments in X-Ray Imaging Detectors. *Nuclear Instruments and Methods in Physics Research A* **422**:23-37.
- National Electrical Manufacturers Association (2004).** Digital Imaging and Communications in Medicine (DICOM). Part 1: Introduction and Overview. **PS 3.1-2004**. Rosslyn, Virginia: National Electrical Manufacturers Association.

National Radiological Protection Board (1993). Estimates of Late Radiation Risks to the UK Population. *Documents of the NRPB Vol. 4, No. 4*. Chilton, UK: National Radiological Protection Board.

National Radiological Protection Board (1996). Risk From Deterministic Effects of Ionising Radiation. *Documents of the NRPB 7(3)*. London: HMSO.

Neofotistou V., Vanõ E., Padovani R., Kotre J., Dowling A., Toivonen M., Kottou S., Tsapaki V., Willis S., Bernardi G. and Faulkner K. (2003). Preliminary Reference Levels in Interventional Cardiology. *European Radiology 13*:2259-2263.

Nicholson R., Tuffee F. and Uthappa M.C. (2000). Skin Sparing in Interventional Radiology: the Effect of Copper Filtration. *British Journal of Radiology 73*:36-42.

Obuchowski N.A. (2003). Receiver Operating Characteristic Curves and Their Use in Radiology. *Radiology 229*:3-8.

Obuchowski N.A. (2005). ROC Analysis. *American Journal of Roentgenology 184*:364-372.

Oda N., Nakate H., Murakami S., Terada K., Nakamura K. and Yoshida A. (1996). Optimal Beam Quality for Chest Computed Radiography. *Investigative Radiology 31*:123-131.

Padovani R., Bernardi G., Malisan M.R., Vanõ E., Morocutti G. and Fioretti P.M. (2001). Patient Dose Related to the Complexity of Interventional Cardiology Procedures. *Radiation Protection Dosimetry 94*:189-192.

Paisley E.M., Eatough J.P., Mountford P.J., Frain G. and Pickerill J. (2004). Patient Radiation Doses During Invasive Cardiac Procedures Categorised by Clinical Code. *British Journal of Radiology 77*:1022-1026.

Pärtan G., Partik B., Mayrhofer R., Pichler L., Urban M., Gindl K. and Hruby W. (2000). Feasibility of 0.3mm Cu Additional Beam Filtration for Digital Gastrointestinal Fluorography. *Radiation Protection Dosimetry 90*:217-220.

Persliden J., Larsson P., Noren B. and Wirell S. (1997). Absorbed Dose and Image Quality in Examinations of the Colon With Digital and Analogue Techniques. *Acta Radiologica 38*:1010-1014.

Radke P.W., Kaiser A., Frost C. and Sigwart U. (2003). Outcome After Treatment of Coronary in-Stent Restenosis: Results From a Systematic Review Using Meta-Analysis Techniques. *European Heart Journal* **24**:266-273.

Raman S.V., Morford R., Neff M., Attar T.T., Kukielka G., Magorien R.D. and Bush C.A. (2004). Rotational X-Ray Coronary Angiography. *Catheterization & Cardiovascular Interventions* **63**:201-207.

Redlich U., Hoeschen C. and Dohring W. (2005). Assessment and Optimisation of the Image Quality of Chest-Radiography Systems. *Radiation Protection Dosimetry* **114**:269-272.

Reilly A.J. and Sutton D. (1997). Catalogue of Diagnostic X-Ray Spectra and Other Data. **Report No. 78.** York, UK: Institute of Physics and Engineering in Medicine.

Rosenthal L.S., Beck T.J., Williams J., Mahesh M., Herman M.G., Dinerman J.L., Calkins H. and Lawrence J.H. (1997). Acute Radiation Dermatitis Following Radiofrequency Catheter Ablation of Atrioventricular Nodal Reentrant Tachycardia. *Pacing and Clinical Electrophysiology* **20**:1834-1839.

Ross R.D., Joshi V., Carravallah D.J. and Morrow W.R. (1997). Reduced Radiation During Cardiac Catheterization of Infants Using Acquisition Zoom Technology. *American Journal of Cardiology* **79**:691-693.

Rossi R.P., Harnisch B. and Hendee W.R. (1982). Reduction in Radiation Exposure in Radiography of the Chest. *Radiology* **144**:909-914.

Ruiz-Cruces R., Ruiz F., Perez-Martinez M., Lopez J., Tort Ausina I. and Diez de los Rios A. (2000). Patient Dose From Barium Procedures. *British Journal of Radiology* **73**:752-761.

Ryan T.J., Faxon D.P., Gunnar R.M., Kennedy J.W., King S.B., Loop F.D., Peterson K.L., Reeves T.J., Williams D.O., Winters W.L., Fisch C., DeSanctis R.W., Dodge H.T., Reeves T.J. and Weinberg S.L. (1988). Guidelines for Percutaneous Transluminal Coronary Angioplasty: a Report of the American College of Cardiology/American Heart Association Task Force on Assessment of Diagnostic and Therapeutic Cardiovascular Procedures (Subcommittee on Percutaneous Transluminal Coronary Angioplasty). *Circulation* **78**:486-502.

Samei E., Dobbins J.T., Lo J.Y. and Tornai M.P. (2005). A Framework for Optimising the Radiographic Technique in Digital X-Ray Imaging. *Radiation Protection Dosimetry* **114**:220-229.

Sandborg M. and Alm Carlsson G. (1992). Influence of X Ray Energy Spectrum, Contrasting Detail and Detector on the Signal-to-Noise Ratio (SNR) and Detective Quantum Efficiency (DQE) in Projection Radiography. *Physics in Medicine and Biology* **37**:1245-1263.

Sandborg M., Carlsson C.A. and Alm Carlsson G. (1994a). Shaping X-Ray Spectra With Filters in X-Ray Diagnostics. *Medical & Biological Engineering & Computing* **32**:384-390.

Sandborg M., Dance D.R., Alm Carlsson G. and Persliden J. (1993). Monte Carlo Study of Grid Performance in Diagnostic Radiology: Factors Which Affect the Selection of Tube Potential and Grid Ratio. *British Journal of Radiology* **66**:1164-1176.

Sandborg M., Dance D.R., Alm Carlsson G. and Persliden J. (1994b). Monte Carlo Study of Grid Performance in Diagnostic Radiology: Task Dependent Optimization for Screen-Film Imaging. *British Journal of Radiology* **67**:76-85.

Sandborg M., Tingberg A., Dance D.R., Lanhede B., Almen A., McVey G., Sund P., Kheddache S., Besjakov J., Mattsson S., Mansson L.G. and Alm Carlsson G. (2001). Demonstration of Correlations Between Clinical and Physical Image Quality Measures in Chest and Lumbar Spine Screen-Film Radiography. *British Journal of Radiology* **74**:520-528.

Seymour R. (1997). Patient Dose Reduction by Audit of Grid Usage in Barium Enemas. *British Journal of Radiology* **70**:489-491.

Shope T.B. (1996). Radiation-Induced Skin Injuries From Fluoroscopy. *Radiographics* **16**:1195-1199.

Shrimpton P.C., Wall B.F., Jones D.G., Fisher E.S., Hillier M.C., Kendall G.M. and Harrison R.M. (1986). A National Survey of Doses to Patients Undergoing a Selection of Routine X-Ray Examinations in English Hospitals. **NRPB-R200**. Chilton, UK: National Radiological Protection Board.

Siegel S. and Castellan N.J. (1988). Nonparametric Statistics for the Behavioral Sciences. Second Edition. Singapore: McGraw-Hill.

Silber S., Dorr R., Zindler G., Muhling H. and Diebel T. (1997). Impact of Various Compression Rates on Interpretation of Digital Coronary Angiograms. *International Journal of Cardiology* **60**:195-200.

Skinner C.L. Implementation of IR(ME)R in cardiac angiography. In: Proceedings of UK Radiological Congress 2002; 2002 June 9-11; Birmingham, UK. London, UK: British Institute of Radiology, 2002.

Smiddy P.F., Quinn A.D., Freyne P.J., Marsh D. and Murphy J.M. (1996). Dose Reduction in Double Contrast Barium Enema by Use of Low Fluoroscopic Current. *British Journal of Radiology* **69**:852-854.

Sousa J.E., Serruys P.W. and Costa M.A. (2003a). New Frontiers in Cardiology: Drug-Eluting Stents: Part I. *Circulation* **107**:2274-2279.

Sousa J.E., Serruys P.W. and Costa M.A. (2003b). New Frontiers in Cardiology: Drug-Eluting Stents: Part II. *Circulation* **107**:2383-2389.

Sovik E., Klow N.E., Hellesnes J. and Lykke J. (1996). Radiation-Induced Skin Injury After Percutaneous Transluminal Coronary Angioplasty. Case Report. *Acta Radiologica* **37**:305-306.

Spahn M., Strotzer M., Volk M., Bohm S., Geiger B., Hahm G. and Feuerbach S. (2000). Digital Radiography With a Large-Area, Amorphous Silicon, Flat-Panel X-Ray Detector System. *Investigative Radiology* **35**:260-266.

Strotzer M., Gmeinwieser J., Spahn M., Volk M., Frund R., Seitz J., Spies V., Alexander J. and Feuerbach S. (1998a). Amorphous Silicon, Flat-Panel, X-Ray Detector Versus Screen-Film Radiography: Effect of Dose Reduction on the Detectability of Cortical Bone Defects and Fractures. *Investigative Radiology* **33**:33-38.

Strotzer M., Gmeinwieser J., Volk M., Frund R., Seitz J. and Feuerbach S. (1998b). Detection of Simulated Chest Lesions With Normal and Reduced Radiation Dose: Comparison of Conventional Screen-Film Radiography and a Flat-Panel X-Ray Detector Based on Amorphous Silicon. *Investigative Radiology* **33**:98-103.

- Strotzer M., Volk M., Wild T., von Landenberg P. and Feuerbach S. (2000).** Simulated Bone Erosions in a Hand Phantom: Detection With Conventional Screen-Film Technology Versus Cesium Iodide-Amorphous Silicon Flat-Panel Detector. *Radiology* **215**:512-515.
- Sund P., Herrmann C., Tingberg A., Kheddache S., Mansson L.G., Almen A. and Mattsson S. (2000).** Comparison of Two Methods for Evaluating Image Quality of Chest Radiographs. *Proceedings of SPIE* **3981**:251-257.
- Tapiovaara M.J. and Sandborg M. (1995).** Evaluation of Image Quality in Fluoroscopy by Measurements and Monte Carlo Calculations. *Physics in Medicine and Biology* **40**:589-607.
- Tapiovaara M.J. and Sandborg M. (2004).** How Should Low-Contrast Detail Detectability Be Measured in Fluoroscopy? *Medical Physics* **31**:2564-2576.
- Tapiovaara M.J. and Wagner R.F. (1985).** SNR and DQE Analysis of Broad Spectrum X-Ray Imaging. *Physics in Medicine and Biology* **30**:519-529.
- The Council of the European Union (1997).** Council Directive 97/43/Euratom on Health Protection of Individuals Against the Dangers of Ionizing Radiation in Relation to Medical Exposure. *Official Journal of the European Communities* **L180**:22-27.
- The Ionising Radiation (Medical Exposure) Regulations 2000.** Statutory Instruments 2000, No. 1059. London: The Stationery Office, 2000.
- The Ionising Radiations Regulations 1999.** Statutory Instruments 1999, No. 3232. London: The Stationery Office, 1999.
- Tingberg A., Herrmann C., Besjakov J., Rodenacker K., Almen A., Sund P., Mattsson S. and Mansson L.G. (2000).** Evaluation of Lumbar Spine Images With Added Pathology. *Proceedings of SPIE* **3981**:34-42.
- Tingberg A., Bath M., Hakansson M., Medin J., Sandborg M., Alm Carlsson G., Mattsson S. and Mansson L.G. (2004).** Comparison of Two Methods for Evaluation of Image Quality of Lumbar Spine Radiographs. *Proceedings of SPIE* **5372**:251-262.
- Trout E.D., Kelley J.P. and Cathey G.A. (1952).** The Use of Filters to Control Radiation Exposure to the Patient in Diagnostic Roentgenology. *American Journal of Roentgenology* **67**:946-962.

- Tsapaki V., Kottou S., Vanō E., Faulkner K., Giannouleas J., Padovani R., Kyrozi E., Koutelou M., Vardalaki E. and Neofotistou V. (2003).** Patient Dose Values in a Dedicated Greek Cardiac Centre. *British Journal of Radiology* **76**:726-730.
- Uffmann M., Neitzel U., Prokop M., Kabalan N., Weber M., Herold C.J. and Schaefer-Prokop C. (2005).** Flat-Panel-Detector Chest Radiography: Effect of Tube Voltage on Image Quality. *Radiology* **235**:642-650.
- Ullman G., Sandborg M., Dance D.R., Hunt R. and Alm Carlsson G. (2005a).** Distributions of Scatter-to-Primary and Signal-to-Noise Ratios Per Pixel in Digital Chest Imaging. *Radiation Protection Dosimetry* **114**:355-358.
- Ullman G., Sandborg M., Dance D.R., Yaffe M. and Alm Carlsson G. (2005b).** A Search for Optimal X-Ray Spectra in Iodine Contrast Media Mammography. *Physics in Medicine and Biology* **50**:3143-3152.
- van de Putte S., Verhaegen F., Taeymans Y. and Thierens H. (2000).** Correlation of Patient Skin Doses in Cardiac Interventional Radiology With Dose-Area Product. *British Journal of Radiology* **73**:504-513.
- Vanō E., Arranz L., Sastre J.M., Moro C., Ledo A., Garate M.T. and Minguez I. (1998a).** Dosimetric and Radiation Protection Considerations Based on Some Cases of Patient Skin Injuries in Interventional Cardiology. *British Journal of Radiology* **71**:510-516.
- Vanō E., Goicolea J., Galvan C., Gonzalez L., Meiggs L., Ten J.I. and Macaya C. (2001a).** Skin Radiation Injuries in Patients Following Repeated Coronary Angioplasty Procedures. *British Journal of Radiology* **74**:1023-1031.
- Vanō E., Gonzalez L., Guibelalde E., Fernandez J.M. and Ten J.I. (1998b).** Radiation Exposure to Medical Staff in Interventional and Cardiac Radiology. *British Journal of Radiology* **71**:954-960.
- Vanō E., Gonzalez L., Ten J.I., Fernandez J.M., Guibelalde E. and Macaya C. (2001b).** Skin Dose and Dose-Area Product Values for Interventional Cardiology Procedures. *British Journal of Radiology* **74**:48-55.

- Vanõ E., Guibelalde E., Fernandez J.M., Gonzalez L. and Ten J.I. (1997).** Patient Dosimetry in Interventional Radiology Using Slow Films. *British Journal of Radiology* **70**:195-200.
- Vanõ E., Guibelalde E., Morillo A., Alvarez-Pedrosa C.S. and Fernandez J.M. (1995).** Evaluation of the European Image Quality Criteria for Chest Examinations. *British Journal of Radiology* **68**:1349-1355.
- Vanõ E., Prieto C., Fernandez J.M., Gonzalez L., Sabate M. and Galvan C. (2003).** Skin Dose and Dose-Area Product Values in Patients Undergoing Intracoronary Brachytherapy. *British Journal of Radiology* **76**:32-38.
- Vehmas T. (1997).** Hawthorne Effect: Shortening of Fluoroscopy Times During Radiation Measurement Studies. *British Journal of Radiology* **70**:1053-1055.
- Verdun F.R., Capasso P., Valley J.F. and Schnyder P. (1998).** Dose Evaluation in Fluoroscopy. *Radiation Protection Dosimetry* **80**:139-141.
- Villagran J.E., Hobbs B.B. and Taylor K.W. (1978).** Reduction of Patient Exposure by Use of Heavy Elements As Radiation Filters in Diagnostic Radiology. *Radiology* **127**:249-254.
- Volk M., Strotzer M., Holzkecht N., Manke C., Lenhart M., Gmeinwieser J., Link J., Reiser M. and Feuerbach S. (2000).** Digital Radiography of the Skeleton Using a Large-Area Detector Based on Amorphous Silicon Technology: Image Quality and Potential for Dose Reduction in Comparison With Screen-Film Radiography. *Clinical Radiology* **55**:615-621.
- Wagner L.K., Eifel P.J. and Geise R.A. (1994).** Potential Biological Effects Following High X-Ray Dose Interventional Procedures. *Journal of Vascular and Interventional Radiology* **5**:71-84.
- Wagner L.K., McNeese M.D., Marx M.V. and Siegel E.L. (1999).** Severe Skin Reactions From Interventional Fluoroscopy: Case Report and Review of Literature. *Radiology* **213**:773-776.
- Waite J.C. and Fitzgerald M. (2001).** An Assessment of Methods for Monitoring Entrance Surface Dose in Fluoroscopically Guided Interventional Procedures. *Radiation Protection Dosimetry* **94**:89-92.

Warren-Forward H.M., Haddaway M.J., Temperton D.H. and McCall I.W. (1998). Dose-Area Product Readings for Fluoroscopic and Plain Film Examinations, Including an Analysis of the Source of Variation for Barium Enema Examinations. *British Journal of Radiology* **71**:961-967.

Widmark A., Forsmark H., Einarsson G., Grundtoft P., Hjordemaal O., Leitz W. and Pukkila O. (2001). Guidance Levels in the Nordic Countries: a Preliminary Report for Selected Interventional Procedures. *Radiation Protection Dosimetry* **94**:133-135.

Widmark A. and Hellesnes J. Acute radiation injury after percutaneous transluminal coronary angioplasty (PTCA): a case report. In: Joint WHO/ISH Workshop on Efficacy and Radiation Safety in Interventional Radiology; 1995 October 9-13; Munich-Neuherberg. Salzgitter, Germany: Bundesamt für Strahlenschutz, 1997.

Willis C.E. and Bencomo J.A. (1990). Logistic Representation of the Sensitometric Response of Screen-Film Systems: Empirical Validation. *Medical Physics* **17**:676-680.

Wilson D.L., Jiang Y., Srinivas Y. and Manjeshwar R.M. (2003). Optimization of Flat Panel Detector Characteristics and Processing Using Quantitative Image Quality Techniques. *Proceedings of SPIE* **5030**:48-59.

Wong L. and Rehm J. (2004). Radiation Injury From a Fluoroscopic Procedure. *The New England Journal of Medicine* **350**:e23.

World Health Organization. (2000). Efficacy and Radiation Safety in Interventional Radiology. Geneva: World Health Organization.

Yakoumakis E., Tsalafoutas I.A., Sandilos P., Koulentianos H., Kasfiki A., Vlahos L. and Proukakis C. (1999). Patient Doses From Barium Meal and Barium Enema Examinations and Potential for Reduction Through Proper Set-Up of Equipment. *British Journal of Radiology* **72**:173-178.

Yoshinaga H., Takeshita K., Sawada S., Russel V.W. and Antoku S. (1967). Estimation of Exposure Pattern and Bone Marrow and Gonadal Doses During Fluoroscopy. *British Journal of Radiology* **40**:344-349.

Yu S.K., Cheung Y.K., Chan T.L., Kung C.M. and Yuen M.K. (2001). Reduction of Radiation Dose to Patients Undergoing Barium Enema by Dose Audit. *British Journal of Radiology* **74**:162-165.

Zamenhof R.G. (1982). The Optimization of Signal Detectability in Digital Fluoroscopy. *Medical Physics* **9**:688-694.

Zhou X.-H. and Gao S. (1997). Confidence Intervals for the Log-Normal Mean. *Statistics in Medicine* **16**:783-790.

Zhu X.R., Yoo S., Jursinic P.A., Grimm D.F., Lopez F., Rownd J.J. and Gillin M.T. (2003). Characteristics of Sensitometric Curves of Radiographic Films. *Medical Physics* **30**:912-919.